How Does the Atmospheric Jet Stream Affect the Atlantic Ocean?

Liping Ma

A thesis presented for the degree of

Doctor of Philosophy

Department of Earth, Ocean and Ecological Sciences

School of Environmental Sciences

University of Liverpool, United Kingdom

12th September 2021

Email: Liping.Ma@liverpool.ac.uk

Abstract

The role of the atmospheric jet stream in driving North Atlantic ocean surface variables and interior variables and circulations are examined. Seasonal-timescale ensemble hindcasts from the UK Met Office Hadley Centre are analysed for each winter from 1980 to 2014, which for each year includes 40 ensemble members initialised at the start of November. The spread between ensemble members that develops during a season is interpreted to represent the ocean response to stochastic atmospheric variability. The atmospheric jet is defined by its speed and latitude. The seasonal coupling between the winter atmosphere and the ocean over much of the North Atlantic reveals anomalies in surface heat loss. In turn, air-sea heat flux anomalies control subsequent sea surface temperature anomalies with a characteristic tripole pattern, and sea-ice fraction with a dipole pattern. The surface temperature anomalies affect the mixed layer thickness, consequently driving temperature vertically penetrating into the subsurface by convection due to surface heat flux anomalies and entrainment processes via the mixed layer depth.

The atmospheric jet speed and latitude affect patterns of surface wind stress anomalies, resulting in the driving of AMOC anomalies on seasonal timescales. The AMOC is decomposed into three dynamical components, the Ekman component, geostrophic component and external mode component. The AMOC cells strengthening over the subtropics and weakening

over the subpolar are strongly caused by the surface wind stress induced Ekman MOC associated with jet indices.

On the seasonal timescale, the effect of jet speed is more pronounced than that of jet latitude on the ocean response, although the effect of jet latitude is important in altering the extent of the ocean subtropical and subpolar gyres.

Supervisors: Prof.Ric Williams and Prof.Tim Woollings, Dr.Vassil Roussenov

Acknowledgements

Acknowledgements

I would like to express my thanks to NERC for funding this project with studentship NE/L002469/1. I would like to thank the University of Liverpool for providing all facilities to implement this work.

I would like to thank my primary supervisor Prof. Ric Williams for his advice, support and organising things during my PhD study. I also would like to thank co-supervisor Prof. Tim Woollings from the University of Oxford for being with us providing scientific support. I would like to thank co-supervisor Dr. Vassil Roussenov for his support.

I would like to thank Dr. Doug Smith and his research team from the Met Office Hadley Centre for supplying the ensemble model data for this project and for introducing me the Python Iris package. I would like to thank Dr. Bablu Sinha from the National Oceanography Centre, Southampton, for introducing me to ocean NEMO model data with some advice on how to use it.

I would like thank to JASMIN team provideing excellent Linux workstation service so that I can deal with large ensemble data and computing.

Contents

Declaration

The work in this thesis is based on research carried out at the Department of Earth, Ocean and Ecological Sciences, University of Liverpool, England. No part of this thesis has been submitted elsewhere for any other degree or qualification, and it is the sole work of the author unless referenced to the contrary in the text.

Some of the work presented in this thesis has been published in journals and conference proceedings - the relevant publications are listed below.

Publications

Ma, L., T. Woollings, R.G. Williams, D. Smith and N. Dunstone, 2020. How does the winter jet stream affect surface temperature, heat flux and sea ice in the North Atlantic? *Journal of Climate*, Volume 33 No. 9 page 3711 - 3730.

Note: I have done all the work: analysis, computing, plots and writing. Prof.Tim Woollings and Prof.Ric Williams set the study plan at the beginning and gave me feedback and comments to improve this study. Dr. Doug Smith and Dr. Nick Dunstone provided Hadley Centre DePreSys3 model data.

List of Figures

List of Tables

Table 1: Definitions of Weather Regime

Weather Regimes	Geographic regions			
	Iceland (25°W-16.5°W 60°N-70°N)	Azores (28.5°W-20°W 36°N-40°N)	Scandinavia (20°W-30°E 50°N-65°N)	Central Atlantic (40°W-20°W 35°N-60°N)
NAO+ (21%) (1320 days out of 6137 days)	Azores GHTA minus Iceland GHTA > 170m			
NAO- (24.8%) (1547 days out of 6137 days)	Azores GHTA minus Iceland GHTA < -170m			
SBL (20%) (1272days out of 6137 days)			GHTA > 100m	
AR 18% (1126 days of out 6137 days)				GHTA > 95m
AT (19%) (1214 days out of 6137 days)				GHTA < -100m

(note: GHTA refers to geopotential height anomalies at 500 hPa (units: m); each region mean is taken an area average over an X-Y region given. SBL refers to Scandinavian Blocking; AR refers to central Atlantic Ridge. AT refers to central Atlantic Trough.)

Chapter 1

Introduction

This thesis aims to investigate how the atmosphere and ocean interact over the North Atlantic. Hence, I begin with a literature review and summarise what important results have been achieved in this field and what is new work in my thesis. Finally, I revise the fundamental phenomena of atmosphere and ocean over the North Atlantic.

1.1 Previous study for the connection between atmosphere and ocean

Mid-latitude atmospheric variability is known to strongly influence the underlying ocean, in particular by modulating surface heat fluxes and wind-induced Ekman circulations and consequently, changes in ocean buoyancy forcing and changes in AMOC variability. The atmospheric influence on the North Atlantic

Ocean is often viewed in terms of the North Atlantic Oscillation (NAO) which is strongly associated with a tripole pattern in sea surface temperatures (Bjerknes, 1964; Visbeck et al., 2003; Marshall and Coauthors, 2001; Eden and Willebrand, 2001). The influence of this atmospheric forcing linked to the NAO includes local and teleconnection responses which impact ocean heat storage over the North Atlantic. Anomalies in air-sea heat flux drive ocean convection and interannual changes in local heat content over the subpolar gyre (Visbeck et al., 2003; Grist et al., 2010), while changes in wind stress drive variations in subtropical heat content (Lozier et al., 2008; Williams et al., 2014). The inter-gyre transfers between the subtropical and subpolar gyres (Marshall et al., 2001) are due to changes in circulation associated with NAO. The combined effect of wind stress and air-sea buoyancy flux changes drive variations in the meridional overturning (Lozier et al., 2010; Robson et al., 2012), which in turn alters the gyre-scale convergence in heat transport (Williams et al., 2014, 2015b) and controls multi-year and decadal changes in ocean heat content due to meridional overturning circulation variation changes in heat transport.

For decadal variability, quasi-stochastic forcing by the atmosphere (buoyancy fluxes and wind stress) is an important driver of ocean MOC (Meridional Overturning Circulation) variability (Drijfhout and Hazeleger, 2007; Ortega et al., 2017). The mechanism of AMOC (Atlantic Meridional Overturning Circulation) decadal variability might be affected by the NAO decadal oscillation (Delworth and Zeng, 2016; Lozier et al., 2010). The study by Ortega et al. (2017) found

that the Labrador Sea density variability has an important role in influencing the subpolar gyre and AMOC variability in the upper 1500 m. Their study revealed that there are three key factors influencing the Labrador Sea density: (i) local heat flux associated with NAO variability in interannual timescale; (ii) the Greenland–Scotland Ridge outflows in multidecadal to centennial timescale due to changes in freshwater exporting through the East Greenland Current and changes in density in the Denmark Strait Overflow; (iii) the Labrador Sea densities associated with NAO variability in decadal timescale. The deep convection in the Labrador sea is a significant donor to North Atlantic Deep Water (NADW) formation, which consequently influences the strength of the deep western boundary current (DWBC) (Haine et al., 2008; Hodson and Sutton, 2012). Modelling studies (e.g. Delworth et al. 1993; Eden and Willebrand 2001) suggest that Labrador Sea waters can influence both the AMOC and the subpolar gyre strength and hence affect decadal variability in the wider North Atlantic. However, the OSNAP measurements reveal strong variability of transport in the region and show that deep water formation in the Labrador Sea may not be the major determinant of AMOC variability (Lozier et al., 2019).

1.2 The Thesis Study

1.2.1 Why do I choose eddy-driven jet stream to represent atmospheric variability to interact with the ocean instead of multi-weather regimes?

In this thesis I focus on the eddy-driven jet stream at low level 850hPa. Fundamentally, the dominant atmospheric phenomenon in the mid latitudes is the eddy-driven jet stream, affecting the formation and passage of synoptic-scale weather systems (Hoskins et al., 1983; Woollings et al., 2010; Hall et al., 2015; Madonna et al., 2017). Some recent studies discovered that the atmospheric variability associated with weather patterns such as NAO reflects eddy-driven jet components. Also, the eddy-driven jet can contribute to wind variation (Thompson et al., 2003; Lorenz and Hartmann, 2003). Secondly, the NAO is a statistical measure for the state of the atmosphere and is typically defined from the mean sea level pressure using principal component analysis or a simple point difference (Hurrell and Deser, 2010). As such, the NAO only empirically relates to the underlying atmospheric phenomena and may be affected by any circulation which projects onto its spatial pattern (Johnson et al., 2008). However, the majority of the variance of the NAO is known to represent variations of the North Atlantic eddy-driven jet stream (Thompson et al., 2003). Changes in both the strength and

the latitude of the jet project onto the NAO, so that a positive NAO may indicate a strengthening, or a northward shift of the jet, or both (Woollings et al., 2010). The implications of the NAO and other weather regimes, including atmospheric blocking, on the surface ocean have been investigated using nonlinear, regime-based methods (Cassou et al., 2004, 2011; Barrier et al., 2014). The East Atlantic pattern (EA) is also important (Woollings et al., 2010; Madonna et al., 2017) which has positive phase EA+ and negative phase EA-. In other studies, the EA is replaced by another name which is the central Atlantic Ridge (AR) Cassou et al. (2011). Where, the AR is the negative phase of the East Atlantic patterns.

Although combined in the NAO, there is evidence that the strength and position of the jet are physically-distinct structures of variability, for example having quite different seasonal cycles and power spectra, and they are generally uncorrelated in terms of interannual variability (Woollings et al., 2014). In addition, idealised models suggest that the jet indices have different sensitivities, for example with the jet latitude responding most strongly to local heating on either side of the jet maximum, while the jet speed is sensitive to heating in the deep tropics (Baker et al., 2017). These differing sensitivities can largely be understood as reflecting changes in the strength or location of the maximum meridional temperature gradient which can affect the growth of baroclinic eddies. The variation of jet latitude may be adjusted by the jet speed on decadal timescales linked to possible effects on ocean decadal variability (Woollings et al., 2018; Czaja, 2009;

Häkkinen et al., 2011). The behaviour of the jet stream speed and latitude location associated with different weather regimes is re-analysed in chapter 2. The eddy-driven jet stream behaviours are strongly linked with different weather regimes as revealed previously in a study by Madonna et al. (2017) and Woollings et al. (2010). Their studies demonstrated that eddy-driven jet speed and latitude variations can reflect multiple weather regimes.

Hence, I chose the eddy-driven jet stream to examine the influence of atmospheric variability on the North Atlantic ocean from surface to interior from the jet stream perspective, treating the jet position and strength separately. These jet indices are relatively simple, neglecting for example the meridional tilt of the jet (Madonna et al., 2017), but have the advantage of providing simple time series comparable to the multiple indices of weather regimes.

An additional motivation for this separation is that the NAO seems to reflect a different balance of the two jet indices on different timescales, with the jet latitude dominating on inter-annual timescales, but the jet speed becoming more important on multi-decadal timescales (Woollings et al., 2015).

Atlantic multi-decadal variability takes significant role on regional climate (Knight et al., 2006; Sutton and Dong, 2012) which the ocean plays an important part in this variability (Gulev et al., 2013; O'Reilly et al., 2016). Climate models generally underestimate multi-decadal variability in both the ocean and the atmosphere (Kravtsov, 2017; Kim et al., 2018; Simpson et al., 2018), in particular

in the speed of the jet rather than its latitude (Bracegirdle et al., 2018). Hence the differing effects of jet latitude and speed on the ocean may be of importance for understanding Atlantic multi-decadal variability.

1.2.2 Set up the thesis context in chapter 2 - re-investigate previous work

In chapter 2, in order to build up this project's context and background to understand the mechanism for why there is a connection between atmospheric variability and the variability of the underlying ocean, I revisit (i) the definition and frequency of weather regimes over the North Atlantic based on the data itself rather than clustering analysis. (ii) how the weather regime thermally impacts on ocean surface air-sea heat flux which consequently changes the sea surface temperature; as well as how the weather regimes dynamically impact ocean surface wind field, horizontal and vertical circulation. (iii) the connection between weather regimes and atmospheric jet stream.

1.2.3 New work for my thesis which the previous studies have not revealed yet

Previous studies explored the interaction between the atmosphere and ocean focusing on the atmosphere forcing the ocean by simply using NAO indices based in different timescales with observations or one single model simulations. Nevertheless, they did not reveal causality between atmosphere and ocean. On the other hand, previous studies viewed NAO as atmospheric variability. However, NAO only represents a small part of the atmospheric variability.

In my thesis, the interaction between atmosphere and ocean is set up based on two main new aspects: (i) Using data from the Hadley Centre DePreSys3 hindcast model simulations which includes 40 ensembles initialised in the November of each year, allowing clear separation of causality and stronger statistical confidence than can be obtained from a single model run. For each season, the evolution of forty individual ensemble members provides the ocean and atmosphere internal variability; (ii) Eddy-driven jet stream speed strength and latitude shifts over the Atlantic sector can reflect all five multi-weather regimes over the Atlantic which include the majority of the atmospheric variability at mid-latitudes over the Atlantic. New work and assumption for each main chapter is as follows:

a. Science questions for chapter 3 - How does the winter jet stream affect surface temperature, heat flux and sea ice in the North Atlantic?

In chapter 3, the study is focused on the connection between atmosphere and the Atlantic ocean surface variables from the eddy-driven jet stream aspect. The indices of the eddy-driven jet stream are derived from the lower tropospheric

zonal winds that provide direct measures of a time-averaged wind, as well as acting to integrate the effects of the transient weather systems which drive the jet (Hoskins et al., 1983).

The connection between the variability of jet speed strength and latitude shifts versus sea surface temperature across 40 ensembles over 35 years is explored in chapter 3. The jet speed strength and latitude shifts are viewed as independent precursors respectively to predict following months SST. Conversely, SST is taken as a precursor to forecast following months jet speed and latitude across 40 ensembles. The primary assumption is that the spread in ocean variables between ensemble members over the following few months is determined by their different realisations of the chaotic atmospheric variability. Analysis across the ensembles allows the sensitivity of the ocean to jet latitude and jet speed to be identified. On the other hand, the sensitivity of the jet speed and latitude to the SST across the ensemble is analysed.

b. Scientific questions for chapter 4 - How does the atmospheric jet stream affect Atlantic subsurface temperature and mixed layer thickness? The scientific hypotheses in chapter 4 are that the jet stream strength and location affect ocean temperature at depth, the mixed layer thickness and the upper ocean heat balance. The seasonal sensitivity of the ocean mixed layer depth and temperature within the mixed layer to the jet indices will be explored in chapter 4.

c. Scientific questions for chapter 5 - How does the atmospheric jet stream affect Atlantic Meridional Overturning Circulation (AMOC) and horizontal circulations? The scientific hypotheses in chapter 5 are the jet stream strength and latitude variation affect the basin-scale AMOC cells and horizontal circulations from monthly to seasonal time scales. This will be explored in chapter 5.

The seasonal sensitivity of the depth-integrated horizontal flow and Meridional Overturning Circulation to the wind strength and wind latitude shifts will be explored.

d. Data and method are new compared to previous studies

Hadley Centre DePreSys3 hindcast 40 ensemble data is employed to investigate the causality for atmosphere driving ocean or the other way round. Hindcasts are started using the 1st November initial conditions provided by the assimilation run. An ensemble is created by providing different seeds to a stochastic physics scheme (see Bowler et al. (2009)). The ensemble dataset provides many more realisations of internal variability than are available from the observations, providing much more robust statistics on the relationships between the atmosphere and ocean. Furthermore, the ensemble members start from nearly identical conditions in November allowing the growth of perturbations to be explored.

The primary scientific hypothesis is that the spread in ocean variables between ensemble members over the following few months is determined by their different

realisations of the chaotic atmospheric variability. Sensitivity analysis across the ensembles allows the sensitivity of the ocean to jet latitude and jet speed to be identified. Another scientific assumption is that the spread in atmospheric variability (jet stream) between ensemble members over the following few months is determined by their different realisations of the perturbed ocean variability.

1.3 Fundamental phenomena of atmosphere and ocean over the Atlantic

1.3.1 Fundamental phenomena of atmosphere circulations over the North Atlantic

1.3.1.1 Jet Stream

Jet streams are fast wind belts that often blow from west to east across the planet. They influence much of the weather and climate in the mid-latitudes (Woollings, 2019). The planet has three main jet streams in each hemisphere: (i) the subtropical jet (ii) the eddy-driven jet and (iii) the polar night jet. The subtropical jet is driven by the thermally overturning circulation, that is, Hadley Cell, between the tropics and the subtropics, and it is mostly restricted near the subtropical latitudes (30°N and 30°S) near the tropopause. The polar night jet forms in the stratosphere around the latitude of 60°N of the winter hemisphere

due to the strong meridional temperature gradients that set up when the polar night commences.

The eddy-driven jet is formed when cold polar air meets warm subtropical air in the mid latitudes and is the result of the large meridional temperature gradient. The temperature difference can be increased by land-sea contrast, orography and ocean currents. Storm tracks can be determined locally by the presence of increased temperature gradients and significant vertical shear. Storms are eddies which form due to the meridional temperature gradient from baroclinic instability. Circular eddies do not initiate any net meridional momentum flux, but as they gain strength they lose their circularity and lean over, causing convergence of momentum either side of the latitude of the storm track. Convergence of momentum flux together with heat forcing coming from passing mid-latitude eddies produces the eddy-driven jet.

The subtropical jet is relatively shallow and limited to the upper troposphere which is at the level of the upper branch of the Hadley cell. The eddy-driven jet runs deeper throughout the depth of the troposphere down to surface. Hence, the eddy-driven jet can be separated by examining flow at lower levels, in particular, when the two jets are mixing at subtropical latitudes, only they both can be separated at low level (Woollings et al., 2010).

Over the North Atlantic, cyclones outside of the tropics form along the North Atlantic storm track. They often cross south of Greenland and Iceland (Hoskins

and Hodges, 2002) where they convey much of the heat and moisture meridionally towards the Arctic (Trenberth and Caron, 2001; Trenberth and Stepaniak, 2003; Mayer and Haimberger, 2012; Binder et al., 2017), with large effects on the climate.

This thesis investigates the connection between atmosphere and ocean so that the eddy-driven jet stream is defined at low level 850 hPa which reveals eddy-jet stream only, as well as the jet stream close to the ocean surface.

1.3.1.2 Weather regimes

Previous studies revealed that the NAO and other weather regimes are statistical measures for the state of the atmosphere using a simple point difference in the North Atlantic defined as either atmospheric sea level pressure (SLP) or geopotential height at 500hPa between the Icelandic Low and the Azores High (Hurrell and Deser, 2010; Wallace and Gutzler, 1981). Over the North Atlantic, the positive phase NAO+ and negative phase NAO- have been the dominant modes of variability over recent decades (Pinto and Raible, 2012). NAO most pronounced impacts are during the boreal winter. There are four Atlantic-Europe weather regimes from 1958 to 2002 in winter time based on 500hPa geopotential height according to the study by Cassou et al. (2011) based on the k-mean cluster method, where percentages of the mean frequency occurrence of each regime over 1958 to 2002 are NAO+ (29.9%), NAO- (22.4%), Atlantic Ridge (AR, 23.3%)

and Scandinavian Blocking (SBL, 24.5%). The recent study by Woollings et al. (2010) revealed the circulation for different combinations of the NAO and the East Atlantic (EA) pattern. In their study, the EA+ shows negative anomalies over the central Atlantic and positive anomalies over the subtropics and western Europe; whereas, the EA- has an opposite phase. The EA- looked like AR and the EA+ is the opposite phase in the study by Woollings et al. (2010).

1.3.2 Fundamental phenomena of the ocean over the North Atlantic

Thermodynamically, the middle latitude atmospheric eddy-driven jet stream in different strengths and latitude locations move polar cold air equatorwards and subtropical warm air polewards at the ocean surface and above. Dynamically, meandered jet streams create cyclones or anticyclones which represent different weather regimes over the ocean surface. Finally, the jet streams bring strong winds to the ocean surface. These three atmospheric effects in thermodynamics, dynamics and wind will lead to changes in ocean buoyancy conditions, stratifications and circulations. In this section, the ocean phenomena which are buoyancy-driven, wind-driven as well as turbulence impacted due to wind effect are reviewed.

1.3.2.1 Ocean Gyre

An ocean gyre is a basin-scale of circulating ocean currents driven by global wind patterns and forces , generated by Earth's rotation and confined to the continents. Friction between the wind and the ocean surface triggers water movement in the same direction that the wind blows but is deflected by the Coriolis forces due to Earth's spin. A subpolar gyre is a cyclonic ocean currents circulation that lies under an area of low atmospheric pressure, such as, low pressure overlying Iceland. The subpolar gyre consists of the Labrador, North Atlantic, Irminger, and East Greenland Currents. A subtropical gyre is an anticyclonic circulation sitting below a subtropical high pressure, such as Azores high pressure. Across the North Atlantic, the subtropical gyre comprises the Gulf Stream, Azores, Canary, and North Equatorial Currents. Strong currents are located at the western boundaries due to the effect of the Coriolis parameter varying with latitude, which is called the β effect (Marshall and Plumb, 2008; Vallis, 2019).

1.3.2.2 Meridional Overturning Circulation (MOC) - Thermohaline circulation

Compared with the horizontal ocean gyre circulations, the meridional overturning circulation (MOC) is a meridional and vertical circulation which is also called thermohaline circulation. In the upper top kilometer, where there is a net northward flow of warm thermocline and intermediate waters throughout the Atlantic

basin. This is balanced by a net southward flow of colder North Atlantic Deep Water (NADW) at depths between approximately 1000m and 3000m. Sinking is related with the colder, saltier (hence denser) surface waters of the subpolar North Atlantic. Rising occurs with the warmer (hence less dense) waters in the tropical and subtropical Pacific, Indian ocean and Southern ocean. Some of the rising occurs in upwelling zones in the Southern ocean or linked to the enhanced mechanical mixing (Johnson et al., 2019). Differences in density create these circulations, and are associated with variations in temperature and salinity so that it is called thermohaline variations.

Atlantic Meridional Overturning Circulation (AMOC), contributing to the transport of the MOC, is a component of the ocean meridional overturning circulation in the North Atlantic. The AMOC transports heat northwards at the surface moving warm waters from low latitudes to higher latitudes in the northern hemisphere. Thus, the climate system carries heat towards the north pole from lower latitudes . Variations in this important circulation system are likely to have had a crucial role in past climate changes and probably again in the future.

The meridional overturning circulation (MOC) is measured by a streamfunction ψ on the depth-latitude plane. It can be calculated from the meridional transport using the following equation (see (Marshall and Plumb, 2008; Stepanov et al., 2016)):

$$\psi(y,z,t) = \int_{z}^{surface} dz \int_{x_w}^{x_e} v(x,y,z,t)dx \tag{1.1}$$

Where:

x: longitudinal (zonal) direction (+v eastward)

y: latitudinal (meridional) direction (+v northward)

z: height (+v upward), the vertical coordinate, z $<$ 0 with depth

t: time

x_w and x_e: are western and eastern boundaries, for AMOC, they are western and eastern boundaries of the Atlantic.

v: meridional velocity component

ψ unit: Sv (1 Sv = 10^6 m^3 s^{-1}).

1.3.2.3 Ekman transport

a. Ekman horizontal transport

In the large-scale ocean circulation, water follows the same fluid dynamics as the atmosphere. In the interior ocean, the currents are fairly weaker, averagely about 5 to 10 cm s^{-1}, thus, Rossby number $R_0 = \frac{U}{fL} \sim 10^{-3}$, which is much smaller than in the atmosphere where $R_0 \sim 10^{-1}$. Thus, in the horizontal equations, the D/Dt can be neglected. In the ocean surface near the top one hundred meters, the wind produces turbulence. The turbulence conveys wind momentum downwards into the interior. Hence, the force in the momentum equations is described as wind stress, τ_{wind} which varies with depth. The horizontal momentum equation

can be written as follows (Marshall and Plumb, 2008):

$$\begin{aligned} -fv + \frac{1}{\rho_{ref}}\frac{\partial p}{\partial x} &= \frac{1}{\rho_{ref}}\frac{\partial \tau_x}{\partial z} \quad ; \\ fu + \frac{1}{\rho_{ref}}\frac{\partial p}{\partial y} &= \frac{1}{\rho_{ref}}\frac{\partial \tau_y}{\partial z} \end{aligned} \tag{1.2}$$

Eq. (1.2) expresses the balance of forces in the wind-driven circulation, which is a three components balance between the Coriolis force, the horizontal pressure gradient and the wind stress forcing. The direct effect of wind forcing declines with depth. At the bottom of the Ekman layer z = - δ, the stress has disappeared and $\tau = 0$. The horizontal flow is split into geostrophic and ageostrophic components. The ageostrophic component is written as follows:

$$f\hat{\boldsymbol{z}} \times \boldsymbol{u}_{ag} = \frac{1}{\rho_{ref}}\frac{\partial \tau}{\partial z} \tag{1.3}$$

Depth-Integrating Eq. (1.3) across the layer from the surface where $\tau = \tau_{wind}$ down to bottom of the Ekman layer z = - δ, where $\tau = 0$, then multiplying by ρ_{ref}, we gain:

$$f\hat{\boldsymbol{z}} \times \boldsymbol{M}_{Ek} = \tau_{wind} \tag{1.4}$$

Where

$$\boldsymbol{M}_{Ek} = \int_{-\delta}^{0} \rho_{ref}\boldsymbol{u}_{ag}\,\mathrm{d}z$$

The above relation is rearranged to write:

$$\boldsymbol{M}_{Ek} = \frac{\tau_{wind} \times \hat{\boldsymbol{z}}}{f} \tag{1.5}$$

Eq. (1.5) is the mass transport of the Ekman layer is to the right of the surface wind in the northern hemisphere since $\hat{\boldsymbol{z}}$ is a unit vector pointing vertically upwards. We can see the $\boldsymbol{M}_{Ek}$ is based on τ_{wind} and f. According to the Ekman

spiral theory, all Ekman transport within the Ekman layer is integrated, the net Ekman mass transport is at a 90° angle to the right of the surface wind in the northern hemisphere.

b. Ekman pumping and suction

As the above section (a) shows, Ekman transport is pointed to the right at a 90° angle to the wind direction. Hence, over the subtropical gyre in the North hemisphere, there is an anticyclonic atmospheric circulation, the Ekman horizontal flow is convergent with the Ekman layer, and divergent in the cyclonic circulation over the subpolar gyre. The convergent Ekman flow drives water downwelling vertically which is called Ekman pumping; the divergent Ekman flow drives water upwelling vertically which is called Ekman suction. The Ekman convergence over the subtropical gyre can explain why the sea surface height is higher in the subtropics than the subpolar region. This downwelling presses the $\sigma = 26.5$ surface to bend down in the subtropics. Whereas, over the subpolar ocean, Ekman suction pulls up water from the interior into the Ekman layer. Thus, isopycnals are pulled up to the surface around latitude 60°N, S. The Ekman pumping/suction vertical velocity relation based upon wind stress will be introduced in chapter 2 section 2.4.4. The Ekman pumping and suction forced on large scale ocean interior geostrophic flow gives rise to Sverdrup balance which will be introduced in the next section.

1.3.2.4 Sverdrup Theory

Geostrophic balance holds in the ocean interior below the Ekman layer. The vertical downwelling/upwelling motion from the Ekman layer imposes on the geostrophic flow. To consider this vertical motion effect, the continuity equation is applied. Meanwhile, on a planetary scale, the variation of f with latitude needs to be considered. Thus, we use horizontal divergence of the geostrophic flow relation (Marshall and Plumb, 2008):

$$\begin{aligned} \nabla_h \cdot \boldsymbol{u}_g &= \frac{\partial}{\partial x}\left(-\frac{1}{\rho_{ref} f}\frac{\partial p}{\partial y}\right) + \frac{\partial}{\partial y}\left(\frac{1}{\rho_{ref} f}\frac{\partial p}{\partial x}\right) \\ &= -\frac{1}{\rho_{ref} f}\frac{\partial^2 p}{\partial x \partial y} + \frac{1}{\rho_{ref} f}\frac{\partial^2 p}{\partial x \partial y} - \frac{1}{\rho_{ref}}\frac{\partial p}{\partial x}\frac{1}{f^2}\frac{\partial f}{\partial y} \\ &= -\frac{1}{\rho_{ref} f}\frac{\partial p}{\partial x}\frac{1}{f}\frac{\partial f}{\partial y} = -\frac{\beta}{f} v_g \end{aligned} \tag{1.6}$$

Vertical stretching of a water column causes divergence of horizontal flow, hence, we have the relation as follows:

$$\nabla_h \cdot \boldsymbol{u}_g + \frac{\partial w}{\partial z} = 0 \tag{1.7}$$

In Eq. (1.7), replace $\nabla_h \cdot \boldsymbol{u}_g$ with $-\frac{\beta}{f} v_g$ as shown in Eq .(1.6), then we have the very valuable relation:

$$\beta v_g = f \frac{\partial w}{\partial z} \tag{1.8}$$

Eq.(1.8) sets up a connection between horizontal and vertical currents. If the vertical velocity in the abyss is very weak we can regard it as approximately is zero. Then Eq. (1.8) shows when $w_{ek} < 0$ ocean current will have an equatorward component and northward current when $w_{ek} > 0$.

Cross-differentiating Eq. (1.2), removing pressure gradient and using the continuity equation, we get the following relation:

$$\beta v = f\frac{\partial w}{\partial z} + \frac{1}{\rho_{ref}}\frac{\partial}{\partial z}(\frac{\partial \tau_y}{\partial x} - \frac{\partial \tau_x}{\partial y})$$

Integrating the above equation from the bottom of the sea to the very top, assume $w = 0$ and $\tau = 0$ at the sea bottom, $w = 0$ and $\tau = \tau_{wind}$ at the top surface, we have:

$$\begin{aligned} \beta V =& \frac{1}{\rho_{ref}}(\frac{\partial \tau_{wind_y}}{\partial x} - \frac{\partial \tau_{wind_x}}{\partial y}) \\ =& \frac{1}{\rho_{ref}}\hat{\boldsymbol{z}} \cdot \nabla \times \tau_{wind} \quad (a) \\ Where, \quad V =& \int_{-D}^{0} v \, \mathrm{d}z \quad (b) \end{aligned} \tag{1.9}$$

In Eq. (1.9), relation (a) is well known as the Sverdrup relation, which connects the depth-integrated meridional flow to the wind stress curl. When the interior ocean responds to Ekman pumping, the Sverdrup transport starts taking a role to conserve potential vorticity.

1.3.2.5 Ocean geostrophic flow

In this study, the geostrophic motion at the ocean surface and interior are a matter of interest. Large-scale motion in the free atmosphere and ocean obeys geostrophic balance (Marshall and Plumb, 2008).

a. Ocean surface geostrophic flow

Geostrophic vector and zonal and meridional components in the local Cartesian geometry coordinate have been written as:

$$\begin{aligned} \boldsymbol{u}_g &= \frac{1}{f\rho}\hat{\boldsymbol{z}} \times \nabla p \\ (u_g, v_g) &= (-\frac{1}{f\rho}\frac{\partial p}{\partial y}, \frac{1}{f\rho}\frac{\partial p}{\partial x}) \end{aligned} \tag{1.10}$$

In the ocean, integrating the hydrostatic relation from depth horizontal surface at constant surface z up to the free surface at z=η, where p = p_s, which is atmospheric pressure, then we get:

$$p(z) = p_s + \int_z^\eta \rho g \, \mathrm{d}z = p_s + g\langle\rho\rangle(\eta - z) \tag{1.11}$$

If we neglect daily variations of atmospheric pressure in Eq. (1.11), the near-surface pressure gradient equals to the gradient in surface elevation: $(\partial p/\partial x, \partial p/\partial y) = g\rho_{ref}(\partial\eta/\partial x, \partial\eta/\partial y)$ (Marshall and Plumb, 2008). Hence, the geostrophic flow just below the surface is associated with sea surface height gradient, it has been written as follows:

$$\begin{aligned} \boldsymbol{u}_{g_{surface}} &= \frac{g}{f}\hat{\boldsymbol{z}} \times \nabla\eta \\ (u_{g_{surface}}, v_{g_{surface}}) &= (-\frac{g}{f}\frac{\partial\eta}{\partial y}, \frac{g}{f}\frac{\partial\eta}{\partial x}) \end{aligned} \tag{1.12}$$

Eq. (1.12) is completely analogous to the peer relationship $\boldsymbol{u}_g = \frac{g}{f}\hat{\boldsymbol{z}}_p \times \nabla_p z$ for geostrophic flow on the atmospheric pressure surface. In the atmosphere, for example, on the 500hPa surface, the approximate geostrophic wind of 15 m s^{-1} associated with pressure surface slopes down by a height Δz = 800 m over a meridional distance L = 5000 km. Whereas, ocean current is weaker than atmospheric flow, thus, there is a much gentler slope of pressure surface in the

ocean. Based on Eq. (1.11), the sea surface height variation can be estimated with observational surface currents. $\Delta\eta$ is about 1 m in 1000 km distance if U = 10 m^{-1} and f=10^{-4} s^{-1}.

b. Geostrophic flow at depth

At ocean depth, variations of density take an important role. If we again neglect the variations of atmospheric pressure imposing on the water surface, horizontal pressure variations at depths are yielded accordingly based on Eq. (1.11):

$$\hat{\boldsymbol{z}} \times \nabla p = g\langle\rho\rangle\hat{\boldsymbol{z}} \times \nabla\eta + g(\eta - z)\hat{\boldsymbol{z}} \times \nabla\langle\rho\rangle \tag{1.13}$$

Therefore, setting $\rho = \rho_{ref}$, the geostrophic flow at the depths is described as follows:

$$\begin{aligned} \boldsymbol{u} &= \frac{1}{f\rho_{ref}}\hat{\boldsymbol{z}} \times \nabla p \\ &= \frac{g}{f\rho_{ref}}\left[\langle\rho\rangle\hat{\boldsymbol{z}} \times \nabla\eta + (\eta - z)\hat{\boldsymbol{z}} \times \nabla\langle\rho\rangle\right] \\ &\simeq \frac{g}{f}\hat{\boldsymbol{z}} \times \nabla\eta + \frac{g(\eta - z)}{f\rho ref}\hat{\boldsymbol{z}} \times \nabla\langle\rho\rangle \end{aligned} \tag{1.14}$$

Note: in Eq. (1.14) we can take $\langle\rho\rangle \simeq \rho_{ref}$ approximately since where we are not taking its gradient. Eq. (1.14) tells us there are two components for geostrophic flow in the deep water: (i) the first term is related to free-surface height variations; (ii) the second term is associated with interior ocean density gradients. If we take the ocean density to be uniform into account, the second term will be zero, and the geostrophic flow at depth would be the same as that at the surface. In reality, the geophysical flows are balanced by the two terms on the right hand side of Eq. (1.14). Geostrophic flow in the deep water is also associated with eastern and

western boundaries contrast based on the thermal wind balance relation which will be introduced in detail in section 5.5.2 in chapter 5.

1.3.2.6 Mixed layer Depth

At the ocean surface, there is a mixed layer which directly communicates with the overlying atmosphere. Over the vastness of the ocean, the mixed layer communicates with the underlying thermocline. In some latitudes, such as the North Atlantic subpolar region and around Antarctica, the mixed layer depth is very deep $>$ 1 km and hence directly communicates with the abyss (Marshall and Plumb, 2008). The mixed layer communicates between the atmosphere and ocean interior and controls ocean ventilation (Williams and Follows, 2011).

Surface buoyancy loss drives vertical convection which mixes the mixed layer properties so that the properties in the mixed layer are approximately uniform vertically. Most processes, such as heat loss and evaporation, radiative heating and cooling, and wind driven turbulence occur within the mixed layer.

The turbulent movement due to surface wind stirring within the mixed layer can entrain cold water upward across the mixed layer base from the thermocline. Meanwhile, since the base of the mixed layer depth slopes exist, horizontal currents can carry the properties, for example, warm water from the mixed layer getting into the thermocline is called " subduction." The mixed layer vertical 1-D theory will be introduced in section 4.4 and 3-D processes will be analysed in

section 4.4 in Chapter 4.

a. The mixed layer depth definitions

If the mixed layer depth is solely based on a temperature-based criterion, that is, temperature difference from the surface to the base of the depth, then it is called isothermal layer depth (ILD). Generally, the mixed layer depth (MLD) estimate is evaluated using a density-based criterion that includes the effects of salinity (Schneider and Müller, 1990; Lewis et al., 1990), or a temperature-based criterion that includes the effects of salinity (Kara et al., 2003; Obata et al., 1996). Or the MLD estimation is based on density and temperature with turbulence measurements (Brainerd and Gregg, 1995), or a density-based estimation only. Over most of the world's oceans, a strong thermocline results in the ILD and MLD being found to have the same depth. In my study, in the ensemble model data, the MLD is based on $\Delta\sigma_\theta$ as 0.01 kg m^{-3} between the density at the depth and the density at near-surface reference level at 2.5 m.

b. The mixed layer depth seasonal variation

The mixed layer thickness varies seasonally and regionally from 30m to 1000 m. The mixed layer is deepest at about 100 m over the subpolar gyre at the end of winter, typically February to March over the North Atlantic (Marshall and Plumb, 2008; Levitus and Boyer, 1994; Levitus et al., 1994; Kara et al., 2003). The mixed layer becomes shallower from spring and is the shallowest in summer, and starts deepening from September. You will see regional and seasonal variation

examples in section 4.3 and 4.8 in Chapter 4.

Chapter 2

Weather Regimes over the North Atlantic Ocean

2.1 Introduction

Mid-latitude atmosphere influence on the North Atlantic Ocean is often viewed in terms of the North Atlantic Oscillation (NAO) which is strongly associated with a tripole pattern in sea surface temperatures (Bjerknes, 1964; Visbeck et al., 2003; Marshall and Coauthors, 2001; Eden and Willebrand, 2001). The North Atlantic–European region weather regimes, such as Atlantic Ridge (AR), Scandinavian blocking regime (SBL), and two NAO phases (NAO^+ and NAO^-), occurrence and strength have an influence on the variability of the North Atlantic surface ocean variables, such as surface wind fields, surface air temperature and SST (Cassou et al., 2011, 2004). The imprint of this atmospheric forcing associ-

ated with the NAO involves both local and far-field responses affecting the ocean heat storage over the North Atlantic. Anomalies in air-sea heat flux drive ocean convection and interannual changes in local heat content over the subpolar gyre (Visbeck et al., 2003; Grist et al., 2010), while changes in wind stress drive variations in subtropical heat content (Lozier et al., 2008; Williams et al., 2014) and inter-gyre transfers between the subtropical and subpolar gyres (Marshall et al., 2001). The combined effect of wind stress and air-sea buoyancy flux changes associated with the NAO index drive variations in the meridional overturning (Lozier et al., 2010; Robson et al., 2012), which in turn alters the gyre-scale convergence in heat transport (Williams et al., 2014, 2015b) and controls multi-year and decadal changes in ocean heat content. The four weather regimes capture the interannual variability of the surface ocean forcing and affect the ocean circulation anomalies which are greater in winter months (Barrier et al., 2014).

In this chapter, in order to provide context for this project, I consider the link between weather regimes and ocean, and the link between weather regimes and atmospheric jet stream. So I revisit (i) the definition and frequency of weather regimes for the Atlantic based on the data itself instead of the clustering method; (ii) how the weather regimes thermally impact on ocean surface air-sea heat flux and consequently change sea surface temperature; (iii) how the weather regime dynamically impacts ocean horizontal and vertical circulation; and (iv) and how the eddy-driven jet stream connects with weather regimes.

2.2 Data

In this chapter, NCEP/NCAR reanalysis 1 (NCEP/NCAR, accessed 2017) daily mean data from 1948 to 2016 December to February are analysed for the following purposes. All the following variables are using the same daily coverage. Geopotential height fields at 500 hPa are derived from 17 pressure levels (hPa) because daily geopotential height data sets are stored as a file for each year which includes 17 pressure levels in each file. Mean Daily Sea Level Pressure (SLP) is analysed. Both the geopotential height at 500 hPa and SLP have the same spatial coverage of 2.5° × 2.5° global grids (144 × 73), 0.0°E to 357.5°E, 90.0°N to 90.0°S. Mean daily data for geopotential height at 500 hPa and mean SLP are analysed for weather regimes definitions.

In order to explore how the weather regimes impact on ocean surface air-sea heat flux, NCEP reanalysis mean daily surface sensible heat flux and latent heat flux are investigated. Note, both sensible heat flux and latent heat flux data are directly downloaded from NCEP reanalysis data and not calculated through bulk aerodynamic formulae from winds and temperatures (Cayan, 1992). The spatial coverage of surface flux is T62 Gaussian grid with 192 × 94 points, 88.542°N-88.542°S, 0°E-358.125°E. Level is surface or near the surface (0.995 sigma level).

Surface air temperature, and zonal and meridional wind daily data fields are used to investigate how air temperature, wind fields and Ekman circulation change in

response to the weather regimes. The data sets spatial coverage are the same as for the surface flux data. The air temperature is at 2m above the sea level and zonal and meridional wind fields are at 10m height above the sea level. The 2m air temperature and 10m wind fields have the same spatial coverage as surface heat flux data.

Mean daily data for 850 hPa zonal wind is derived from 17 pressure levels (again, daily zonal wind data sets are stored as a file for each year which includes 17 pressure levels in each file), and it has the same spatial coverage as geopotential height data. This data is used to explore the low level eddy-driven jet stream strength and latitude location corresponding to the weather regimes in winter time.

2.2.1 Why are the geopotential height at 500 hPa and mean sea level pressure data chosen to define weather regimes?

A. Definitions

Geopotential height is defined as the height of a given point in the atmosphere in units proportional to the potential energy of unit mass (geopotential) at this height relative to sea level (AMS, accessed 2020a). The relation, in SI units, between the geopotential height Z_g(h) and the geometric height z is: $Z_g(h) = \frac{1}{g_0}\int_0^z g(\phi, z)dz$, $g(\phi, z)$ is the acceleration due to gravity, ϕ is latitude, and z is

the geometric elevation. g_0 is the standard acceleration due to gravity at sea level ($g_0 = 9.80665$ m s^{-2}), thus, the two heights are numerically convertible for most meteorological purposes. One geopotential metre is equal to 0.98 dynamic metres.

The geopotential height of the 500 hPa pressure surface shows air altitude in the atmosphere where the pressure falls to 500 hPa (i.e.500 millibars). On average, this level is about 5500 m above sea level, and it is usually reviewed as air motion direction. The 500 hPa geopotential can provide the wind direction from the height pattern at which the wind moves parallel to the height contours with lower heights to the left of the wind direction and higher heights to the right of the wind direction. Based on the 500 hPa geopotential height map, we also can estimate wind speed. If there is a high density of geopotential contours and therefore strong geopotential height gradients, this implies a strong wind. The winds usually blow from west to east, following the wavelike shape of the height contours. The weather systems below the level, close to the Earth's surface, roughly move in the same direction as the winds at the 500 hPa level. The height contours clearly reveal the major tropospheric waves which impact our weather. Low heights represent troughs and cyclones in the middle troposphere; whereas, high heights represent ridges and anticyclones. At many locations around the globe, the height above sea level where the air pressure falls to 500 hPa is measured by sending instrumented weather balloons upward. The data from around the world is collected and maps of the current 500 hPa height are generated. The actual

pattern of the 500 hPa heights evolves daily. Thus, in this chapter the weather regimes are defined using 500 hPa geopotential height (ECMWF, accessed 2020a).

Sea level pressure is the atmospheric pressure at mean sea level. If the land surface is above sea level, then the pressure at any point on the surface is reduced to what it would be at a point directly below it, assuming the air temperature remained the same all the way down. It is customary to use the mean temperature for the preceding 12 hours instead of the temperature at the time of measurement only. Anomalies in the pressure field in mountainous regions are often due to this method of reducing pressure to sea level (AMS, accessed 2020b).

The SLP weather charts show high and low pressure patterns which are associated with different weather types. Normally, low pressure systems (cyclones or depressions) bring changeable weather. Whereas, high pressure systems (anticyclones) are link to stable weather. Wind speed is roughly proportional to the distance between isobars where dense concentration of isobars indicates strong winds, and vice versa (ECMWF, accessed 2020b).

B. Reasons why weather regimes are defined at 500 hPa geopotential height

The following are reasons why the weather regimes are defined at 500 hPa geopotential height:

(i) A considerable number of previous studies defined weather regimes using 500 hPa level geopotential height (e.g. Hoskins et al., 1983; Cheng and Wallace, 1993;

Hannachi, 2010; Cassou et al., 2011; Woollings et al., 2010). Previous studies (e.g. Blackmon, 1976) revealed that 500 hPa geopotential field has a a dominant low frequency variability. Another study also found that low frequency flow is approximately barotropic in character (Blackmon et al., 1977). Thompson et al. (2003) study showed that the Northern Hemisphere annular mode (NAM) appeared to have very similar patterns at the geopotential height and zonal wind fields throughout the depths at 250 hPa, 500 hPa, 850 hPa, 1000 hPa. Meanwhile, the structure of the NAO in the atmospheric circulation showed similar patterns at 500 hPa geopotential height and at sea level pressure.

I re-visit and analyse northern hemispheric atmospheric circulations at 1000 hPa, 850 hPa, 500 hPa, 300 hPa and 250 hPa geopotential heights, as well as look at sea level pressure (SLP) field in winter season based on NCEP monthly reanalysis data in Fig. 2.1. We can see that mean atmospheric circulation shows more zonal and low frequency variability especially at low latitudes at 500 hPa, 300 hPa and 250 hPa geopotential height maps (Fig. 2.1 c, b, a). They all have lower heights (troughs) and higher heights (ridges) at the same regions. Below 500 hPa levels, there are high frequency oscillations particularly at 1000 hPa level and sea level. From the sea level pressure map (Fig. 2.1 f), we can see where there are low pressure centres (cyclones) at sea level then they have low heights (troughs) above the air column from 1000hPa until upper levels up to 200 hPa; whereas, where there are high pressure centres (anticyclones) located at sea level, then they have high heights (ridges) from 1000 hPa up to 250 hPa.

The important characteristics for weather definition at the 500 hPa level is: firstly, it is located at the mid-level not too far from the surface but without surface friction influence. It is just like a mirror resembling atmospheric circulations main features both below and above it. Secondly, it shows low frequency variability and more zonal structure which gives us a more stable atmospheric state on large-scale spatial patterns to forecast.

On the other hand, previous studies also defined weather regimes on sea level pressure anomalies field (Hurrell and Deser, 2010) which are very similar patterns to other studies which defined weather regimes at 500 hPa geopotential heght anomalies (Cassou et al., 2011). Hurrell (1995) defined NAO index using SLP anomalies. In this chapter, in section 2.3.3.2, my definitions of weather regimes using both 500 hPa geopotential height anomalies and SLP anomalies show the same weather patterns (see Fig. 2.5 and Fig. 2.6).

Hence, we can draw a conclusion that weather regimes can be defined both at sea level pressure field and 500 hPa geopotential height field.

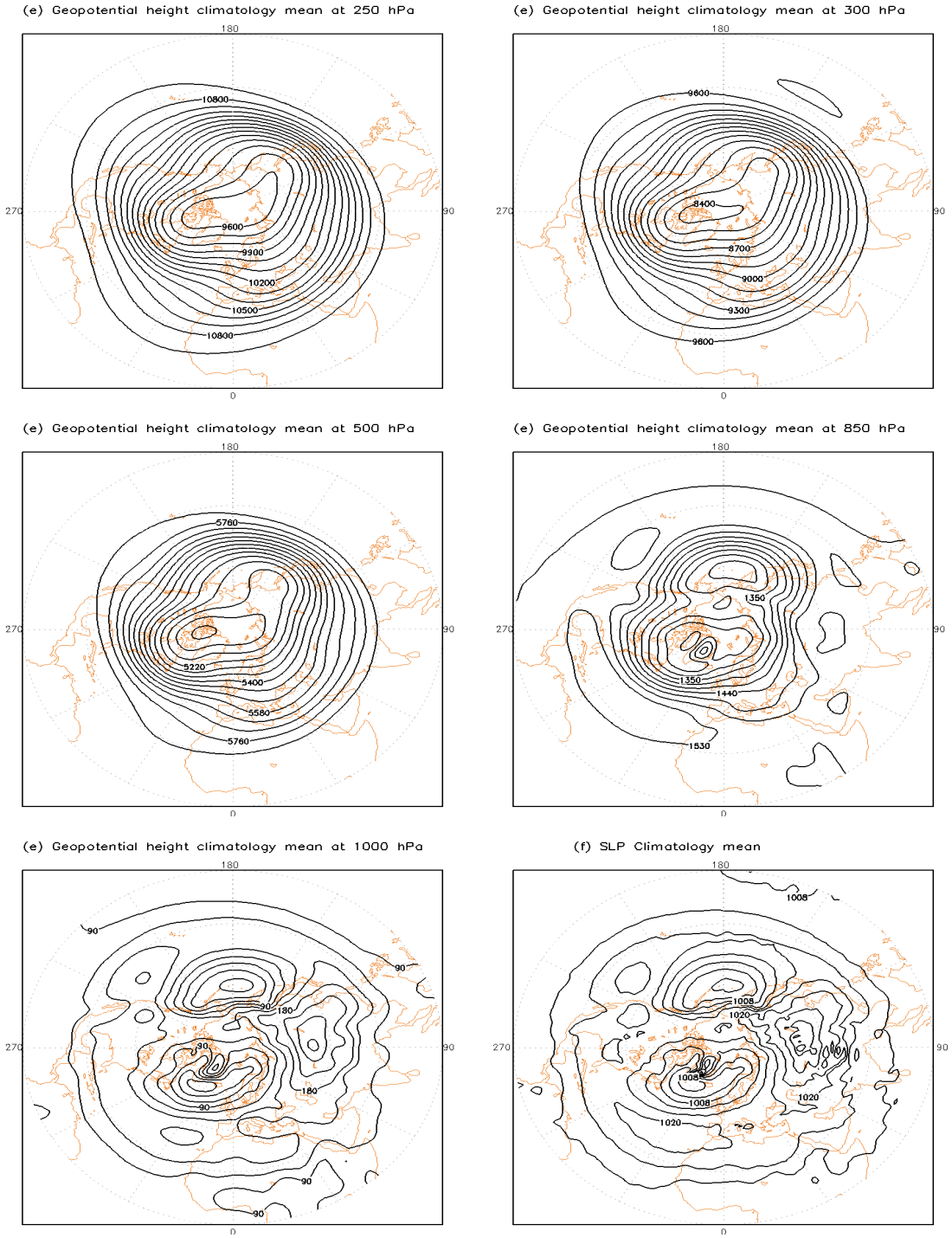

Figure 2.1: Geopotential height climatology mean (units: meters) (a) at 250 hPa (b) at 300 hPa (c) at 500 hPa (d) at 850 hPa (e) at 1000 hPa and (f) Sea level pressure (SLP, units: hPa) in DJF (December to February mean) from 1950 to 2017

.

2.2.2 Why is the zonal wind at 850 hPa height chosen to explore the connection between the eddy-driven jet and the weather regimes ?

Mid-latitude jet stream from the troposphere down to the ground is the eddy-driven jet stream associated with storm tracks contributing to much of the weather and climate in the mid-latitudes. The reasons why the eddy-driven jet stream is chosen at 850 hPa in this study are:

The eddy-driven jet runs deeper throughout the depth of the troposphere down to surface than the subtropical jet; whereas, the subtropical jet is relatively shallow and confined to the upper troposphere. Hence, the lower-level zonal wind at 850hPa is considered best for diagnosing the variability of the eddy-driven jet (Woollings et al., 2010).

Additionally, since this thesis is examining the connection between atmosphere and ocean, zonal wind is analysed at this lower level.

2.3 Weather Regime Definitions

Different weather regimes occur over the Atlantic ocean, bringing cyclonic or anticyclonic pressure patterns overlying the ocean. Consequently, some weather regimes bring cold and dry air to the North Atlantic from the North American

continent or from the North pole, or even from Europe. Other weather regimes transport warm and moist air from low latitudes. All these weather patterns affect the surface ocean leading to changes in ocean temperature and heat storage and changes in water density. Dynamically, different weather regimes bring changes in ocean circulations, such as Ekman upwelling and downwelling, Ekman horizontal transport and horizontal geostrophic advection. If a weather pattern remains in one location for several days, even for several weeks, there is a significant impact to the underlying ocean.

Hence, in this section, I analyse which weather regimes pass over the Atlantic and how to define them, and assess the frequency of these weather regimes in winter since the atmospheric dynamical processes are more active in winter than in summer (e.g. Gastineau and Frankignoul, 2015; Van der Swaluw et al., 2007). The study by Liu et al. (2020) found clearer signals of the compensation between the atmosphere and ocean's heat transport variations and more active interaction between ocean and atmosphere in winter than in summer. Therefore, winter time is chosen to investigate the connection between the atmospheric variability and the ocean.

2.3.1 Blocking weather regime definition

The blocking weather regime is an extreme weather event which can have great impacts. Blocks are areas of high pressure that persist nearly stationary for a

few days or perhaps weeks and distort the usual eastward movement of weather systems.

For a blocking regime, the blocking index is defined by equations (2.1) and (2.2) to identify winter blocking days. The blocking index was developed by Lejenäs and Økland (1983) and modified by Tibaldi and Molteni (1990) to be defined by a 500 hPa geopotential gradient reversal. This study is an extension of the Tibaldi and Molteni (1990) blocking index to a two-dimensional map of blocking frequencies at every latitude and longitude grid point. The 500 hPa geopotential field is evaluated on a 2.50° by 2.50° regular latitude-longitude grid covering the northern hemisphere based on daily 500 hPa data. In this study the data is processed as a 5 days' running mean prior to calculating GHGS and GHGN to isolate potential blocking episodes of sufficient duration (NOAA, accessed 2017).

$$GHGS = \left[\frac{Z(\phi_0) - Z(\phi_s)}{\phi_0 - \phi_s}\right] \quad (a)$$
$$GHGN = \left[\frac{Z(\phi_n) - Z(\phi_0)}{\phi_n - \phi_0}\right] \quad (b) \qquad (2.1)$$

Where:

$Z(\phi_0)$ = geopotential height at latitude ϕ_0;

$Z(\phi_s)$ = geopotential height at latitude ϕ_s;

$Z(\phi_n)$ = geopotential height at latitude ϕ_n;

ϕ_n = [y+ 20] + Δ;

ϕ_0 = y + Δ;

ϕ_s = [y - 20] + Δ;

y represents starting latitude which is from 20°N. Note, other studies only calculate middle latitude blocking 1-D index time series, where they chose $\phi_0 = 60°$N. Δ = -2.5°, 0°, or 2.5°; Δ has options: Δ = -2.5°, $\Delta = 0°$, or $\Delta = 2.5°$, respectively, which allows latitude extension when calculating one-dimensional blocking index at given ϕ_n, ϕ_0 and ϕ_s (see Tibaldi and Molteni (1990)). A given longitude is then defined as 'blocked' at a given time if the following conditions are satisfied for at least one value of Δ:

(1) GHGS > 0 and (2) GHGN $<$ -10 m/deg lat. (metre per degree lat), this is counted as one blocking episode at a given location.This gives some flexibility in latitude.

In my study, for a two-dimensional blocking index map, every latitude grid point is examined between 0°N to 70°N with 2.5° steps (see similar method in Scherrer et al. (2006)). The difference between the central latitude ϕ_0 and the northern ϕ_n and southern latitudes ϕ_s for which the linear gradient is computed is taken to be 20°. Hence, every latitude grid point is treated as one central latitude ϕ_0, then each latitude grid point between 0°N and 70°N has its own ϕ_0, ϕ_s, ϕ_n. Following GHGS and GHGN definitions in equation (2.1), then the geopotential height gradients GHGS and GHGN are calculated for each latitude and longitude grid point. When the GHGS and GHGN thresholds are satisfied and when GHGS is greater than 0 and when GHGN is less than 10m per degree latitude, then blocking is identified at that day and location.

In my study, a two-dimensional blocking frequency map in DJFM from 1950 to 2016 over the middle latitudes to high latitudes of the north hemisphere is shown in Fig. 2.2.

2.3.2 Blocking days frequency and distribution

There are two blocking centres over the Atlantic: British Isles/Scandinavian blocking with up to 800 to 900 blocking events out of 8002 days during DJFM from 1950 to 2015; and Greenland blocking occurring for about 500 to 600 events (Fig. 2.1). Also there is a weak blocking region over the Iceland/Nordic Sea for 400 to 500 events. The highest frequency of blocking events is displayed over North-east Russia and North Pacific with over 1000 blocking events.

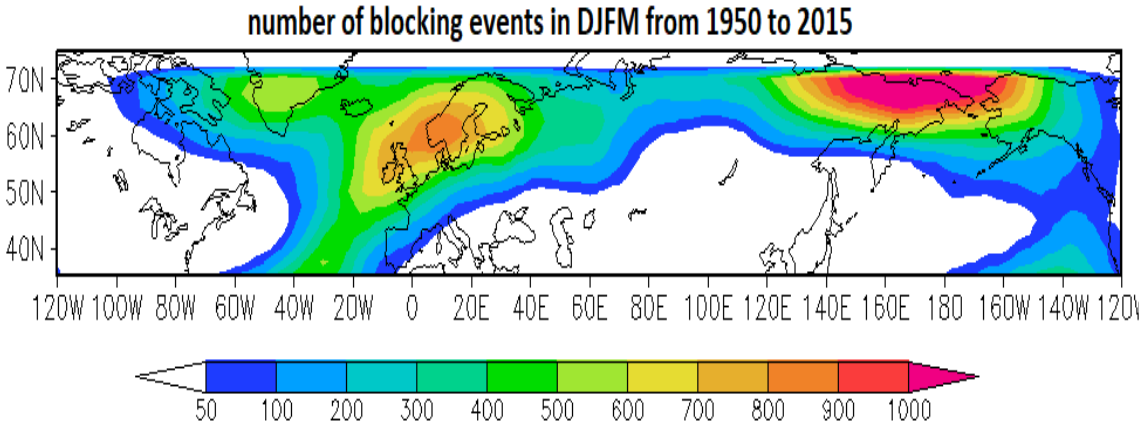

Figure 2.2: Number of blocking events (consecutive 5 days as one blocking event) in DJFM from 1950-2015 based on NCEP reanalysis mean daily 500 hPa geopotential height field.

2.3.3 Definitions of North Atlantic weather patterns

2.3.3.1 Previous work for North Atlantic weather regimes

The early paper by Wallace and Gutzler (1981) defined the North Atlantic Oscillation, the Pacific Oscillation, zonal symmetric seesaw and the Pacific/North American pattern based on a 500hPa geopotential height field. Wallace and Gutzler (1981) identified each pattern's geographical centre in latitude and longitude points in terms of geopotential height and sea level pressure anomalies. They revealed that the Pacific and North Atlantic both have north-south oscillations. There is meridional oscillations of geopotential variation in zonal flow between the North Atlantic and North Pacific, such as North Atlantic Oscillation (NAO) and North Pacific Oscillation (NPO). Some studies used the clustering method statistically to classify weather regimes and occurrence (Hannachi, 2010; Cassou et al., 2011; Michelangeli et al., 1995; Madonna et al., 2017; Michel and Rivière, 2011). There are four Atlantic-Europe weather regimes from 1958 to 2002 winter time based on 500hPa geopotential height according to the study by Cassou et al. (2011) based on the k-mean cluster method (see Fig. 2.3). The weather regimes are: NAO+, NAO-, Atlantic Ridge (AR) and Scandinavian Blocking (SBL).

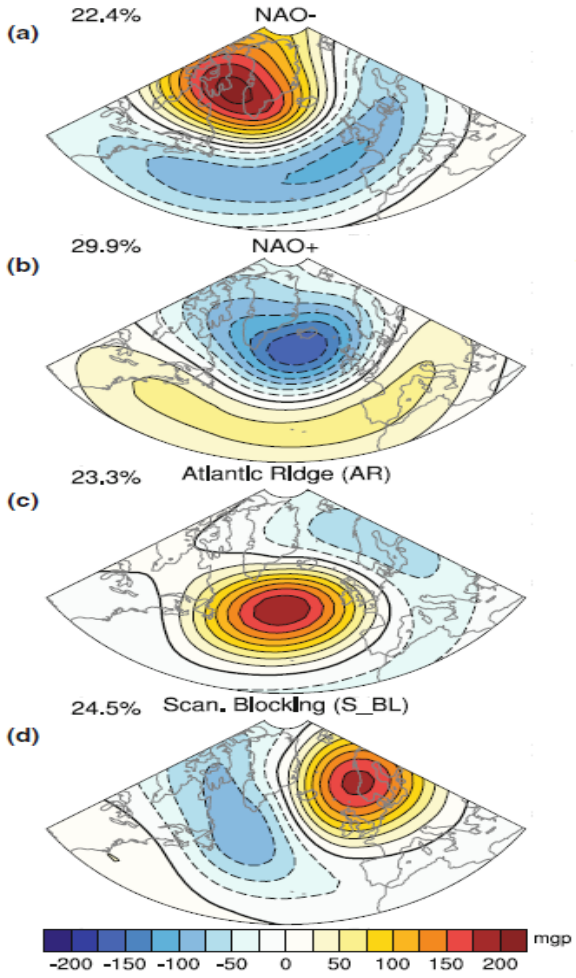

Figure 2.3: a–d Centroids of the four wintertime NAE Z500 weather regimes (m). Each percentage represents the mean frequency occurrence of the regime computed over 1958–2002 from 1 December to 31 March. Contour intervals are 25 m. This figure is from the study Fig.1 by Cassou et al. (2011).

Other studies used different names for the central Atlantic ridge. The study by Wallace and Gutzler (1981) originally defined the eastern Atlantic (EA) pattern. In this study, a positive pattern index of EA showed high anomalies for 500hPa height over the Atlantic and low height anomalies over the subtropical Atlantic and eastern Europe; a negative index of EA is in opposite phase which is distinctly different from the EA pattern in recent study. Recently, the EA pattern

is often viewed as a southward shifted NAO pattern (see NOAA (accessed 2020) website). The recent study by Woollings et al. (2010) revealed the circulation for different combinations of the NAO and EA patterns. In their studies, the EA+ shows negative anomalies over the central Atlantic and positive anomalies over the subtropics and western Europe; whereas, the EA- has an opposite phase. Interestingly, the EA+ in a study by Wallace and Gutzler (1981) looks like the EA- patterns in a recent study by Woollings et al. (2010); whilst, EA- in the study by Wallace and Gutzler (1981) looks like EA+ patterns in the recent study by Woollings et al. (2010) (see Fig. 2.4). The sign is arbitrary in their patterns. Hence, I suggest in my definition, EA- in the study by Woollings et al. (2010) is called the central Atlantic ridge; whereas, EA+ is the central Atlantic trough, which are named by the atmospheric ridge and trough circulations.

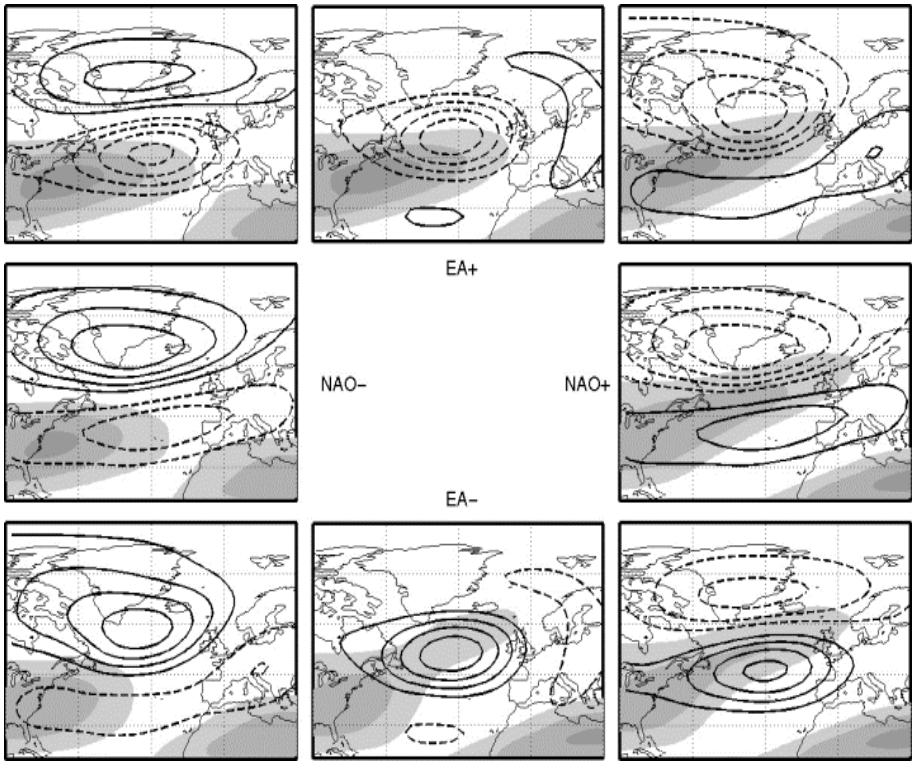

Figure 2.4: Summary of the circulation at different locations in NAO/EA space. The horizontal axis of the grid of plots is the NAO and the vertical axis is the EA. Z500 anomalies are contoured every 20 m per standard deviation of the principal component time series, and 300 hPa zonal wind is shaded every 10 m s^{-1} starting at 20 m s^{-1}. The corner plots are given by adding the respective NAO and EA maps and scaling by 1/2. This figure is from the study by Woollings et al. (2010).

2.3.3.2 My definitions of North Atlantic weather patterns on 500hPa geopotential height anomalies

Combining the previous studies (Wallace and Gutzler, 1981; Cassou et al., 2011; Woollings et al., 2010), there should be five weather regimes over the North Atlantic in winter time which are NAO+, NAO-, Scandinavian Blocking (SBL), EA+ and EA-. As has been seen, EA- looks like AR and EA+ is the opposite phase (Woollings et al., 2010).

My thesis aim is to explore the interaction between atmosphere and ocean. Thus, in order to be familiar the atmospheric circulations, the weather regimes are defined over the Atlantic ocean and west Europe based on 500 hPa geopotential height daily data from 1948 to 2016 in DJF for 6137 days. There are five weather regimes in my definition which are NAO+, NAO-, SBL, central Atlantic Ridge (AR) and central Atlantic Trough (AT). The AT is the AR's opposite phase. My definitions in detail for weather regimes are show in Table 1:

Table 2.1: Definitions of Weather Regime

Weather Regimes	Geographic regions			
	Iceland (25°W-16.5°W 60°N-70°N)	Azores (28.5°W-20°W 36°N-40°N)	Scandinavia (20°W-30°E 50°N-65°N)	Central Atlantic (40°W-20°W 35°N-60°N)
NAO+ (21%) (1320 days out of 6137 days)	Azores GHTA minus Iceland GHTA > 170m			
NAO- (24.8%) (1547 days out of 6137 days)	Azores GHTA minus Iceland GHTA < -170m			
SBL (20%) (1272days out of 6137 days)			GHTA > 100m	
AR 18% (1126 days of out 6137 days)				GHTA > 95m
AT (19%) (1214 days out of 6137 days)				GHTA < -100m

(note: GHTA refers to geopotential height anomalies at 500 hPa (units: m); each region mean is taken an area average over an X-Y region given. SBL refers to Scandinavian Blocking; AR refers to central Atlantic Ridge. AT refers to central Atlantic Trough.) .

How are definition thresholds for the weather regimes defined (see Table 2.1) ? (i) 6137 days in DJF from 1948 to 2016 weather maps of 500 hPa geopotential height anomalies and height are generated and stored as a weather map library. Before I calculate weather regimes indices, each day's weather pattern is looked at to familiarise myself with all the weather patterns. (ii) calculate NAO index through 6137 samples, which is geopotential height anomalies over the Azores

regional mean minus its counterpart over the Iceland regional mean. (iii) ordered the NAO index from high to low, for NAO+ index order index values from high positive to low positive values, when the index value is smaller than 170m, the weather map does not show a NAO+ pattern any longer; a similar method is used for NAO-, but negative values from high to low (high negative values at top), when the negative index value is greater than -170m, the weather map does not show a NAO- pattern. (iv) for central Atlantic ridge, when the 500 hPa geopotential height anomalies regional mean over the central Atlantic is less than 95m, the weather map does not show a central Atlantic ridge pattern. (v) for the central Atlantic trough, when the 500 hPa geopotential height anomalies regional mean over the central Atlantic is greater than -100m, the weather map does not show a central Atlantic trough pattern. (vi) for Scandinavian blocking pattern, when the 500 hPa geopotential height anomalies regional mean over Scandinavia is greater than 100m, the weather map shows the blocking pattern.

Note, some days' weather patterns are none of these weather regimes, but their geopotential height anomalies are weak, so I do not focus on them.

In my study, there are some advantages in using my definition:(i) these definitions are independent of the data set; (ii) it allows some days to be in more than one regime or in none. Traditionally, the k-mean clustering method is generally used to classify weather regimes and occurrence (Hannachi, 2010; Cassou et al., 2011; Michelangeli et al., 1995; Madonna et al., 2017; Michel and Rivière, 2011).

However, the k-mean clustering has some disadvantages (Hannachi et al., 2017): (i) it is not clear how to choose the number of clusters, and results are often very sensitive to this; (ii) days which are mid-way between two regimes are forced into one or the other, which is very common.

For revealing the five weather regime patterns, a composite analysis is employed in geopotential height anomalies at 500hPa through all data for the different regimes. Each regime's composite days are formed of days shown in Table 1, which include all the days satisfying my regime definition criteria through all data by 6227 days in DJF from 1948 to 2016. The positive phase of the NAO reflects below normal heights across the high latitudes of the North Atlantic and above normal heights and pressure over the central North Atlantic, the eastern United States and western Europe (Fig. 2.5 a). The negative phase reflects an opposite pattern of height anomalies over these regions (Fig. 2.4 b). The central Atlantic Ridge (AR) weather regime (see Fig. 2.5 c) is defined by a high pressure ridge over most of the middle latitude Atlantic and the below normal heights over the eastern United States and western Europe. The central Atlantic Trough in Fig. 2.5 d shows the opposite heights anomalies over these regions compared to the AR. The Scandinavian blocking (SBL) weather pattern in Fig. 2.5 e shows positive anomalies of geopotential height over the British Isles to Scandinavia and below normal heights from Greenland meridionally across the Atlantic.

To compare the five weather regimes at sea level, a composite analysis is employed

at mean sea level pressure anomalies through all data for the different regimes (Fig. 2.6). Each regime's composite days are formed of the same composite days as shown in Fig. 2.5. The five weather regimes' patterns strongly agree from mean sea level pressure to high level at 500 hPa geopotential height. At sea level, low pressure anomalies patterns, i.e. cyclones or trough regions correspond with low geopotential height anomalies at 500 hPa whilst the high pressure anomalies, i.e. anticyclones correspond with high geopotential height anomalies. The approximate anomalies magnitudes are about ± 2.5 hPa at sea level pressure versus ± 25 m at 500 hPa geopotential height anomalies.

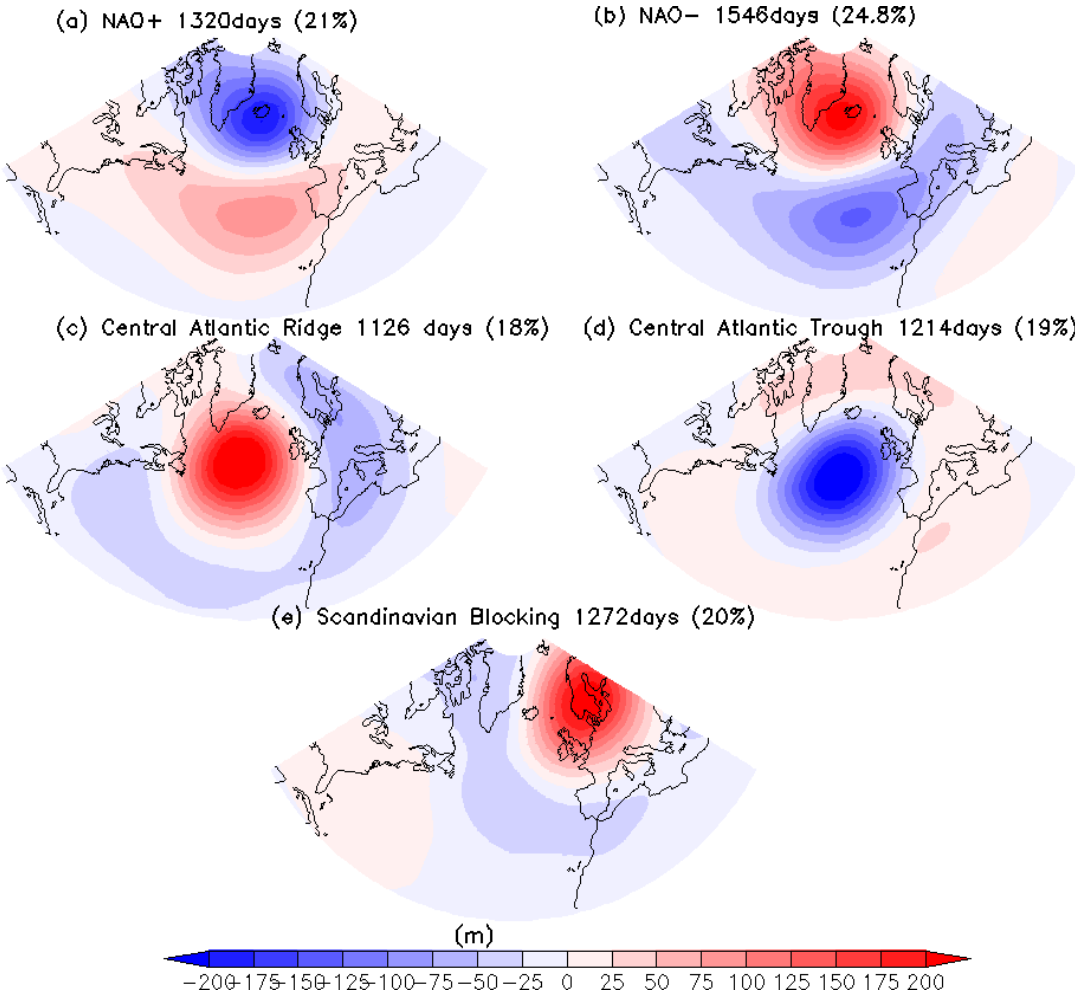

Figure 2.5: A composite mean of 500hPa geopotential height anomalies for each weather regime from 1948 to 2016 DJF (a) NAO+ 1320 days (b) NAO- 1546 days (c) AR 1126 days (d) AT 1214 days (e) SBL 1272 days; based on NCEP reanalysis daily data. units: metres; each interval is 25m.

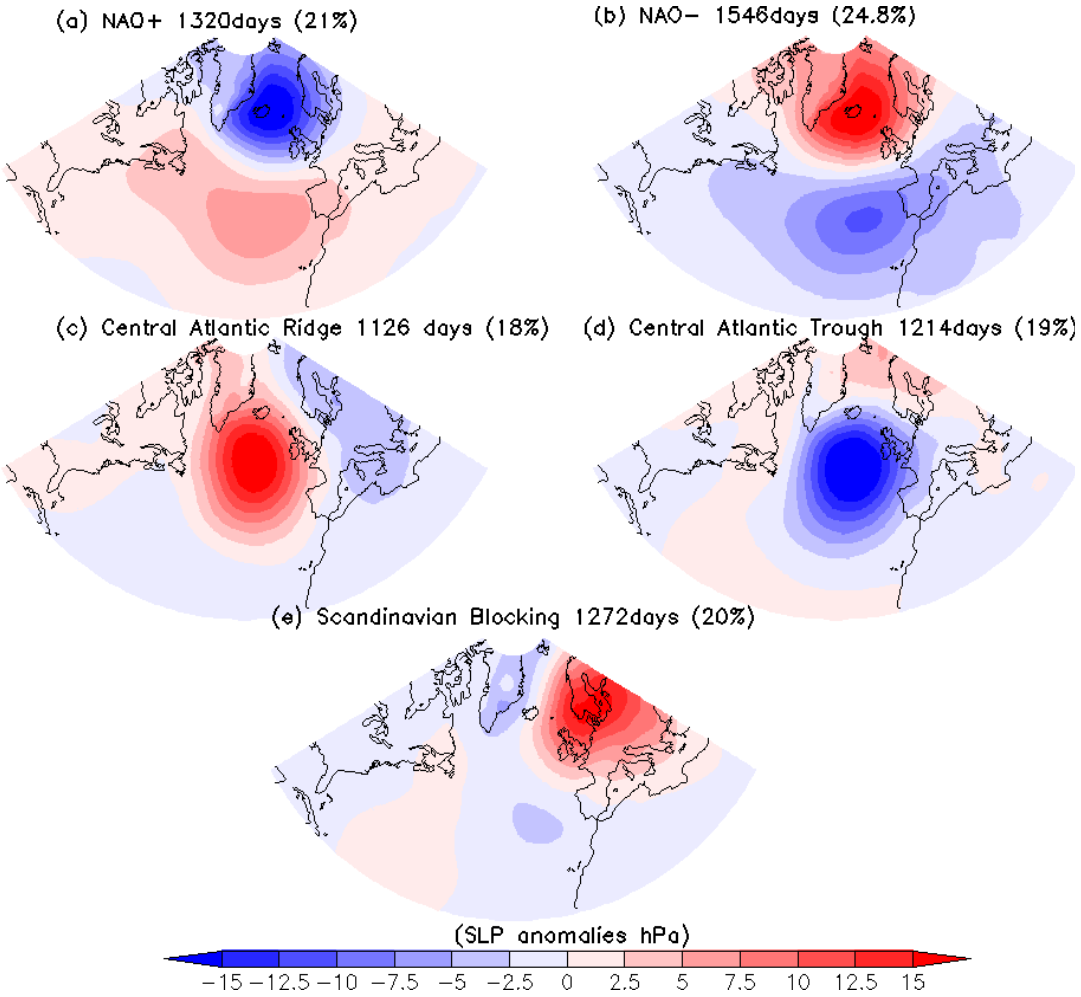

Figure 2.6: A composite mean of sea level pressure anomalies for each weather regime from 1948 to 2016 DJF (a) NAO+ 1320 days (b) NAO- 1546 days (c) AR 1126 days (d) AT 1214 days (e) SBL 1272 days; based on NCEP reanalysis daily data. units: hPa; each interval is 2.5 hPa.

2.4 Effects of weather regimes on ocean surface variables

Cassou et al. (2011) revealed that the different weather regimes affect changes in the Atlantic ocean surface variables, for instance, changes in surface air temperat-

ure and surface wind pattern. In this section, I analyse how the weather regimes affect the Atlantic surface temperature, surface wind pattern, surface air-sea heat flux and wind-induced Ekman vertical and horizontal transport.

2.4.1 Changes in 10m wind fields under the five weather regimes

Different weather regimes cause changes in wind strength, location and direction (Fig. 2.7, Fig. 2.8). Comparing the 10m wind climatology pattern (Fig. 2.7 f) with the NAO+ pattern, surface wind is convergent centred to a cyclone over the Iceland, and there is a north-westerly wind from the Labrador Sea, and an enhanced westerly wind from central latitudes northward to the east side of the North Atlantic (Fig. 2.8 a). Over the subtropics, there is an anticyclonic wind circulation over the Azores, and wind divergence there (Fig. 2.7 a) an enhanced easterly wind along 30°N. With the NAO- pattern, there is an easterly wind below Iceland (Fig. 2.8 b) that is an anticyclonic wind circulation centred on Iceland (Fig. 2.7 b). There is an enhanced easterly wind below 40°N (Fig. 2.8 b). With the central Atlantic ridge pattern, an anticyclonic circulation is dominating over the central Atlantic below Iceland (Fig. 2.7 c, Fig. 2.8 c). The central Atlantic trough shows a strong cyclonic wind circulation over the central Atlantic below Iceland (Fig. 2.7 d, Fig. 2.8 d). In the Scandinavian pattern, due to a block high located over Scandinavia, the strong southerly or south-westerly wind crossing

north of Scandinavia tends to bypass the block high over the north side (Fig. 2.7 e, Fig. 2.7 e).

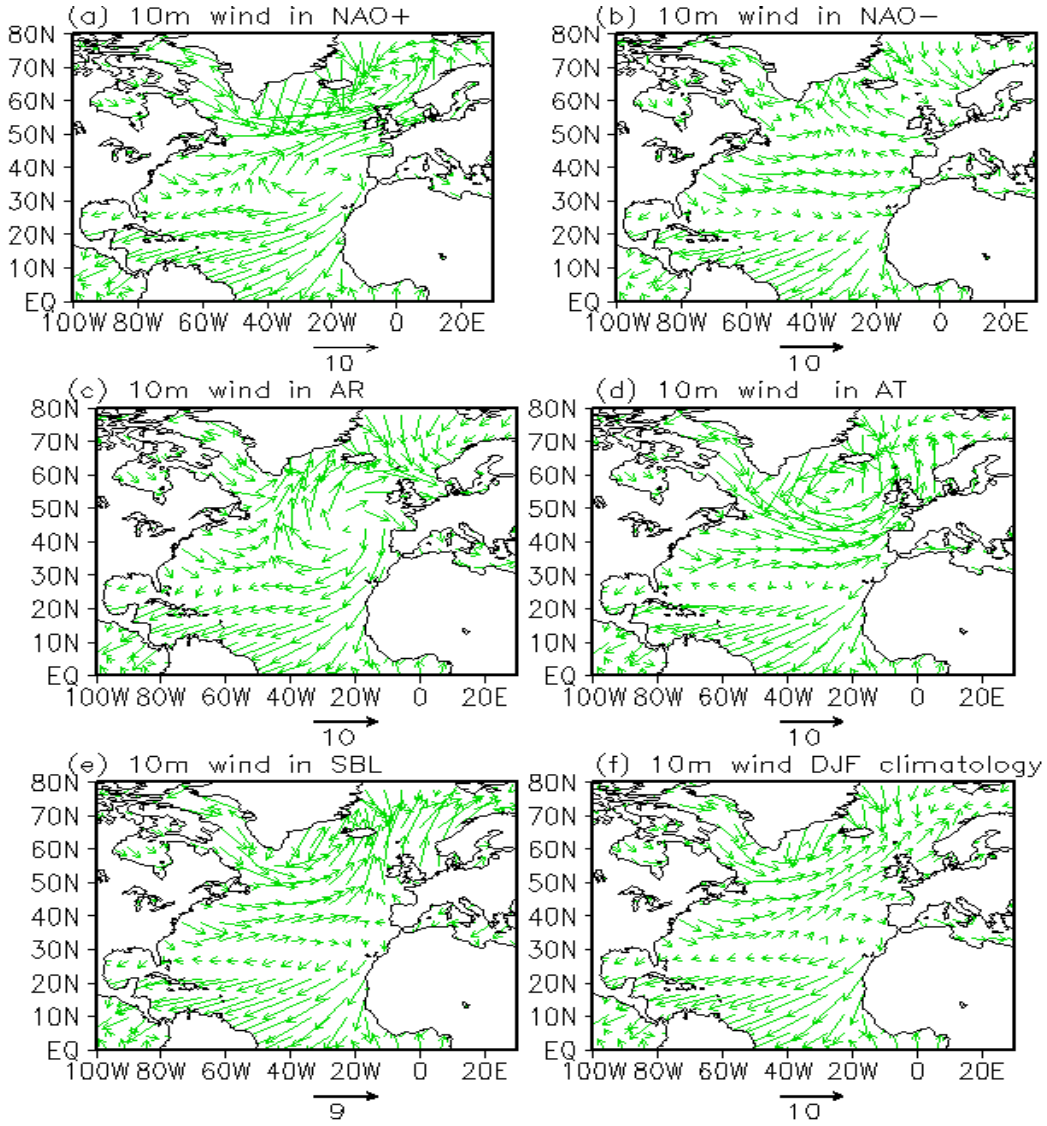

Figure 2.7: A composite mean of 10m wind vector fields under each weather regime from 1948 to 2016 DJF (a) in NAO+ 1320 day mean (b) in NAO- 1546 days) (c) in AR 1126 days (d) in AT 1214 days (e) in SBL 1272 days (f) DJF climatological mean from 1948 to 2016; based on NCEP reanalysis daily data. units: m s^{-1}.

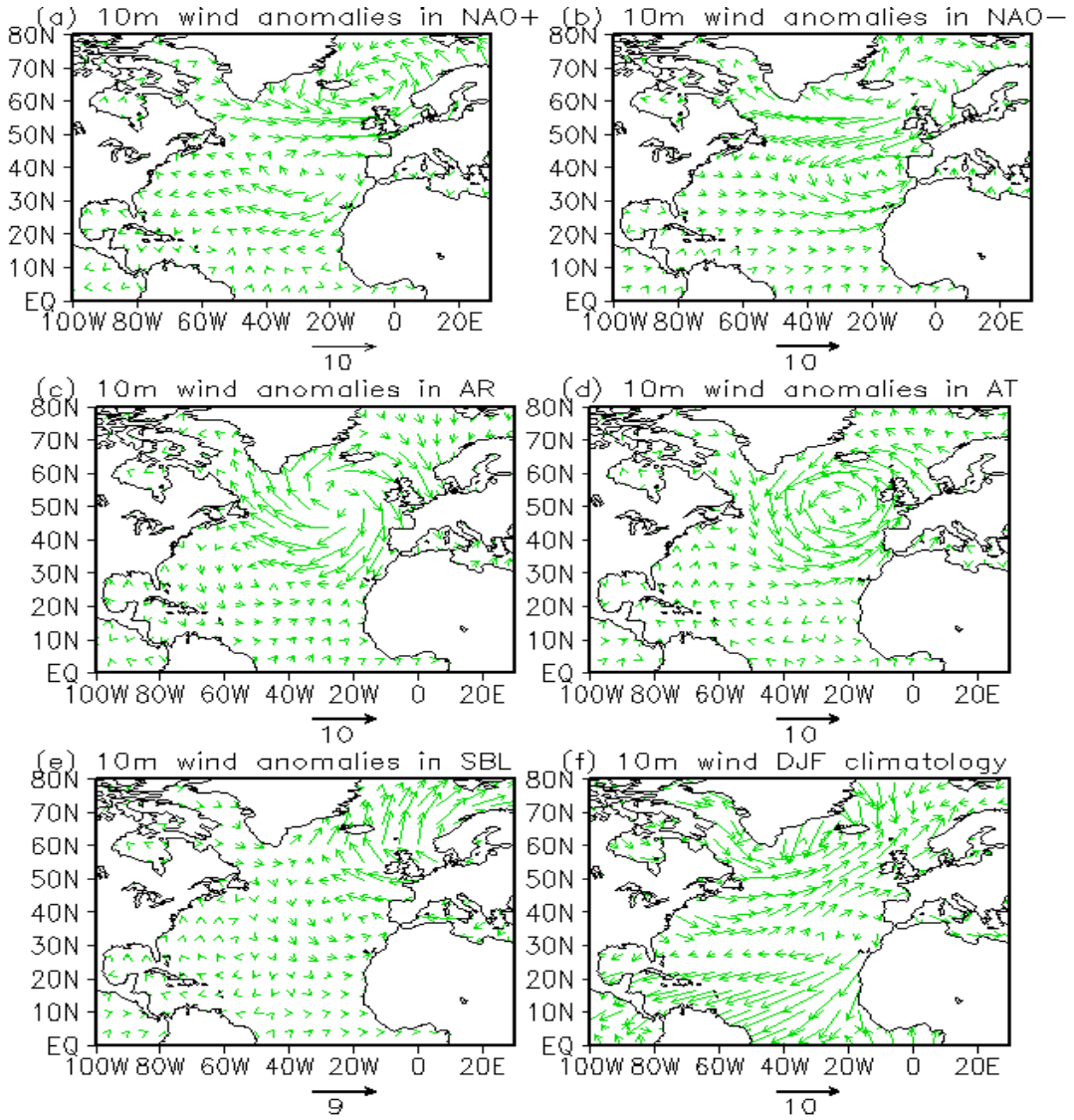

Figure 2.8: A composite mean of 10m wind vector anomalies fields under each weather regime from 1948 to 2016 DJF (a) in NAO+ 1320 day mean (b) in NAO- 1546 days) (c) in AR 1126 days (d) in AT 1214 days (e) in SBL 1272 days (f) DJF climatological mean from 1948 to 2016; based on NCEP reanalysis daily data. units: m s^{-1}.

2.4.2 Changes in surface air temperature under the five weather regimes

In comparison, the positive air temperature anomalies over 4K are located where there is an abnormally high height and where there is anticyclonic wind circulation (Fig. 2.5, Fig. 2.7, Fig. 2.9) due to less heat loss (Fig. 2.10). Noticeably, over high latitudes, when the southerly or south-westerly wind gets there from middle latitudes it leads to warmer anomalies, see NAO+ and SBL patterns (Fig. 2.5 a, e, Fig. 2.7 a, e, Fig. 2.9 a, e) due to warm air transported there. Negative air temperature anomalies over -4K are associated with low height anomalies which are dominated by cyclonic wind circulation due to greater surface heat loss (Fig. 2.10). At high latitudes, the negative air temperature anomalies are controlled by strong northerly winds from the North pole or from North America. (Fig. 2.7 b, c and d, Fig. 2.9 b, c and d).

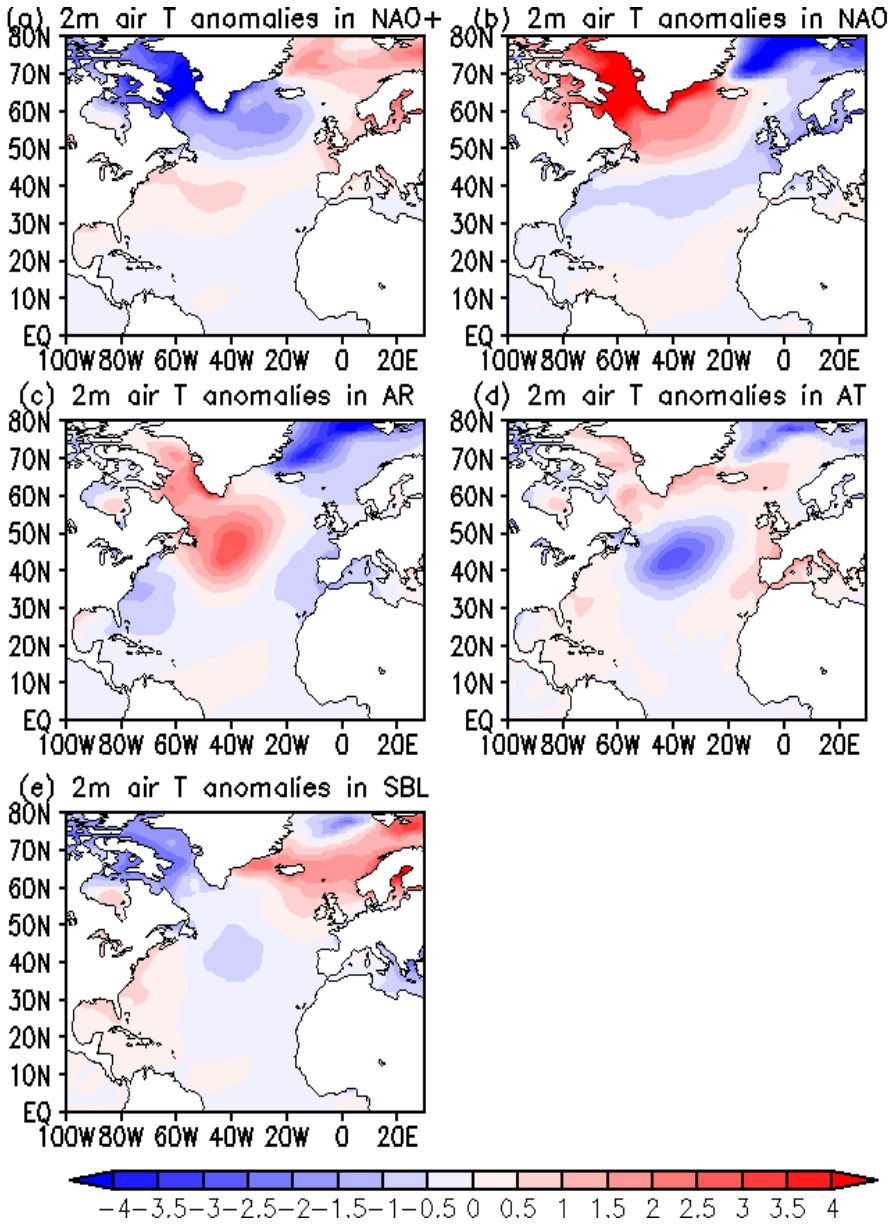

Figure 2.9: A composite mean of 2m air temperature anomalies under each weather regime from 1948 to 2016 DJF (a)in NAO+ 1320 day mean (b) in NAO- 1546 days (c) in AR 1126 days (d) in AT 1214 days (e) in SBL 1272 days; based on NCEP reanalysis daily data. units: K, each interval is 0.5K.

2.4.3 Changes in air-sea heat flux under the five weather regimes

In this section, upward heat flux has a positive value, i.e the ocean loses heat, and downward heat flux is a negative value i.e. the ocean gained heat or showed less heat loss. Net heat flux anomalies are defined as the sum of the sensible heat and latent heat flux anomalies. Sensible and latent heat flux data are directly from NCEP reanalysis daily dataset (see section 2.2 description):

$$H = (H_l + H_s) \tag{2.2}$$

H_l: net latent heat flux anomalies

H_s: net sensible heat flux anomalies

Heat flux unit: all in W m^{-2}

On the synoptic-time scale, positive air-sea heat flux anomalies over 150 W m^{-2} are located mostly where the surface temperature anomalies are negative which implies heat loss leading to surface cooling. In contrast, negative net heat flux anomalies over about -150 W m^{-2} are dominant over regions where there are positive surface temperature anomalies which implies that the ocean gains heat or has less heat loss. The temperature and air-sea heat flux over the central Atlantic anomalies are mostly dominated by central Atlantic Ridge and central Atlantic Trough patterns (Fig. 2.9 c and d, Fig. 2.10 c and d). NAO+ and

NAO- are dominant for changes in surface air-sea heat flux and temperature over the subpolar gyre and high latitudes (Fig. 2.9 a and b, Fig. 2.10 a and b). While, Scandinavian blocking pattern influences changes in air-sea heat flux and temperature mainly over the Nordic Sea (Fig. 2.9 e and Fig. 2.10 e).

In order to explain the mechanism for why the air-sea heat flux responds to weather regimes in different manners, I re-visit the to latent and sensible heat flux formulae (Cayan, 1992):

$$\begin{aligned} H_l &= \rho L C_E u(q_s - q_a) \quad (a) \\ H_s &= \rho C_p C_H u(T_s - T_a) \quad (b) \end{aligned} \tag{2.3}$$

where u, q_a, and T_a are the wind speed, specific humidity and temperature of the air in the boundary layer, and q_s and T_s are the saturation specific humidity and surface temperature; ρ is air density, L is the latent heat of evaporation, C_p is the specific heat capacity of air at constant pressure, C_E and C_H are transfer coefficients for latent heat and sensible heat, respectively.

According to equations (2.3), for example, during NAO+ phase, over the subpolar region, air temperature at 2m drops about -1.5K (Fig. 2.9 a) due to cold air transported there Fig. 2.8 a), which can enhance temperature different between SST and air temperature leading to more sensible heat loses from the ocean to the atmosphere. Meanwhile, cold and dry air from strong westerly wind creates high humidity difference between ocean surface and air leading to more latent heat loss from the ocean to the atmosphere. Furthermore, strong westerly winds from North America cause to more both sensible and latent heat flux loss from

the ocean. As a results, there is positive heat flux anomalies meaning more heat upward about 150 W m^{-2} located here. At the same time. Similar processes can be seen from other regimes. The study by (**?**) revealed that basin scale heat flux anomalies are controlled by the atmospheric circulation, which is proved in my analysis. The relationship between air-sea heat flux anomalies and tendency of SST will be explored in the chapter 3.

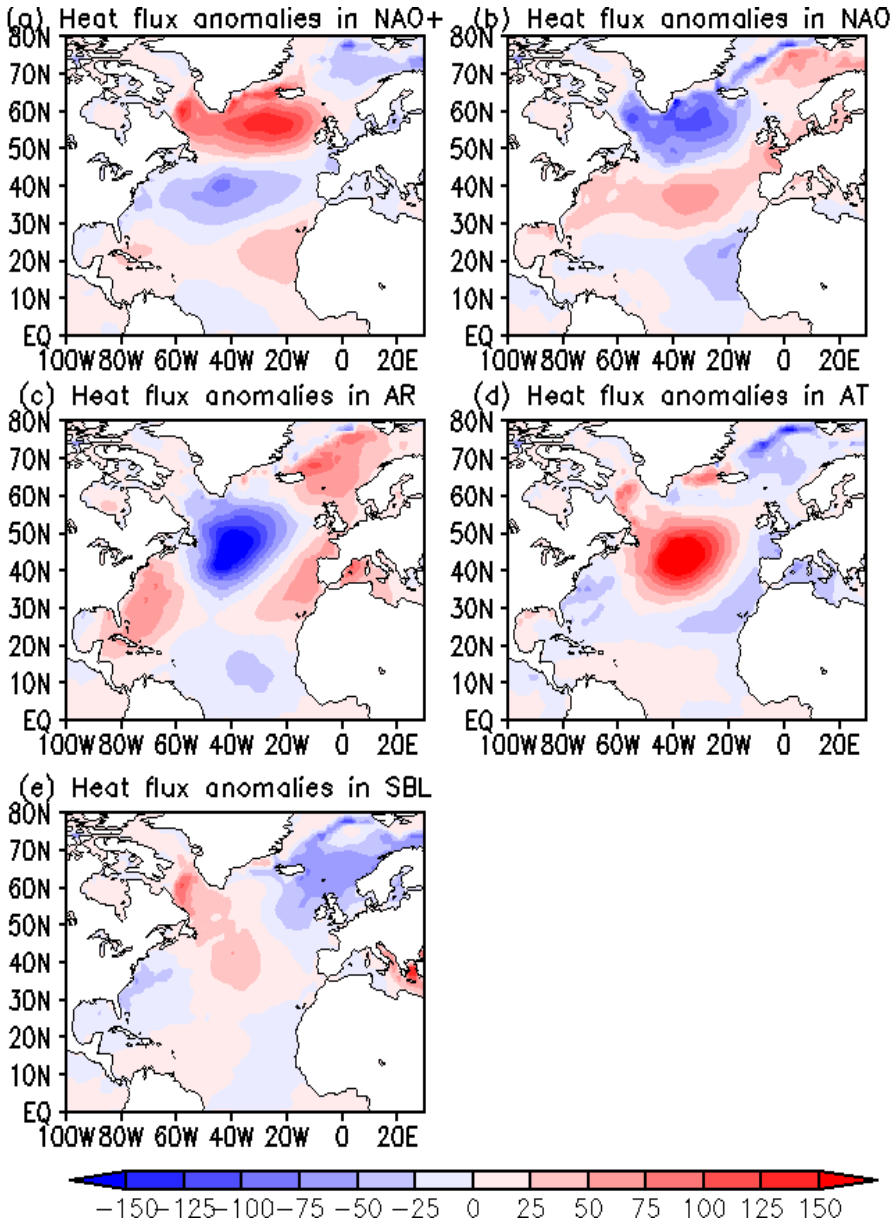

Figure 2.10: A composite mean of surface air-sea heat flux anomalies under each weather regime from 1948 to 2016 DJF (a)in NAO+ 1320 day mean (b) in NAO- 1546 days (c) in AR 1126 days (d) in AT 1214 days (e) in SBL 1272 days; based on NCEP reanalysis daily data. units: W m^{-2}, each interval is 25 W m^{-2}. Note: upward heat flux has a positive value, i.e the ocean loses heat, and downward heat flux is a negative value, i.e the ocean gains heat or less heat loss.

2.4.4 Changes in wind stress and wind-induced Ekman transport under the five weather regimes

The ocean surface current patterns have a similarity with that of the low-level winds in the atmosphere. Winds, through turbulent transfer of momentum across the atmospheric boundary layer, exert a stress on the ocean surface that drives ocean current. The surface wind stress is related to the wind velocity through a bulk formula (Marshall and Plumb, 2008):

$$(\tau_{wind_x}, \tau_{wind_y}) = \rho_{air} C_D u_{10}(u, v) \tag{2.4}$$

where, τ_{wind_x}, τ_{wind_y} are zonal and meridional stress components, respectively, C_D is a bulk transfer coefficient for momentum, $C_D = 1.5{\times}10^{-3}$, ρ_{air} is surface air density, u_{10} is the speed of the wind at a height of 10m, u and v are zonal and meridional wind components at a height of 10m, respectively.

The wind stress will be communicated downward by turbulence, this downward motion is confined to the near surface layers of the ocean, which is the Ekman layer. With a given surface wind stress we can compute the horizontal components of the total mass transport integrated over the Ekman Layer. At the surface, the wind stress $\tau = \tau_{wind}$, at the bottom of the Ekman layer depth $z = -\delta$, where $\tau = 0$, so that we have Ekman mass transport:

$$M_{EK} = \frac{\tau_{wind} \times \hat{z}}{f} \tag{2.5}$$

Equation (2.5) only depends on surface wind stress τ_{wind} and f, thus, the Ekman mass transport layer is exactly to the right of the surface wind (see Figure 10.5) in the book by Marshall and Plumb (2008). Hence, we have horizontal Ekman mass transport in x and y directions, $M_x = \frac{1}{f}\tau_{wind_y}$, $M_y = -\frac{1}{f}\tau_{wind_x}$.

Because Ekman transport is to the right of the wind in the northern hemisphere, there is water convergence due to anticyclonic circulation, then there is downward Ekman pumping in the subtropics. Over the subpolar gyres, the flow is divergent due to cyclonic circulation and Ekman suction is induced, drawing water upward into the Ekman layer. We can gain a simple expression for the pattern and magnitude of the Ekman pumping/suction in terms of wind stress:

$$w_{EK} = \left(\frac{\partial(\tau wind_y/\rho f)}{\partial x} - \frac{\partial(\tau_{wind_x}/\rho f)}{\partial y}\right) = \nabla \times \left(\frac{\tau_{wind}}{\rho f}\right) \cdot \hat{z} \tag{2.6}$$

In equation (2.6), Ekman vertical velocity (left hand side) is related to wind stress curl vertical component (right hand side). Positive wind stress curl indicates cyclonic wind stress which contributes to Ekman upwelling; whilst negative wind stress curl indicates anticyclonic wind stress which contributes to Ekman downwelling.

In this chapter, composites of the five weather regimes' wind stress anomalies are computed based on formula (2.4) using the same days as shown in table 1. For each weather regime, for every day, for each grid point over the North Atlantic (i) 10m zonal and meridional component wind anomalies are calculated ; (ii) wind speed anomalies calculated (iii) wind stress and curl anomalies calcu-

lated; (iv) total days wind stress and curl anomalies are composited and yield each weather regime's mean map shown in Fig. 2.11. Ekman horizontal volume transport is calculated using same processes based on relations: $Q_x = \frac{1}{\rho_{ref}} M_x$, $Q_y = \frac{1}{\rho_{ref}} M_y$ (Marshall and Plumb, 2008). Ekman pumping/suction velocity is calculated based on equation (2.5). Again, for each weather regime, every day's Ekman horizontal transport and pumping/suction velocity are calculated, then total days are composited, then mean maps are made (see Fig. 2.12).

Over the North Atlantic, with the NAO+ weather regime, there is an enhanced cyclonic circulation around Iceland, then enhanced westerly wind stress there (see Fig. 2.11 a), which enhanced southward Ekman horizontal transport below the Iceland cyclonic circulations. Also, wind stress vectors pointed outwards from the cyclonic centre where Ekman vertical velocity shows positive implying an Ekman upwelling and positive wind stress curl around the Iceland sea (see Fig. 2.12 a). On the one hand, there is enhanced anticyclonic circulation over the Azores, so that there is an enhanced northward Ekman volume transport along 30°N due to enhanced easterly wind stress. Thus, we can see that strong convergence occurs along 40°N where southward and northward Ekman transport merge causing Ekman downward pumping (see Fig. 2.12). In a similar manner, such processes take place for the rest of the regimes, that is, where there is cyclonic circulation there is enhanced westerly wind stress at the south of the cyclonic circulation which leads to enhanced southward Ekman horizontal transport and Ekman upwelling there. For anticylonic circulations, the processes are just opposite.

Noticeably, the central Atlantic ridge and trough patterns show strong Ekman vertical velocity anomalies and wind stress anomalies, as well as Ekman horizontal volume transport (Fig. 2.11 c and d, Fig. 2.12 c and d) over the central Atlantic. With the Scandinavian Blocking regime, the wind stress anomalies and Ekman transport take place over the Nordic Sea (Fig. 2.11 e, Fig. 2.12 e).

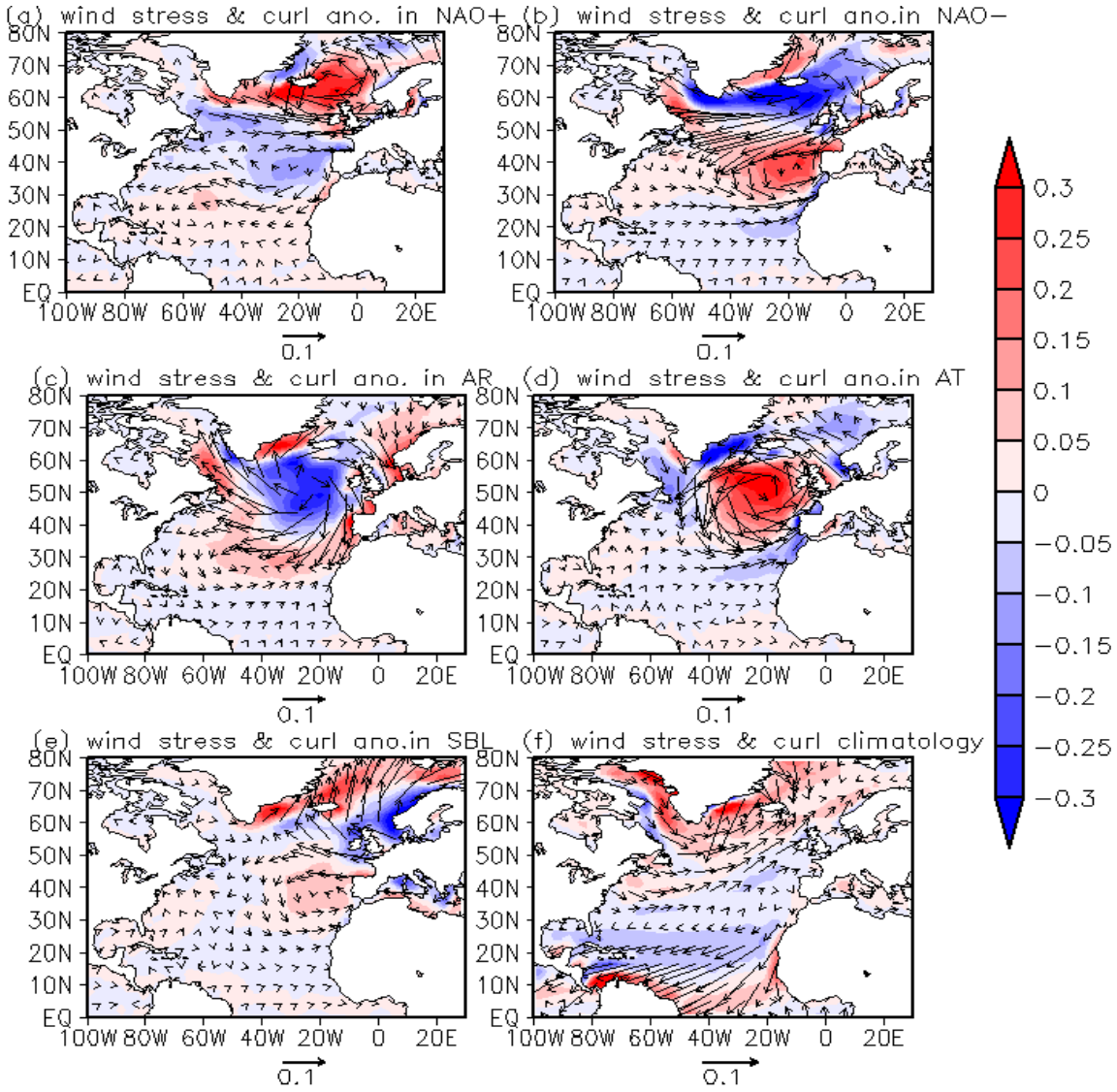

Figure 2.11: A composite mean of surface wind stress anomalies and curl of wind stress anomalies under each weather regime from 1948 to 2016 DJF (a)in NAO+ 1320 days mean (b) in NAO- 1546 days (c) in AR 1126 days (d) in AT 1214 days (e) in SBL 1272 days; based on NCEP reanalysis daily data. Wind stress: vectors, unit: N m^{-2}. Curl of wind stress curl: shaded colour, units: 10^{-5} N m s^{-3}, positive values represent cyclonic wind stress curl, negative values represent anticyclonic wind stress curl.

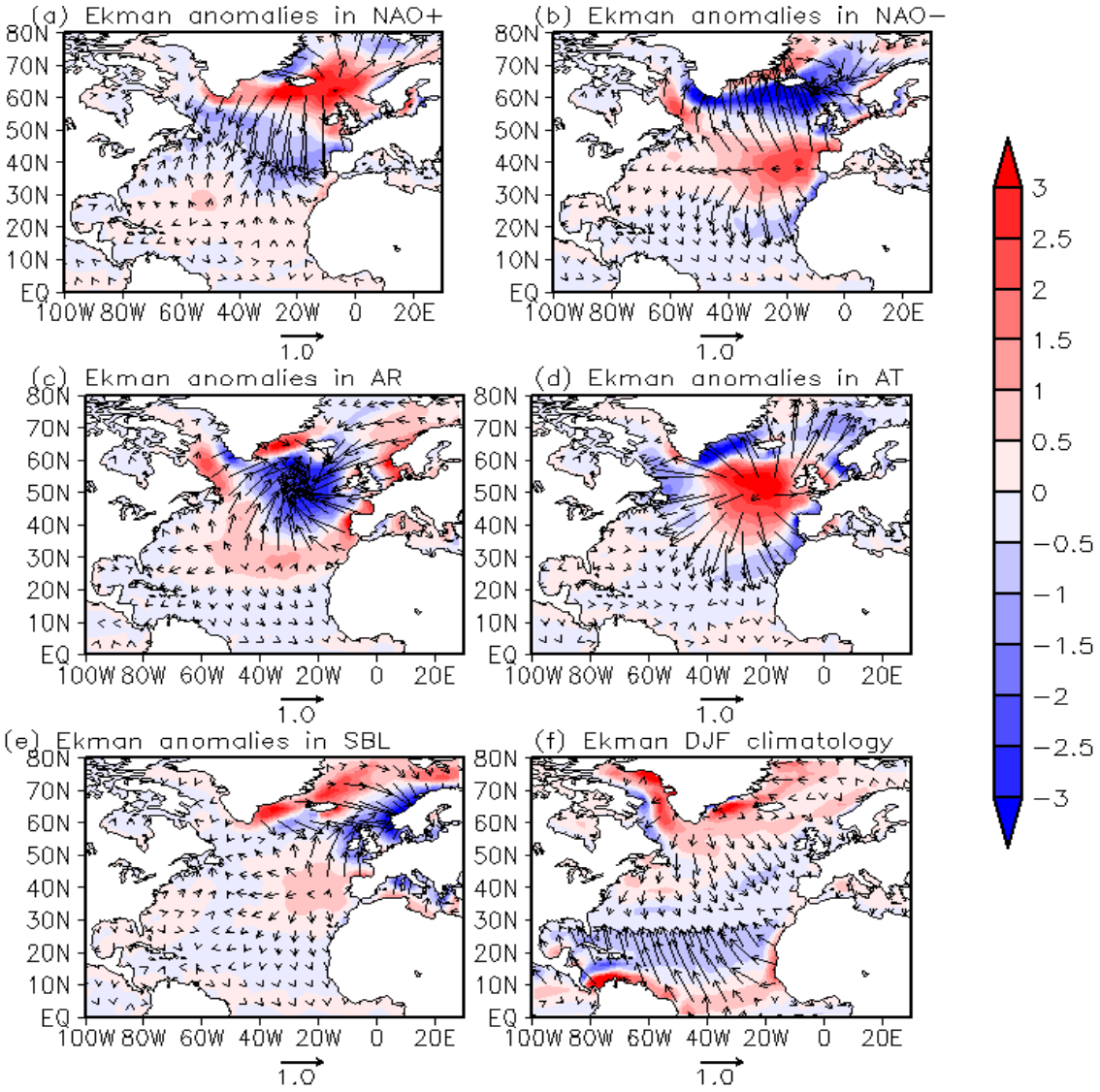

Figure 2.12: A composite mean of Ekman horizontal volume transport anomalies and vertical anomalies under each weather regime from 1948 to 2016 DJF (a)in NAO+ 1320 days mean (b) in NAO- 1546 days (c) in AR 1126 days (d) in AT 1214 days (e) in SBL 1272 days; based on NCEP reanalysis daily data. Ekman horizontal volume transport:Ekman horizontal volume transport: vectors, unit: $m^2\ s^{-1}$. Ekman vertical velocity: shaded colour, units: 10^{-5} m s^{-1}.

2.5 Atmospheric jet stream speed and location corresponding to different weather regimes

Previous studies revealed the connection between the jet stream and weather regimes (Woollings et al., 2010; Hall et al., 2015; Madonna et al., 2017). Hence, in this section the connection between weather regimes and atmospheric eddy-driven jet stream is revisited to provide a context for the project.

Fundamentally, the general circulation of the atmosphere is affected by the role of the large-scale eddies and their behaviour and the feedback onto the mean flow (Hoskins et al., 1983). The atmospheric variability in the North Atlantic is associated with variations in the eddy-driven component of the zonal flow (e.g. Woollings et al., 2010; Hall et al., 2015; Madonna et al., 2017). The eddy-driven jet stream is most robust when it crosses over the ocean, also variation of the atmospheric mean flow is more undulating over the ocean (Blackmon, 1976).

2.5.1 Connection between eddy-driven jet stream and weather regimes

The eddy-driven jet is so deep throughout the level of the troposphere, due to the effect of transient eddy forcing to strengthen the westerlies at low levels. (Hoskins et al., 1983; Woollings et al., 2010). Hence, the eddy-driven jet stream is best

diagnosed from the zonal wind at lower levels. Importantly, this study is focused on how the eddy-driven jet stream interacts the ocean, and the jet at the low level of 850 hPa is close to the ocean surface.

In this section, the connection between atmospheric jet stream and each weather regime is analysed. The zonal wind at 850hPa level corresponding to different weather regimes over the Atlantic is examined. Each regime's composite days are formed of days shown in Table 1, which include all the days satisfying my regime definition criteria through all data in DJF from 1948 to 2016. During the NAO+ state, the jet stream strength is relatively strong between 15 m s^{-1} to 24 m s^{-1} zonally crossing the Atlantic at a central latitude at 50°N (see Fig. 2.13 a). For the NAO- state, the jet stream crosses the Atlantic at a more southward latitude at or below 40°N with a relatively weaker speed of about 10 m s^{-1} to 12 m s^{-1} (see Fig. 2.13 b). The zonal wind strength and latitude location corresponding to NAO regimes suggests that a positive NAO indicates a strengthening, or a northward shift of the jet, or both (Woollings et al., 2010). This positive correlation between jet speed or latitude with NAO index is also revealed in DePreSys3 hindcast monthly ensemble data in chapter 3.

For the central Atlantic Ridge weather regime, the jet stream passes northern latitudes (Fig. 2.11 c). For the central Atlantic Trough regime, the jet stream passes over the middle latitudes between 40°N to 50°N with medium speed over about 12 m s^{-1} and is directed more zonally due to no blocking downstream. For

the Scandinavian blocking regime, the jet stream passes the Atlantic with mixed latitudes with southern latitude at the west side of the ocean then with northern latitude at the west side of Scandinavian with 8 to 16m s^{-1}.

In previous studies, these four jets associated with weather regimes are called central jet, southern jet and northern jet, and mixed jets associated with NAO+, NAO-, AR or EA- and SBL respectively (Woollings et al., 2010; Madonna et al., 2017).

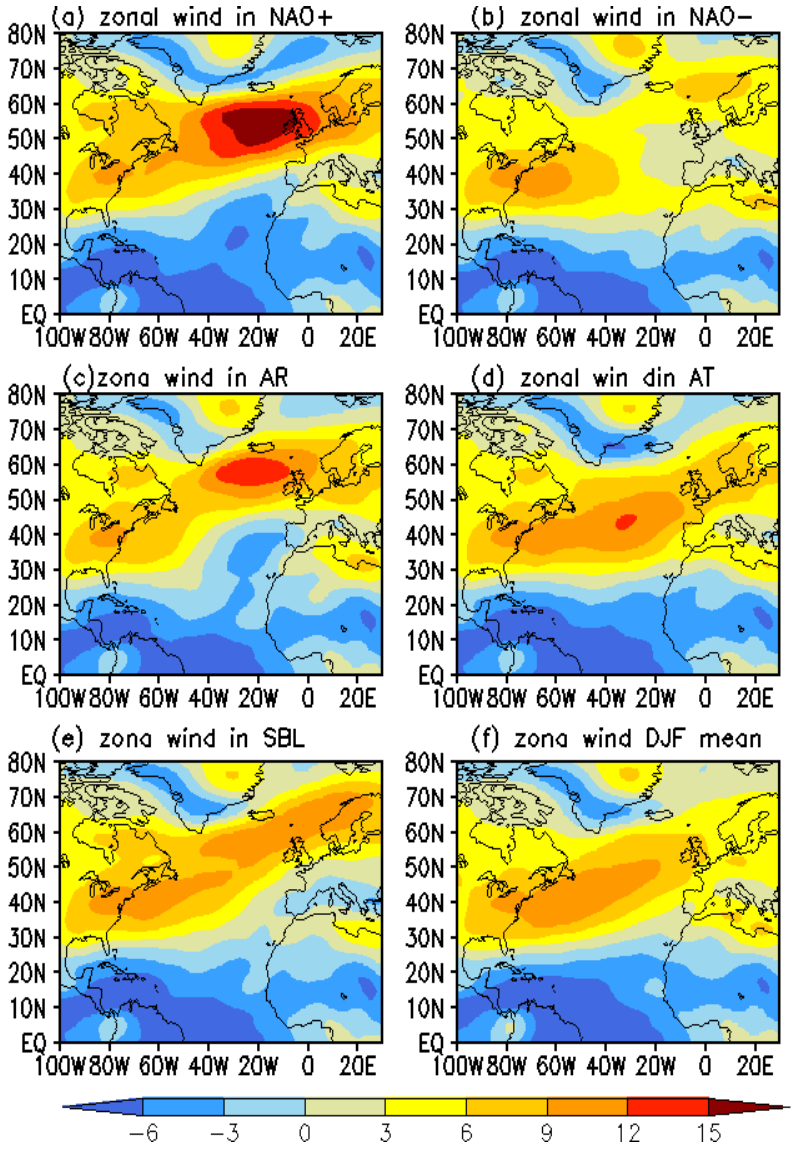

Figure 2.13: A composite mean of zonal wind at 850hPa under each weather regime from 1948 to 2016 DJF (a) in NAO+ 1320 days mean (b) in NAO- 1546 days) (c) in AR 1126 days (d) in AT 1214 days (e) in SBL 1272 days (f) DJF climatological mean from 1948 to 2016; based on NCEP reanalysis daily data. units: m s^{-1}.

2.6 Conclusion and Discussion

Combining the previous studies (Wallace and Gutzler, 1981; Cassou et al., 2011; Woollings et al., 2010), there should be five weather regimes over the North Atlantic in winter time. Hence, I redefined weather regimes on 500hPa geopotential height fields. The weather patterns' maps and indices are generated based on daily 500hPa geopotential height and anomalies. There are five weather regimes in winter time over the North Atlantic: NAO+ (21%), NAO- (24.8%), central Atlantic Ridge (18%), central Atlantic trough (19%) and Scandinavian Blocking (20%). The percentages refer to each weather regime occurrence out of total days in DJF from 1948 to 2016 (see in Table 1).

Composite analysis is employed for each regime affecting ocean variables and circulation. Composite days are formed of days shown in Table 1, including over all the days in DJF from 1948 to 2016 for each weather regime which satisfies my regime definition criteria throughout all data in DJF from 1948 to 2016.

After revisiting the winter weather regimes definition, frequency, and atmospheric circulation, it can be understood how the weather regimes affect ocean surface circulation and variables in winter time over the North Atlantic.

Horizontally, different weather regimes represent different atmospheric circulations which bring cyclonic and anticyclonic circulation over the ocean surface. Consequently cold and warm air masses are transported to the ocean zonally and

meridionally, which result in changes to air-sea heat flux, which in turn changes sea surface temperature. Meanwhile, different weather regimes lead to different surface wind patterns which causes changes in ocean surface horizontal circulation.

Vertically, the cyclonic and anticyclonic circulation associated with different weather regimes affect Ekman vertical upwelling and downwelling regions shifting them further northward or further southward corresponding to different weather regimes. In particular, the central Atlantic ridge and trough are vital to change central Atlantic surface variables and circulation, especially Ekman horizontal and vertical transport (see Fig. 2.7 c and d, Fig. 2.8 c and d, Fig. 2.10 c and d).

The linkage to atmospheric eddy-driven jet stream variability shows the central jet has the strongest speed which corresponds to NAO+. The southern jet has a relatively weak speed which is associated with NAO-. The northern jet has a relatively strong speed which is associated with the central Atlantic Ridge regime or EA- regime. The jet stream associated with Scandinavian blocking crosses the Atlantic at southern latitudes from the west side of the ocean then at northern latitudes at the west side of Scandinavia, which is called the mixed jet. The link between eddy-driven jet stream variability and weather regimes in the North Atlantic-European sector was revealed in previous studies by Woollings et al. (2010) and Madonna et al. (2017), and are consistent with my analysis here.

2.7 Which of the results are well established and which are new?

After I analyse the weather regimes over the Euro-North Atlantic in winter time, the following results are well established: (i) The weather regimes' patterns and frequency using my own definitions are matching well with pevious studies. (ii) Weather regimes strongly affect the underlying ocean. (iii) Low level zonal wind at 850 hPa reveals eddy-driven jet stream speed and latitude locations well. Eddy-driven jet stream speed and latitude locations can reflect multi-weather regimes.

Previous studies have four weather regimes using different names. For example, the study using the k-mean cluster method showed there are four North Atlantic-Europe weather regimes: NAO+, NAO-, central Atlantic Ridge (EA- in other studies) and Scandinavian Blocking (Cassou et al., 2011) without EA+. Another study revealed the circulation for different combinations of the NAO and EA patterns NAO+, NAO-, EA+ and EA- (EA - is equivalent to central Atlantic Ridge, and EA+ is the opposite phase) (Woollings et al., 2010).

In my analysis, the five weather regimes include all the regimes NAO+, NAO-, central Atlantic Ridge, central Atlantic Trough and Scandivian Blocking which are revealed either in both studies. The new aspects in my study are: (i) The sign is arbitrary in EA+ and EA- patterns in previous studies. Hence, in my definition, EA- in the study by Woollings et al. (2010) is called the central Atlantic ridge;

whereas, EA+ is the central Atlantic trough, which are named by the atmospheric ridge and trough circulations. (ii) My definition for obtaining five weather regimes is based on real data and weather maps instead of the clustering method.

2.8 The thesis new work

Previous studies have investigated atmosphere and ocean interaction associated with the NAO or other weather regimes. The disadvantages of choosing NAO or any other weather regime is that they only account for part of the atmospheric variability. Too much unnecessary work will be involved if all multi-weather regimes are chosen to investigate interaction between the atmosphere and the ocean.

The jet stream speed and latitude location can reflect multi-weather regimes. Therefore, using the jet indices to look at how the atmosphere affects the ocean is a key new approach in the thesis. This chapter sets the scene by linking this to weather regimes. The advantages of choosing the speed and latitude of the jet: (i) can represent more atmospheric variability due to the variability of jet speed and latitude being able to reflect at least these five weather regimes; (ii) the jet speed and latitude are simple and more direct indices to use rather than using five weather regimes' indices.

Chapter 3: How does the winter jet stream affect surface temperature, heat flux and sea ice in the North Atlantic? And are there signals of an ocean feedback on

the atmospheric jet stream?

Chapter 4: How Does the atmospheric jet stream affect Atlantic subsurface temperature, mixed layer and heat content?

Chapter 5: How does the atmospheric jet stream affect Atlantic Meridional Overturning Circulation (AMOC)?

Chapter 3

How does the winter jet stream affect surface temperature, heat flux and sea ice in the North Atlantic?

3.1 Introduction

In chapter 2, it has been revealed that mid-latitude weather regimes including NAO affect Atlantic ocean surface variables in both thermal and dynamical ways. Eddy-driven jet stream wind speed strength and latitude shift reflect the multi weather regimes.

In this chapter, the mid-latitude eddy-driven jet stream is viewed as mid-latitude

atmospheric variability overlaying the Atlantic ocean and explores how the jet influences the North Atlantic surface in winter time in monthly and seasonal time scales. The jet stream wind speed and latitude shift are viewed as jet stream strength and latitude location.

The aim of this chapter is to examine the influence of atmospheric variability on the surface North Atlantic Ocean from the jet stream perspective, treating the jet position and strength separately. The position and strength of the eddy-driven jet are identified using jet indices based on the maximum of the zonally-averaged zonal wind (Woollings et al., 2018). These jet indices are relatively simple, neglecting for example the meridional tilt of the jet (Madonna et al., 2017), but have the advantage of providing simple time series comparable to the NAO. The jet indices explain much of the variability associated with both the NAO and the East Atlantic (EA) pattern (Woollings et al., 2010), i.e. the two leading empirical orthogonal functions (EOFs) in the region, but not that associated with higher order EOFs such as the Scandinavian pattern. An additional motivation for this separation is that the NAO seems to reflect a different balance of the two jet indices on different timescales, with the jet latitude dominating on inter-annual timescales, but the jet speed becoming more important on multi-decadal timescales (Woollings et al., 2015).

Atlantic multi-decadal variability has considerable regional climate impact (Knight et al., 2006; Sutton and Dong, 2012) with the ocean playing an important role

in this variability (Gulev et al., 2013; O'Reilly et al., 2016). Climate models generally underestimate multi-decadal variability in both the ocean and the atmosphere (Kravtsov, 2017; Kim et al., 2018; Simpson et al., 2018), in particular in the speed of the jet rather than its latitude (Bracegirdle et al., 2018). Hence the differing effects of jet latitude and speed on the ocean may be of importance for understanding Atlantic multi-decadal variability.

Analyses of ocean-atmosphere coupling in observations have limited ability to identify causal relationships due to the several different mechanisms operating on different timescales between the ocean, the local atmosphere and potential remote drivers. Hence, although some comparison is made with reanalysis data in this chapter, the majority of my analysis focuses on a large ensemble of historical model simulations, in which inferences of causality are less problematic.

For each season I compare the evolution of forty individual ensemble members, each initialised with identical ocean states and small perturbations in the atmosphere. My primary assumption is that the spread in ocean variables between ensemble members over the following few months is determined by their different realisations of chaotic atmospheric variability. Analysis across the ensembles allows the sensitivity of the ocean to jet latitude and jet speed to be identified. One caveat to this approach is that sensitivities are only considered on monthly to seasonal timescales, so do not include delayed responses that may be important in explaining decadal changes in surface warming (Robson et al.,

2012). Heat loss from the ocean to the atmosphere is often strongly modulated by synoptic-timescale processes, such as mid-latitude cyclones (Parfitt and Seo, 2018) and the related cold air outbreaks (Papritz and Spengler, 2017; Vannière et al., 2017). These events are themselves modulated by low-frequency variability of the large-scale flow (Kolstad et al., 2009; Woollings et al., 2016).

In this chapter, I focus on the seasonal evolution of the coupled system and hence I investigate the role of the large-scale circulation, following studies such as Visbeck et al. (2003), Zhai et al. (2004) and Cassou et al. (2011). I use indices of the eddy-driven jet stream derived from the lower tropospheric zonal winds that provide direct measures of a time-averaged wind, as well as act to integrate the effects of the transient weather systems which drive the jet (Hoskins et al., 1983). Despite the importance of synoptic and smaller scale processes, It shows that large fractions of the variance in surface heat flux on seasonal time scales can be accounted for by the flow variations summarised by these two simple jet indices.

3.2 Ensemble model data description

Seasonal hindcasts are analysed from the Met Office decadal prediction system3 (DePreSys3) (Smith and Murphy, 2007; Smith et al., 2007; Dunstone et al., 2016), designed to make global and regional climate predictions over seasonal to decadal timescales. DePreSys3 is based on the HadGEM3-GC2 coupled climate model

(Williams et al., 2015a) with an atmospheric horizontal resolution of 0.83° × 0.55°. Hindcasts are initialised using the 1st November conditions provided by the assimilation run from years 1980 to 2014:

(i) The ensemble members are created by random seeds to the stochastic physics scheme (Bowler et al., 2009). Each member represents a realisation of the chaotic variability of the climate system that could have occurred due to tiny perturbations such as a butterfly flapping its wings.

(ii) The hindcast ensemble dataset provides many more realisations of internal variability than are available from the observations, providing much more robust statistics on the relationships between the atmosphere and ocean. Furthermore, the ensemble members start from nearly identical conditions in November allowing the growth of perturbations to be studied.

Hindcast length is 16 months. Taking 1980 as an example, starting with November 1980, go December and 12 months in 1981, then covering the second DJF winter months, ending in February 1982. Then repeat every year between 1980 and 2014.

(iii) The initial conditions are actually the same for each member, even in the atmosphere. But the stochastic physics gives different random numbers for each member, and these small differences grow according to chaos theory, such that the individual weather patterns in each member are different.

This model data set then comprises 40 ensembles over each month of the 35 years

(hereafter named ensemble data). The model analysis is also compared with ERA-Interim reanalysis monthly and daily data from the same period from 1980 to 2014.

In this study, surface latent heat flux, sensible heat flux, sea surface temperature, sea level pressure, air temperature at 1.5 meters in ensemble data and 2 metres in reanalysis daily data, sea-ice fraction, 850hPa zonal wind, and 10 metre winds for the ensemble and monthly and daily reanalysis data sets from ECWMF interim reanalysis from years 1980 to 2014 are employed. In the ensemble data, surface temperature is defined by the temperature of the surface land and ice where they occur, and elsewhere represent sea surface temperature; so that in polar regions, surface temperature may reach -30° to -40°C.

3.3 Scientific Process

The ensemble dataset of 40 realisations provides much more robust statistics on the relationships between the atmosphere and ocean. Hence, in this study, the causality relationship is explored. The primary assumption is that the spread in ocean variables between ensemble members over the following few months is determined by their different realisations of the chaotic atmospheric variability. Secondary assumption is that the spread in atmospheric variability (jet stream) between ensemble members over the following few months is determined by their different realisations of the perturbed ocean variability.

Analysis across the ensembles allows us to understand how the ocean is sensitive to jet latitude and jet speed variability and how the atmosphere jet speed and latitude are sensitive to the ocean variability.

If the correlation relationship is made across 35 years it provides interannual connection between atmosphere and the ocean variables rather than causality between atmosphere variability and ocean variability. This is not the purpose for this chapter.

3.4 Method

3.4.1 Ensemble sensitivity analysis

This chapter aims to explore the causality operating between the atmosphere and ocean by applying an ensemble sensitivity analysis to the hindcast data. It estimates the sensitivity of some target outcome J to a precursor variable x. Basically, it amounts to a lagged linear regression across an ensemble. Normalisation gives sensible units (change in J per standard deviation of x across the ensemble). It also includes a correlation across ensembles and its significance condition test: sensitivities are strongly damped if the correlation between x and J is below a chosen significance level. Torn et al. (2015) used an 80-member ensemble of experimental Global Forecast System (GFS) forecasts initialized five days prior to landfall to investigate the track of Hurricane Sandy. Dacre and Gray (2013) used

linear regression analysis to quantitatively evaluate the sensitivity of extratropical cyclone intensity to atmospheric precursor fields. The ensemble sensitivity analysis is based on analysis of the spread in the evolution of the ensemble members from their similar initial state. While there may be a systematic evolution common to the members, representing an underlying dynamical control or possibly a systematic effect of the ocean, the divergence of the ensembles on the seasonal timescale largely represents the effects of stochastic processes originating in the atmosphere.

The sensitivity of an outcome J to a precursor variable x is evaluated from the covariance of J and x, which may represent air-sea heat flux and jet speed respectively. The normalised sensitivity is defined by the ratio of the covariance and the standard deviation of the precursor,

$$\frac{\partial J}{\partial x} = \frac{cov\{J, x\}}{std\{x\}}, \tag{3.1}$$

where the normalisation has provided units of J per standard deviation of x across the ensembles.

For ensemble sensitivity analyses, a two stage process is applied to assess correlations between variables in the ensembles: (i) the correlation between jet indices and surface ocean variables across the 40 ensemble members for each winter month in each individual year of the 35 years is evaluated, for instance, the correlation between January jet indices and February sea surface temperature is calculated across 40 ensembles in each year, so that there are 40 samples for each year's

correlation calculation (rather than the 1400 samples of the entire data set), as a result, there are 35 correlation maps created; and (ii) a mean is then taken over these 35 maps to provide a climatological mean map. In addition, to assess their significance, a t-test is employed using the 40 samples, where each ensemble is taken to be independent. The correlation passes statistical significance tests with confidence levels of 90% at ±0.26, 95% at ±0.31 and 99% at ±0.40.

3.4.2 Jet structure in the ensemble hindcast dataset

The speed and latitude of the atmospheric jet stream is defined by the maximum value of the monthly-mean zonal wind at 850hPa averaged longitudinally over the North Atlantic sector (60°W to 0°) (Woollings et al., 2010). In the ensemble data, there are 4200 separate ensemble members made up of 40 ensemble members per month for each of the three winter months, which provide more variability of jet than reanalysis data, and repeated over 35 years (Fig. 3.1a) . There is a trimodal latitudinal structure for the jet with frequent occurrences at 45°N, 49°N and 55°N for the winter period December to February (Fig. 3.1), as well as a relatively weak occurrence at 35°N. These monthly distributions with a trimodal latitudinal distribution are similar to daily analyses based on reanalysis data (Fig. 3.1c) and the study by Woollings et al. (2018) for a similar daily figure. Comparison of the ensemble model monthly and reanalysis daily and monthly data distributions (Fig. 3.1) reveals that the model generally captures the observed distribution of

weather time-scale jet variability well, and so the ensemble monthly data is a suitable tool to investigate the impacts of jet variability on the underlying ocean.

In both the ensemble data and the reanalysis data sets, the jet latitude and speed are not linearly correlated, and represent two physically distinct pieces of information on the jet. Analysis of the ensemble data reveals a strong relationship between the jet indices and NAO index during winter time (December to February mean, 40 ensemble members and 35 years, total 1400 samples) with the strength of the jet associated with a positive NAO with a 0.72 correlation coefficient, while the the jet latitude is associated with a positive NAO with a 0.57 correlation coefficient. Hence, a positive NAO may indicate a strengthening, or a northward shift of the jet, or both (Woollings et al., 2010).

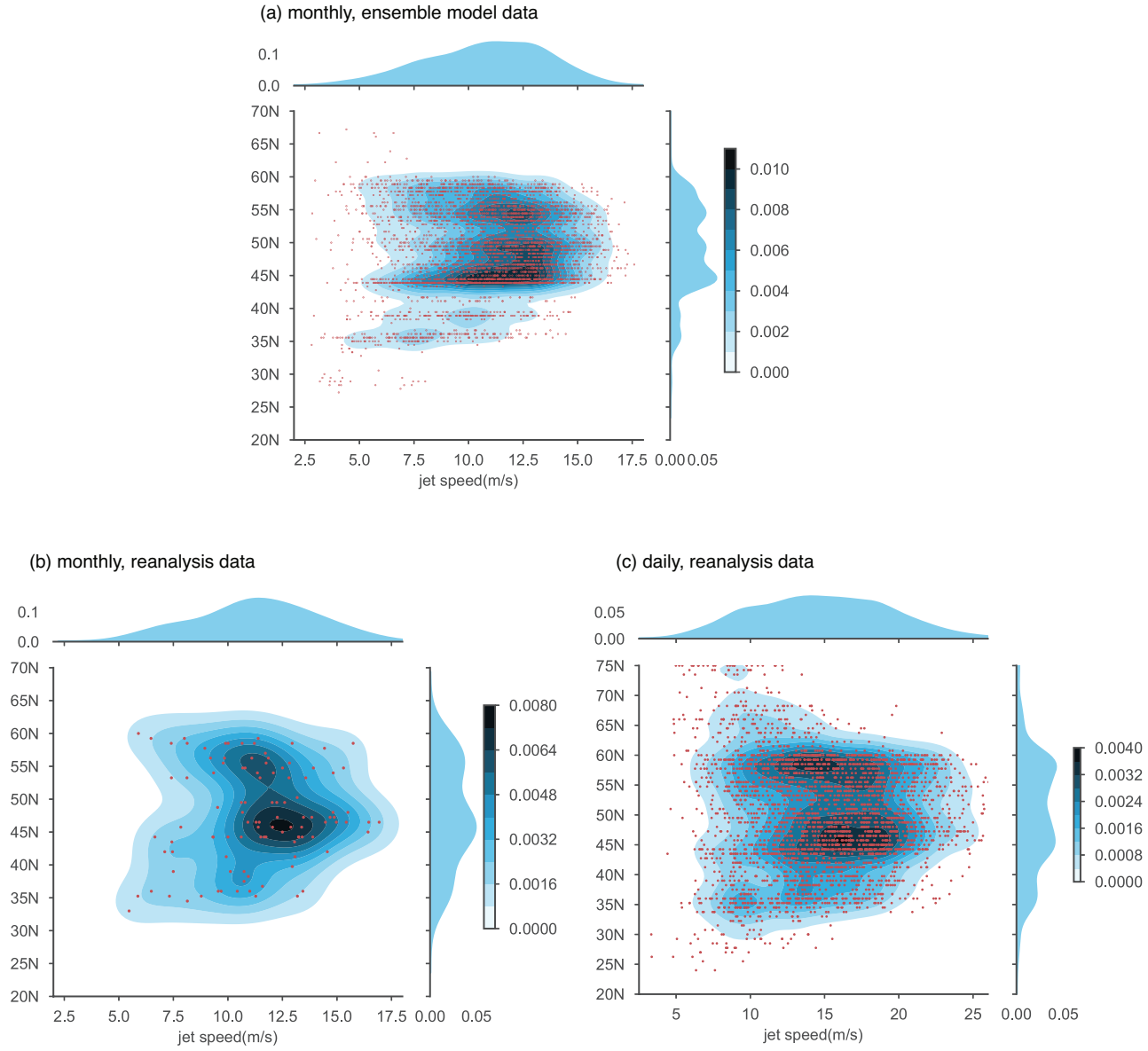

Figure 3.1: Jet stream speed versus latitude density distribution structure in winter time (December to February) 1980 to 2014 over the North Atlantic based on (a) the ensemble monthly data (b) the reanalysis monthly data and (c) reanalysis daily data. Coloured contours represent the density, i.e the number of points per 0.55°N degree bin m s^{-1} speed in 0.55N m s^{-1} in ensemble data and the number of points per 0.75°N degree bin m s^{-1} speed in 0.75°N m s^{-1} in reanalysis data; Top side panel represents the probability density of jet speed; right side panel represents the probability density of jet latitude. The probability density of the jet is mapped using a kernel density estimation where each speed versus latitude point is identified and the density of points is shown as the number of points per 0.55°N m s^{-1} and per 0.75°N m s^{-1} for ensemble and reanalysis data, respectively.

3.5 The effect of the atmospheric jet on the surface wind and air temperature advection

In this section, the effects of the atmospheric jet speed and latitude are explored on the ocean surface wind patterns, and the wind-induced Ekman horizontal and vertical transport are evaluated, as well as the air temperature advection, $-v \cdot \nabla T_a$, whihc is estimated from the 10 metre wind and air temperature at 1.5 metres in ensemble data and 2 metres in reanalysis daily data.

To highlight this dependence on the jet indices, a composite analysis is applied to consider the pattern and strength of the surface wind fields and air temperature advection from the ensemble data by comparing ensembles for the top 200 high and low jet indices. The 200 highest and 200 lowest jet indices ensembles are chosen across the years 1980 to 2014 in the same months. The ensemble model data reveals many more extreme events, in particular in terms of weak cases for the jet speed compared with the reanalysis data (Fig. 3.1a, b). In my analysis of the ensemble, very weak jet speed events which are lower than 5 ms^{-1} are excluded so that the 200 lowest jet speed cases range in strength from 5 ms^{-1} to 8.7 ms^{-1}, while the jet highest speed events range in strength from 17.5 ms^{-1} to 14 ms^{-1}. For the jet latitude ranges, the 200 highest jet latitude cases extending

between 56°N to 66°N are considered and those events higher than 66°N are excluded, while the lowest 200 jet latitude cases extending between 30°N to 43°N and events below 30°N are excluded.

For a composite of the strong jet cases, a strong jet brings cold air from west Greenland and Baffin Bay or the North American continent down to the south Greenland Sea and subpolar gyre, with cold air advection reaching over -10K per day over the boundaries (Fig. 3.2 a). On the other hand relatively warm air is transported from the subtropics from 30°N to 40°N with warm air advection reaching over 1 to 2K per day directed north-eastward to the British Isles then transported cyclonically over the Nordic Seas and eventually meets cold air from north Greenland. By contrast, in a composite of the 200 weakest jet cases, the surface westerly wind is fairly weak and tilts southwest to northeast over most of the middle latitudes, and leads to warm air advection from the subtropics up to the south of Iceland and the region north of Iceland is dominated by a cold northerly wind from the Arctic (Fig. 3.2 b). For a composite of high jet latitude, the central Atlantic warm air about 3K per day is transported further north but not as far as the Nordic Sea and cold air is constrained to a narrower region around the south of Greenland (Fig. 3.2 c). In a composite of the low latitude cases, the warm air temperature advection is spread over a wider area limiting the spread of the cold air (Fig. 3.2 d). Finally, the differences in both the wind fields and air temperature advection between high and low jet speed states reveal that a strong jet enhances warm air advection by 1 to 3 K per day to the north

and east Iceland and the cold air advection anomalies are around -1 to -4 K per day over the most of the subpolar region (Fig. 3.2 e). The difference in anomalies between high and low jet latitude show similar patterns but are shifted farther north (Fig. 3.2 f).

Repeating the composite analysis for the differences in the wind patterns and air temperature advection associated with jet strength and position for daily reanalysis data (Fig. 3.2 g, h) reveals similar patterns as the monthly fields from the ensemble (Fig. 3.2 e, f) and the reanalysis (not shown). Note that the anomaly magnitudes are slightly larger in the daily data, as the variations in the jet indices are larger in the daily data. This larger range is especially true for the high jet speed events, which are in the range 19 to 25 ms^{-1} in the daily data, so that the range in jet speed in the composite is increased by 60%. There are also some detailed differences with more prominent northerly and north-westerly winds in daily fields associated with a strong jet along east Greenland and the Labrador Sea (Fig. 3.2 g). These differences may reflect the greater importance of meridional wind on the daily timescale, as highlighted by Ogawa and Spengler (2019), who raised the concern that monthly analyses might be misleading as a result. However, my synoptic-timescale analysis suggests that this is a minor effect for the jet indices. In a similar manner, the impacts of jet latitude on wind direction and air temperature advection patterns based on daily reanalysis data are very similar to the ensemble monthly fields. Note here, advection is calculated based on (average u).grad (average T). Another method is based on

average (u.grad T) see in Supplement Fig. 3.1 (the supplementary Fig. 3.1 is at the end of the chapter). Both methods of calculating temperature advection have the same results based on monthly data. Noticeably, using reanalysis daily data, the temperature advection absolute fields corresponding to different jet indices states using the two methods show slight differences. However, the differences of the temperature advection between a composite of the highest jet indices minus that for the lowest jet indices are the same based on the two methods using daily data (Fig. 3.2 g and h and Supplement Fig. 3.1 g and h).

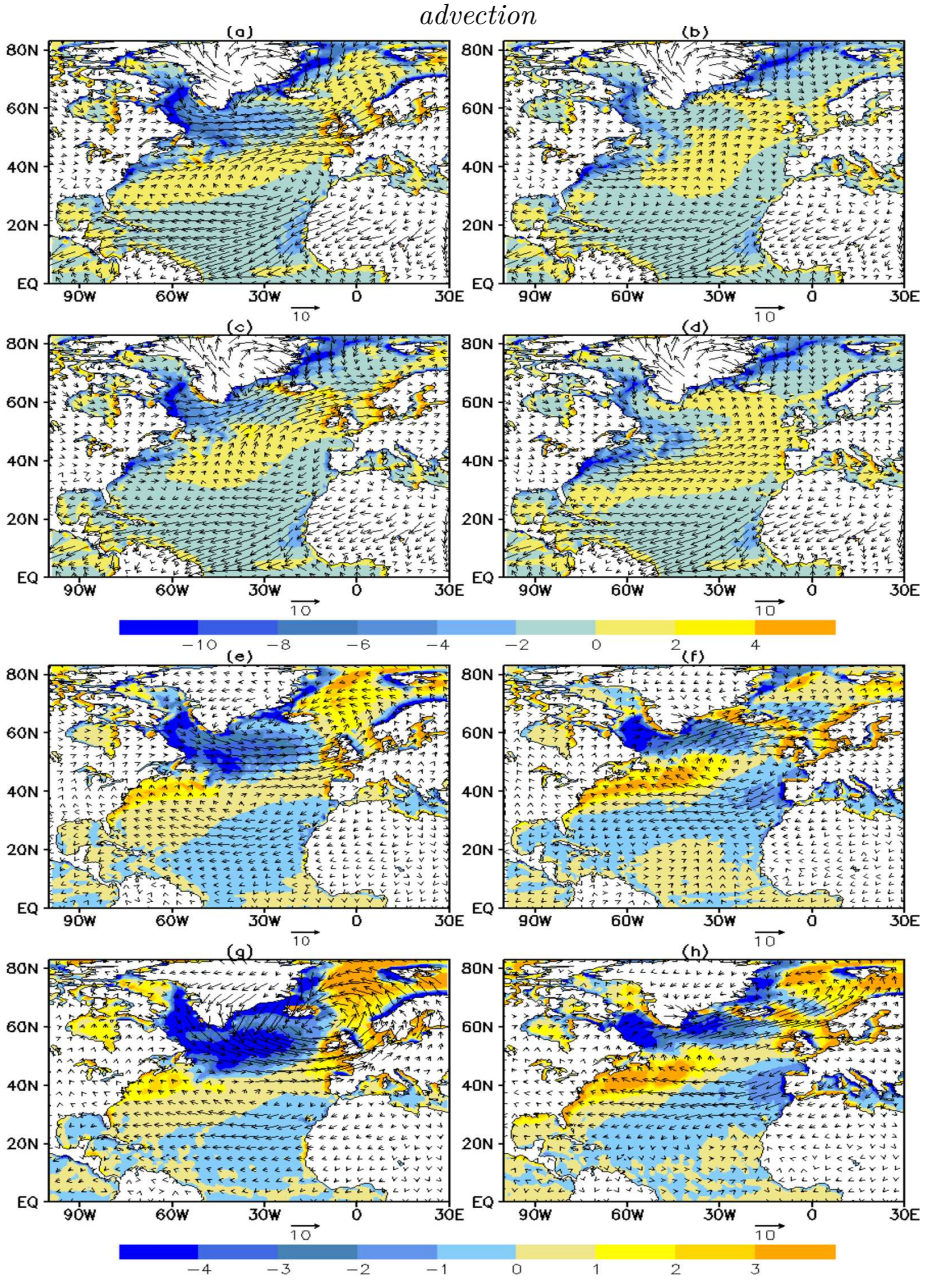

Figure 3.2: A composite mean of 200 January months from ensemble data of 10 metre wind and air temperature advection during (a) high jet speed state, (b) low jet speed state, (c) high jet latitude state, and (d) low jet latitude state; the differences in 10 metre wind and air temperature advection between a composite of 200 January months of (e) the highest jet speed minus that for the lowest jet speed and (f) the highest jet latitude minus that for the lowest jet latitude; the differences in 10 metre wind and air temperature advection (calculated from 10m wind and 2m air temperature) from reanalysis daily data between a composite of 200 January days of (g) the highest jet speed minus that for the lowest jet speed and (h) the highest jet latitude minus that for the lowest jet latitude. Units: wind vectors: m s^{-1}, air temperature advection: K per day (shaded colour). Note: advection is calculated based on (average u).grad (average T).

For the strong jet state, the magnitude of Ekman upwelling and downwelling velocities from the ensemble data are enhanced over most of the subpolar and subtropical region, reaching over 4×10^{-5} m s^{-1} and around -2×10^{-5} m s^{-1}, respectively (Fig. 3.3 a). Meanwhile, Ekman southward volume transport is enhanced reaching -3 m^2 s^{-1} over most of the subpolar gyre due to a strong westerly wind; whereas, the northward Ekman transport is enhanced too due to an enhanced trade wind.

Notably, in Fig. 3.3, the Ekman velocity and volume horizontal transport composite mean is calculated from the averaged 10m wind. These results are the same as the Ekman transport and velocity is calculated from each individual month's 10m wind then a composite mean is calculated which is shown in Supplement Figure (Fig. 3.2, the supplementary Fig. 3.2 is at the end of the chapter).

However, the pattern of Ekman volume transport and upwelling for the composites of the 200 highest jet latitude cases shift farther north than their counterparts during the 200 highest speed cases (Fig. 3.3 c). For the 200 lowest jet latitude states, the Ekman transport and vertical velocity patterns are shifted farther south (Fig. 3.3 d). Ekman upwelling is driven by cyclonic circulation or low pressure centre and downwelling is driven by anticyclonic circulation or high pressure centre. Thus, the strong jet enhances cyclonic circulation over Iceland and anticyclonic circulation over the Azores, while the northward-shifted jet shifts both cyclonic and anticyclonic circulation northward.

Overall, the jet stream strength and latitude change surface atmospheric circulation, and in turn alter zonal and meridional transport of cold and warm air.

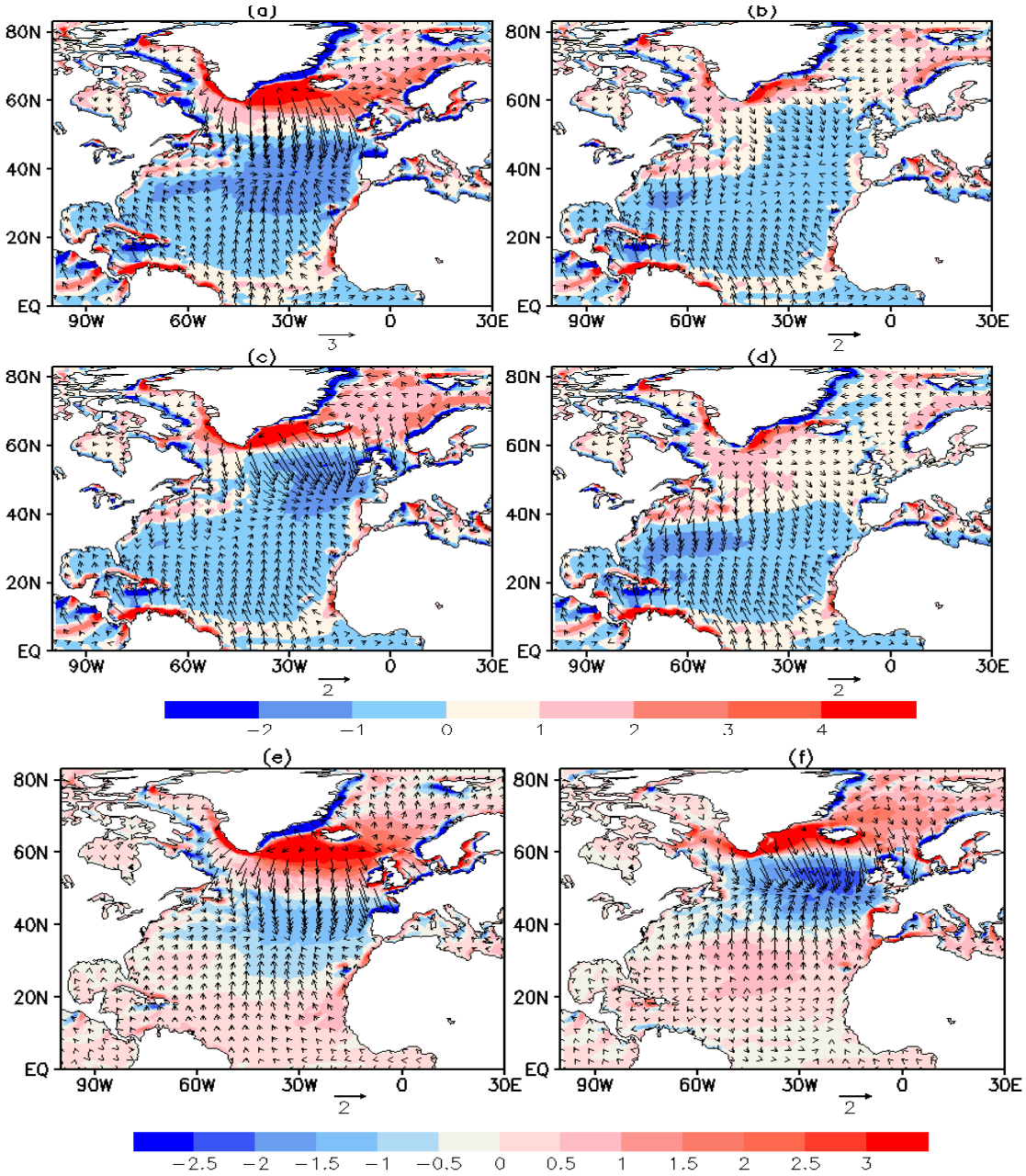

Figure 3.3: A composite mean of 200 January months from ensemble data of Ekman horizontal volume transport (vectors, unit: $m^2\ s^{-1}$) and Ekman upwelling velocity (shaded colour, units: 10^{-5}m s^{-1}, the positive means upwelling, the negative means downwelling) during (a) high jet speed state, (b) low jet speed state, (c) high jet latitude state, and (d) low jet latitude state. Ekman horizontal volume transport and vertical velocity difference between a composite of 200 January months of (e) the highest jet speed minus that for the lowest jet speed and (f) the highest jet latitude minus that for the lowest jet latitude.

3.6 The surface temperature response to heat flux anomalies

Before exploring the links between jet stream and ocean variability, the connection between the surface temperatures and heat fluxes are examined in the ensemble data sets, as their interaction is crucial in determining the influence of the atmosphere on the ocean.

For the surface air-sea heat fluxes, the latent and sensible heat fluxes, F_l and F_s, are related to the wind speed and the difference in the specific humidity and temperature, respectively, between the sea surface and the air in the boundary layer through bulk aerodynamic formulae (Cayan, 1992; Isemer and Hasse, 1987):

$$H_l = \rho L C_E u(q_s - q_a) \tag{3.2}$$

$$H_s = \rho C_p C_H u(T_s - T_a) \tag{3.3}$$

where u, q_a, and T_a are the wind speed, specific humidity and temperature of the air in the boundary layer, and q_s and T_s are the saturation specific humidity and surface temperature; ρ is air density, L is the latent heat of evaporation, C_p is the specific heat capacity of air at constant pressure, C_E and C_H are transfer coefficients for latent heat and sensible heat, respectively. In this study, sensible and

latent heat flux data are directly from ensemble model data outputs, a positive flux represents an ocean loss of heat.

3.6.1 The effect of surface heat flux on surface temperature

The anomalies in the surface heat flux are taken as the sum of anomalies in surface sensible and latent heat flux and are now correlated with both the surface temperature anomaly and its tendency. The tendency of surface temperature is defined based upon the surface temperature difference of the months before and after the central month, such as February minus December, following Cayan (1992). In order to assess the role of the atmosphere in driving sea surface temperature variability, we consider a local heat balance connects the anomalies in the tendency in surface temperature and the air-sea heat flux,

$$\frac{\partial T^{'}_{sst}}{\partial t} = -\frac{1}{\rho C_p}\frac{F^{'}}{h} \tag{3.4}$$

where F' is the total air-sea heat flux anomaly which is taken to be the sum of the latent and sensible heat flux anomalies (defined as positive when out of the ocean), h is the thickness of the mixed layer, the prime represents a deviation from a time mean. Sea surface temperature variability is also driven by horizontal and vertical advection and mixing, such as involving instability of boundary currents and jets.

The mean correlation of the surface heat flux anomaly and tendency of sea surface temperature anomalies reveals the expected local heat balance holding over most of the North Atlantic, where greater surface heat loss drives a reduction in surface temperature: the heat flux generally correlates well with the negative tendency in surface temperature anomaly for the same month, but not for the subsequent month (Fig. 3.4 a, c). This relationship leads to the heat flux in January correlating more strongly with the temperature anomaly in February, rather than in January (Fig. 3.4 b, d). However, this local heat balance does not hold over the Gulf Stream, where the advection of heat becomes important in controlling the surface temperature evolution (Fig. 3.4 a and d) (Roberts et al., 2017).

The heat flux anomalies are weakly connected to surface temperature anomalies for the same month over most of the domain (Fig. 3.4 b), although there is a positive correlation over the Gulf Stream suggesting air-sea heat fluxes respond to the advection of warm ocean anomalies (Roberts et al., 2017). Overall, the strong effect of heat flux on temperature tendency (Fig. 3.4 a) leads to a clear impact on sea surface temperature in the following month (Fig. 3.4 d).

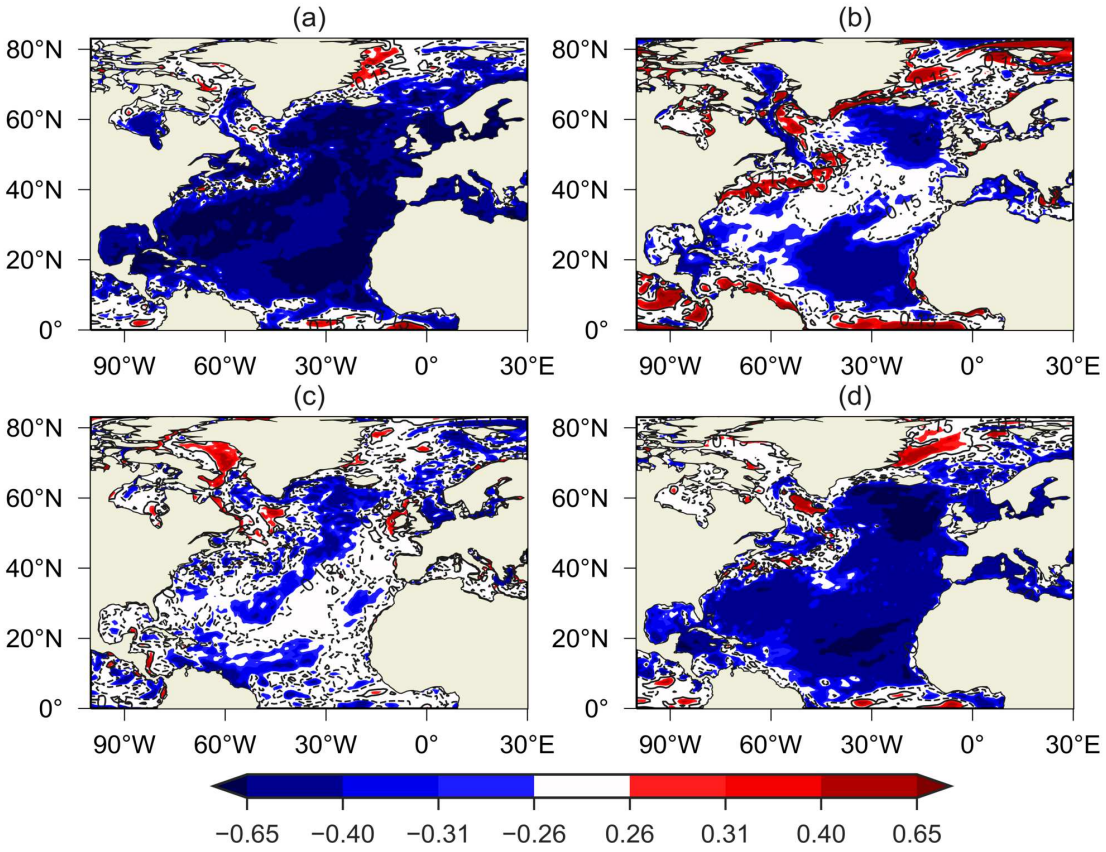

Figure 3.4: The correlation between January heat flux anomaly and (a) January tendency of surface temperature anomalies, (b) January surface temperature anomalies, (c) February surface temperature tendency anomalies, (d) February surface temperature anomalies. Correlations are calculated across the 40 ensembles for each year and then averaged over 35 years. Colours represent the correlation passing statistical significance tests with confidence levels of 90% at ±0.26, 95% at ±0.31 and 99% at ±0.40.

3.6.2 The relationship between heat flux and sea-ice extent

The relationship between surface heat flux and sea-ice extent is now considered due to their effect on the signals along the ocean boundaries in Fig. 3.4.

There are two different regimes with a dipole pattern exhibiting different re-

sponses for the connection between sea-ice cover and air-sea heat flux (Fig. 3.5 a) east of Greenland towards the Nordic Sea and west of Greenland in the Labrador Sea.

Over the Labrador Sea, there is a positive correlation between January heat flux and January sea-ice fraction, reaching 0.4 to 0.55 (Fig. 3.5 a), implying that more heat loss is associated with more sea ice formation. This response is consistent with the expected negative correlation between anomalies in air-sea heat flux and surface temperature tendency (Fig. 3.4 a, b and d), which involves surface cold air coming from upstream (see Fig. 3.2), cooling the ocean surface and encouraging sea-ice formation.

However, along the eastern side of Greenland there is a strong negative correlation up to -0.6 between anomalies in the air-sea heat flux and the same and following month's sea-ice fraction (following month correlation map not shown). During winter there is a relatively large fraction of sea ice here (see Fig. 3.5 b) that acts to limit the heat loss from the warmer sea to the colder atmosphere. However, if the extent of sea ice reduces, there is more heat loss from the ocean to the atmosphere due to a greater extent of warmer open surface in contact with the atmosphere (Fig. 3.5 a). The localised positive correlation between anomalies in the surface heat flux and surface temperature (Fig. 3.4 b and d) also suggests that the extent of the sea ice may have a controlling effect on the air-sea heat fluxes, rather than always responding to the air-sea heat fluxes.

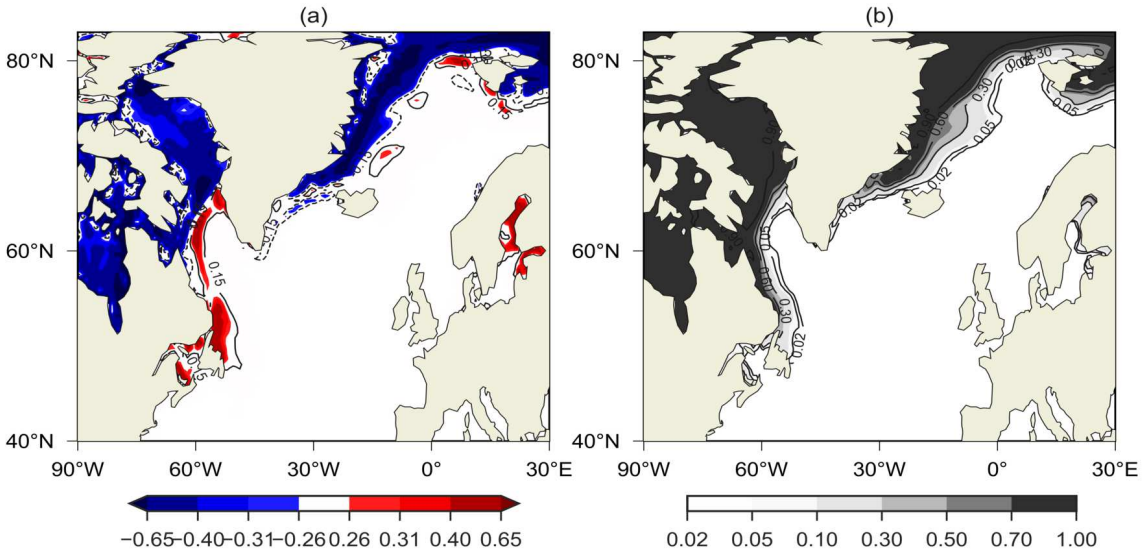

Figure 3.5: (a) The correlation between January surface heat flux anomaly and January sea-ice fraction anomaly across the 40 ensembles for each year and then averaged over 35 years. Colours represent the correlation passing statistical significance tests as in Fig.4, (b) Jan sea-ice fraction climatology mean.

3.7 The effect of the atmospheric jet on the surface ocean

Variations in the jet stream bring different air masses zonally and meridionally over the Atlantic and the air-sea exchange of heat, altering the surface temperature and sea-ice distributions. A composite analysis is next provided to help validate the relationships emerging from the model ensemble versus the reanalysis and then a sensitivity analysis is provided for the ensemble data.

3.7.1 Composite analysis of how surface ocean properties connect to jet indices

The monthly ensemble data over 35 winters are analysed in terms of how the jet indices connect to anomalies in the surface properties, based on the difference in January for a composite of 200 months of the highest index minus the same for the lowest index (following the same selection rules as in section 3). These 200 ensemble members for high and low indices are spread over the entire time record from 1980 to 2014, rather than being biased to particular decades.

A composite analysis for the combined anomalies in surface latent and sensible heat fluxes associated with a stronger jet reveals a clear tripole pattern over the North Atlantic (Fig. 3.6 a) with a greater ocean heat loss by 90 W m^{-2} over much of the subpolar region and eastern side of the tropics, together with an ocean heat gain by -70 W m^{-2} along the Gulf Stream. Changes in the jet latitude provide a broadly similar tripole pattern, but with more localised loss of heat over the subpolar gyre and a more extensive gain of heat over the subtropics (Fig. 3.6 b).

The corresponding composite analysis for surface temperature reveals that increasing jet speed or latitude is associated with colder surface waters over the Labrador and Irminger Sea with anomalies reaching -1.0^{o}C, parts of the subpolar gyre and the eastern tropics up to -0.5 to -0.7^{o}C, but warmer surface waters over much of the subtropics about 0.5 - 0.7^{o}C and the Nordic Sea is over 1.0^{o}C

(Fig. 3.6 c,d) which we know may due to warm air advection transported there (see Fig. 3.2 e, f, g, h). Over most of the domain the sign of the sea surface temperature anomaly is consistent with a greater surface heat loss driving cooling. The more northern jet is particularly associated with a northward extension of the subtropical gyre (Fig. 3.3 c).

There are broadly similar patterns when the composites are evaluated from ERA-Interim reanalysis monthly and daily data during winter from years 1980 to 2014. The daily time-scale fields have very similar tripole patterns to the ensemble monthly fields, albeit with a greater heat loss of 150 W m^{-2} in the subpolar region (Fig. 3.7 e, f). This increased magnitude is simply explained by the increased range of jet speed in the daily data compared to the monthly. This comparison reveals that the ensemble model and reanalysis data exhibit similar relationships between jet stream and surface ocean variability, supporting the use of the ensemble data to investigate causality in this relationship.

There are some detailed differences in the surface heat flux and sea surface temperature anomalies in monthly ensemble and reanalysis fields. Firstly, a stronger jet in the reanalysis is associated with a greater surface heat loss extending over the eastern side of the Atlantic and hence lower sea surface temperatures compared to the model (Fig. 3.7 a, c). This response might reflect the observed association between the jet speed and Atlantic Multidecadal Variability in surface temperature since NAO variablity is dominated by jet speed strength with

timescales greater than 30 years (Woollings et al., 2015; Häkkinen et al., 2011). Secondly, a more northern jet in the reanalysis is associated with an anomalous gain in ocean heat in the subtropical region and a more extensive downstream increase in surface temperature compared to the model (Fig. 3.7 b, d, f). The contrasting patterns of heat flux associated with the jet latitude and speed indices may indicate different effects on the ocean subtropical and subpolar gyres, with their climatological boundaries indicated by the climatological Ekman upwelling (black lines in Figs. 3.6 a, b and 3.7 a, b). The variations in jet latitude are seen to be particularly closely related to the gyres: a more northern jet leads to the northern region of upward heat flux anomaly lying entirely within the subpolar gyre and the downward heat flux anomalies closely following the boundary between subtropical and subpolar gyres (Fig. 3.6 b, Fig. 3.7 b).

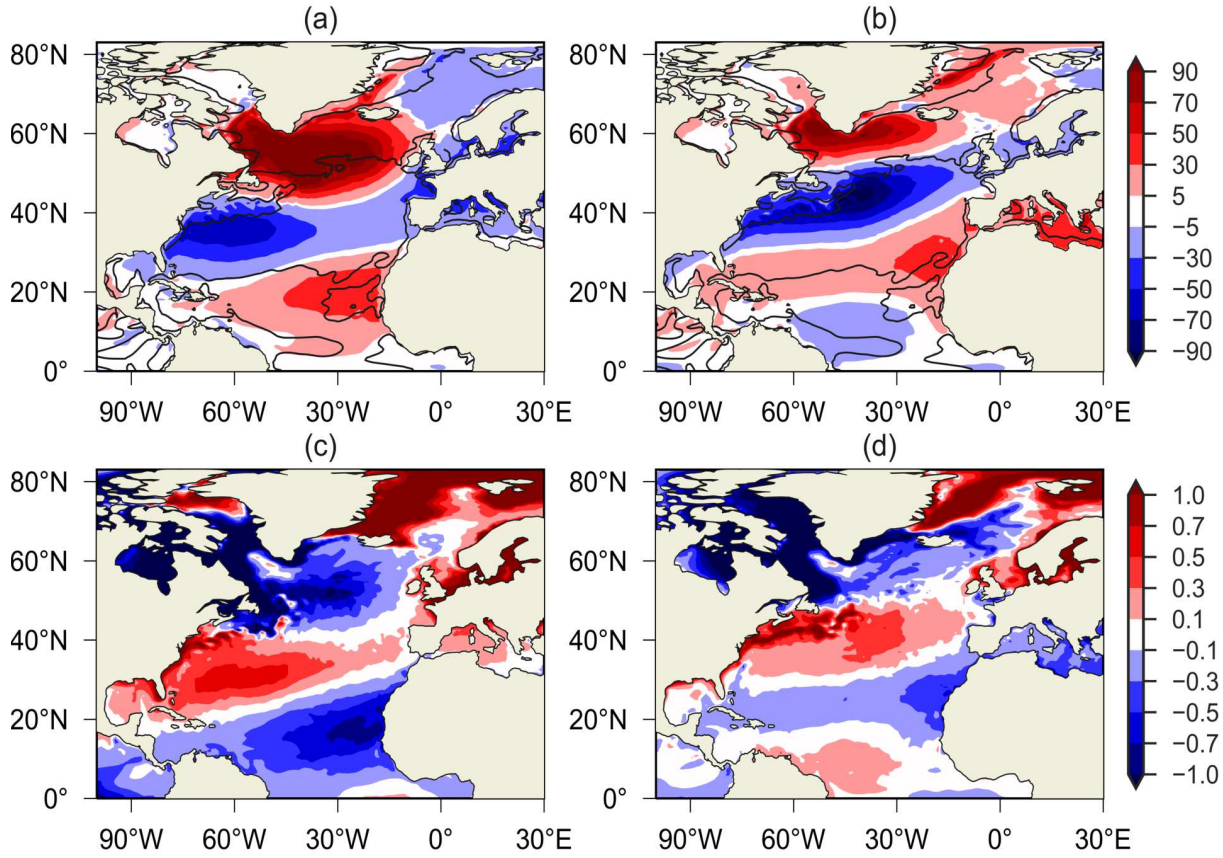

Figure 3.6: Surface heat flux difference (W m^{-2}) using ensemble data across 1980 to 2014 between a composite of 200 January months of (a) the highest jet speed minus that for the lowest jet speed and (b) the highest jet latitude minus that for the lowest jet latitude (where a positive represents a greater ocean heat loss). Surface temperature difference (°C) between a composite of 200 January months of (c) the highest speed minus that for the lowest jet speed and (d) the highest jet latitude minus that for the lowest jet latitude. The demarcation of the ocean gyres are indicated by the zero lines in the climatological-mean Ekman upwelling velocity in (a) and (b).

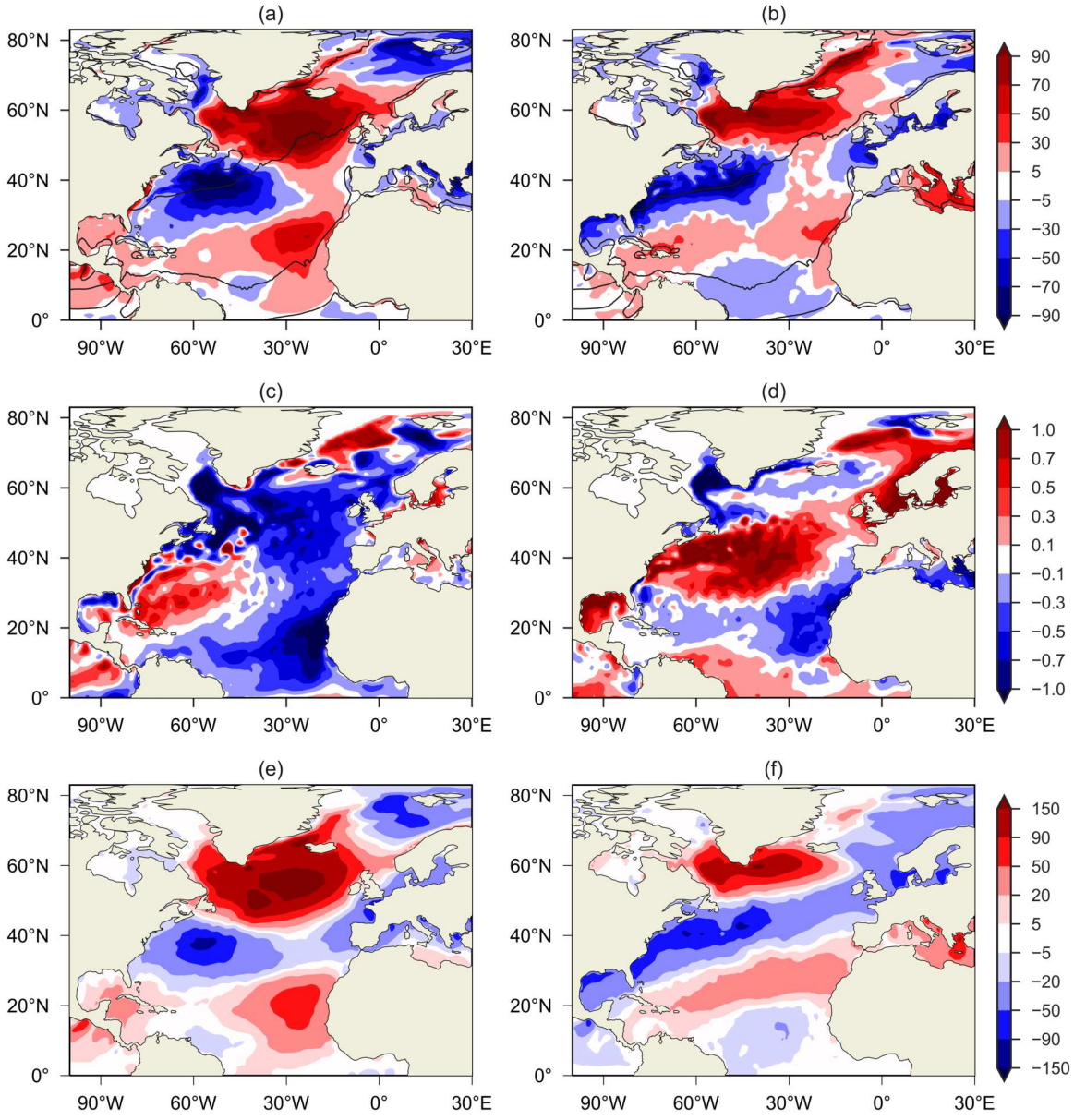

Figure 3.7: Surface heat flux difference (W m^{-2}) using ERA-Interim reanalysis monthly data across 1980 to 2014 between a composite of 7 January months of (a) the highest jet speed minus that for the lowest jet speed and (b) the highest jet latitude minus that for the lowest jet latitude (where positive represents a greater ocean heat loss). February surface temperature differences (^{o}C) between a composite of January months for (c) the highest jet speed minus that for the lowest jet speed and (d) the highest jet latitude minus that for the lowest jet latitude. Surface heat flux difference (W m^{-2}) using ERA-Interim reanalysis daily data across 1980 to 2014 between a composite of 200 January days of (e) the highest jet speed minus that for the lowest jet speed and (f) the highest jet latitude minus that for the lowest jet latitude (where positive represents a greater ocean heat loss). The demarcation of the ocean gyres are indicated by the zero lines in the climatological-mean Ekman upwelling velocity in (a) and (b).

3.7.2 The sensitivity of the surface heat flux to the jet indices

To begin the sensitivity analysis, the correlation across the 40 ensemble members initialised at the start of November is calculated for each winter month between the precursor jet indices and target heat flux fields over the North Atlantic. The mean correlations of January jet speed and latitude with January heat flux show robust tripole patterns over the entire North Atlantic (Fig. 3.8), which implies the North Atlantic surface sensible and latent heat flux are strongly sensitive to the jet speed and latitude shifts in wintertime.

The correlation signals are similar to the composite anomaly patterns (Fig. 3.6 a, b and Fig. 3.7 a, b and e, f). The positive correlation centres are located over much of the subpolar region and the tropics. The maximum positive correlation reaches values over 0.6 around the subpolar region, so that strong and northward shifted jets both cause greater heat loss from the ocean to the atmosphere. However, an opposite correlation is seen over the subtropics, which suggests that strong and northward shifted jets reduce heat loss from the ocean to the atmosphere in this region. The correlation patterns for the ensemble show subtle differences, with jet speed affecting heat fluxes more strongly in the tropical and subpolar regions, but jet latitude affecting heat fluxes by shifting their pattern further north in both tropical and subtropical regions. (Fig. 3.8 a, b).

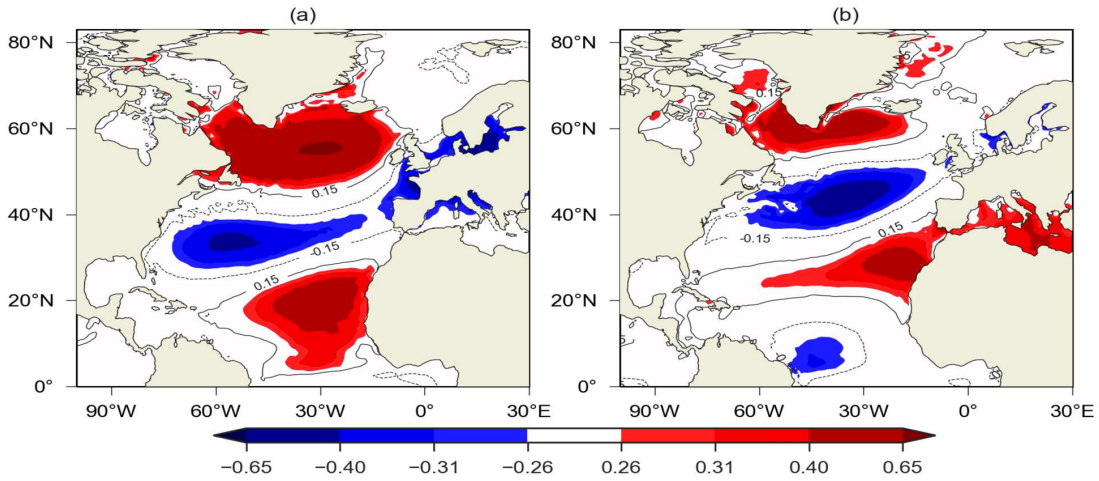

Figure 3.8: The correlation between January surface heat flux and (a) January jet speed and (b) January jet latitude across the 40 ensembles for each year and then averaged over 35 years. Colours represent the correlation passing statistical significance tests as in Fig.4

3.7.3 The sensitivity of sea surface temperature to the jet indices

In a similar manner, the ensemble sensitivity analysis for surface temperature and jet speed again reveals the characteristic tripole pattern (Fig. 3.9 a, b, c and d). Their correlation is relatively weak when comparing January jet speed and January surface temperature (Fig. 3.9 a), but strengthens when comparing January jet speed and February temperature with large regions exceeding the 99% confidence level (Fig. 3.9 b), and this signal persists into March and only weakens by April (Fig. 3.9 c, d). Hence, a strong jet speed causes more heat flux to be released from the ocean to the atmosphere, driving a cooling of surface temperature that persists for at least four months.

The ensemble sensitivity for surface temperature and jet latitude only reveals a weak connection for the same month of January in regions around the north of Iceland and the north west Labrador Sea (Fig. 3.9 e, f, g and h). The characteristic tripole pattern only appears in the following months, peaking again at a one month lag in February (Fig. 3.9 f), but then the signal is relatively short lived and decays from March to April (Fig. 3.9 g, h).

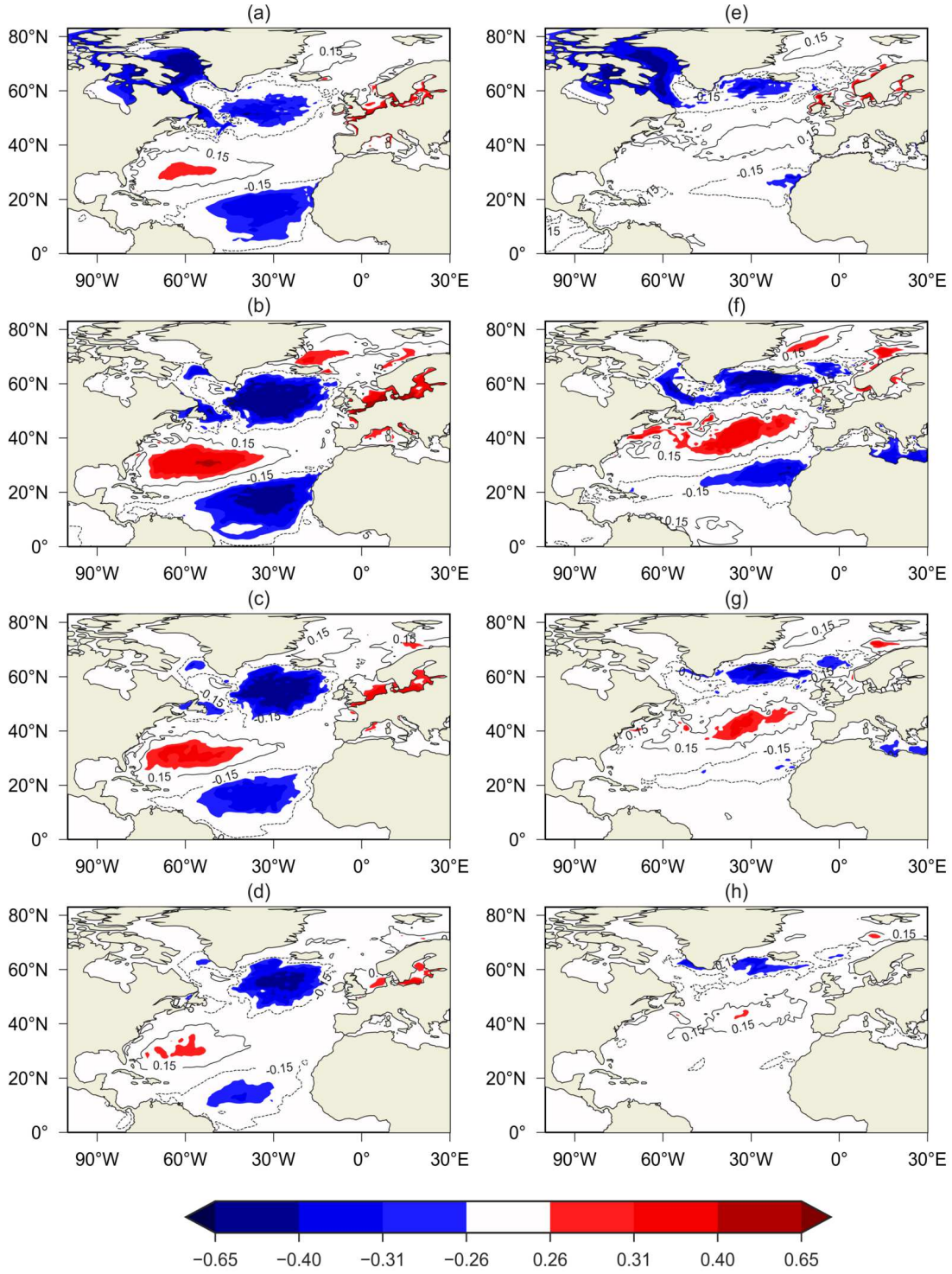

Figure 3.9: The correlation between January jet speed and (a) January surface temperature, (b) February surface temperature, (c) March surface temperature, and (d) April surface temperature, and the correlation between January jet latitude and (e) January surface temperature, (f) February surface temperature, (g) March surface temperature, and (h) April surface temperature. Correlations are taken across the 40 ensembles for each year and then averaged over 35 years. Colours represent the correlation passing statistical significance tests as in Fig. 3.4

3.7.4 Composite analysis and sensitivity of sea ice to the jet indices

The sensitivity of the sea ice extent is now considered in terms of the jet indices. Changes in sea-ice coverage, motion and thickness have been previously associated with different atmospheric states, as defined by the NAO and AO (Arctic Oscillation) (Alexander et al., 2004; Hilmer and Jung, 2000). The relationship between the jet indices and surface temperature around the boundaries of the subpolar gyre, particularly for the Greenland and Labrador Seas, may be associated with direct effects of the air-sea heat fluxes and changes in sea-ice extent. Using both ensemble and reanalysis data, the composite analysis for sea-ice fraction reveals that a stronger or more northern jet is associated with reduced sea ice cover north of Iceland and around the Nordic Sea (Fig. 3.10). This signal is consistent with the jet stream extending to higher latitudes. In addition, a stronger jet is associated with greater heat loss over the Labrador Sea acting to cool surface waters and enhance the fraction of sea ice by 30% (Fig. 3.10 a, c). In contrast, a more northern or stronger jet typically leads to a 20 to 30% reduction in sea-ice fraction over the east Greenland Sea (Fig. 3.10) due to warm air advection transported there (Fig. 3.2 e, f and g, h).

The ensemble sensitivity of the sea-ice fraction reveals that there is a stronger effect of the jet speed and latitude when evaluated over the whole winter period,

December to February (DJF) (Fig. 3.11), rather than for individual months. The correlation between winter-mean jet speed and February sea-ice fraction across 40 ensembles reveals a dipole pattern with positive signals along the Labrador Sea boundary and negative signals along the east Greenland Sea, which implies sea ice fraction is increasing over the Labrador Sea and decreasing over the east Greenland Sea during strong jet speed periods (Fig. 3.11 a). A similar correlation dipole pattern is shown between winter jet latitude and the February sea-ice fraction (Fig. 3.11 b). There is also a similar correlation pattern between the sea ice fraction and NAO based upon the ensemble sensitivity analysis (not shown).

A stronger or northward-shifted jet increases cold air advection from west Greenland and Baffin Bay or the continent (Fig. 3.2) which may affect the sea ice fraction in the Labrador Sea in two different ways: (i) a thermal effect of cold air causing more surface heat loss, decreasing the water surface temperature and growing more sea ice and (ii) a mechanical effect of more sea ice blown to the Labrador sea from upstream - west Greenland and Baffin Bay, in particular with a strong jet having more effect than jet latitude over Baffin Bay where we can see there is a negative correlation implying a reduction of sea ice fraction there (Fig. 3.11 a).

The response over the east Greenland Sea may involve different variants on these thermal and mechanical responses: (i) a stronger or northward-shifted jet enhances the warm air transported there (Fig. 3.2) reducing ice cover and leading

to an increase in surface temperature as the open ocean replaces sea-ice coverage; and (ii) a strong northerly wind along the east Greenland coast blows surface ice away from the Fram Strait and may also be linked to AO-related wind changes over the Arctic basin which encourage a thinning of the ice (Rigor et al., 2002). There is a noticeable difference over the west of Iceland where sea ice increases to the west of Iceland under a northern jet (Fig. 3.11 b) likely due to an extension of the Labrador cold air advection around the southern tip of Greenland (Fig. 3.2 c).

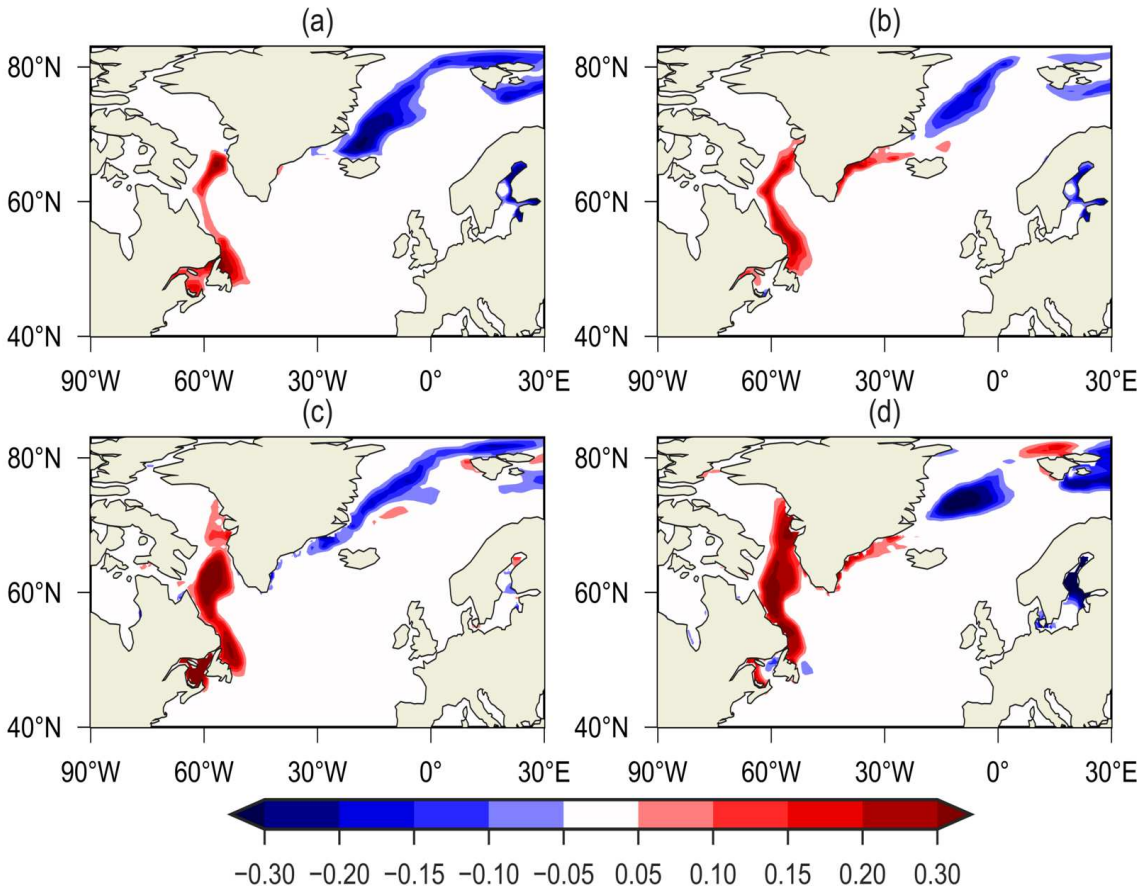

Figure 3.10: February Sea-ice fraction difference between a composite of 200 January months from ensemble data of (a) the highest jet speed minus that for the lowest jet speed and (b) the highest jet latitude minus that for the lowest jet latitude. February sea-ice fraction difference between a composite of 7 January months from reanalysis data of (c) the highest jet speed minus that for the lowest jet speed and (d) the highest jet latitude minus that for the lowest jet latitude.

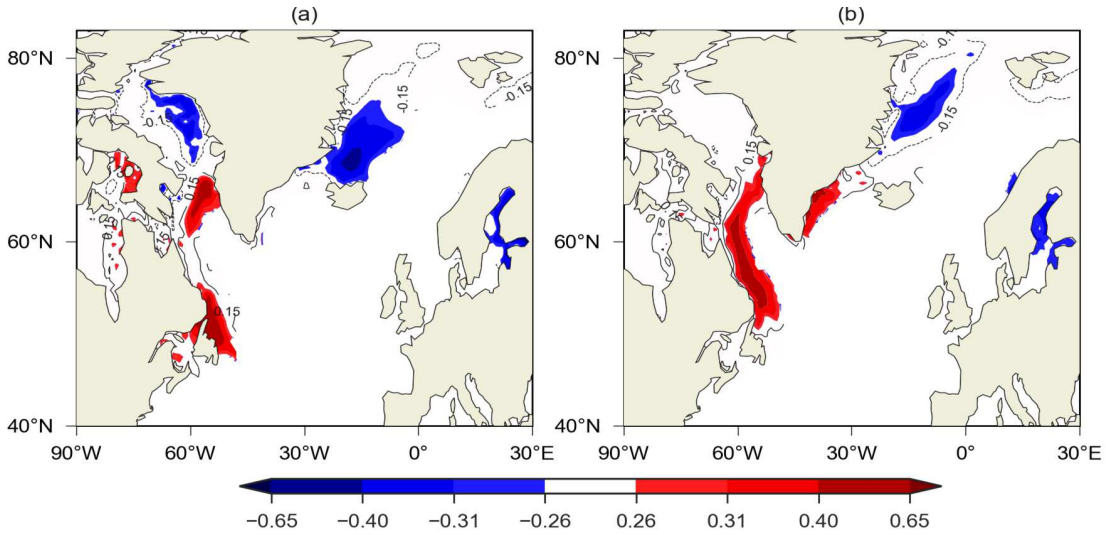

Figure 3.11: The correlation between (a) Winter DJF mean jet speed and February sea-ice fraction, (b) Winter DJF mean jet latitude and February sea-ice fraction. Correlations are taken across the 40 ensembles for each year and then averaged over 35 years. Colours represent the correlation passing statistical significance tests as in Fig.4.

3.8 Quantifying the sensitivity of the ocean surface variables to the jet indices

3.8.1 Normalisation of the sensitivity analyses

The ensemble sensitivity analysis is now normalised to quantify changes in surface heat flux, surface temperature and sea-ice fraction resulting from changes in jet speed and latitude. The normalisation expresses units of change in outcome J per standard deviation of predictor x across the ensemble using equation (3.1). The normalisation reveals that a standard deviation in January jet speed is associated with a change in the January surface heat flux by up to 35 to 40 W m^{-2} over the

subpolar region (Fig. 3.12 a) and a change in the February surface temperature by up to 0.3^{o}C across large regions of the open sea (Fig. 3.12 c). A standard deviation change in jet latitude leads to a similar magnitude response in the heat flux anomalies, although of a reduced extent (Fig. 3.12 b), and the ocean temperature response is also weaker apart from a band of strong positive anomalies of over 0.5^{o}C along the Gulf Stream (Fig. 3.12 d).

A standard deviation in winter-mean jet speed or latitude leads to changes in February sea-ice fraction of around 10% to 15% (Fig. 3.12 e, f).

3.8.2 The proportion of surface ocean variability controlled by the jet indices

The extent that the atmospheric jet affects the variability of the surface ocean is assessed by performing a linear regression between both the surface heat flux, sea surface temperature and sea-ice fraction with the indices for jet speed and latitude across 40 ensembles each year, then a climatological mean is taken over 35 years. The regression estimate of January surface heat flux based on January jet speed suggests that 40% to 50% of the total variance in heat flux over parts of the subpolar region and up to 35% of the variance over the rest of the ocean is explained by the variance in jet speed (Fig. 3.13 a); whereas, surface heat flux variance explained by jet latitude variance takes only up to 35% over most of the regions. the shaded values in Fig. 3.13 are expressed in terms of R^2 which

measures the ratio of the explained variance to the total variance.

Meanwhile, the regression estimate of February surface temperature based on January jet speed suggests that 35% of the surface temperature variation in February is explained by the January jet speed (Fig. 3.13 c). The regression estimates of surface heat flux variation and surface temperature explained by changes in jet latitude are weaker than those based on jet speed (Fig. 3.13 b, d). This response implies that nearly half of the heat flux variance and a third of the temperature variance is explained by the jet indices with jet speed showing a stronger relationship than jet latitude.

The regression estimate of February sea-ice fraction variance based on winter jet indices explains about 20% to 35% of the variance in the Labrador Sea, whereas the February sea-ice fraction variance is explained by the winter jet indices of about 20% and a smaller region reaching 35% in the east Greenland Sea (Fig. 3.13 e, f).

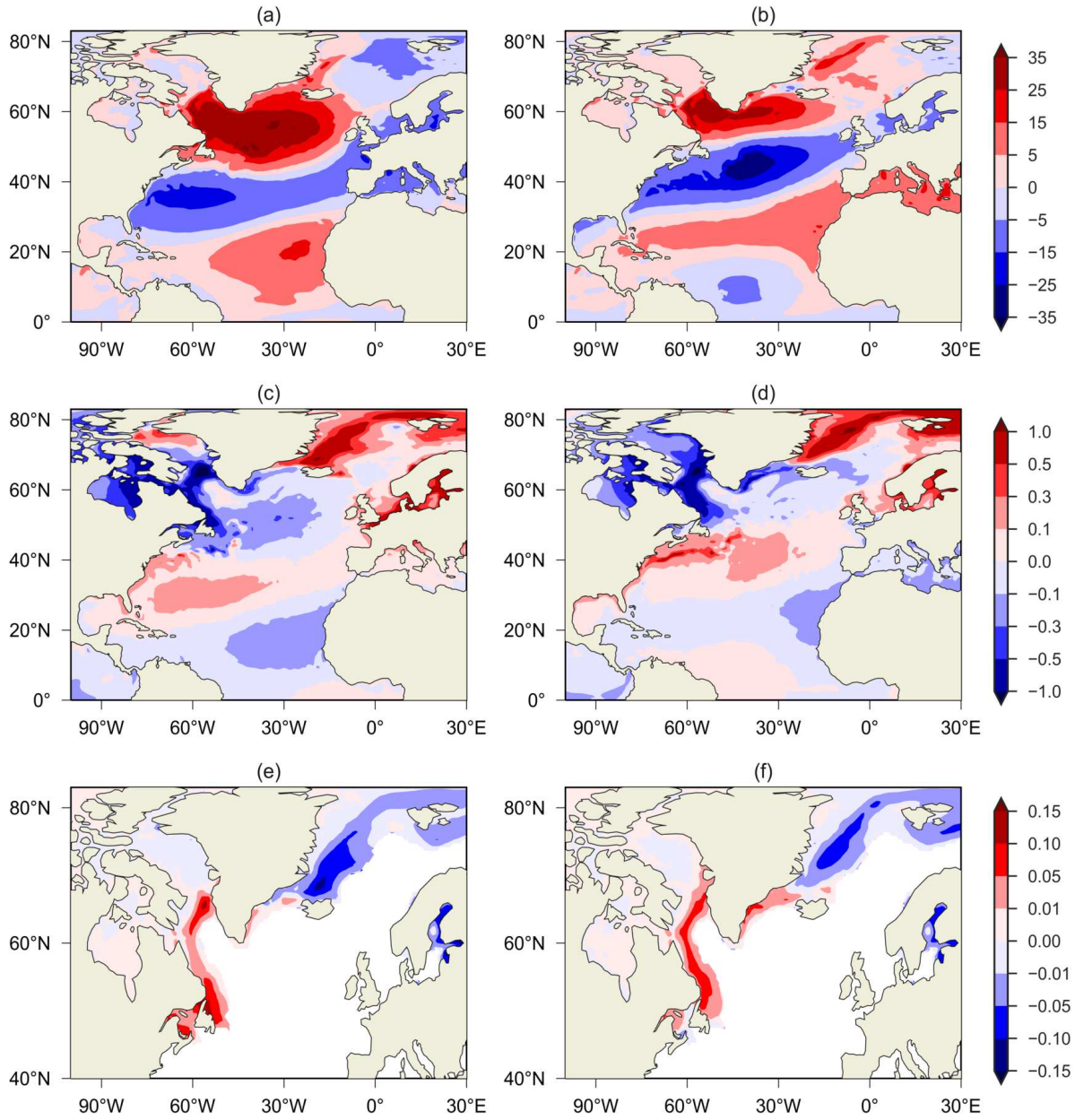

Figure 3.12: Normalised dependence of (a) January surface heat flux (W m^{-2}) per standard deviation of January jet speed, (b) January surface heat flux (W m^{-2}) per standard deviation of January jet latitude, (c) February surface temperature (^{o}C) per standard deviation of January jet speed, (d) February surface temperature (^{o}C) per standard deviation of January jet latitude, (e) February sea-ice fraction per standard deviation of DJF mean jet speed, and (f) February sea-ice fraction per standard deviation of DJF mean jet latitude. Normalisations are made across the 40 ensembles for each year and then averaged over 35 years.

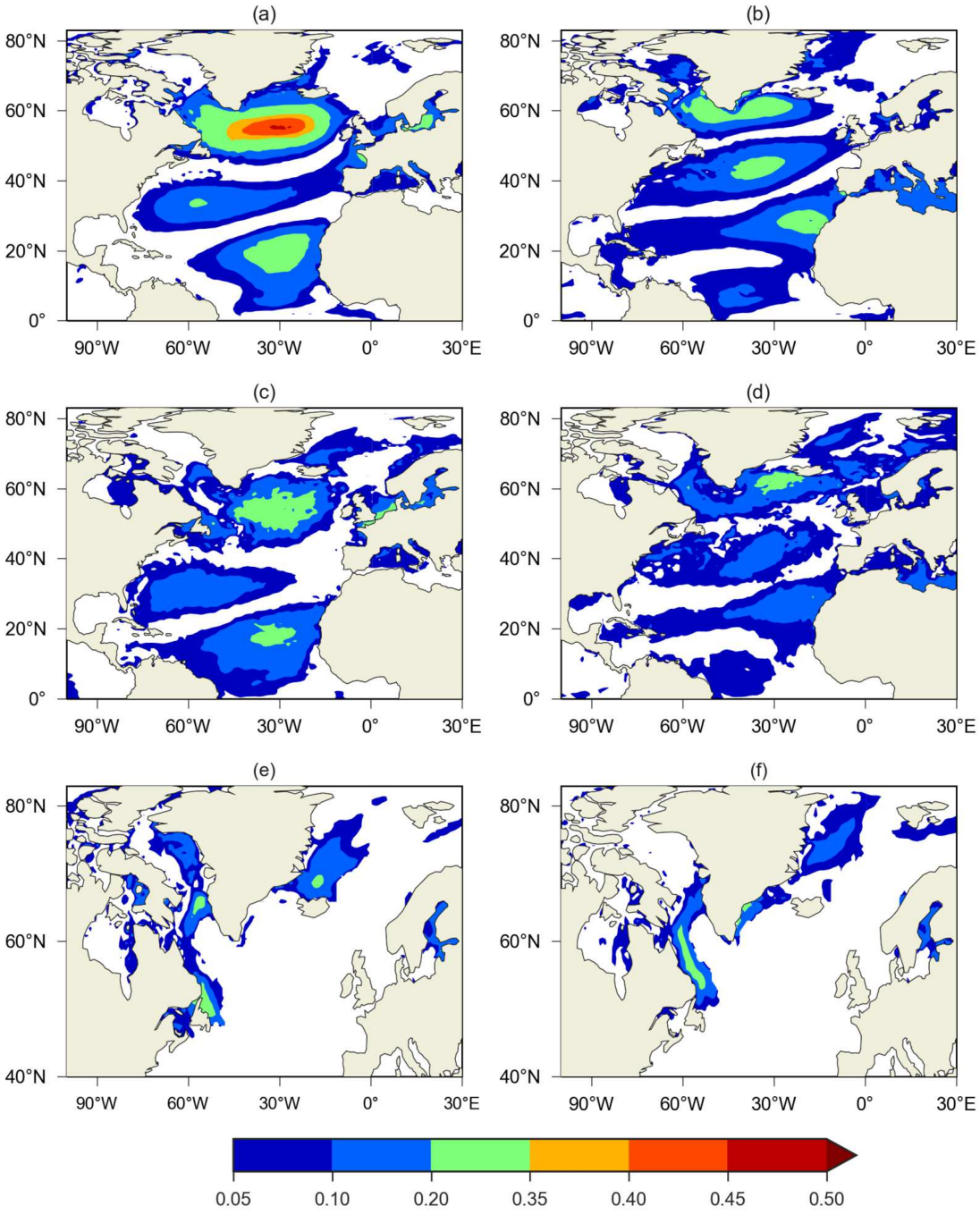

Figure 3.13: The proportion of the variance of the January surface heat flux that is explained by a linear regression between surface heat flux and (a) January jet speed and (b) January jet latitude; and the proportion of the variance of the February surface temperature explained by a linear regression between surface temperature and (c) January jet speed and (d) January jet latitude; and the proportion of the variance of the February sea-ice fraction explained by a linear regression between sea-ice fraction and (e) DJF jet speed and (f) DJF jet latitude. Linear regressions are made across 40 ensembles for each year and then averaged over 35 years.

3.9 The effect of spread in Sea surface temperature variability on the jet speed and latitude variability

The result is negative for the ocean influence on the atmosphere on a monthly to seasonal timescale. The spread in ocean variability does not influence atmospheric jet stream variability. For monthly and seasonal timescales, using the ensemble sensitivity analysis method I examine that the spread in sea surface temperature as an initial precursor predicts the following months atmospheric jet speed and latitude variability as outcome J across 40 ensembles over 35 years. Repeat the same process as in section 3.7.3, but choose SST as precursor instead to predict following months jet speed and latitude across 40 ensembles for each year. January SST is taken to forecast jet speed and latitude in February, March, and April respectively. There are no sensitive signals when when 35 years correlations are averaged.

The results reveal that atmospheric jet speed strength and latitude shifts are not sensitive to spread in ocean surface temperature, so there is no significant sensitivity signal when averaged over 35 years, but possible weak effects for individual years. However, there could be more of an influence on longer timescales based on atmosphere-only model (Rodwell et al., 1999; Czaja and Frankignoul, 2002;

Baker et al., 2019). A previous study by (Dunstone et al., 2016) shows that the preceding SST can predict the following winter's NAO based on DePreSys3 hindcast ensemble model data. The correlation is simply across 35 years under three different circumstances: (i) the observed DJF NAO timeseries correlated with the preceding November SST across 35 years; (ii) the ensemble mean DJF1 NAO timeseries is correlated with the preceding November ensemble mean SST across 35 years; (iii) the ensemble mean DJF2 (i.e. months 14-16, the following years DJF) NAO timeseries correlated with the preceding November2 (i.e. month 13) ensemble mean SST across 35 years.

In summary, Dunstone et al. (2016) made an ensemble mean first for the winter NAO and preceding November SST, then made a correlation across 35 years. My correlation is made across 40 ensembles to explore how the spread in atmospheric variability influences ocean surface temperature variability; and how the spread in SST influences atmospheric variability on a seasonal timescale. Both methods reveal different scientific issues and quite different metrics. However, my correlation is across 40 ensembles for each year, repeated for 35 years, then averaged the 35 years' correlations which provides much more robust statistics on the relationship between the atmosphere and ocean.

3.10 Discussion and Conclusions

The role of the atmosphere in driving the surface ocean in the North Atlantic is explored here on monthly and seasonal timescales. The dominant atmospheric phenomenon in the mid latitudes is the eddy-driven jet stream, affecting the formation and passage of synoptic-scale weather systems, and the emergence of weather regimes and blocking patterns (Madonna et al., 2017; Woollings et al., 2010). The sensitivity of the air-sea heat flux, sea surface temperature and sea-ice extent are explored using a coupled atmosphere-ocean model data set made up of 40 ensemble members initialised each November and repeated over 35 years.

The atmospheric jet strongly affects the wintertime pattern of air-sea latent and sensible heat flux anomalies, altering sea surface temperature anomalies, and the winter sea-ice distribution. For example, a standard deviation change in the jet speed or latitude typically results in surface heat flux anomalies of the order of 20 to 30 W m^{-2} over much of the North Atlantic together with surface temperatures anomalies of typically 0.2 to 0.3^{o}C in the open ocean, and changes in sea ice fraction of 15% in the Labrador and Greenland Sea regions. The effect of the atmospheric jet on the surface heat flux anomalies leads to a corresponding imprint on surface temperature anomalies. Over most of the surface ocean, enhanced surface heat loss drives the expected surface cooling (Cayan, 1992; Gulev et al., 2013).

Variability in the atmospheric eddy-driven jet strongly affects seasonal variability in the surface ocean over the North Atlantic, controlling nearly half of the variance in air-sea heat fluxes and over a third of the subsequent surface temperature variance. There is also a strong imprint on sea-ice fraction, a stronger jet acting to enhance the sea-ice fraction in relatively ice-depleted regions, but to reduce the sea-ice fraction in relatively ice-extensive regions. There are subtle differences in how indices of jet speed and location affect the surface ocean with the effect of jet speed being generally more pronounced than that of jet latitude, although the effect of jet latitude is important in defining the location of the regional response.

The patterns of surface ocean response are broadly consistent with the relationship between the empirical mode of the North Atlantic Oscillation and the surface ocean (Marshall and Coauthors, 2001; Visbeck et al., 2003). However, the speed and latitude of the jet are two physically distinct types of atmospheric variability. While both types of variability project onto the NAO and are related to tripole patterns in heat flux and sea surface temperature, the jet indices have subtly different effects on the surface ocean. Both jet strength and latitude lead to different thermodynamical and dynamical effects. For example, a thermodynamical effect of the jet is in altering the surface circulation and the advection of warm and cold air anomalies (as in Fig. 3.2), which are crucial for air-sea heat exchange. A dynamical effect of the jet is by a strong jet enhancing the magnitude of the wind-induced Ekman horizontal and vertical transport (as in Fig. 3.3), and the jet latitude altering their pattern and so shifting the position of the ocean gyre

boundaries. On a timescale of several months, the jet speed is shown to have a stronger affect on the ocean surface anomalies than jet latitude, with stronger heat flux anomalies leading to larger surface temperature anomalies that persist for longer.

The atmospheric jet alters the sea-ice distribution over winter in two different ways. In regions of extensive ice cover, such as along the eastern side of Greenland, a stronger jet is associated with a reduction in sea ice connected with an emergence of warmer surface waters, which in turn drives a greater surface heat loss. In contrast, in regions of less ice extent, such as in the Labrador Sea, a stronger jet is associated with a greater surface cooling which leads to more sea ice cover.

My study assesses the effect of the atmospheric jet on the surface ocean using monthly ensemble data, which omits the effect of sub-monthly synoptic weather variability that may be important Ogawa and Spengler (2019). To test this simplification, I compare how the jet indices connect to surface heat flux using daily reanalysis data versus monthly ensemble and reanalysis data and find that their relationships are broadly similar. While synoptic meridional winds generate large heat flux anomalies on a daily timescale, the alternating effects of southerly and northerly winds to a large extent cancel out in the monthly average, as indeed suggested by Ogawa and Spengler (2019). Hence, monthly timescale variability in the eddy-driven jet alone can account for a significant fraction of the North

Atlantic sea surface temperature changes that develop during the winter. The remaining sea surface temperature variance will likely be influenced by other large scale atmospheric patterns, as well as synoptic variability and ocean internal dynamics. Ocean dynamics is important in generating ocean internal variability, which may possibly also modify atmospheric variability. However, my sensitivity analysis of the spread in ensembles for each year reveals that ocean surface temperature is not correlated to subsequent monthly estimates of the jet speed strength and latitude shifts, so I have not found any statistically-significant signals of the ocean variability driving subsequent changes in the atmospheric jet stream when averaged over the 35 years of model data. There may be individual winters where a preceding winter has some effect on the subsequent winter, such as related to re-emergence of sub-surface temperature anomalies, but these signals are not statistically significant when averaged over the full record.

In comparison, there are studies arguing that the jet stream is influenced by ocean surface temperature on longer, interannual timescales, where the NAO is found to be sensitive to imposed surface temperature in an atmosphere-only model (Rodwell et al., 1999) and where there may be a positive feedback between the atmospheric circulation and surface temperature (Czaja and Frankignoul, 2002). Recently, Baker et al. (2019) used an atmosphere-only linear statistical-dynamical model to identify that indices of jet latitude and jet speed are sensitive to surface temperature, finding that each of these two indices depends upon subtly different patterns of North Atlantic surface temperature. Comparing their sensitivity maps

to my results shows agreement between several of the anomalies, so that the temperature anomalies due to jet variability are similar to the patterns of surface temperature that could force the jet.

In summary, my analysis evidence supports the primary assumption that the spread in ocean variables between ensemble members over the following few months can be determined by their different realisations of the chaotic atmospheric variability.

However, on a monthly to seasonal timescale, a negative result is shown for the secondary assumption that the spread in ocean variability does not influence following months atmospheric jet stream variability. Ocean water is slow moving, and a large mass body. These features determine that any small perturbation on a short timescale does not cause sufficient chaos which may feed back to changes in atmospheric variability. Ocean's feedback on the atmosphere needs to be considered on a longer timescale, such as SST Atlantic Multidecadal Variability (AMV) on multi-decadal timescales will have an influence on atmosphere and climate.

Hence, the rest of this thesis chapters 4 and 5 are based on monthly to seasonal timescales which only investigate the jet stream variability influence on the ocean.

In the next two chapters, I will explore how the ocean interior responds to atmospheric jet stream variability.

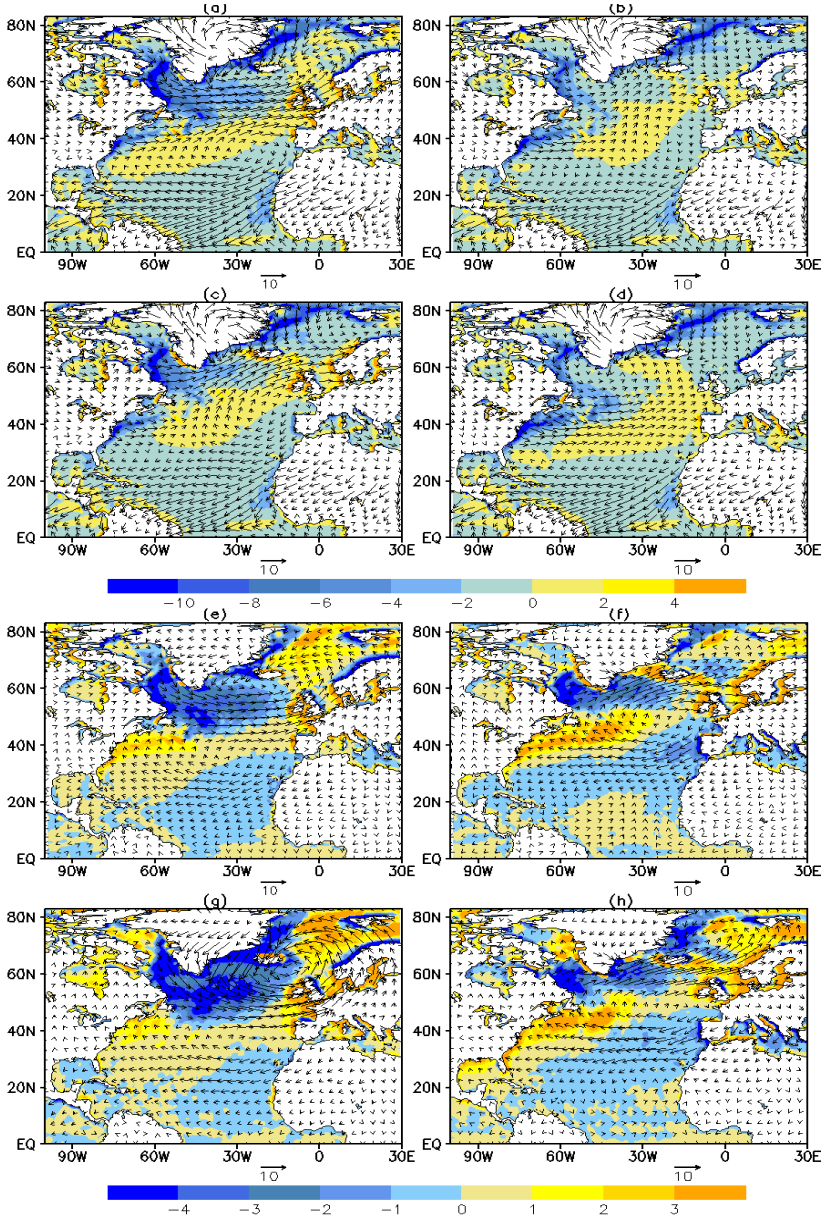

Supplementary Figure 3.1: A composite mean of 200 January months from ensemble data of 10 metre wind and air temperature advection during (a) high jet speed state, (b) low jet speed state, (c) high jet latitude state, and (d) low jet latitude state; the differences in 10 metre wind and air temperature advection between a composite of 200 January months of (e) the highest jet speed minus that for the lowest jet speed and (f) the highest jet latitude minus that for the lowest jet latitude; the differences in 10 metre wind and air temperature advection (calculated from 10m wind and 2m air temperature) from reanalysis daily data between a composite of 200 January days of (g) the highest jet speed minus that for the lowest jet speed and (h) the highest jet latitude minus that for the lowest jet latitude. Units: wind vectors: m s^{-1}, air temperature advection: K per day (shaded colour). Note: calculated advection from 10m wind and 1.5m air temperature in ensemble data and 2.0m air temperature in reanalysis data based on average (u.grad T).

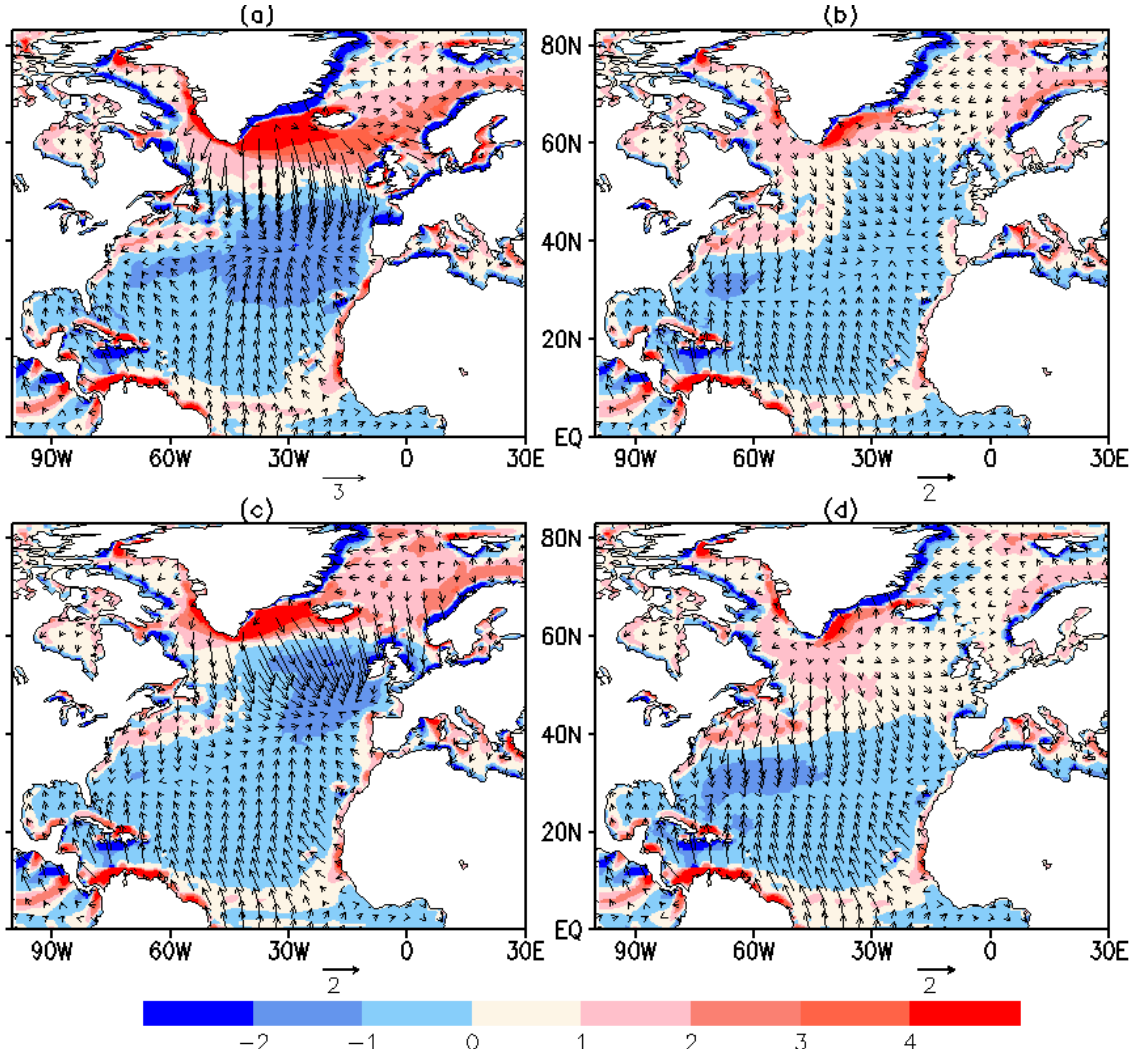

Supplementary Figure 3.2: A composite mean of 200 January months from ensemble data of Ekman horizontal volume transport (vectors, unit: $m^2\ s^{-1}$) and Ekman upwelling velocity (shaded colour, units: 10^{-5}m s^{-1}, the positive means upwelling, the negative means downwelling) during (a) high jet speed state, (b) low jet speed state, (c) high jet latitude state, and (d) low jet latitude state. Note: each individual Ekman veloctiy and volume horizontal transport are calculated from individual 10m wind field, then average is made from 200 individuals.

Chapter 4

How Does the Atmospheric Jet Stream Affect Atlantic Subsurface Temperature and Mixed Layer Thickness?

4.1 Introduction

It was revealed in chapter 3 that the atmospheric eddy-driven jet stream at low level 850hPa crosses the North Atlantic with different latitude shifts and different speeds. The eddy-driven jet stream at different latitudes and speeds brings dry, cold, or wet, warm air and strong winds to different locations over the ocean surface. This can cause changes in air-sea heat flux and subsequently changes

in surface temperature, sea-ice fraction, and also changes in surface ocean circulation. Jet streams also bring strong surface winds which affect turbulence and surface stirring.

The oceanic observation and 1-D model theoretical study showed that in winter, ocean mixed layer thickness is much deeper than other seasons and changes in mixed layer depth and temperature are mainly dominated by the surface heat loss (Kraus and Turner, 1967).

In ocean physics, most of the processes, such as heat loss and evaporation, radiative heating and cooling, and wind driven turbulence occur within the mixed layer. The mixed layer thickness varies seasonally and regionally from 30m to 500m. The mixed layer at its deepest is of about 500 m over the subpolar gyre at the end of winter, typically February to March (see Fig. 4.1 from a study by Kara et al. (2003); De Boyer Montégut et al. (2004)) and Fig. 4.2 is plotted using DePreSys3 hindcast Ocean NEMO ensemble model data based on a density-based criterion. The mixed layer is defined using the threshold method, for which the mixed layer depth is the depth at which temperature or potential density changes by a given threshold value relative to the one at a near-surface reference depth (see the thresholds summary in Table 1 by the study De Boyer Montégut et al. (2004)).

In the upper ocean, there is a pycnocline located between the mixed layer and deep ocean where water density increases rapidly with depth because of changes

in temperature and/or salinity. The pycnocline is often associated with a thermocline where the water temperature decreases dramatically with depth. The mixed layer is the interface between the atmosphere and ocean interior and determines ocean ventilation. Ventilation involves fluid in the mixed layer being transferred into the ocean interior to become part of the stratified thermocline or the weaker stratified deep ocean (Williams and Follows, 2011).

Coupled ocean-atmosphere model studies have revealed that the NAO affected the ocean surface temperature with a tripole pattern (Bjerknes, 1964; Visbeck et al., 2003; Marshall and Coauthors, 2001). In chapter 3, my study revealed that the atmospheric jet stream strongly affects sea surface temperature and air-sea surface heat flux with a triple pattern on a seasonal time scale. Previous studies have revealed that the ocean heat content and thermocline, and thermal anomalies were affected by atmospheric forcing in a decadal time scale, such as the NAO (Williams et al., 2014, 2015b; Lozier et al., 2008).

In this chapter, the hypothesis is that the jet stream affects the mixed layer thickness over the North Atlantic ocean due to heat flux anomalies. Consequently, the surface temperature anomalies associated with jet stream latitude location and speed penetrate into the upper ocean interior via the mixed layer by convection.

In order to prove the hypothesis, the following scientific questions will be answered in this study:

(i) How does the mixed layer respond to ocean surface heat anomalies associated

with the atmospheric jet stream strength and location?

(ii) How does the subsurface ocean temperature respond to the jet stream or how do surface temperature anomalies associated with jet indices penetrate into depth?

(iii) How is the temperature variation vertically balanced?

I will answer these questions. The ocean mixed layer depth response to heat flux is firstly examined in the winter time, then the mixed layer depth response to the jet stream is examined and then the response of the water temperature of the ocean interior. Fourthly, how the surface anomalies penetrate into the subsurface interior via the mixed layer is investigated. Finally, temperature 3-D balance within the mixed layer is investigated.

4.2 Methods

(i) Composite analysis is used to test how much the mixed layer depth changes in terms of high and low jet speed and latitude location.

(ii) Sensitivity analysis is used to find out how the mixed layer depth is sensitive to heat flux and how is the mixed layer sensitive to the jet latitude and speed. How the subsurface temperature is sensitive to the jet latitude and speed is also examined.

(iii) Analyse the temperature vertical heat balance over the mixed layer depth

over a year based on 1-D theory and 3-D processes to estimate heat budget and explore which process is dominant for changes in ocean surface temperature penetrating into interior via the mixed layer depth in different seasons.

4.3 Data and mixed layer structure

4.3.1 Data

DePreSys3 hindcast Ocean NEMO 0.25°×0.15° resolution (40 ensembles) monthly data from DePresys3 from the Hadley Centre is used. Temperature T data, velocity U, V and W data in winter months (DJF) from 1980 to 2000 are taken from the Met Office Hadley Centre DePreSys3 to investigate (i) the linkage between subsurface temperature and jet strength and latitude location; (ii) the linkage between heat flux and the mixed layer depth; (iii) the heat budget within the mixed layer to understand the processes of how the surface temperature anomalies penetrate into depth. In the temperature file, the ocean depth potential temperature, ocean mixed layer thickness and net downward heat flux are employed; In velocity U, W, V files, the zonal current, meridional current, vertical velocity, and vertical eddy diffusivity are extracted (see ocean data description details in Appendix A). In the ensemble model data, the ocean mixed layer thickness definition is based on density increase from the surface, i.e., the vertical density gradient where the sigma-theta σ_θ difference, $\Delta\sigma_\theta$ is 0.01 kg m^{-3} between

the density at the depth and the density at near-surface reference level at 10 m depth. σ_θ of sea water is the potential density (i.e. the density when a water parcel is moved adiabatically to a reference pressure) of water having the same temperature and salinity, minus 1000 kg m^{-3}.

Also atmospheric jet stream speed and latitude indices for zonal wind at 850 hPa from DePreSys3 hindcast atmospheric monthly ensemble data are used (as in Chapter 3) to investigate how the ocean mixed thickness and subsurface temperature respond to jet speed strength and latitude location shift over the North Atlantic ocean in winter time.

4.3.2 Mixed layer depth variation

A previous study by Kara et al. (2003) revealed the global ocean monthly variation of climatology of mixed layer depth using the subsurface temperature and salinity data from the World Ocean Atlas 1994 (Levitus and Boyer, 1994; Levitus et al., 1994). The study demonstrated that the mixed layer depth at 45°N, 30°W in the North Atlantic has clear seasonal variations along with temperature and salinity (Fig. 4.1) based on density and temperature criteria (Kara et al., 2003). The study revealed that there is a deepest mixed layer depth between 400m to 500m in February, then the mixed layer shallows rapidly reaching only about 30m to 40m in May, the shallowest depth is in July to August when it is about 20m to 30m. From September, the mixed layer depth gradually deepens again starting

another seasonal cycle (Fig. 4.1). Notably, when the mixed layer depth definition is based on ΔT (surface temperature minus the temperature at the base of the mixed layer), different thresholds (Fig. 4.1) show different depths.

In this study, I revisit the mixed layer depth distribution over the North Atlantic in February using DePreSys3 hindcast Ocean NEMO ensemble monthly data to investigate how the surface temperature anomalies associated with the jet stream penetrate into depth. In the ensemble data, the MLD is based on $\Delta\sigma_\theta$ as 0.01 kg m^{-3} between the density at the depth and the density at near-surface reference level at 2.5 m. The deepest mixed layer of about 500m is located over the Greenland Sea below Iceland, the Labrador Sea and and Nordic Sea (Fig. 4.2). Over the subtropical gyre, there is a relatively deep mixed layer depth of about 250m along the Gulf Stream, and east side between subpolar and subtropical gyre of about 300m to 350m (Fig. 4.2). Over the North Atlantic, the mixed layer depth climatological thickness in February based on ensemble data is similar to the mixed layer depth estimation in the study by De Boyer Montégut et al. (2004) based on temperature criterion, ΔT=0.2°C and based on a density criterion $\Delta\sigma_\theta$ = 0.03 kg m^{-3}.

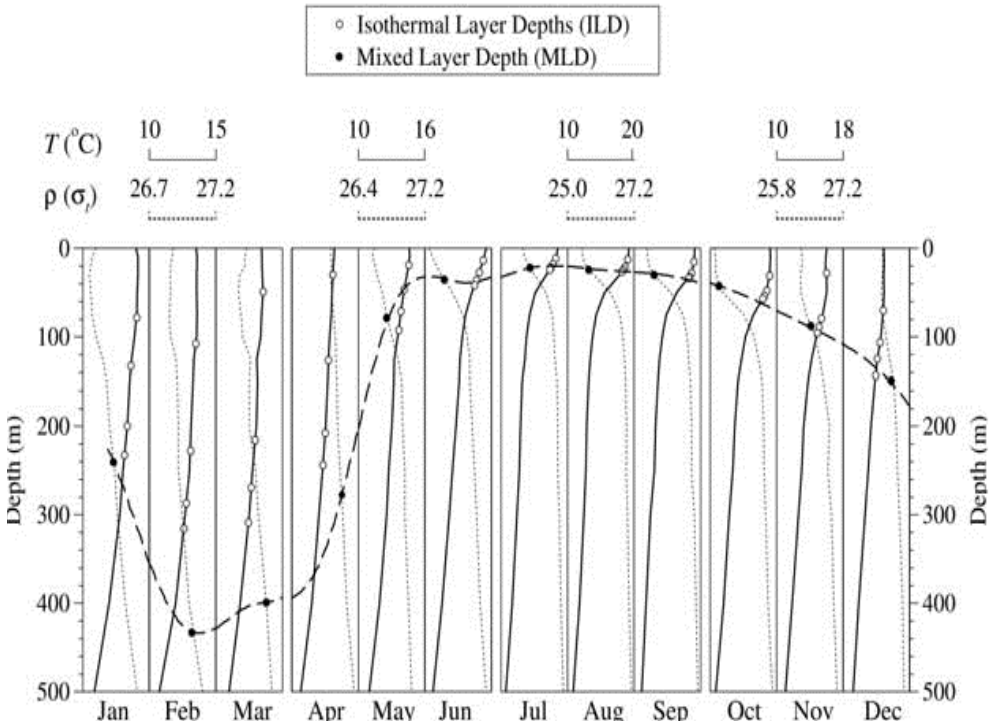

Figure 4.1: Monthly averaged temperature (T) and density (ρ) profiles constructed from the Levitus data at (45°N, 30°W) in the North Atlantic. The mixed layer depth (MLD) is obtained using a 0.8°C temperature difference and includes the effect of salinity. The MLD is shown with a solid circle on the density profile of each month. Similarly, isothermal layer depths (ILDs) based solely on a temperature change from the surface of ΔT = 0.1°, 0.5°, 0.8°, and 1.0°C are shown by open circles on the temperature profiles. The dashed line highlights the annual cycle of MLD. Figure and caption are from Kara et al. (2003).

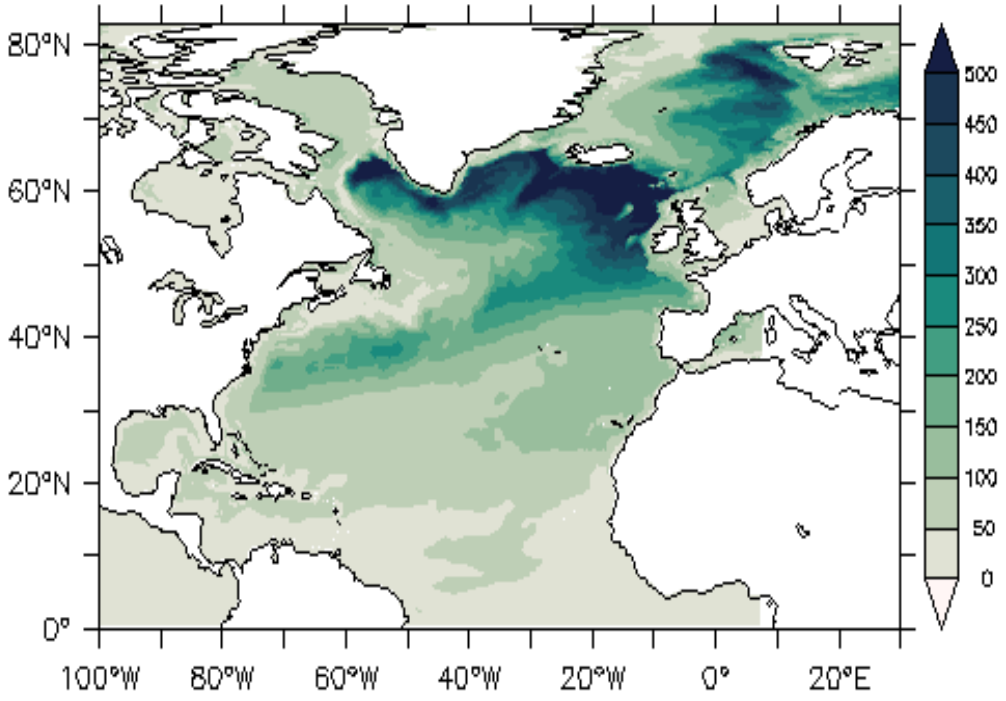

Figure 4.2: The mixed layer climatological mean of ensemble means in February is based on ensemble data. Units: metre. Note: a 40 ensemble mean is made in each February, then a 21 year February mean is made from the ensemble means.

4.4 The general theory of 1-D mixed layer models

Previous studies have revealed that the formation of the mixed layer is controlled by convection produced by the absorption of heat in depth and a loss at the surface, without being affected significantly by horizontal velocities, advection or rotation (Kraus and Rooth, 1961; Kraus and Turner, 1967; Turner and Kraus, 1967; Gill and Niller, 1973). A theory of the mixed layer formation based on energy relations which are the non-adiabatic heating at a depth h can be explained by the convergence of the penetrating component of solar radiation and heat

exchanges associated with the flux due to infrared radiation, sensible heat and evaporation (Kraus and Turner, 1967). Considering water temperature changes, heat flux, the entrainment due to downward heat flux, the thermal balance equation can be written as in equation (4.1).

$$h\frac{dT_s}{dt} + \Lambda(T_s - T_h)\frac{dh}{dt} = S + H - Se^{-\beta h} \approx S + H \tag{4.1}$$

Λ is the Heaviside unit function, defined to be:

$$\begin{aligned} \Lambda \equiv \Lambda(\frac{dh}{dt}) = 1 \quad for \quad \frac{dh}{dt} > 0 \\ = 0 \quad for \quad \frac{dh}{dt} < 0 \end{aligned}$$

h is the mixed layer; $\frac{dT_s}{dt}$ is changes in mixed layer temperature, T_s is surface or the mixed layer temperature, T_h is thermocline temperature. $\frac{\Lambda(T_s - T_h)}{h}\frac{dh}{dt}$ represents entrained temperature flux at the bottom of the mixed layer h. $T_s - T_h$ represents the temperature contrast between the mixed layer and the base of the mixed layer depth. $\frac{dh}{dt}$ represents rate of the mixed layer depth varying with time. T_s is lowered by the entrained water with the temperature T_h from the thermocline. Or, the temperature T_h rises due to heat transfer from the T_s.

$Se^{-\beta h}$ is convergence of the penetrating component of solar radiation. Below a depth of about ten centimetres, the absorption of solar radiation is approximately exponentially decreased, where β^{-1} is around 10 to 20 metres in the sub-tropical ocean. The absorption of radiation below depth h is likely to be small ($\beta h > 1$). Thus, $Se^{-\beta h}$ can be neglected.

S + H: $(S, H) = \frac{1}{\rho C_P}(S^*, H^*)$, S^* is solar radiation and H^* is flux due to infrared radiation, sensible heat and evaporation.

Using heat balance due to surface heat exchange and a mechanical energy balance caused by surface stirring from wind, gives a mechanical energy equation described as equation (4.2) (Kraus and Turner, 1967):

$$\frac{1}{2}\frac{dT_s}{dt}h^2 + \Lambda(T_s - T_h)\frac{dh}{dt}h = G - D + \frac{S}{\beta} \tag{4.2}$$

In equation (4.2), at left hand side, $\frac{1}{2}\frac{dT_s}{dt}h^2$ represents potential energy change associated with the change in temperature in the mixed layer, $\Lambda(T_s - T_h)\frac{dh}{dt}h$ represents potential energy change due to entrainment when the mixed layer deepens. At right side, G is the kinetic energy input from the wind stirring, D is the dissipation within the layer. $\frac{S}{\beta}$ is convection due to internal heating.

Now, we have the thermal balance in equation (4.1) due to heat input and the mechanical energy balance (4.2) due to mechanical energy input. Use these two equations to calculate changes in the mixed layer depth and temperature with time. Combine the thermal balance equation (4.1) and the mechanical balance (4.2) into one, then we have changes in temperature and the mixed layer depth separately for discussion conveniently in equations (4.3) and (4.4):

$$\frac{dT_s}{dt} = \frac{2}{h^2}\Big[(S + H)h - (G - D + \frac{S}{\beta})\Big] \tag{4.3}$$

$$\Lambda(\frac{dh}{dt}) = \frac{1}{(T_s - T_h)h}\left[2(G - D + \frac{S}{\beta}) - (S + H)h\right] \tag{4.4}$$

In winter, the mixed layer gets deeper so that $\frac{dh}{dt} > 0$, thus, $\Lambda = 1$ so that equations (4.3) and (4.4) can calculate changes in temperature and the mixed layer depth with time.

In the summer, the mixed layer is shallowing, thus, $\frac{dh}{dt} < 0$, thus, $\Lambda = 0$, there is no entrainment. Hence, equation (4.4) is changed into (4.5) to calculate the mixed layer depth in summer:

$$h = 2\frac{G - D + \frac{S}{\beta}}{S + H} \tag{4.5}$$

In this chapter, the general theory of 1-D mixed layer models based on Kraus and Turner (1967) sets up a context for how the temperature and the mixed layer vary with time. In fact, a 3-D heat balance will be applied in a later section (section 4.9) to investigate what are all the possible processes for surface temperature anomalies. There are two reasons for using 3-D heat budget equation (4.6) in section 4.9 instead of 1-D model equations being introduced here:

(i) G and D data are not available in model output as we need to use in 1-D heat equations;

(ii) Compared to the study in 1967 by Kraus and Turner (1967), there are more processes involved in the heat budget within the mixed layer depth in recent studies (Vijith et al., 2020; Menkes et al., 2006; Peter et al., 2006; Alexander et al., 2000).

4.5 The sensitivity of mixed layer thickness to air-sea heat flux

Before exploring the links between jet stream and ocean mixed layer thickness variability, the connection between the mixed layer and air-sea heat flux is examined. The sensitivity analysis (see explanation in chapter 3, section 3) between air-sea heat flux and mixed layer thickness is used in the ensemble data sets, as their interaction is vital in determining the influence of the atmospheric jet stream on the ocean mixed layer thickness in winter time.

In order to make the sensitivity correlation across 40 ensembles over the 21 years between air-sea heat flux (resolution 432×324 rectilinear grid data) and ocean mixed layer thickness (resolution 1442×1201 curvilinear coordinate data), the mixed layer data is interpolated on rectilinear grid data at the same resolution as air-sea heat flux so that these two data sets have the same resolution to calculate the correlation for each grid point over the North Atlantic. (i) The correlation across 40 ensembles for each grid point over the North Atlantic between the precursor air-sea heat flux and the outcome mixed layer for each winter month in each individual year of the 21 years over the North Atlantic is calculated; (ii) then a mean is calculated over these 21 maps to provide a mean correlation map.

As expected there is a robust positive correlation between January heat flux and February mixed layer thickness. There is a strong correlation of over 0.6 located

over most of the subpolar gyre and Nordic seas (Fig. 4.3), due to a deep mixed layer located there (see Fig. 4.2); also a positive correlation of about 0.31 to 0.6 is distributed along the Gulf Stream. The correlation signals between mixed layer depth and heat flux are matching up where the heat flux is mostly loss from the ocean to the atmosphere in climatology and more heat loss associated with a strong and a more northward jet (see chapter 3), and where the mixed layer is deepest. The positive correlations indicate that the mixed layer thickness deepens when there is a surface heat loss in winter time. The atmospheric jet stream drives patterns of surface heat flux, resulting in changes to the mixed layer thickness. How the atmospheric jet stream links to mixed layer thickness is explored in the next section.

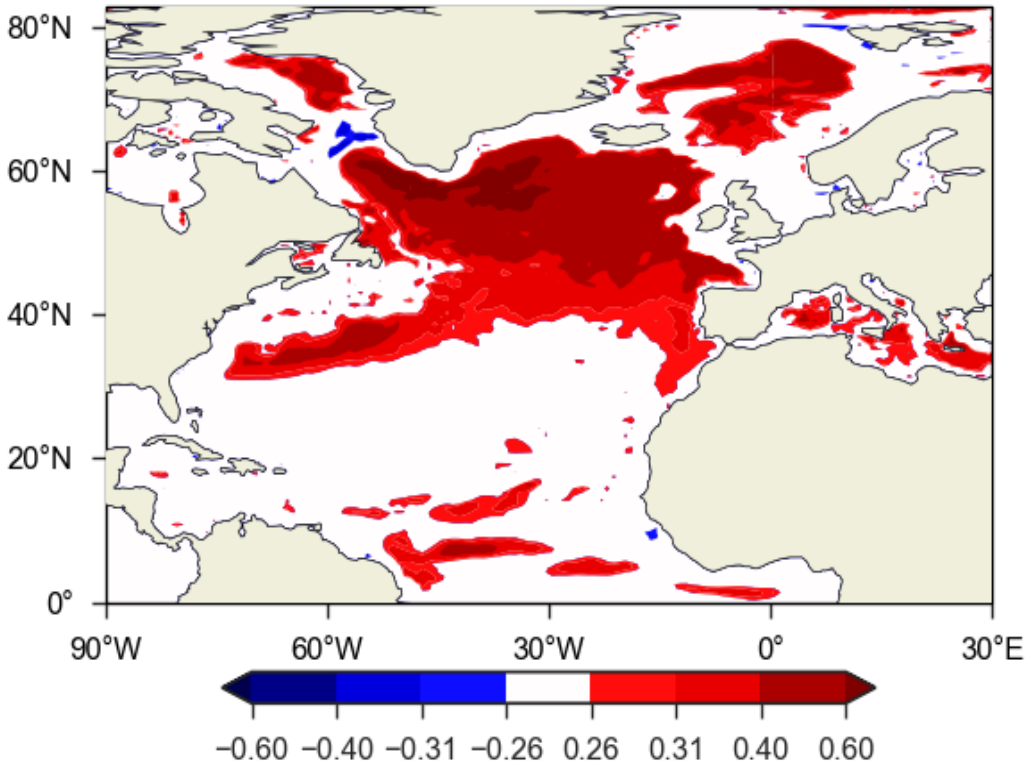

Figure 4.3: The correlation based on ensemble data between January air-sea heat flux (total of sensible and latent heat flux) and February mixed layer thickness; across the 40 ensembles for each year and then averaged over 21 years. Colours represent the correlation passing statistical significance tests with confidence levels of 90% at ±0.26, 95% at ±0.31 and 99% at ±0.40.

4.6 The effect of the atmospheric jet on the ocean mixed layer thickness

The study in chapter 3 has revealed that jet stream strength and latitude location change wind forcing and heat flux loss as well as horizontal and vertical circulation (see chapter 3 section 3.3 and 3.4). Therefore, in this section, how the mixed layer depth responds to jet stream speed and latitude is investigated.

4.6.1 Composite analysis of how the ocean mixed layer connects to jet indices

The mixed layer depth climatological mean over the Atlantic is the deepest, about 400 to 500 metres, in the winter month of January over the subpolar region around Iceland, the western boundary of the subpolar gyre and the Nordic sea (see Fig. 4.2). The mixed layer is relatively shallow, about 100 to 300 metres, over the rest of the North Atlantic. The mixed layer depth of the subpolar gyre deepens in response to a strong or more northward jet (see Fig. 4.4 c and b, Fig. 4.5 c). The subpolar region is important in ocean biology due to the increased supply of nutrients to the euphotic zone coming from the vertical exchange of water between the surface layer and the ocean interior. The mixed layer depth difference anomalies between a composite of 50 January months of the highest jet speed minus that for the lowest speed reveals a tripole pattern (Fig. 4.4 c), which is consistent with the surface heat flux anomalies associated with the jet stream (Fig. 3.6 a). Enhanced heat loss associated with a strong jet or more north jet leads to a deepening mixed layer by about 60 metres over the subpolar gyre; whereas, less heat loss (Fig. 3.6 a) decreases the mixed layer thickness by about 20 metres over the subtropical region along the Gulf Stream (see Fig. 4.4 c). There is a little increase in anomalies over the tropics of about 10m. By contrast, the jet latitude shifts affect the mixed layer showing similar magnitude anomalies over the subpolar gyre but much restricted narrow regions below the

Greenland sea and Iceland; whereas, over the subtropical region, the negative anomalies of about 20m are located farther north and east side of the subtropical gyre (see Fig. 4.5 c).

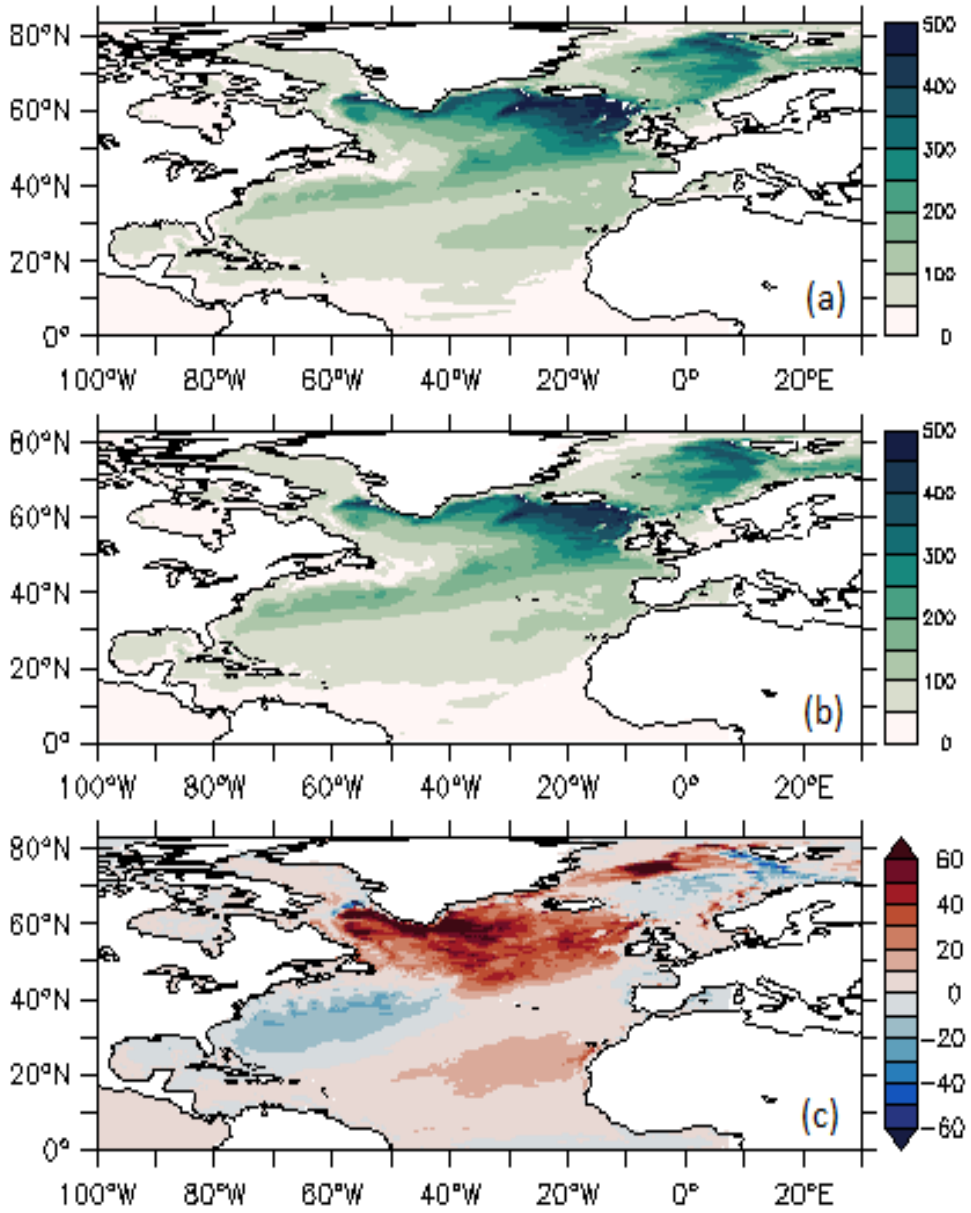

Figure 4.4: A composite mean of 50 January months from ensemble data of mixed layer thickness (unit: metres) (a) high jet speed state, (b) low jet speed state, (c) the difference between a composite of 50 January months of the highest speed minus that for the lowest jet speed. (unit: metres)

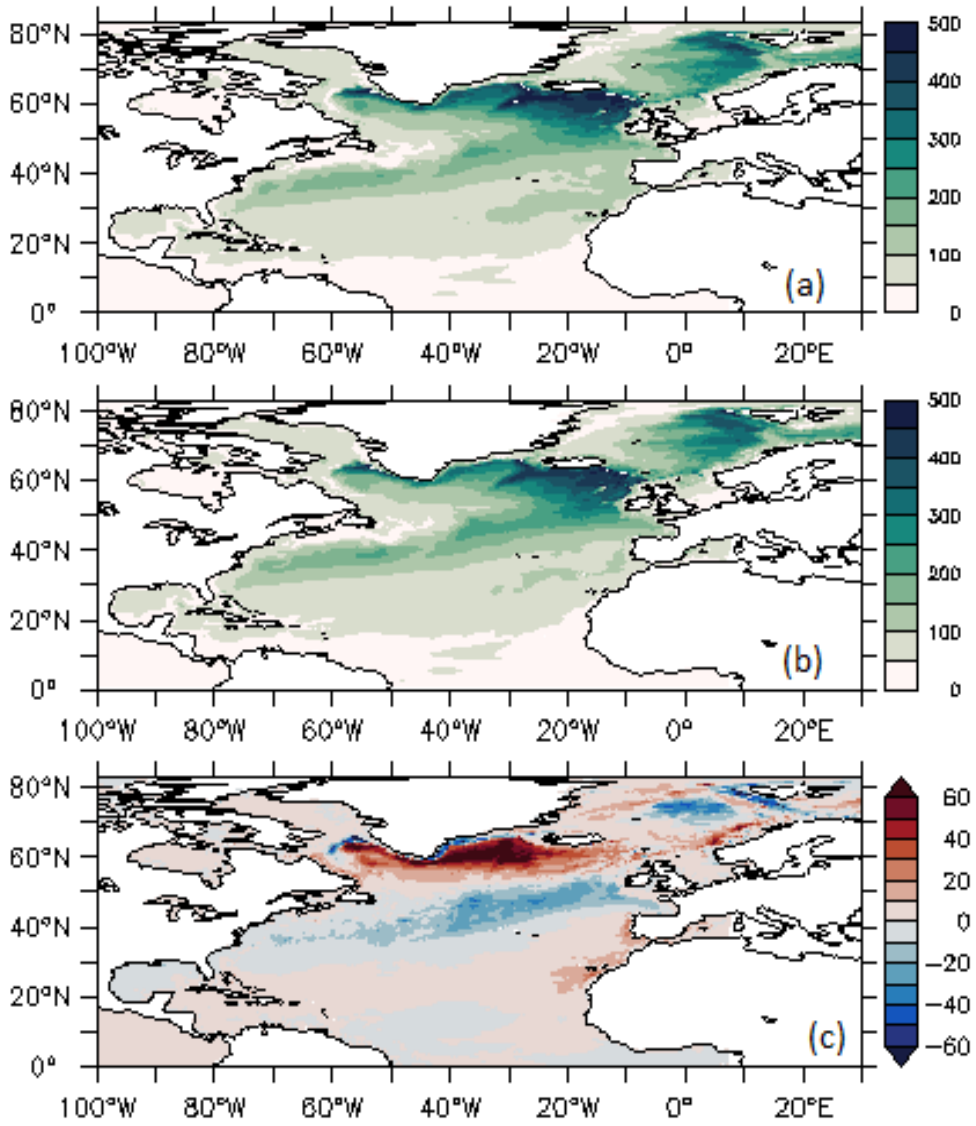

Figure 4.5: A composite mean of 50 January months from ensemble data of mixed layer thickness (unit: metre) (a) high jet latitude state, (b) low jet latitude state, (c) the difference between a composite of 50 January months of the highest latitude minus that for the lowest jet latitude. (unit: metres).

4.6.2 The sensitivity of the mixed layer thickness to the jet indices

The sensitivity analysis method is explained in chapter 3 (see chapter 3 section 2). In this section, the sensitivity of the mixed layer thickness to the jet stream strength and latitude location is evaluated in the following manner:

(i) The correlation between the precursor January jet indices and target February mixed layer thickness across the 40 ensemble members is calculated for each winter month in each individual year of the 21 years over the North Atlantic. (ii) a mean is then taken over these 21 maps to provide a mean correlation. Note, the sensitivity of January jet indices and February mixed layer thickness is investigated because in chapter 3 we have already revealed that jet indices affect the surface temperature with the maximum signal occurring in the following month.

The strong positive correlation signal of over 0.5 coefficient is only located over the subpolar region, suggesting that the mixed layer is sensitive to jet strength and latitude location over the subpolar region, but not elsewhere (Fig. 4.6). The sensitivity signals are slightly different between the mixed layer thickness and jet speed (Fig. 4.6 a), and between the mixed layer and jet latitude (Fig. 4.6 b). The strong jet speed correlating with a deepening in the mixed layer is a stronger and more widespread signal over most of the subpolar gyre; whereas, the northward

jet latitude correlated with a deepening in the mixed layer shifts farther north and within a much smaller and narrower region. These sensitivity signals are consistent with the sensitivity signals between jet indices and heat flux over the subpolar region (see Fig. 3.6 a and b). Note, the sensitivity significance signals' levels are used in the same way as in the analysis of the jet stream and heat flux signals. The correlation passes statistical significance tests with confidence levels of 90% at ± 0.26, 95% at ± 0.31 and 99% at ± 0.40. By comparison, the negative anomalies of the subtropical in the composites of the mixed layer depth associated with jet speed and latitude do not correspond to a significant correlation here. So that it suggests that the mixed layer depth response to the jet speed strength and latitude location mainly occurs over the subpolar gyre.

Why is the mixed layer depth not so sensitive to jet speed and latitude in the subtropical gyre compared to the subpolar gyre in winter time? In chapter 3, sensitivity and composite analysis reveal that the less heat loss over the subtropical gyre causes warming there associated with a strong and more north jet Fig. 3.6, Fig. 3.7, Fig. 3.8, Fig. 3.9. The mixed layer 1-D theory shows that surface heat loss deepens the mixed layer in the winter. Hence, a strong or more north jet inhibits heat loss of the subtropical gyre, as a result, it slightly shallows the mixed layer here as seen from composite analysis which shows negative anomalies in Fig. 4.4 c and Fig. 4.5 c. However, the negative anomalies do not correspond to significant correlation here in sensitivity analysis in Fig. 4.6.

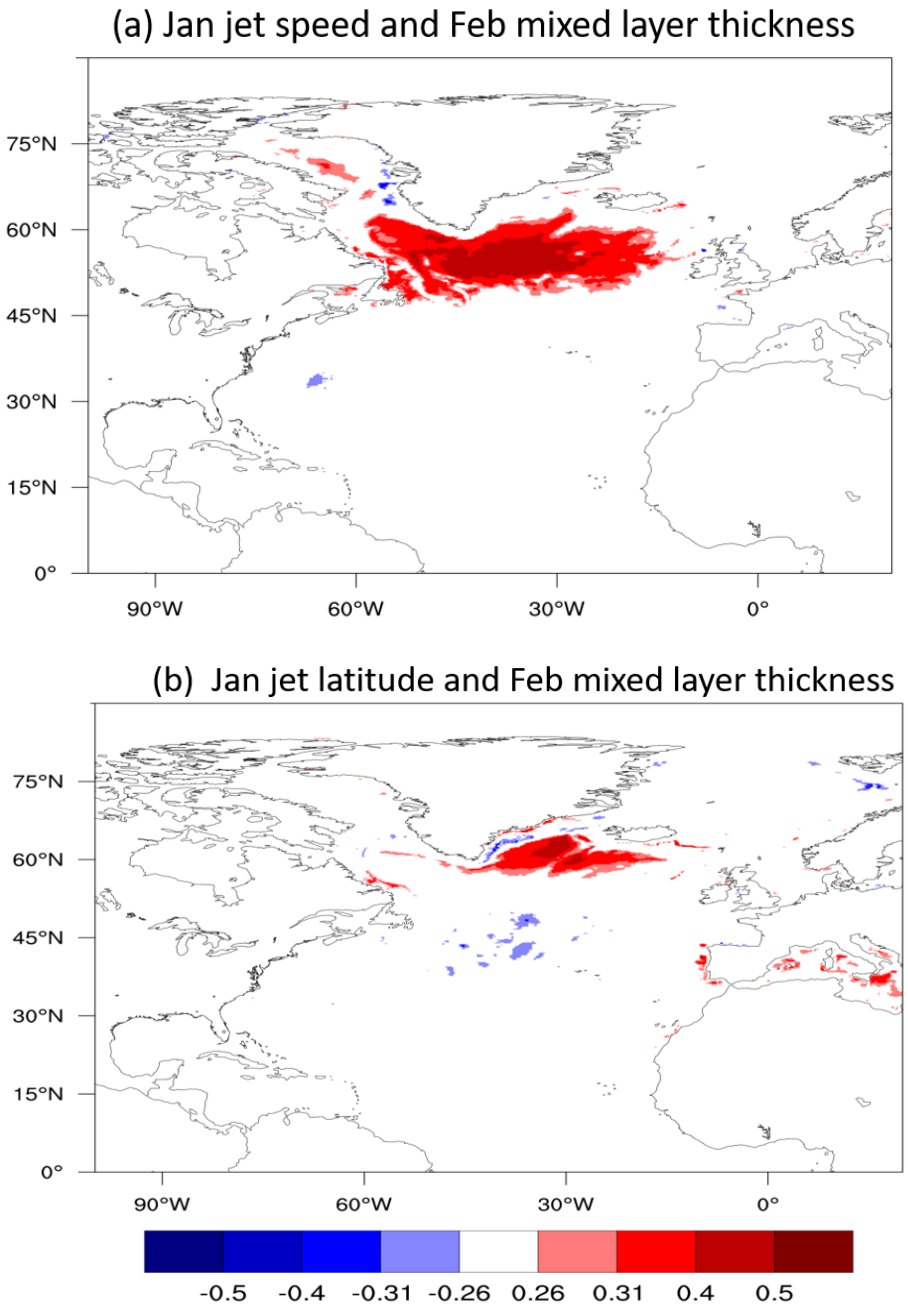

Figure 4.6: The correlation based on ensemble data between (a) January jet speed and February mixed layer thickness; (b) January jet latitude and February mixed layer thickness across the 40 ensembles for each year and then averaged over 21 years. Correlations are calculated across the 40 ensembles for each year and then averaged over 21 years. Colours represent the correlation passing statistical significance tests with confidence levels of 90% at ±0.26, 95% at ±0.31 and 99% at ±0.40.

4.7 The effect of the atmospheric jet on the ocean subsurface temperature

4.7.1 Sensitivity of the subsurface temperature to the jet indices

In this section, the sensitivity between jet stream indices and the ocean interior potential temperature is assessed using sensitivity analysis.

The correlation (i) across 40 ensembles between the precursor jet indices and outcome sea water potential temperature on 8 levels from the surface down to 300 metres depth for each winter month in each individual year of the 21 years over the North Atlantic is computed; (ii) then a mean is calculated over these 21 maps for each depth to provide a mean correlation map in Fig. 4.7 and Fig. 4.8. The tripole correlation pattern between jet indices and potential temperature at each depth is revealed from surface to 47m, which is very similar to that revealed in Fig. 3.9. The negative sensitivity signals remain over the subpolar gyre for depths down to 300m (Fig. 4.7). A strong jet stream leads to greater heat loss over the subpolar gyre, and as a result cools the subpolar ocean surface. The surface colder signals penetrate vertically down to at least 300m in the subpolar gyre. This possible mechanism will be explored in the next section.

The response of ocean surface properties to jet latitude has been revealed in

chapter 3, in that a more northern jet is associated with a northward extension or shift of the subtropical gyre. Similarly, a clear tri-pole correlation pattern extends from the subsurface down to 108m (Fig. 4.8) and a robust signal penetrating 300m over the subpolar region. On the other hand, the jet latitude leads to a positive correlation signal extending from the subtropics shifting into the intergyre region between the subtropics and the subpolar gyre and penetrating deeper down to 300m compared to the jet speed effect in the subtropical region. This response may reflect the subtropical gyre shifting farther north under a more northward jet latitude state, where the mixed layer depth is deeper than south-west of the subtropical gyre, consequently the surface temperature anomalies may penetrate down to 300m. Again, the possible processes will be investigated in the next section.

In comparison, the effect of jet speed is more pronounced than that of jet latitude on the vertical extent of ocean temperature response over the subpolar gyre, due to a strong jet leading to a greater heat loss and deepening of the mixed layer over most of the subpolar gyre. While, a more northward jet stream affects the surface temperature farther north and in a more restricted part of the subpolar gyre (Fig. 4.8), where the mixed layer deepening is restricted too (Fig. 4.5 c and Fig. 4.6).

In the subtropical location, in the west part of the gyre and north-east part of the gyre, the positive signals associated with jet speed and latitude penetrate down

to 200m and 300m, respectively. However, the mixed layer is not sensitive to the jet stream in these regions (Fig. 4.4). How do these signals penetrate down to different depths? The next section will explore what are the possible mechanisms.

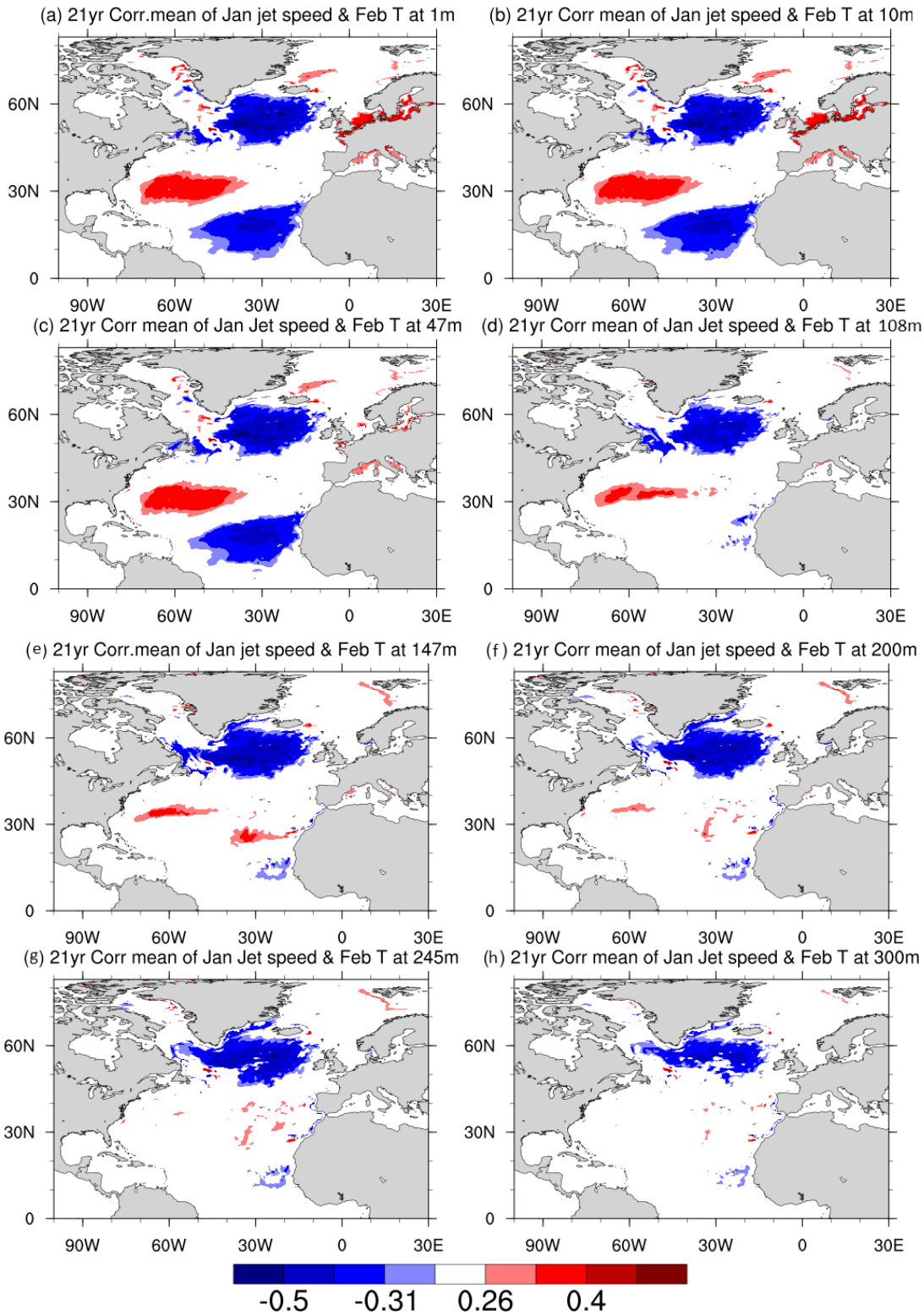

Figure 4.7: The correlation based on ensemble data between January jet speed and February water potential temperature at depth (a) 1m (b) 10m (c) 47m (d) 108m (e) 147m (f) 200m (g) 247m (h) 300m across the 40 ensembles for each year and then averaged over 21 years. Colours represent the correlation passing statistical significance tests as in Fig. 4.1.

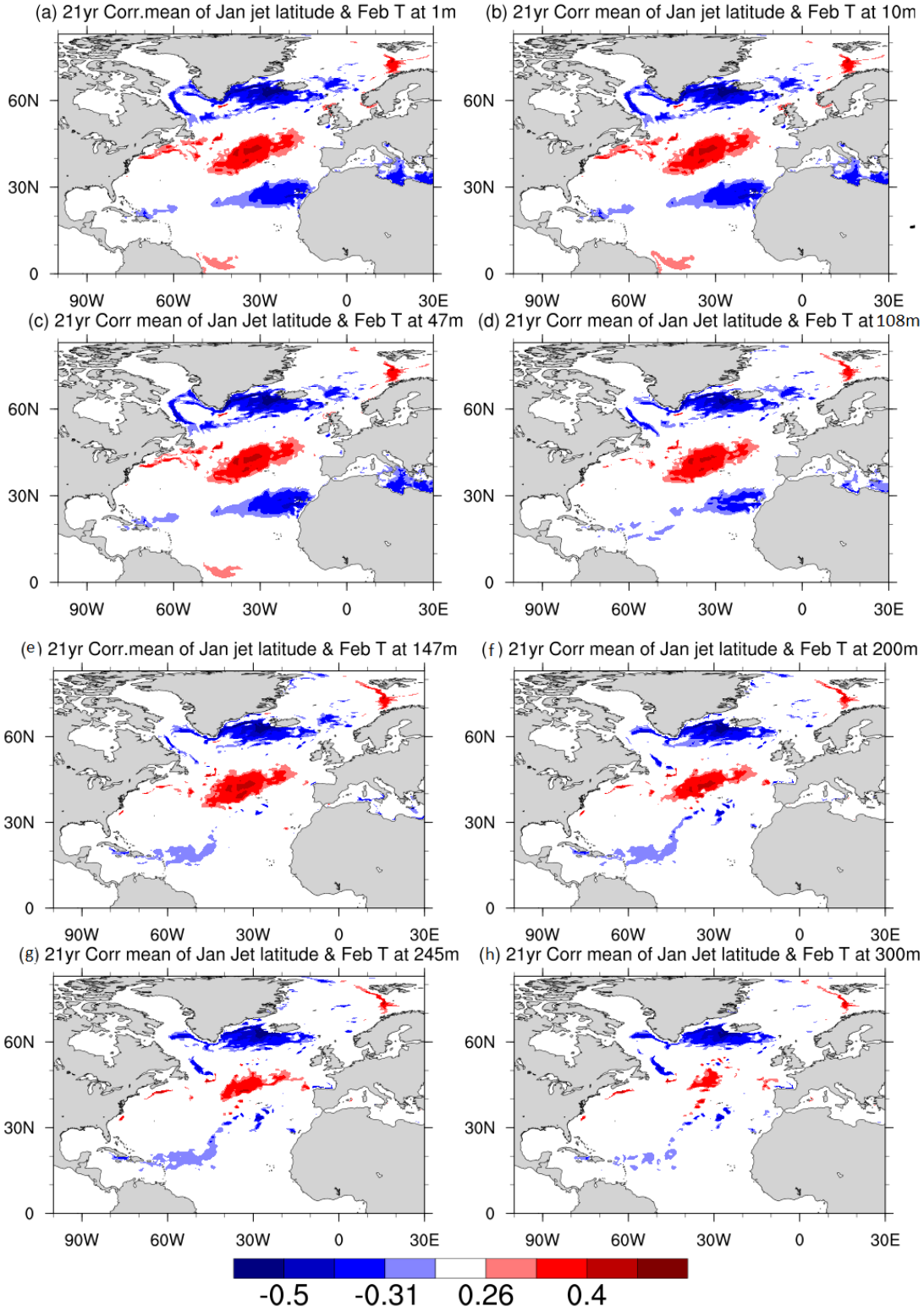

Figure 4.8: The correlation based on ensemble data between January jet latitude and February water potential temperature at depth (a) 1m (b) 10m (c) 47m (d) 108m (e) 147m (f) 200m (g) 247m (h) 300m across the 40 ensembles for each year and then averaged over 21 years. Colours represent the correlation passing statistical significance tests as in Fig. 4.1.

4.8 What are the mechanisms connecting jet variability to subsurface temperature change?

4.8.1 What is the mixed layer depth variation in different key locations?

As sensitivity analysis signals' evidence shows, February surface temperature anomalies associated with January jet speed pulse and latitude shifts penetrate into the upper ocean interior in different ways (Fig. 4.7, Fig. 4.8). There are three key regions, where temperature can penetrate down to different depths associated with jet speed and latitude. The first region is over the subpolar region where the surface temperature anomalies signals penetrate down to at least 300m associated with both jet speed and latitude. The second region is the west side of the subtropical gyre, where the temperature anomalies vertically penetrate down to 150 to 200m associated with jet speed. Thirdly, the east side of the Atlantic where there is a region between the subpolar and subtropical gyre at about 50°N and 20°W, the temperature anomalies in this region, which can penetrate down to 300m, are associated with jet latitude.

Sensitivity analysis reveals that mixed layer depth is sensitive to both jet latitude

and speed over the subpolar region where the positive correlation implies that a strong jet or more north jet deepens the mixed layer there. The mixed layer depth deepens by about 60m with a strong or more north jet over the subpolar gyre. The rest of the the mixed layer depth over the ocean is not sensitive to the jet speed and latitude (Fig. 4.6). Can the surface temperature anomalies over these regions without sensitivity to the jet stream communicate with the interior via the mixed layer depths? The mixed layer depth variation is examined over the three key locations based on a random ocean ensemble monthly data without corresponding to a strong or more north jet being involved. A location at 62°N and 30°W represents the subpolar region (hereafter called subpolar location). 62°N latitude is selected considering the temperature sensitivity signals location associated with both jet speed and latitude in Fig. 4.6 and Fig. 4.7. A location at 36°N and 60°W represents the west part of the subtropical region (hereafter called subtropical location). A location at 50°N and 20°W represents a north-east region between subpolar and subtropical gyres (hereafter called intergyre location). These three locations where the surface temperature anomalies penetrate down to the upper ocean to different depths are associated with jet speed and latitude. In February, the mixed layer depth reaches about 520m (Fig. 4.9 black lines) at the subpolar location where the surface temperature anomalies penetrate at least 300m associated with both jet speed and latitude, which indicates that the temperature anomalies penetrate into depth within the mixed layer.

For the subtropical location, where the surface temperature penetrates down to

200m associated with jet speed, even the mixed layer here is not sensitive to the jet speed, but the mixed layer itself is about 220m deep (Fig. 4.9 red lines) which is deep enough for surface temperature anomalies to penetrate into 200m (Fig. 4.6 f) via the mixed layer.

For the intergyre location, the surface temperature anomalies associated with jet latitude penetrate down to 300m depth (Fig. 4.6 h). In this location, the mixed layer reaches just 300m in February (shown as the green line in Fig. 4.9). The surface temperature anomalies associated with jet latitude may penetrate into the depth where the mixed layer itself is also deep enough to communicate with depth, even here the mixed layer depth is not sensitive to the jets.

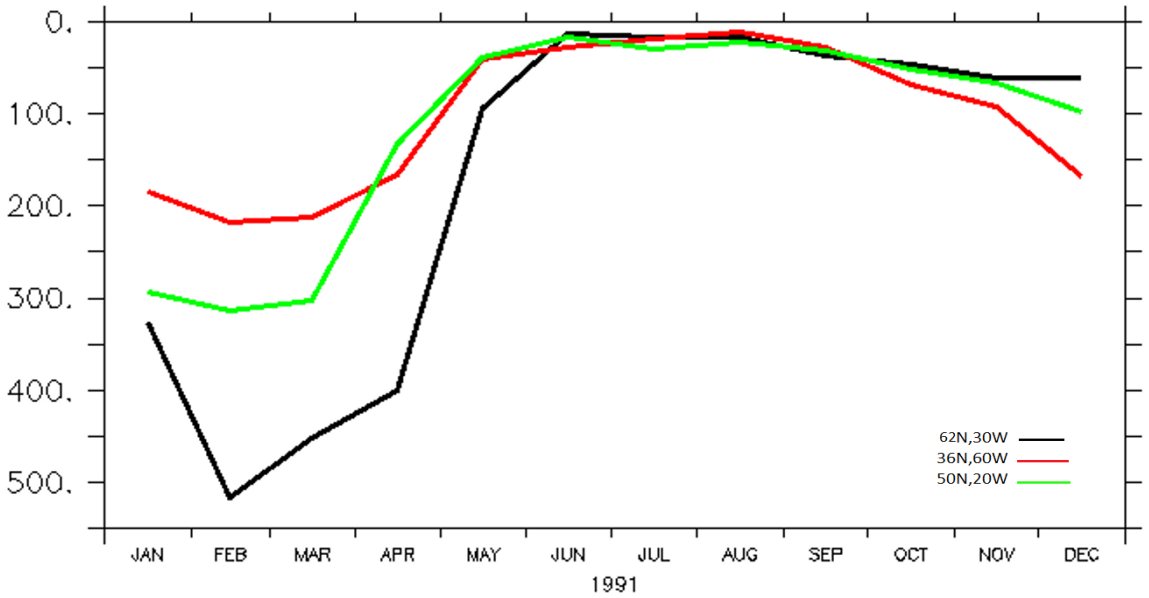

Figure 4.9: The mixed layer depth seasonal variation of one ensemble in 1991 based on ensemble data at three locations. The mixed layer depth definition is based on density difference $\Delta\ \sigma_\theta$. $\Delta\ \sigma_\theta$ is 0.01 kg m^{-3} between the density at the depth and the density at near-surface reference level at 10 m. Y-axis: the mixed layer depth (metres).

4.8.2 How does the temperature vary vertically associated with jet indices in different locations?

February temperature vertical profiles associated with the jet strength and location are displayed at the three key locations to investigate the temperature isothermal layer depth (ILD) variation responding to jet speed and latitude (Fig. 4.10). As I reviewed the definition of ILD and MLD in section 4.3.2, the ILD is generally coincident with the MLD over most of the global ocean due to a strong thermocline (Kara et al., 2003). Evidence shows that the temperature isothermal layer is 400m associated with a weak jet, and 550m associated with a strong jet over the subpolar location (Fig. 4.10 a). The isothermal layer depth variation indicates that a strong jet deepens the mixed layer by about 150m here compared to a weak jet (Fig. 4.10 a). Whilst, the isothermal layer depths are the same associated with either a strong jet or a weak jet (Fig. 4.10 b) over the subtropical location, which agrees with Fig. 4.6a that the mixed layer is not sensitive to the jet strength in this region. However, the mixed layer depth is about 200m which may be why the surface temperature only penetrates to 200m in Fig. 4.7 f .

In a similar manner, a more northern jet deepens the temperature isothermal layer over the subpolar location by about 100m compared to a more southern jet (Fig. 4.10 c). The isothermal layer changes from 400m to 550m associated with

jet latitude shifts from low to high. Again, the mixed layer depth is about 300m and no change is associated with a more north or more south jet (Fig. 4.10 d) over the east of the Atlantic at the intergyre location, where the surface temperature anomalies penetrate to 300m, Fig. 4.8 h. In this location, even the mixed layer depth does not change in association with jet latitude, but the surface temperature anomalies penetrate down to 300m which is just the depth of the isothermal layer.

The evidence reveals that the surface temperature anomalies associated with the jet stream can penetrate into the ocean interior within the mixed layer depth no matter whether changes in the mixed layer depth are sensitive to the jet stream strength and latitude shifts or not. A strong or more north jet is favourable to the surface cooling which causes denser water later to sink into depth which is done via the convection process. Also convection can be caused when there is more evaporation than precipitation. A strong jet brings strong winds which can accelerate evaporation. Surface wind also contributes convection by various mechanisms, in part because winds help to disturb the viscous sublayer at the sea surface, allowing more rapid transport of heat through the surface (Moum and Smyth, 2001). The next section will explore other possible mechanisms.

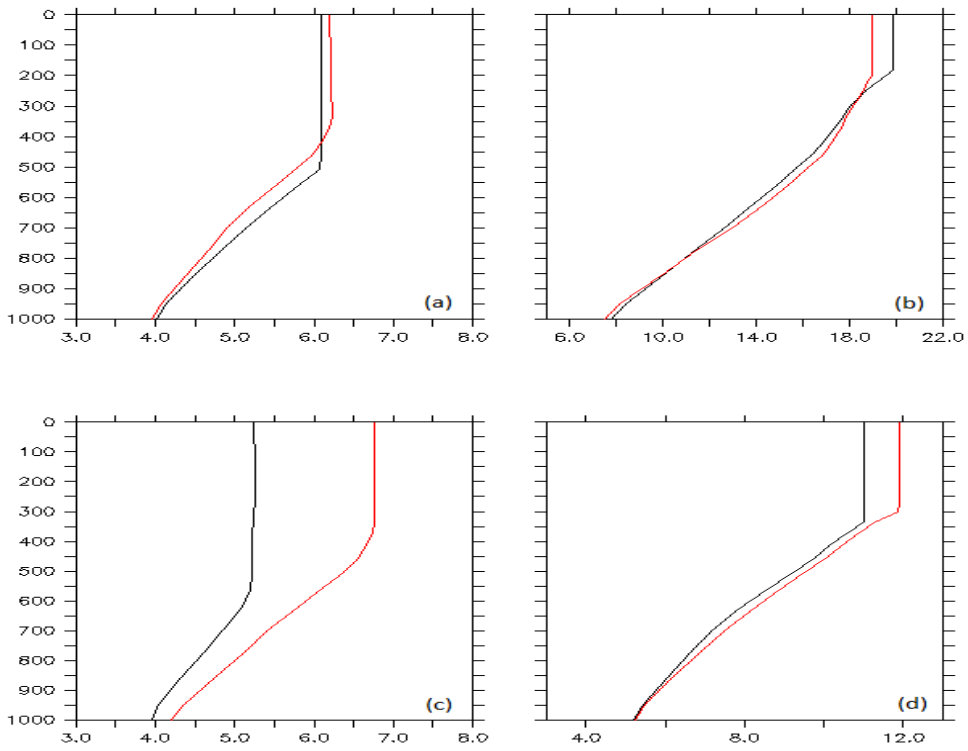

Figure 4.10: February surface temperature corresponds to a January strong and weak jet speed at (a) a subpolar location at (62°N,30°W) and (b) a subtropical location at (36°N,60°W). Black line is associated with a strong jet speed, red line is associated with a weak jet speed. February surface temperature corresponds to January a high and low jet latitude at (c) a subpolar location at (62°N,30°W) and (d) intergyre location between subtropical and subpolar at (50°N,20°W). Black line is associated with a high jet latitude, red line is associated with a low jet latitude.

4.9 Possible processes for the surface temperature variation within the mixed layer depth - 3-D heat budget

Observation and model experiments as well as theoretical studies (Turner and Kraus, 1967; Kraus and Turner, 1967) reveal that changes in subsurface temper-

ature and the mixed layer depth are via convection owing to heating at depth and cooling at the surface. Based on a 1-D theory study by Turner and Kraus (1967); Kraus and Turner (1967), in the thermal balance equation, the basic possible processes involve surface heat loss, vertical advection, surface turbulence, as well as mechanical stirring due to wind forcing, entrained temperature flux caused by the mixed layer and the thermocline depth difference due to the mixed layer depth deepening. Also horizontal advection vertically-averaged, vertical advection at the mixed layer base, lateral induction and vertical mixing due to vertical eddy diffusivity are considered in recent studies (Vijith et al., 2020; Peter et al., 2006). The possible processes are shown in the sketch graphics in Fig. 4.11.

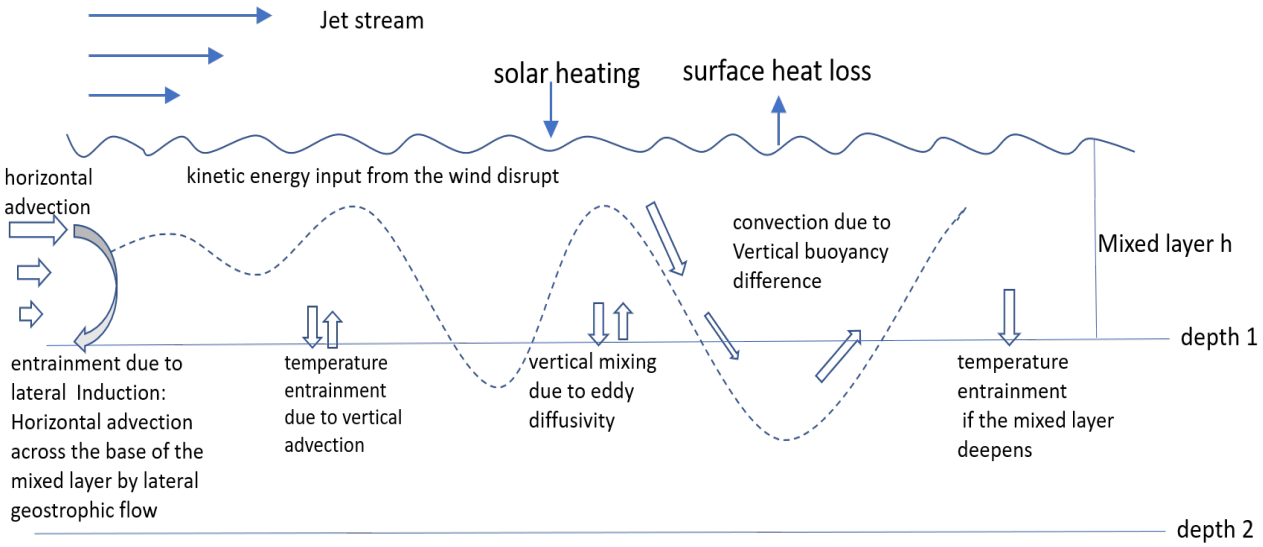

Figure 4.11: Sketch for the possible mechanisms and processes connecting jet variability to subsurface temperature changes.

The temperature heat budget equation can be written based on the processes shown in Fig. 4.11 in the sense of the 1-D heat balance equation (4.3) used by Kraus and Turner (1967) and 3-D possible processes revealed in the other studies

(Vijith et al., 2020; Menkes et al., 2006; Peter et al., 2006; Alexander et al., 2000):

$$\frac{\partial T_s}{\partial t} = \underbrace{-[\frac{(T_s - T_h)}{h}]\left[\underbrace{\frac{dh}{dt}}_{\text{ML vary with time}} + \underbrace{u_{-h}\frac{\partial h}{\partial x} + v_{-h}\frac{\partial h}{\partial y}}_{\text{lateral induction}} + \underbrace{w_{-h}}_{\text{vertical advection}}\right]}_{\text{entrainment}} - \underbrace{\left[u\frac{\partial T}{\partial x} + v\frac{\partial T}{\partial y}\right]_a}_{\text{horizontal advection}} - \underbrace{\frac{1}{h}\left[k_z\frac{\partial T}{\partial z}\right]_{-h}}_{\text{vertical mixing}} + \underbrace{\frac{H}{\rho C_p h}}_{\text{net heat fluxes}} \tag{4.6}$$

Here, T_s is surface temperature, T_h the thermocline temperature, T is the temperature at depths (they are sea water potential temperatures); u, v and w are the zonal, meridional and vertical currents respectively; k_z the vertical heat diffusivity coefficient; h is the mixed layer depth; H is surface net heat flux which includes sensible heat flux, latent heat flux, net longwave radiation and solar net downward radiation. Suffix a represents a vertically-averaged quantity within the mixed layer depth, and suffix h indicates the quantity at the base of the mixed layer depth. In fact, equation (4.6) results from each term's quantity integrated over the mixed layer and dividing by h on both sides.

In equation (4.6), the left hand side represents surface or the mixed layer temperature varying rate with time. The left side term is balanced by the right hand side terms. On the right hand side, the first term is entrainment which includes three components. The second term is horizontal advection vertically-averaged over the mixed layer depth. The third term is vertical mixing due to vertical eddy diffusivity at the base of the mixed layer depth. The fourth term is the effect of the surface heat flux.

Apparently, in equation (4.6), the entrainment term is developed into more components compared to the earlier study by Kraus and Turner (1967). In my test, the first component of entrainment is $\frac{\Lambda(T_s - T_h)}{h}\frac{dh}{dt}$ which is exactly the same as illustrated in the study by Kraus and Turner (1967). However, other terms in entrainment are added by later studies (e.g. Vijith et al., 2020; Menkes et al., 2006; Peter et al., 2006). The second component of the entrainment in equation (4.6) is associated with horizontal advection across a sloping mixed layer base. Horizontal advection across the base of the mixed layer by lateral geostrophic flow, is often referred to as 'lateral induction'. The third component of the entrainment is vertical advection which includes the effects of both upwelling and entrainment cooling.

Estimation of each term in the heat budget in equation (4.6) at the intergyre location (50°N, 20°W) for 15 months is based on one ensemble data from 1990 December to 1992 February (Fig. 4.12). All year round, the maximum upwards net heat flux, i.e. great heat loss from the ocean surface to the atmosphere is in winter months about -200 to -300 W m^{-2} (Fig. 4.12 a). The heat downwards into the ocean is in the summer months about 100 W m^{-2}. The heat flux takes a large contribution of most of the year for changes in the temperature; whereas, a smaller effect in the autumn season (Fig. 4.12 b). The entrainment first term $\frac{\Lambda(T_s - T_h)}{h}\frac{dh}{dt}$ makes an important contribution in autumn and winter, particularly in autumn and early winter (Fig. 4.12 c). The reason why this entrainment contributes to the mixed layer temperature variation may be due to (i) the mixed layer depth

starting to deepen from September (ii) according to the definition, the mixed layer depths are still shallow enough to make this entrainment occur effectively compared to the months in later winter (iii) the large difference between the surface and the thermocline temperature so that the thermocline water is entrained into the mixed layer cooling the temperature within the layer. N.B. when I calculate $\frac{\Lambda(T_s-T_h)}{h}\frac{dh}{dt}$, according to the temperature vertical profile (Fig. 4.10) and previous studies (Kara et al., 2003; De Boyer Montégut et al., 2004), $\Delta T = T_s - T_h$ is fixed at different threshold values, such as ΔT = 0.1°C, 0.2°C, 0.5°C, 0.8°C and 1.0°C (Kara et al., 2003; De Boyer Montégut et al., 2004). The entrainment $\frac{\Lambda(T_s-T_h)}{h}\frac{dh}{dt}$ shows the same effect but different magnitudes in terms of different ΔT criteria. When making the final sum of all terms, the entrainment derived from ΔT = 0.8°C is added since the mixed layer depth based on this ΔT value can indicate how deep turbulent mixing has descended (Kara et al., 2000). The entrainments due to lateral induction and vertical advection at the base of the mixed layer provide very little effect. Horizontal advection vertically- averaged over the mixed layer has a small effect (Fig. 4.12 d). The entrainment due to vertical advection at the base of the mixed layer provides very little contribution. The horizontal advection vertically averaged within the mixed layer depth also takes a very small effect except at the west subtropical location where the horizontal advecton has some contribution at the west subtropical location (see Fig. 4.13).

The vertical mixing due to the eddy diffusion term is not analysed because the

vertical diffusivity coefficient data is uncertain in this model data, vertical eddy diffusivity coefficient magnitudes are about 1 $\times 10^{-1}$ m^2 s^{-1} which is much larger than previous studies where the vertical eddy diffusivity is about 1 $\times 10^{-5}$ to 10^{-4} m^2 s^{-1} (e.g. Cronin et al., 2015; Lohmann et al., 2013; Spall et al., 2000; Webb and Suginohara, 2001). Hence, the vertical mixing term for the temperature balance is not included in Fig. 4.12, Fig. 4.13 and Fig. 4.14. Theoretically, the vertical mixing acts to cool the mixed layer due to the heat in the layer diffusing into the thermocline. However as the mixed layer is directly connected to the atmosphere, on long time scales we won't see a temperature change in the mixed layer. Any heat loss to the thermocline will be balanced by heat gained from the atmosphere. On short timescales, such as a daily time scale, the vertical mixing provides very little cooling effect for changes in the mixed layer temperature (Vijith et al., 2020).

The sum of net heat flux effect, three entrainments , and horizontal advection over the mixed layer reach a good balance of the surface temperature variation during most of the year, in particular, in winter and summer seasons. The net heat flux makes a dominant contribution over the winter and summer seasons. In the autumn season, the entrainment flux due to the mixed layer deepening provides a significant effect.

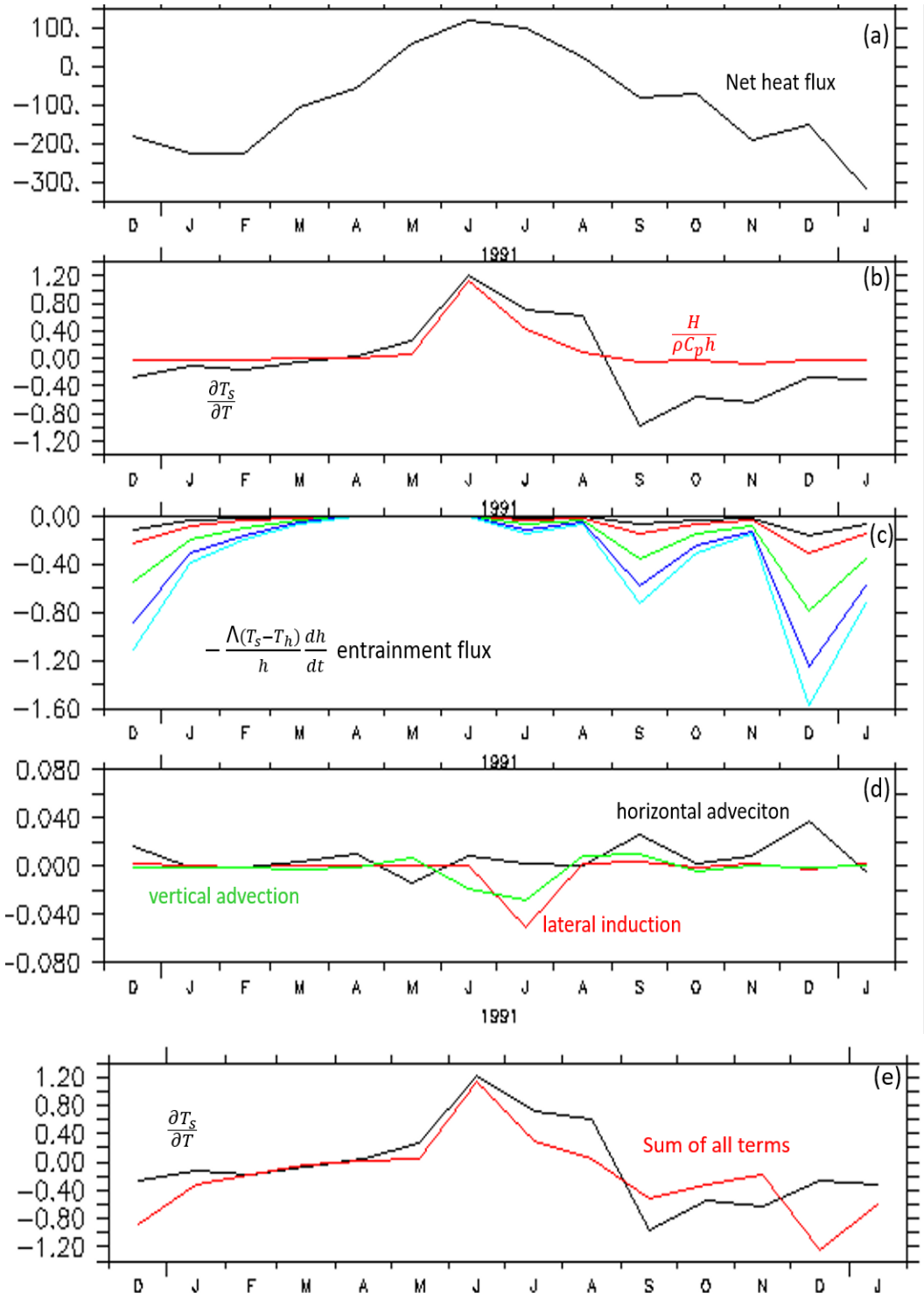

Figure 4.12: caption on next page

Figure 4.12: (Previous page.) Time series of the tendency of surface temperature, the terms of the heat budget and sum of all terms in 15 months from 1990 December to 1992 Jan in equation (4.6) at the subpolar location at (62°N,30°W) based on one ensemble model data. (a) Net heat flux (sum of latent heat flux, sensible heat flux, net outgoing long wave radiation and net downward solar shortwave radiation). Positive denotes upward net heat flux, negative denotes downward net heat flux. Units: W m^{-2}. (b) The tendency of surface temperature (black line, left Y-axis); net heat flux contribution (red line, right Y-axis). (c) entrainment contribution: $-\frac{\Lambda(T_s-T_h)}{h}\frac{dh}{dt}$ is derived from different ΔT criteria. black line: from $\Delta T = (T_s - T_h) = 0.1$°C, red line from ΔT =0.2°C, green line: from ΔT =0.5°C, blue line: from ΔT =0.8°C, light blue: from ΔT =1.0°C. (d) Horizontal advection vertically-averaged over the mixed layer depth (black line); entrainment due to lateral induction (red line); vertical entrainment due to vertical advection at the base of the mixed layer (green line). (e) the tendency of surface temperature (black line, left y-axis) and sum of all terms (red line, right y-axis). (from (b) to (e), units are °C per day.)

The same processes based on equation (4.6) are implemented at the west subtropical, 36°N,60°W and east intergyre 50°N,20°W locations (Fig. 4.13 and Fig. 4.14) . The heat contribution from the terms at these two locations are similar to the subpolar location. One noticeable difference is horizontal advection vertically averaged makes a noticeable contribution of about 0.15 °C per day over the west subtropical at 36°N,60°W in summer months (Fig. 4.14 d) which may due to heat advection input along the Gulf Stream (Roberts et al., 2017).

Summarising over the three key locations, the evidence shows that the sum of the net heat flux, entrainment due to the mixed layer depth deepening, vertical advection and lateral induction are well balanced with surface temperature tendency for most of the year. The net heat flux makes a dominant contribution for the balance; whereas, the entrainment flux due to the mixed layer deepening provides an important effect in autumn and early winter. The later summer and autumn season is not 100% balanced. This may be due to the previous season's

influence on future seasons' heat budget. As was revealed in the previous studies, the cooler waters of the previous winter and spring continue downward diffusion during the summer months, cooling the deep seasonal thermocline (Spall et al., 2000). Other possible effects may be because deep winter mixed layers and the storage of thermal anomalies beneath the shallow mixed layer in summer affect the winter SST anomalies (Alexander et al., 2000; Spall et al., 2000). Therefore, surface temperature balance may need to be considered on longer time scales, for instance, interannual, decadal and multi-decadal timescales.

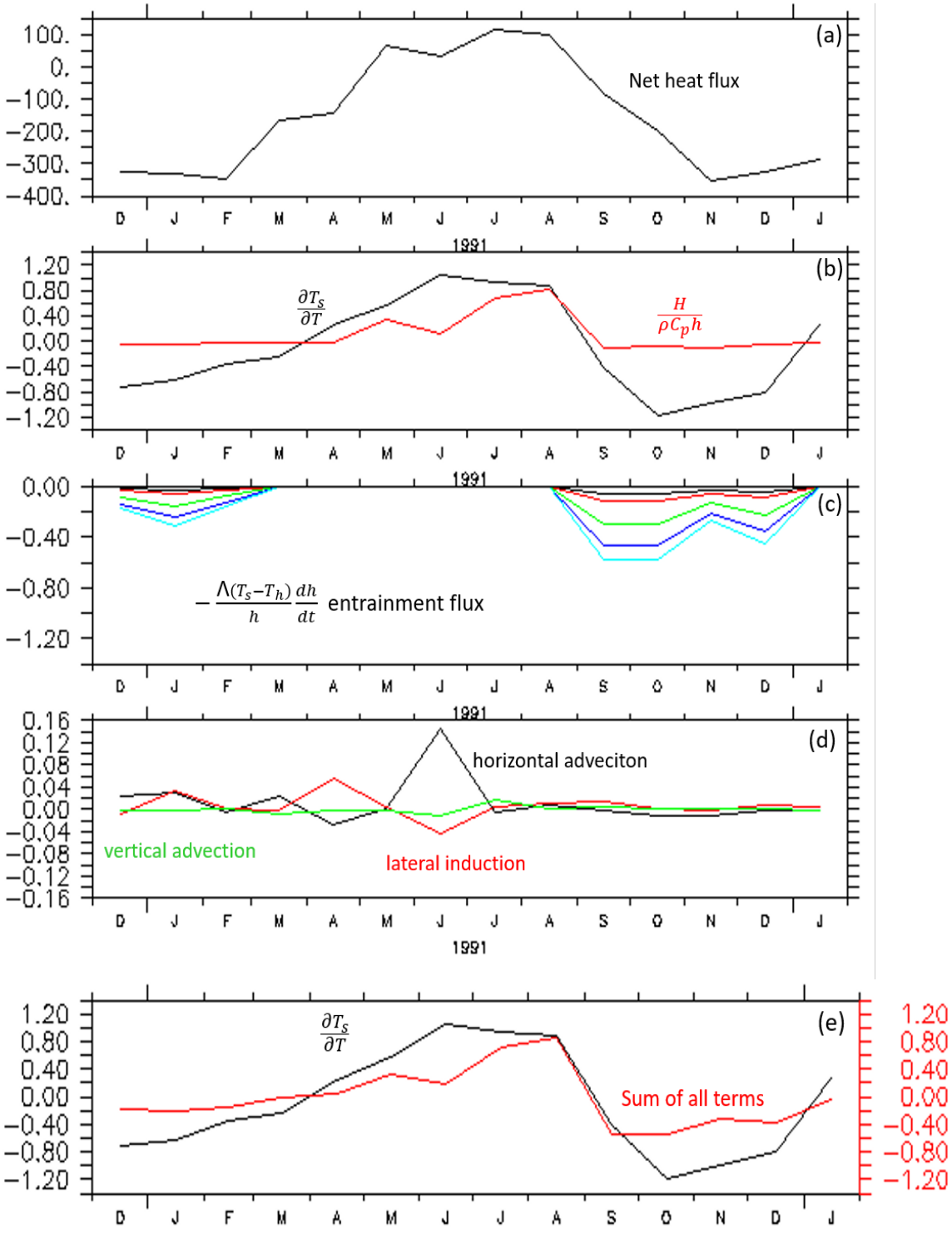

Figure 4.13: Same as Fig. 4.12 but at 36°N,60°W location.

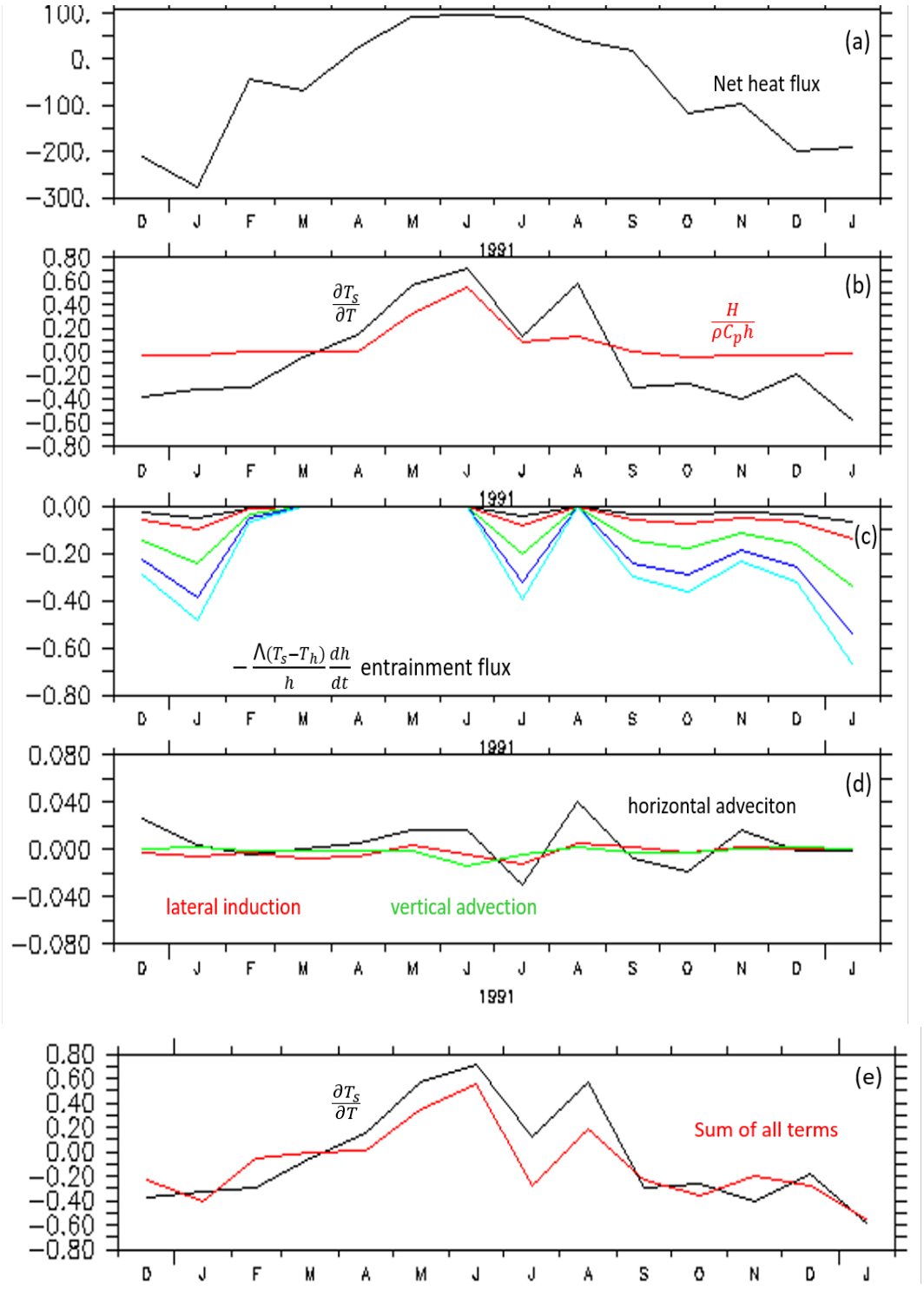

Figure 4.14: Same as Fig. 4.12 but at 50°N,20°W location.

4.10 Additional information about convection

Based on the DePreSys3 ocean ensemble model data, the variable "votkeevd" is the enhanced diffusivity representing parameterisation of convection: convection is done by increasing the vertical diffusivity. As the data illustrates, the enhanced eddy diffusivity time-depths panels show strongest and deepest convection of about 9 to 10 m^2 s^{-1} taking place in the colder month, such as February or March reaching depth at the bottom of the mixed layer; whereas, very shallow and weak convection occurs in summer. Convection gets deeper from autumn. The convection goes down depths coincident with the mixed layer depths in four seasons in three locations (shown in Fig. 4.15). The parameterisation of convection proves that the surface temperature anomalies in winter associated with jet stream penetrating into depth is done by the convection process via the mixed layer depth.

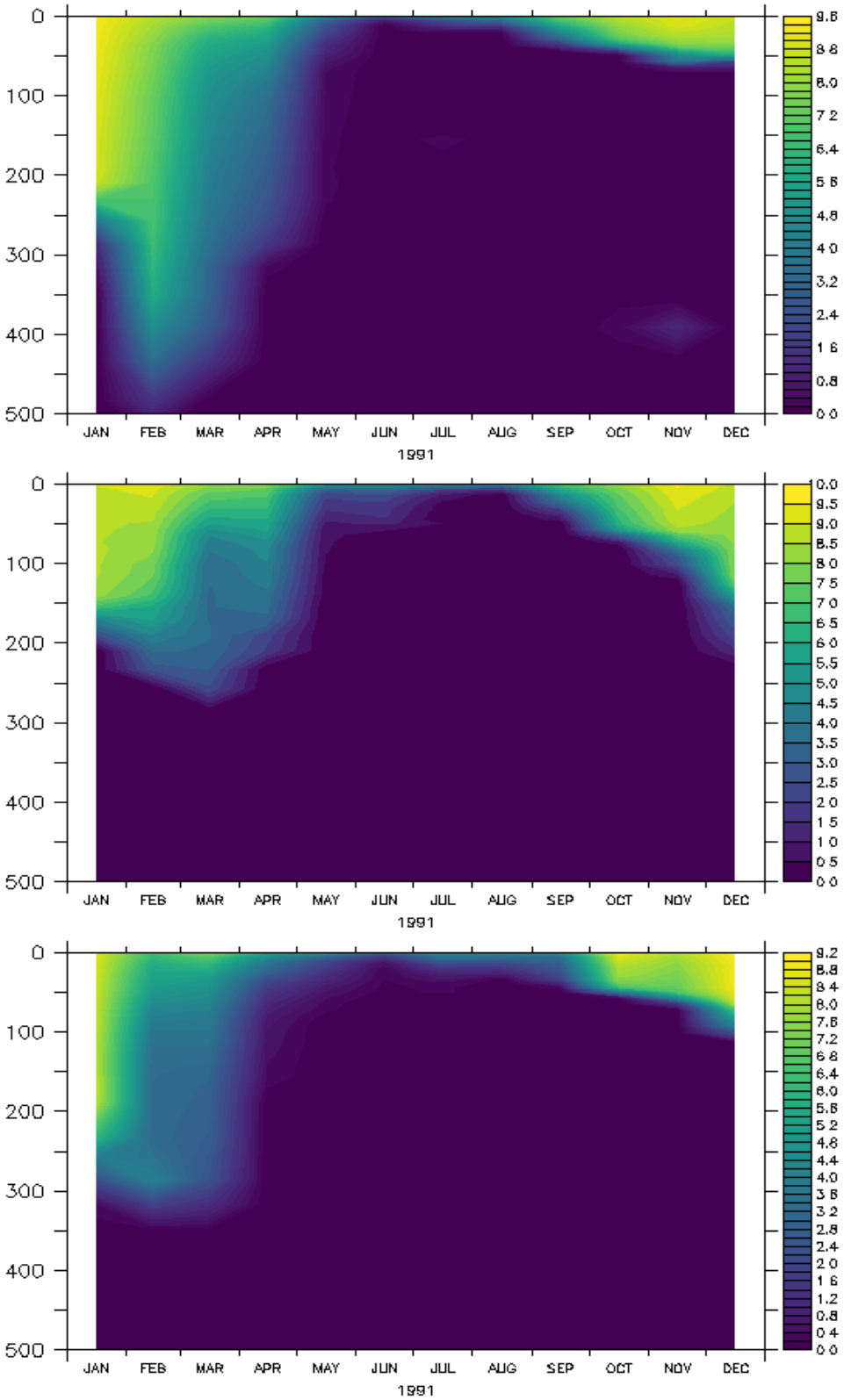

Figure 4.15: Annual enhanced eddy vertical diffusivity distribution at (a) 62°N, 30°W location; (b) 36°N, 60°W location; (c) 50°N, 20°W location; (units: $m^2\ s^{-1}$) in 1991 based on ensemble model data.

4.11 Conclusion and discussion

The ocean interacts with the atmosphere most actively in winter time (Liu et al., 2020). Meanwhile, the mixed layer depth is deepest in winter in this study based on ensemble model data and previous studies, such as (Kara et al., 2003; De Boyer Montégut et al., 2004). The vertical convection is active and deep in winter too. The achievement of this study is as follows:

(i) The sensitivity analysis across ensembles helps us to find causality between atmosphere and ocean. Atmospheric jet stream spread variability causes changes in ocean properties, such as changes in surface temperature, changes in ocean surface wind, ocean surface horizontal and vertical circulation.

(ii) Both sensitivity and composite analyses show that a strong jet enhances ocean surface heat loss. The mixed layer depth is sensitive to the surface heat flux over most of the subpolar gyre, along the Gulf Stream and east subtropical in winter.

(iii) Both sensitivity and composite analyses show that a strong jet enhances surface heat loss, and so thickens the winter mixed layer over most of the subpolar region; whereas, a northward jet latitude increases heat loss and thickens the mixed layer further north over the subpolar gyre and restricted region. The mixed layer depth is not sensitive to the jet speed and latitude over the subtropical gyre and the rest of the North Atlantic according to the sensitivity correlation guide.

(iv) Jet stream strength and location affect ocean surface temperature revealing

a tripole pattern. Evidence shows that over the subpolar gyre, the vertical extent of sub-surface temperature signals extends down to at least 300m due to a climatology deep mixed layer. A deepening layer over the subpolar associated with a strong or more north jet is favourable for surface and interior communication. The surface temperature anomalies over the subtropical gyre associated with jet speed penetrating down to 200m are due to the mixed layer being about 200m in this region even though the mixed layer is not sensitive to the jet speed and latitude here. The temperature anomalies over the subtropical gyre are shifted farther north into the intergyre between the subtropical and subpolar gyres associated with jet latitude. The mixed layer does not respond to the shifts of jet latitude here, but the surface temperature anomalies still penetrate 300m due to the mixed layer depth itself being 300m here.

Temperature vertical profiles analysis shows that the isothermal layer depths (ILDs) are coincident with the density-based criterion mixed layer depths based on ensemble model data. A strong or more northward jet deepening the ILDs over the subpolar location and having hardly any effects on west subtropical and east intergyre locations. The ILDs vertical variation associated with jet indices proves that the mixed layer depth is mainly sensitive to the jet strength and latitude shifts over the subpolar region which helps surface temperature anomalies penetrate into depth by the deepening mixed layer.

(v) The parameterisation of convection depths distribution evidence shows that

the surface temperature cooling anomalies in winter extending into the deep mixed layer is done by enhancing the vertical diffusivity by a convection process via the mixed layer depth.

(vi) The vertical temperature budget case study reveals that the surface temperature anomalies penetrate into depth via two main processes: (1) surface heat loss and colder and denser water sinks by convection. (2) cold water from the thermocline entrained into the mixed layer depth by an entrainment process due to the mixed layer deepening. Entrainment due to vertical advection and lateral induction has little effect.

In the summer season there is surface warming by net downward solar radiation. Also horizontal advection making some heat input effect over the west subtropical location may due to northward heat transport by the Gulf Stream (Roberts et al., 2017).

How well are the conclusions based on the DePreSys3 model likely to translate to the real ocean? The conclusions follow general ocean dynamical and thermodynamical principles well. For example, surface strong wind causes more heat loss, cooling the surface, which generates a density difference leading to colder surface water sinking by a convection process via a deep mixed layer depth. An entrainment process acts to cool the mixed layer due to the thermocline cold water being entrained in it when the mixed layer starts deepening. Also, a large temperature difference between the surface and thermocline helps the entrainment process ac-

cording to this study. However, what level of accuracy the model data achieves is still a challenging question to answer. More observations are needed to compare with the model results in the future.

The remaining question is about the vertical heat balance only being about 50% balanced in later summer and autumn at 36°N,60°W and 60°N,30°W locations when summing up the components. These two locations are in subpolar and west subtropical near the Gulf stream. There are jet streams travelling frequently and cold temperature advection striking more dynamically influenced by strong westerly winds in winter over the subpolar location and heat advection input over the Gulf Stream. There may be other mechanisms for later summer and autumn at different locations either different advection contribution or extra mixing due to the previous seasons' influence which needs further investigation in the future. (Alexander et al., 2000; Spall et al., 2000).

Meantime, SST variability on decadal or multi-decadal timescales shall be considered for the surface temperature balance because SST variability itself has an important role instead of being influenced by surface heat flux. Atlantic multi-decadal variability has a significant regional climate impact (Knight et al., 2006; Sutton and Dong, 2012). The ocean plays an important role in this long timescale in which a warmer SST releases more heat and a colder SST releases less heat (Gulev et al., 2013; O'Reilly et al., 2016). How much do SST interannual and decadal variabilities have an effect on the surface heat budget instead of sea-

sonal surface heat flux and other local processes? This will be the future scientific question to address.

Next chapter - chapter 5, I will explore how the Atlantic Meridional Overturning Circulation (AMOC) and horizonal gyre circulation responds to changes in the atmospheric jet stream in terms of jet speed strength and latitude location on monthly to seasonal time-scales.

Chapter 5

How Does the Atmospheric Jet Stream Affect Atlantic Meridional Overturning Circulation (AMOC) and Gyre Circulations?

5.1 Introduction

The meridional circulation in the Atlantic Ocean is part of a global system of surface and deep currents making up the Meridional Overturning Circulation (MOC). This global "conveyor belt" redistributes huge amounts of heat, salt and nutrients within all oceans. The Atlantic Meridional Overturing Circulation (AMOC) transports heat northward in both hemispheres in the Atlantic basin.

Over the last two decades, observational studies, ocean and climate modelling have provided conceptual understanding and a dynamic framework of the Atlantic Meridional overturning circulation (AMOC) (Buckley and Marshall, 2016; Johnson et al., 2019). A review paper by Johnson et al. (2019) summarised recent progress in understanding AMOC and the key processes which govern AMOC strength, structure and variability. They summarise that the upper kilometre shows northward flow of warm water, with the compensation of southward flow of colder North Atlantic Deep Water. Upper warm, less dense water transforms into deeper colder denser water in the North Atlantic subpolar region where buoyancy is lost. Response of the overturning to changes in wind stress and buoyancy fluxes takes place through boundary and Rossby waves. The location of RAPID at 26°N and Overturning in the Subpolar North Atlantic Programme (OSNAP) observational arrays comprises two legs: (i) one expanding from southern Labrador to the southwestern end of Greenland passing the entrance of the Labrador Sea (OSNAP West); (ii) the second leg from the southeastern end of Greenland to Scotland (OSNAP East).

Modern AMOC observational projects such as the Rapid Climate Change-Meridional Overturning Circulation and Heatflux Array (RAPID-MOCHA) set up in 2004 to monitor the AMOC across the Atlantic at 26°N has now observed the AMOC continuously for 14 years, and revealed greater variability than expected. The OSNAP observation system, launched in the summer of 2014, has been measuring the water flux conveyed by overturning in the high latitudes in the North Atlantic

(Lozier et al., 2019).

Regarding response to climate change, both model and observing studies suggest that the AMOC is slowing down which weakens the ocean transport of heat from the tropics to higher latitudes in the North Atlantic (Quadfasel, 2005; Jackson et al., 2015; Caesar et al., 2018, 2020; Bryden et al., 2005). The possible explanations for this weakening are due to the consequence of global warming introducing more fresh water into the polar and sub-polar Atlantic as well as warm upper waters invading further into the northern North Atlantic owing to northward shift of the Gulf Stream (Caesar et al., 2018; Srokosz and Bryden, 2015). Response in models is clear; while response in data is less robust given only 20 years of data.

For decadal variability, quasi-stochastic forcing by the atmosphere involving buoyancy fluxes and wind stress is an important driver of MOC variability (Drijfhout and Hazeleger, 2007; Ortega et al., 2017). The mechanism of AMOC decadal variability might be affected by the NAO decadal variability (Delworth and Zeng, 2016; Lozier et al., 2010). The study by Ortega et al. (2017) used Labrador Sea density as a precursor of the ocean circulation changes. The major drivers of Labrador Sea density variability are (i) local surface heat fluxes, associated with changes in the North Atlantic Oscillation (Gulev et al., 2013); (ii) multidecadal-to-centennial contributions from the Greenland–Scotland Ridge outflows and (iii) decadal trends in Labrador Sea densities associated with NAO variability. A major contributor to North Atlantic Deep Water (NADW) formation is the deep

convection found in the Labrador Sea (Haine et al., 2008), which can impact on the intensity of the deep western boundary current (DWBC). Modelling studies (e.g. Delworth et al. 1993; Eden and Willebrand 2001) suggest that Labrador Sea waters can influence both the AMOC and the subpolar gyre strength and hence affect decadal variability in the wider North Atlantic. However, the OSNAP measurements reveal strong variability of transport in the region and show that deep water formation in the Labrador Sea may not be the major determinant of AMOC variability (Lozier et al., 2019).

For AMOC variability, different physical processes drive changes in the AMOC. Previous studies revealed that the observed-derived AMOC may be represented as a sum of the geostrophic, Ekman, and external mode components (Lee and Marotzke, 1998; Hirschi and Marotzke, 2007; Buckley and Marshall, 2016). The Ekman component plays a major role on short timescales, whereas the geostrophic component controls on longer (interannual to decadal) timescales (Barrier et al., 2014; Buckley and Marshall, 2016). However, only a few studies explored AMOC variability on short-time scales. The Barrier et al. (2014) study demonstrated that there are opposing anomalies in AMOC over the subpolar and subtropical cells associated with the NAO, which was dominated by wind stress induced Ekman horizontal transport anomalies. Meanwhile, AMOC anomalies associated with different phases of the NAO were dominated by geostrophic transport linked to west-east boundary density contrasts (Lozier et al., 2010) on decadal-time scales. Hence, different physical origins drive AMOC changes on different timescales.

Chapter 3 and chapter 4 revealed that the jet stream wind strength and latitudes location impact on North Atlantic ocean surface to upper ocean heat anomalies. Temperature anomalies from surface to upper ocean associated with jet strength and latitude location lead to changes in ocean buoyancy anomalies on the ocean boundaries. Consequently, there are changes in meridional geostrophic transport. Jet stream strength and latitude shifts also affect surface wind stress patterns and strength which lead to Ekman meridional transport anomalies.

Therefore, in this chapter, the hypothesis is that the jet stream strength and latitude shifts variability affect AMOC mainly due to changes in Ekman transport driven by surface wind on a seasonal timescale. Meanwhile, changes in geostrophic transport provides a small contribution due to jet stream strength and latitude shifts altering changes in buoyancy anomalies in the west and east boundary.

In this chapter, I explore how the basin-scale AMOC cells respond to atmospheric jet stream strength and latitude variation from monthly to seasonal timescales using DePreSys3 ensemble model data in winter months from 1980 to 2014. The following questions are addressed:

(i) How do changes in atmospheric jet stream strength and latitude location affect wind-induced Ekman transport, consequently, affecting AMOC anomalies?

(ii) How does density contrast between east and west boundary impact meridional geostrophic transport, consquently affecting AMOC anomalies?

(iii) How does the surface wind stress anomaly drive Ekman meridional transport

influence on the AMOC variation?

5.2 Data

In order to calculate AMOC and ocean horizontal circulation, the two components of velocity (u, v) in winter months (DJF) were diagnosed over 75 depth levels from 40 ensembles for 1980 to 2014 from Met Office Hadley Centre DePreSys3 high resolution ($0.25° \times 0.15°$) ocean monthly ensemble data. Also ocean potential density ensemble data is employed to diagnose geostrophic transport due to the east-west density contrast, as well as buoyancy forcing across the basin and thermocline depth variation between high and low jet indices (see ocean data details in Appendix B).

From DePreSys3 hindcast atmospheric monthly ensemble data, jet stream speed and latitude indices are extracted from the mean zonal wind at 850hPa over the North Atlantic (the same method as used in Chapter 3); atmospheric 10 metre u and v components are applied to calculate wind stress and Ekman transport; sea level pressure is used to obtain the NAO index.

5.3 Calculating MOC and AMOC method

The meridional overturning circulation (MOC) refers to a streamfunction ψ for the zonally integrated meridional volume transport in depth coordinates. It

can be calculated from the following equation (see (Buckley and Marshall, 2016; Stepanov et al., 2016)):

$$\psi(y,z,t) = \int_{z}^{\eta} \int_{x_w}^{x_e} v(x,y,z,t)dxdz \tag{5.1}$$

Where:

η: is the height of the free surface

x: longitudinal (zonal) direction (+v eastward)

y: latitudinal (meridional) direction (+v northward)

z: height (+v upward), the vertical coordinate, z $<$ 0 with depth

t: time

x_w and x_e: are western and eastern boundaries, for AMOC, they are western and eastern boundaries of Atlantic.

v: meridional velocity component

ψ unit: Sv (1 Sv = 10^6 m^3 s^{-1}).

5.4 The effect of jet stream on AMOC

5.4.1 Composite analysis - the connection between jet stream strength and AMOC

The connection between jet indices and AMOC in the winter time based on DePreSys3 ensemble data is examined in this section. From 1980 to 2014 across

40 ensembles, for each winter month, the 50 meridional current velocity fields corresponding to the 50 highest jet speed states are selected then the mean is taken representing a mean meridional current during a strong jet state. Similarly, another 50 meridional current velocity ensembles corresponding to the 50 lowest jet speed states are chosen then the average is calculated indicating the mean meridional current during a weak jet state. These two strong and weak state meridional currents are taken to calculate the AMOC using equation (5.1) representing AMOC in strong and weak jet states, respectively (see Fig. 5.1).

From both the winter individual month January and winter DJF means, it is shown that with a strong jet stream state, the AMOC demonstrates a strong northward current from tropics up to subtropics latitudes and ceases about at 50°N above the 3500 m depth and maximum flow occurs over the tropics from equator to 15°N with 27 Sv to 32 Sv. The second maximum northward flow is located about 26°N with 27 Sv. The maximum streamfunction occurs at depth 1000m to 1500m and below the 2000m level the streamfunction dramatically decreases (see Fig. 5.1 a and c). The southward flow starts turning at 50°N penetrating into depth first, then until below 4000 m then parallel moving southward at about -3 Sv (see Fig. 5.1 a and c). During a weak jet state, the AMOC northward flow extends from the tropics up to 60°N. The maximum northward flow is about 22 Sv located over the tropics and at 40°N (see Fig. 5.1 b and d). And southward flow starts turning about at 60 °N penetrating into depth first, then until below 3500 m then parallel moving southward at about -3 Sv (see Fig. 5.1

b and d).

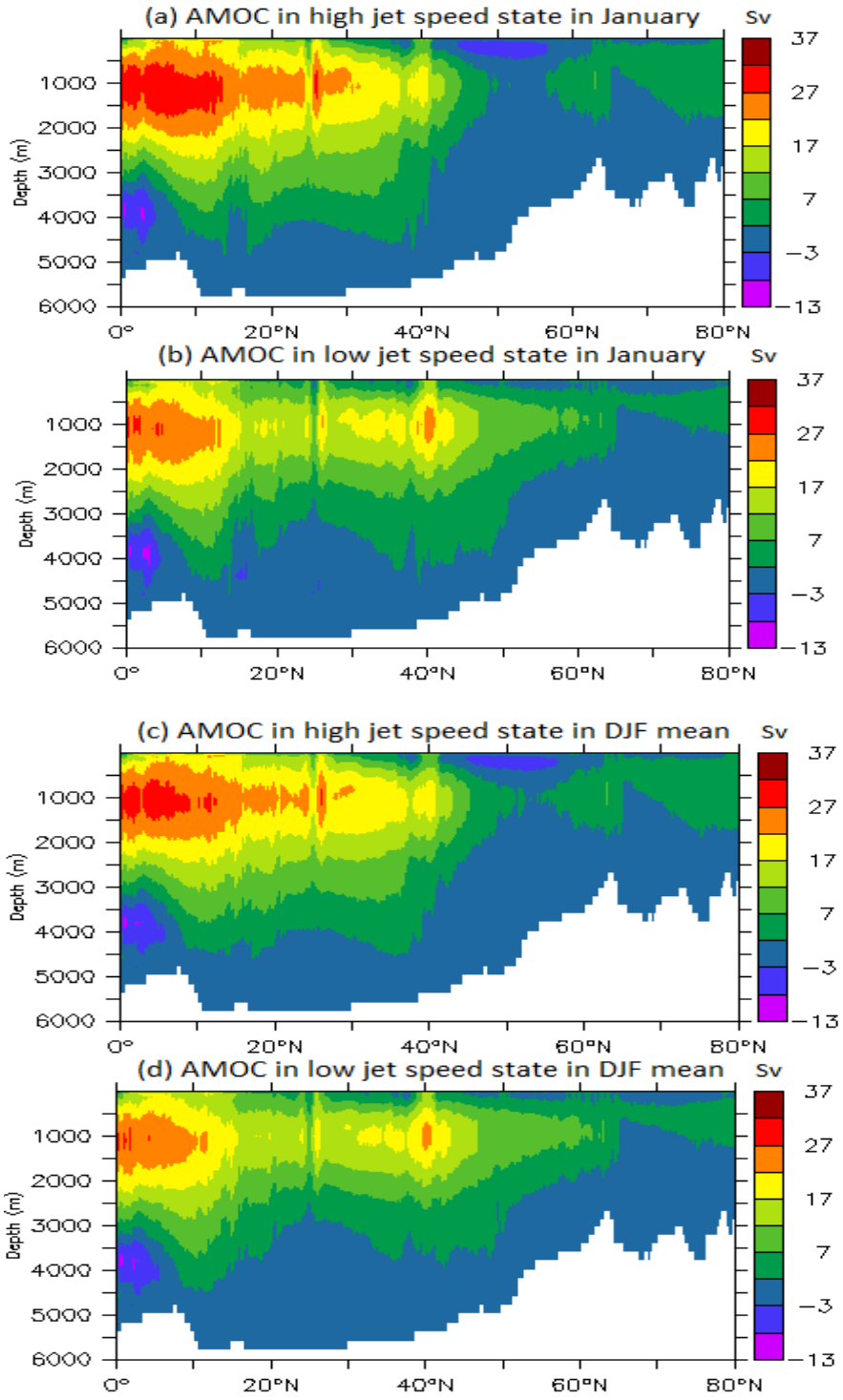

Figure 5.1: A composite mean of 50 January months across 1980 to 2014 from ensemble data of meridional overturning streamfunction during (a) the high jet speed state in January; (b) the low jet speed state in January; (c) the high jet speed state in DJF mean and (d) the low jet speed state in DJF mean. (units: Sv = 10^6 m^3 s^{-1}).

5.4.2 Composite analysis - the connection between jet stream latitude location and AMOC

In this section, the winter month January is chosen for a composite analysis to investigate the connection between jet stream latitude location and AMOC, since AMOC variability in all winter individual months and winter mean response to jet stream have very similar patterns.

The AMOC response to jet latitude shows the AMOC has similar structure but some different characteristics: (i) the magnitude of the AMOC northward transport is relatively weak compared to jet speed impact. During a more northward jet state, the AMOC strong northward transport occurs from equator to 13°N region of about 22 Sv. The second maximum occurs at 40°N in high jet latitude state; also a northward flow maximum of about 22 Sv occurs at 40°N (Fig. 5.2 a); (ii) during a low jet latitude, AMOC northward flow is stronger from equator to 13°N, and extends further north at 60°. Southward flow begins turning at 65° and below 4000 m and 3000m with -3 Sv magnitudes, respectively, associated with high and low latitude.

In next section, the anomalies of AMOC associated with strong and weak jet, or high latitude and low jet latitude are shown for a depth-latitude plane. Also the possible mechanisms will be explored in section 5.5.

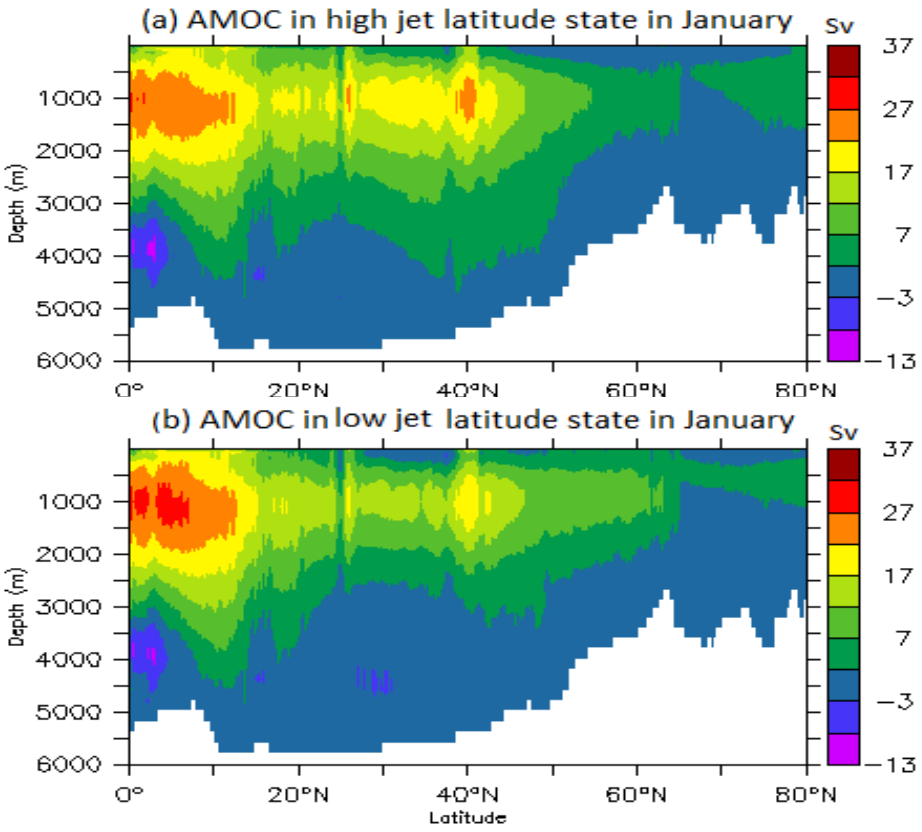

Figure 5.2: A composite mean of 50 months in January across 1980 to 2014 from ensemble data of meridional overturning streamfunction during (a) the high jet latitude state; (b) the low jet latitude state; during the low jet latitude state. (units: Sv = 10^6 m^3 s^{-1}).

5.4.3 The AMOC difference anomalies between high and low jet indices on the depth-latitude plane

The jet speed affects AMOC anomalies showing a tripole pattern on the depth-latitude plane (Fig. 5.3 a). Compared to a weak jet stream, a fast speed jet stream strengthens the northward transport from the equator to 37°N up to a maximum of 9 Sv anomalies at about 22°N to 25°N from the surface extending down to 3000

metres together with a weak signal penetrating down to 5000 metres. Over most of the subpolar gyre from 40°N to 60°N, the AMOC northward transport slows down by about -9 Sv anomalies. This AMOC weakening signal mainly occurs between the surface to 1500 metres, also with weaker anomalies between 3000 to 4000 metres. From 65°N to 80°N, there is a weak positive anomaly in the AMOC of about 3 Sv.

Jet stream latitude location affects the AMOC with a quadrupole pattern (Fig. 5.3 b). With high jet latitude, the tropics AMOC signal shows a weak negative anomaly, the rest of the three signal centres shift further north, in contrast to the effects of jet speed. The strong and extensive regional changes in AMOC occur over most of the subtropics from about 20°N to 50°N and the maximum anomaly is about 7 Sv located around 37°N to 40°N extending down to 4000 metres. The second largest anomalies signal is from around 60°N, about -6 Sv, penetrating to 2500 metres. The rest of the anomalies over the tropics and high latitude regions are weak, about 1 to 2 Sv only and only remain in the surface to the 1500 metre region.

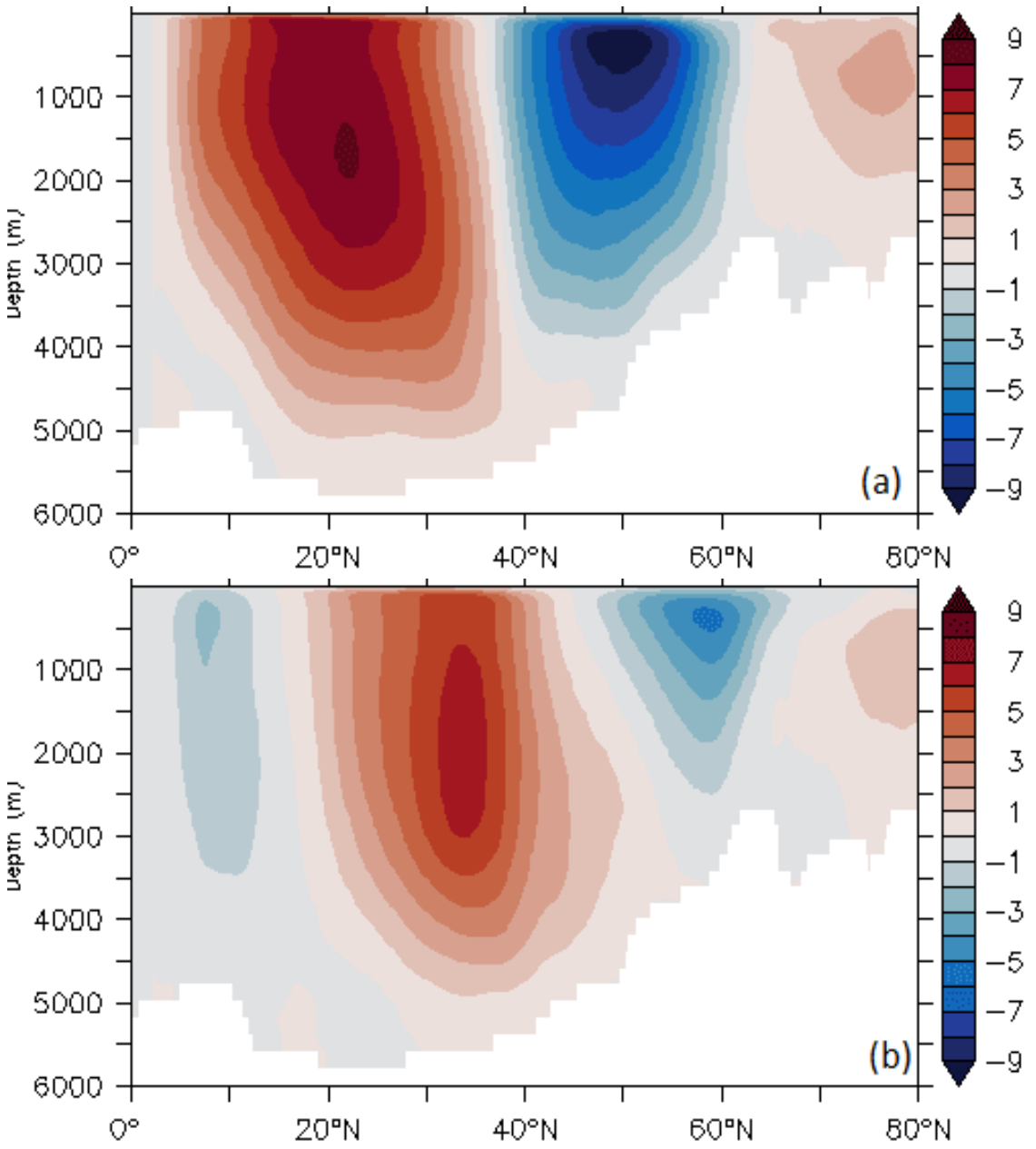

Figure 5.3: Meridional overturning streamfunction difference anomalies between a composite of 50 January months across 1980 to 2014 from ensemble data of (a) the highest jet speed minus that for the lowest jet speed and (b) the highest jet latitude minus that for the lowest jet latitude. (units: Sv = 10^6 m^3 s^{-1}).

5.5 Possible mechanism of AMOC anomalies associated with jet speed and latitude changes

5.5.1 Changes in surface zonal wind stress induced meridional Ekman transport

Previous studies find that AMOC variability on seasonal and intra-annual timescales is mainly influenced by local wind forcing (Buckley and Marshall, 2016; Barrier et al., 2014). While, on interannual to decadal timescales, AMOC changes are primarily dominated by geostrophic transport related to buoyancy anomalies on the western and eastern boundary (Lozier et al., 2010; Buckley and Marshall, 2016).

In my study, how are the AMOC variations associated with the atmospheric jet strength and latitude location focused on a seasonal timescale? Hence, in this section, the hypothesis of linkage between changes in surface wind stress induced Ekman transport variability associated with jet speed strength and latitude location is examined. Before the AMOC is decomposited into different components, first step, how the surface zonal wind stress induced Ekman transport drives meridional transport is examined in this section.

Compared to the climatological mean, the magnitude of Ekman horizontal transport from the ensemble data is enhanced over most of the subpolar and subtropical region, reaching over respectively ±2 to ±3 m^2 s^{-1} during the strong jet state and high latitude jet phase where eastward and westward zonal wind stress are enhanced (Fig. 5.4 a, c). Meanwhile, the maximum Ekman southward volume transport around -3 m^2 s^{-1} occurs at about 50°N during a strong jet compared to a weak jet (Fig. 5.4 a, b, e), and at about 60°N during a more northward jet compared to a southward jet (Fig. 5.4 c, d, f). Meanwhile, the maximum northward Ekman volume transport occurs at about 20°N due to an enhanced trade wind during a strong jet compared to a weak jet, and about 37°N during a more northward jet than a southward jet. Coriolis parameter f is defined as $f = 2\Omega \sin(\varphi)$, Ω is Earth's rotation rate, φ is latitude. f is 0 at the equator, and f increases with increasing latitude. In order to show middle latitude Ekman transport, $V_x = \frac{\tau_y}{\rho_0 f}$ and $V_y = -\frac{\tau_x}{\rho_0 f}$ features associated with the impact of jet speed and latitude shifts, the transport is masked out below 5°N in Fig. 5.4. Noticeably, the weak jet stream affects zonal wind and Ekman horizontal transport weakly over the middle latitude domain; whereas, a southward latitude jet enhances northward transport over the west subtropical gyre with relatively weak magnitudes less than 2 m^2 s^{-1} (Fig. 5.4 d).

Overall, a strong jet enhances southward Ekman transport over most of the subpolar gyre and strengthens northward transport over the subtropical gyre due to surface zonal wind stress being enhanced in these regions. A more northward jet

has a similar effect but anomalies signals shift further north and with relatively weak magnitudes compared to jet speed impact.

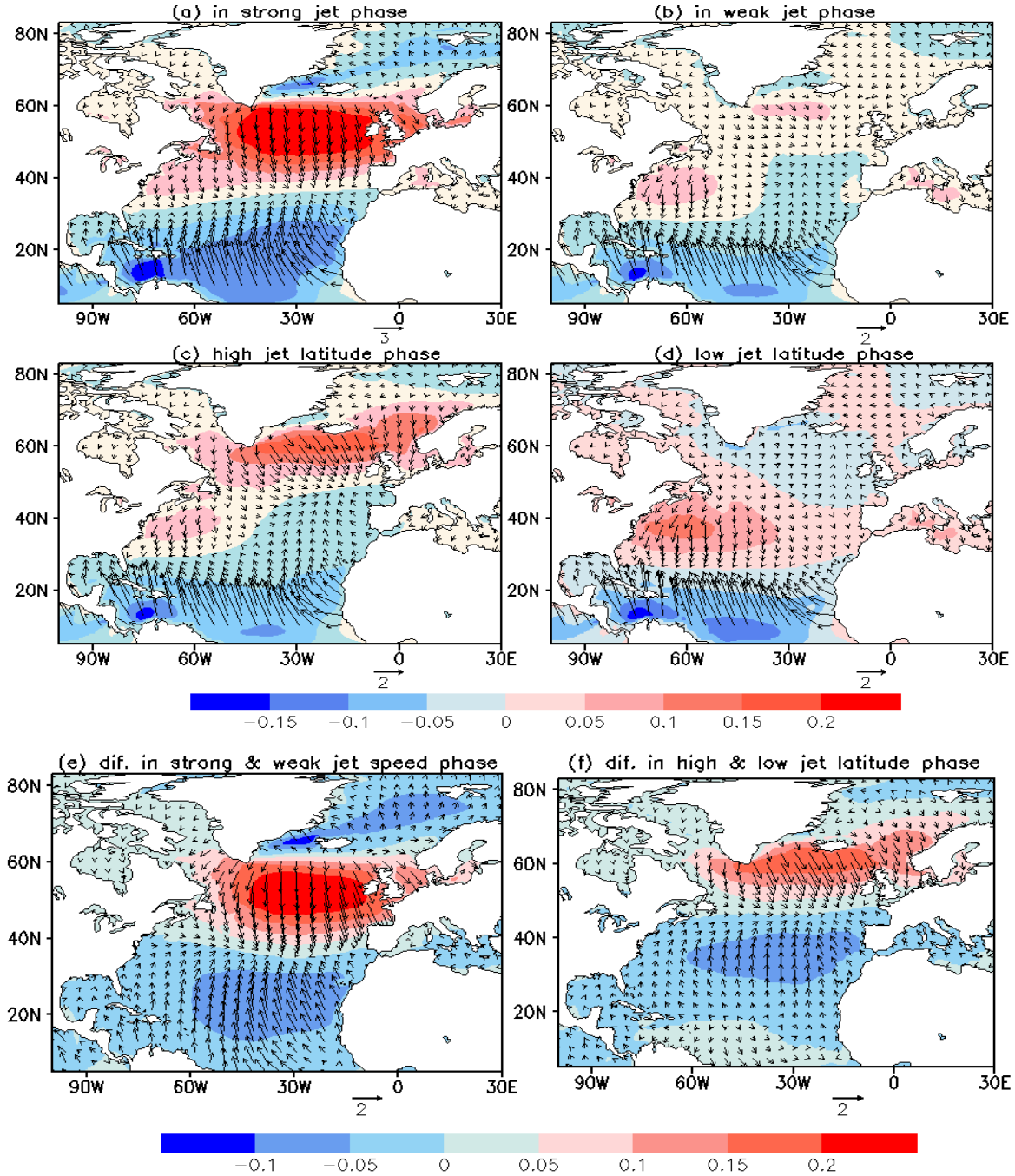

Figure 5.4: A composite mean of 50 January months across 1980 to 2014 from ensemble data of Ekman horizontal volume transport (vectors, units: $m^2\ s^{-1}$) and zonal wind stress component based on 10m wind field (shaded colour, units: $N\ m^{-2}$, the positive means eastward, the negative means westward) during (a) high jet speed state, (b) low jet speed state, (c) high jet latitude state, and (d) low jet latitude state; Ekman horizontal volume transport and Ekman vertical velocity difference between a composite of 50 January months of (e) the highest jet speed minus that for the lowest jet speed and (f) the highest jet latitude minus that for the lowest jet latitude.

The Ekman transport ψ_{EK} is calculated from the zonal wind stress τ_x as in equation (5.2) (Stepanov et al., 2016).

$$\psi_{EK} = -\int_{x_w}^{x_e} \frac{\tau_x}{\rho_0 f} dx \tag{5.2}$$

where x_w and x_e are western and eastern boundaries; τ_x is the zonal wind stress; ρ_0 is a reference density for seawater and f is the Coriolis parameter. Coriolis parameter f is defined as $f = 2\Omega \sin(\varphi)$. f is zero at the equator so that ψ_{EK} is infinite at the equator. Hence, ψ_{EK} is excluded from equator to 5°N.

Comparing the differences of zonal mean wind stress, Ekman meridional transport and AMOC between strong and weak jet strength over the North Atlantic, a maximum westward zonal mean wind stress anomaly of about -0.06 N m^{-2} occurs around 23°N (Fig. 5.5 a) where a maximum northward Ekman transport is about 9 Sv (Fig. 5.5 b) at 50°N, and where meridional streamfunction (represents AMOC) maximum northward strengthening is about 9 Sv (Fig. 5.5 c). Over the subpolar gyre, a maximum eastward zonal mean wind stress around 0.2 N m^{-2} is located at about 50°N where a maximum southward Ekman transport reaches about -8 Sv (Fig. 5.5 c).

The same mechanism is held for the connection between AMOC anomalies and wind stress induced meridional Ekman transport anomalies associated with high and low jet latitudes (Fig. 5.5 d to f). However, the anomalies pattern shifts further north and with relatively weaker magnitudes. Compared to a southward

shifted jet, a more north jet causes AMOC strengthening of about 7 Sv over the subtropical, where Ekman northward transport contributes about 5 Sv. Over the subpolar gyre, Ekman southward transport is about 5 Sv and the AMOC weakening is about 6 Sv during a northward shifted jet compared to a southward shifted jet.

In summary, on a seasonal timescale, jet stream speed strength affects AMOC more robustly than do jet latitude shifts. Surface zonal wind stress anomalies due to jet stream impact inducing surface meridional Ekman transport is fully predominant for changes in AMOC strengthening over the subtropics and 90% of AMOC weakening over the subpolar gyre is associated with jet speed strength. Ekman meridional transport is also a significant contribution, about 80%, for changes in AMOC associated with jet latitude shifts. The AMOC anomalies associated with the jet stream in this study are similar to the AMOC anomalies pattern associated with the NAO according to the study by Barrier et al. (2014). As concluded above, most of the AMOC anomalies are explained by surface wind stress induced Ekman meridional transport. However, mass transport is not fully conserved when the surface Ekman meridional transport contributions to the AMOC anomalies are taken into account. Thus, in the next section, the AMOC dynamical decomposition is performed to explore the mechanisms for changes in meridional transport from interior, such as, surface Ekman transport plus its barotropic flow below the Ekman layer, geostrophic transport link to the density contrast between west-east boundary and bottom velocity contribution (Lee and

Marotzke, 1998; Hirschi and Marotzke, 2007; Buckley and Marshall, 2016).

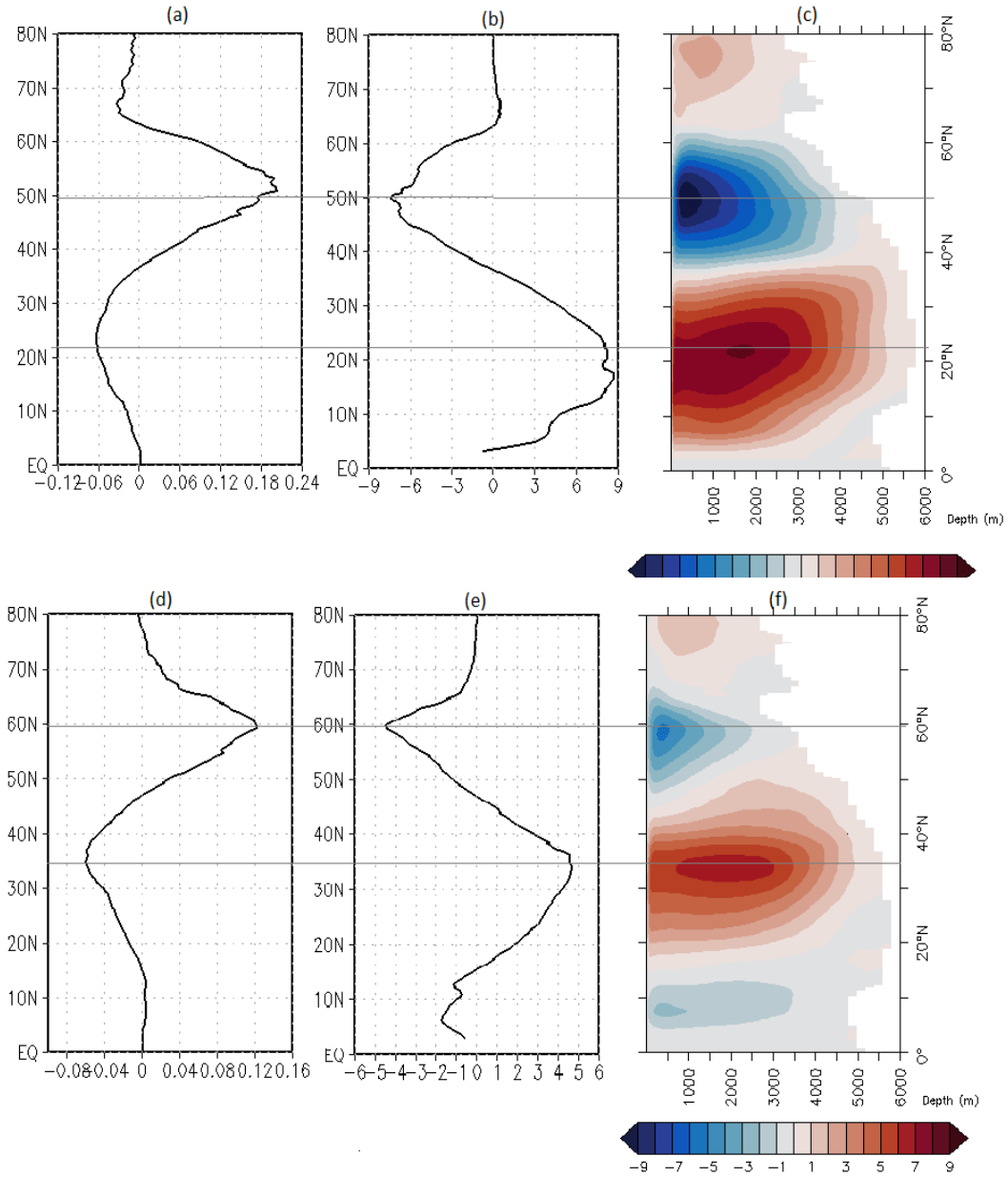

Figure 5.5: The differences between a composite of 50 January months across 1980 to 2014 from ensemble of the highest jet speed minus that for the lowest jet speed for (a) zonal mean wind stress over the North Atlantic (x-axis is wind stress units: N m^{-2}, y-axis is latitude °N); (b) Ekman meridional volume transport over the North Atlantic ($\psi_{EK} = -\int_W^E \frac{\tau_x}{\rho_0 f} dx$, x-axis is volume transport, units: Sv, y-axis is latitude °N); (c) Meridional overturning streamfuncton (shaded colour, units: Sv, x-axis is ocean depth, units: metres, y-axis is latitude °N). The differences between a composite of 50 January months of the highest jet latitude minus that for the lowest jet latitude for; (d) zonal mean wind stress over the North Atlantic (x-axis is wind stress units: N m^{-2}, y-axis is latitude °N); (e) Ekman meridional volume transport over the North Atlantic (x-axis is volume transport, units: Sv, y-axis is latitude °N); (f) Meridional overturning streamfuncton (represented by shaded colour, units: Sv, x-axis is ocean depth, units: metres, y-axis is latitude °N).

5.5.2 Dynamical Decomposition of the AMOC

The AMOC can be decomposed into Ekman and thermal wind/geostrophic components by separating the meridional velocity $v = v_g + v_{ek}$ (Hirschi et al., 2003; Buckley and Marshall, 2016). The Ekman component is associated with the wind stress, and the thermal wind component is related to density contrast anomalies on the ocean boundaries. The vertical shear in v_g can be calculated from the density field ρ using hydrostatic balance and the vertically integrated thermal wind relation from the sea bottom:

$$\begin{aligned} \int_{-H}^{z} \frac{\partial v}{\partial z} dz &= \int_{-H}^{z} -\frac{g}{\rho_0 f} \frac{\partial \rho}{\partial x} dz \quad (a) \\ v_g(z) - v_g(-H) &= -\frac{g}{\rho_0 f} \int_{-H}^{z} \frac{\partial \rho}{\partial x} dz \quad (b) \\ v_g(z) &= -\frac{g}{\rho_0 f} \int_{-H}^{z} \frac{\partial \rho}{\partial x} dz + v_g(-H) \quad (c) \\ v_b &= v_g(-H) \end{aligned} \tag{5.3}$$

Generally, the geophysical flows are vertically structured by separating the flow into a depth-independent component, typically referred to as barotropic, and depth-dependent component, referred to as baroclinic.

Hence, in Eq.(5.3 c), geostrophic flow $v_g(z)$ separates into a depth-dependent component and a depth-independent component. The depth-dependent component is the first term - $\frac{g}{\rho_0 f} \int_{-H}^{z} \frac{\partial \rho}{\partial x} dz$ on the right hand side, which describes baroclinic flow, hereafter named v_{sh}. The depth-dependent component represents shear consisting largely of thermal wind shear balanced by zonal density gradients. The

second component of the right hand side v_b is the depth-independent component which is geostrophic flow at the bottom, v_b, which is a barotropic flow. Actually, it is difficult to measure the geostrophic flow at the ocean bottom.

Hence, the meridional velocity y (x, y, z) is locally decomposed into three dynamical components (reference Lee and Marotzke (1998)):

$$\begin{aligned} v(x,y,z) &= \overline{v} + [v_{ek}(x,y,z) - \overline{v}_{ek}] + v_{sh}(x,y,z) \quad (a) \\ \overline{v} &= \frac{1}{H}\int_{-H}^{0} v(x,y,z)dz \quad (b) \\ \overline{v}_{ek} &= \frac{1}{H}\int_{-H}^{0} v_{ek}(x,y,z)dz \quad (c) \end{aligned} \tag{5.4}$$

In theoretical and modeling studies, the usual approach is to consider the depth-independent flow as the depth-averaged flow, $\overline{v}$, and the departure from the vertical average, v' as the depth-dependent component (Peña-Molino et al., 2014), which is v_{sh} in the Eqs.(5.4) and (5.5). In Eq.(5.4) (a), on the right hand side, the first component is the depth-averaged meridional flow. It expresses the external mode (or barotropic flow) which is influenced by bottom topography, and frictional effects. The external mode impacts the meridional overturning circulation in terms of of zonally nonuniform topography and frictional effects at the ocean boundaries (Lee and Marotzke, 1998). The second component is Ekman flow minus its depth average, i.e., subtracts its projection onto the external mode (note that the external mode includes the vertical average of v_{ek}). Hence, this refers to the surface Ekman flow and its barotropic compensation below the Ekman layer. The third component is vertical shear including mostly of thermal wind shear which is proportional to zonal density gradients and a small ageostrophic shear

associated with friction and nonlinear effects. Notably, this component also sums up to zero over depth because its depth average has been included in the external mode. H is oceanic bottom depth (is a function of x and y) (Lee and Marotzke, 1998). It is difficult to break up thermal wind and ageostrophic shear due to the existence of topography (Lee and Marotzke, 1998). Hence, this study takes the vertical shear as a thermal wind component of the meridional overturning transport. Geostrophic bottom velocity component v_b (the second term in Eq.(5.3 c) right side) has been included in the external mode (Marotzke et al., 1999).

A stream function can then be computed by integrating equation (5.4) zonally and vertically, the MOC ψ is decomposed into three different contributions associated with the barotropic (depth averaged) velocities $\overline{v}$ contribution, it describes external mode; to the geostrophic shear v_{sh}, and to Ekman transports v_{ek} (Lee et al., 1997; Hirschi and Marotzke, 2007; Moreno-Chamarro et al., 2017):

$$\begin{aligned}\psi(z) &= \psi_{ex}(z) + \psi_{sh}(z) + \psi_{ek}(z) \\ &= \int_{-H}^{z} dz \int_{x_w}^{x_e} \overline{v} dx + \int_{-H}^{z} dz \int_{x_w}^{x_e} v_{sh} dx + \int_{-H}^{z} dz \int_{x_w}^{x_e} (v_{ek} - \overline{v}_{ek}) dx\end{aligned} \tag{5.5}$$

where x_w and x_e are the western and eastern limits of the basin, respectively, and H is the oceanic bottom depth (-H $\leq z \leq$ 0).

The first right-hand term in Eq.(5.5) contributes to the MOC in the presence of topography and friction effects at the ocean boundaries which is described as the external mode. The last component is the Ekman meridional transport forced by the zonal wind stress; it is assumed to occur in the upper ocean and compensated by its barotropic flow. Ekman velocity v_{ek} is derived from the theoretical relation

(Hirschi and Marotzke, 2007):

$$v_{ek} = -\frac{1}{\rho_0 f L D_{ek}} \int_{x_w}^{x_e} \tau_x dx \tag{5.6}$$

Where ρ_0, f, L, τ_x and D_{ek} are a reference density, the Coriolis parameter, the basin width at the surface, the zonal wind stress and Ekman layer thickness, respectively. It is assumed that the Ekman transport occurs in a layer of thickness D_{ek} and is compensated by a barotropic return flow:

$$\overline{v}_{ek} = -\frac{1}{\rho_0 f A} \int_{x_w}^{x_e} \tau_x dx \tag{5.7}$$

where A is the total area of the basin longitude–depth section. This assumes that the density across the basin does not adjust quickly enough to alterations in the wind field to permit baroclinic compensation. By integrating $[v_{ek} - \overline{v}_{ek}]$ zonally and vertically, the Ekman contribution to the MOC ($\psi_{ek}(z)$) is obtained which is the third component in Eq.(5.5).

The second component is the vertical shear largely associated with the thermal wind shear balanced by zonal density gradients, which is the first term on the right hand side in Eq.(5.3) (c). For a flat-bottomed ocean, zonal integration of the thermal wind shear is directly proportional to the density difference between the eastern and western boundaries (Marotzke et al., 1999). The relation is shown as follows:

$$\int_W^E \frac{\partial v}{\partial z} dx = -\frac{g}{\rho_0 f} \int_W^E \frac{\partial \rho}{\partial x} dx = -\frac{g}{\rho_0 f} (\rho_E - \rho_W), \tag{5.8}$$

Dividing the right-hand side of Eq.(5.8) by the basin width $L(z)$ and integrating vertically from bottom to z produces a thermal wind meridional velocity com-

ponent:

$$v_{sh}(x,z) = -\frac{g}{\rho_0 f}\int_{-H}^{z}\frac{1}{L(z)}(\rho_E - \rho_W)dz \tag{5.9}$$

We obtain the thermal wind shear velocity contribution to the AMOC by integrating Eq.(5.9) zonally and vertically, which is the second component in Eq.(5.5).

The dynamical decomposition of AMOC anomalies is performed on the composite mean of a composite of 50 January months across 1980 to 2014 ensemble data of the highest jet speed minus that for the lowest jet speed. According to Ekman transport and geostrophic transport definitions, the transport from equator to 5°N is masked out due to the Coriolis parameter f being zero at the equator.

Total streamfunction variation for the high versus low jet speed is dominated by two Ekman component cells at 20°N and 50°N (Fig. 5.6 and Fig. 5.7). The north cell shows strong southward transport of about 9 Sv driven by a strong westerly wind (Fig. 3.2 a) and strong zonal wind stress (Fig. 5.4 a, Fig. 5.5 a) during a strong jet stream crossing the ocean. The south cell indicates strong northward flow of about 8 Sv driven by a strong trade wind and strong easterly wind stress. Both Ekman cells are linearly decreased by their barotropic compensation underneath the surface with depth (Lee and Marotzke, 1998; Hirschi and Marotzke, 2007).

Vertical shear (thermal wind and ageostrophic shear) mainly provides a small contribution above 2000 m over most of the subtropical gyre, it takes about 20% of the total AMOC variability about 2 Sv associated with jet speed on this

timescale due to east-west boundary density contrast Fig. 5.6 c. Below 2000 m, zonal E-W boundary density contrast variation is too little to drive AMOC variations.

The external mode provides a minor role of about only 0.4 Sv accounting for up to a 4% contribution to the total AMOC variation (Fig. 5.6 d).

The sum of the components of Ekman, thermal wind vertical shear and external mode are consistent with the AMOC in terms of changes in strength and location (Fig. 5.6 e). One noticeable difference is the maximum northward transport of the AMOC south cell showing at about 1500m depth. Whereas, the sum of the components of AMOC shows the maximum northward transport near the surface due to the three components' anomalies mostly taking place over the upper ocean. The reason for the difference may be because the three components are based on the assumption of a flat-bottomed ocean with constant depth of 6000m. Also the short timescale in this study for these jet anomalies leads to a dominant Ekman response. Ekman transport mainly occurs at the surface Ekman layer.

Again, the AMOC decomposition components contributions patterns for AMOC anomalies associated with jet latitude have similar effects and contribution compared to jet speed counterparts but further north shifted and with relatively weaker signals (see Fig. 5.7).

The decomposition of AMOC components analysis evidence shows that Ekman flow plus its barotropic compensation can explain a large part of the variations

about 90 to 100% in overturning anomalies responding to jet stream speed strength and latitude shifts on seasonal timescales.

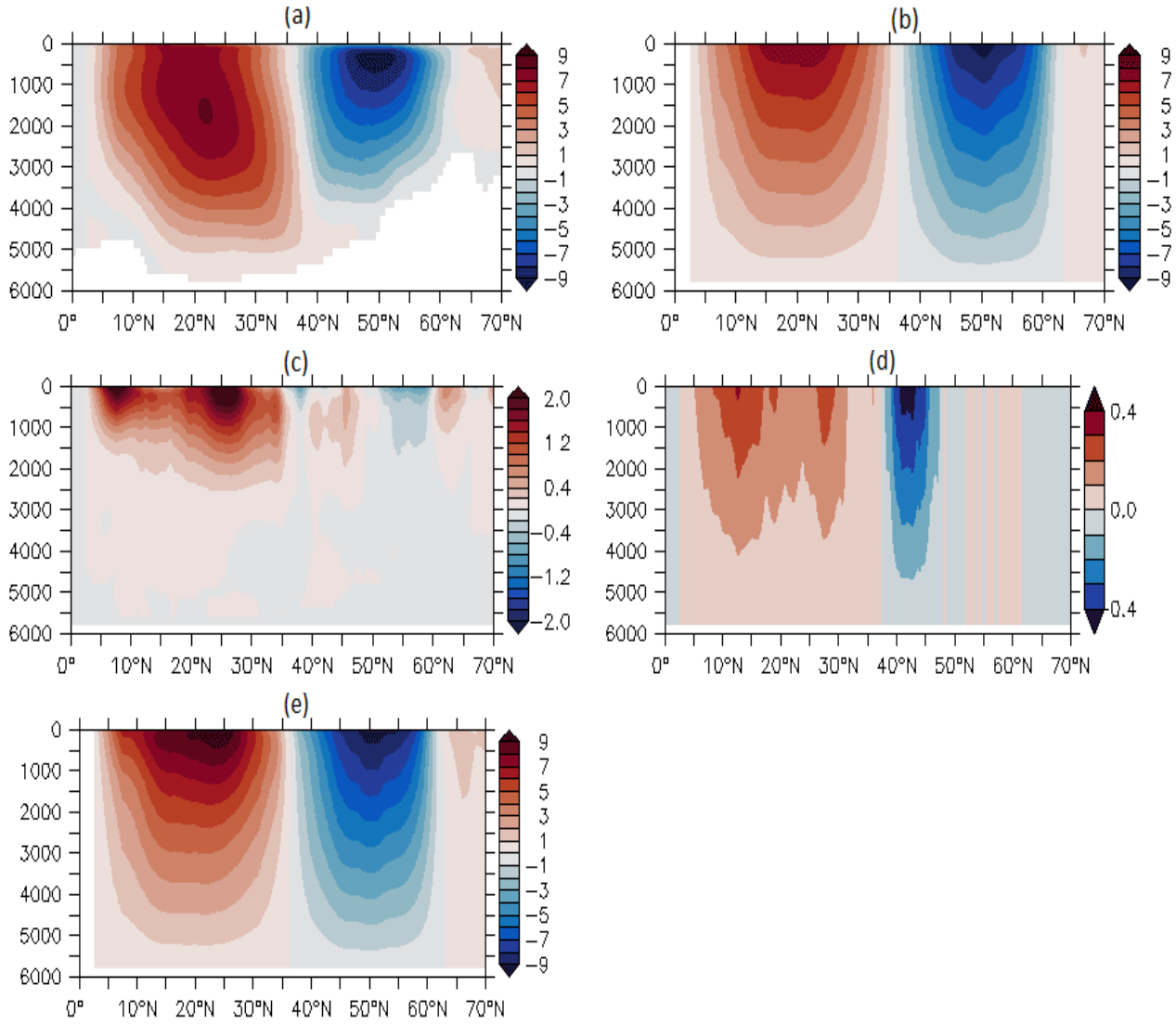

Figure 5.6: North Atlantic Meridional Overturning Circulation (AMOC) decomposition components anomalies between a composite of 50 January months across 1980 to 2014 ensemble data of the highest jet speed minus that for the lowest jet speed: (a) meridional streamfunction anomalies; (b) Ekman contribution; (c) thermal wind contribution; (d) contribution from the external mode; (e) sum of Ekman, thermal wind shear, external mode transport (represented by shaded colour, units: Sv, y-axes are ocean depth, units: metres, x-axes are latitudes.)

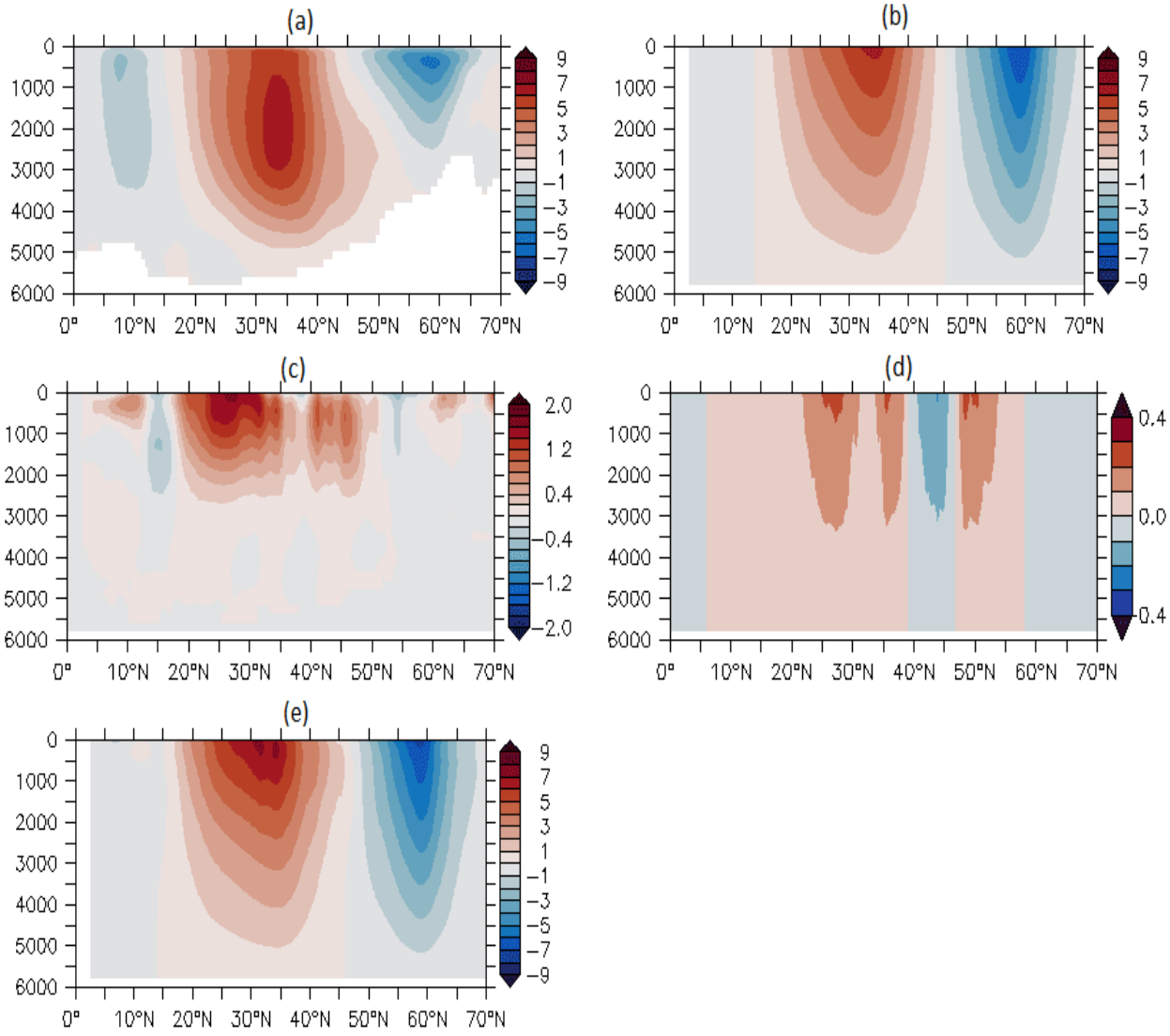

Figure 5.7: North Atlantic Meridional Overturning Circulation (AMOC) decomposition components anomalies between a composite of 50 January months across 1980 to 2014 ocean high resolution ensemble data of the highest jet latitude minus that for the lowest jet latitude: (a) meridional streamfunction anomalies;(b) Ekman contribution; (c) thermal wind contribution; (d) contribution from the external mode; (e) sum of Ekman, thermal wind shear, external mode transport (represented by shaded colour, units: Sv, y-axes are ocean depth, units: metres, x-axes are latitudes.)

5.6 Changes in ocean Sverdrup balance and barotropic flow

5.6.1 Sverdrup balance relation to wind in response to the jet indices

According to my study in chapter 3 and section 5.5 in this chapter, it has been found that a strong jet or more northward jet enhances Ekman pumping over the subtropics and Ekman suction over the subpolar. Also the wind stress induced Ekman transport associated with the jet stream causes the AMOC anomalies.

In this section, how are the changes in Sverdrup transport over the subtropical and subpolar gyres associated with jet speed and latitude variation?

Thus, according to the Sverdrup balance relation, firstly, how the response of the curl of the surface wind stress to the jet speed and latitude variation is checked. Secondly, the response of the depth-integrated meridional transport to the jet is examined. The Sverdrup relation is introduced as follows (referenced from Marshall and Plumb, 2008):

$$\begin{aligned} \beta V &= \frac{1}{\rho_0}\left(\frac{\partial \tau_{wind_x}}{\partial x} - \frac{\partial \tau_{wind_y}}{\partial y}\right) \\ &= \frac{1}{\rho_0}\hat{z}\cdot\nabla\times\tau_{wind} \end{aligned} \tag{5.10}$$

where,

$$V = \int_{-D}^{0} v dz \tag{5.11}$$

Eq.(5.10) is known as the Sverdrup relation and relates the vertically-integrated meridional flow to the curl of the wind stress. The key assumption for this relation is that the Rossby number $\frac{U}{fL}$ must be $\ll 1$. And also flow in the deep ocean must be fairly small so that fractional stress on the ocean bottom and vertical motion can be negligibly small (Marshall and Plumb, 2008). The depth integrated flow must be horizontally non-divergent so that we can introduce streamfunction Ψ:

$$U = -\frac{\partial \Psi}{\partial y}; V = \frac{\partial \Psi}{\partial x} \tag{5.12}$$

Sverdrup theory indicates that df/dy, β, is balanced by thickness changes (dw/dz). Replace V in Eq. (5.12) with the V in Eq. (5.10) and integrating westward from the eastern boundary, at the eastern boundary we set $\Psi = 0$ (no transport via the eastern boundary), then we have streamfunction based on curl of wind stress:

$$\Psi(x, y) = \frac{1}{\rho_0 \beta} \int_{east}^{x} \quad _{boundary} \hat{z} \cdot \nabla \times \tau_{wind} dx \tag{5.13}$$

Eq. (5.13) is very important to predict the ocean gyre circulation and volume transport. For example, negative wind stress curl over the subtropical gyre indicates that $\Psi(x, y)$ is positive over the subtropical gyre due to a minus sign being added as a result of being zonally-integrated from east to west. Positive $\Psi(x, y)$ means a clockwise circulation over the subtropical gyre, which means an equatorward volume transport in the gyre interior (Fig. 5.9 a and e for example).

Over the subtropical gyre, a strong or more northward jet stream enhances westward wind stress curl of about up to -0.2 $\times 10^{-6}$ N m^{-3} (Fig. 5.8 a and e). Consequently, the negative curl is consistent with southward flow in the interior (see black arrow in Fig. 5.9), that is positive values of Sverdrup streamfunction Ψ. The southward flow is of about 40 Sv during a strong jet and anomalies of about 30 Sv when the transport corresponds to a strong jet minus that for a weak jet. Positive Ψ means clockwise circulation. Oppositely, over the subpolar, where the positive curl is about 0.5 $\times 10^{-6}$ N m^{-3} consistent with northward flow in the interior, that is negative values of Ψ about -80 Sv during a strong jet and anomalies are about -30 Sv. Negative Ψ means anticlockwise circulation. Similarly, a more north jet stream offers a similar contribution for Sverdrup transport but whole signals shift further north and with weaker magnitudes.

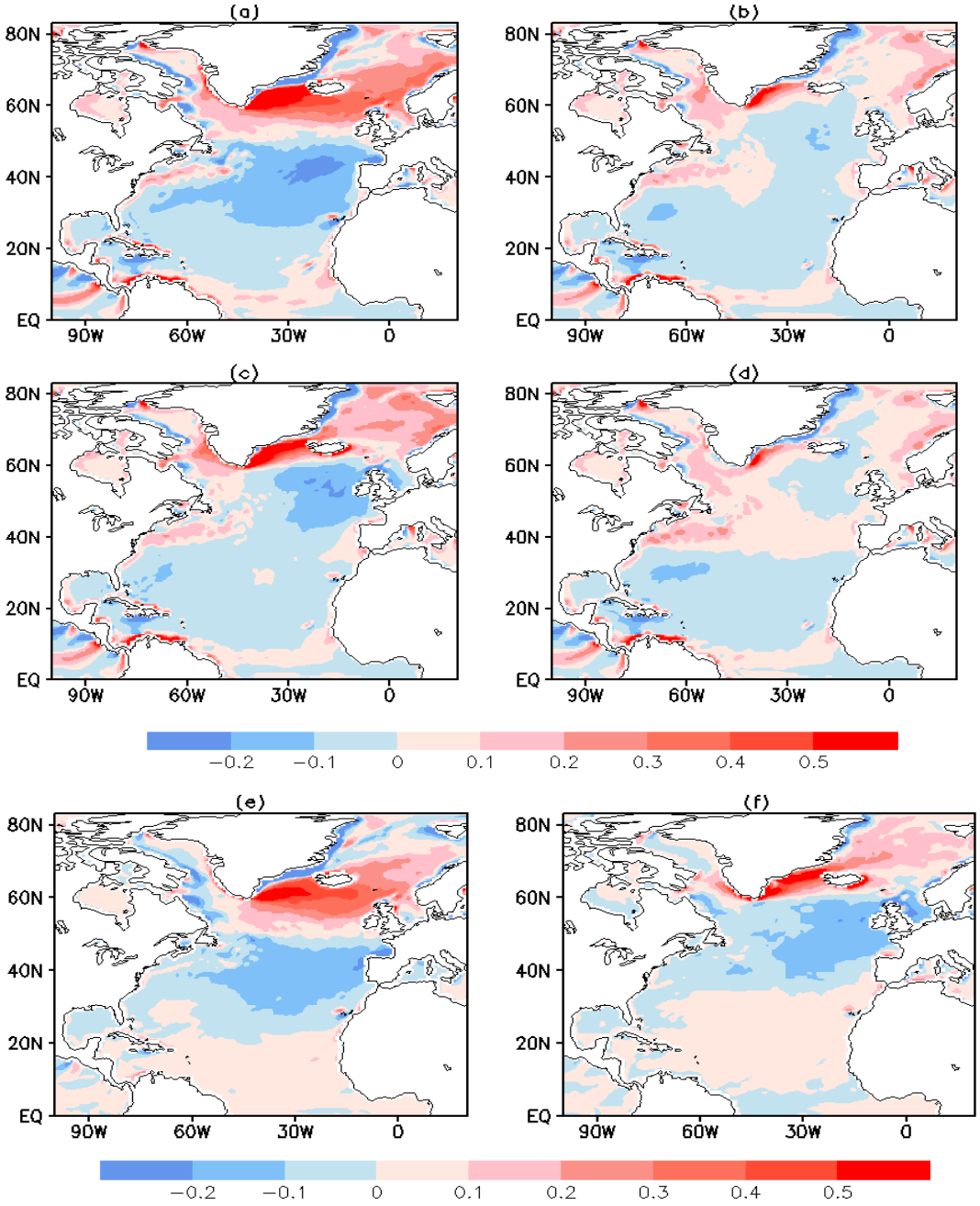

Figure 5.8: A composite mean of 50 January months across 1980 to 2014 from ensemble data of wind stress curl based on 10m wind field (shaded colour, units: 10^{-6} N m^{-3}), the positive means cyclonic circulation, the negative means anticyclonic circulation during (a) high jet speed state, (b) low jet speed state, (c) high jet latitude state, and (d) low jet latitude state; curl difference between a composite of 50 January months of (e) the highest jet speed minus that for the lowest jet speed and (f) the highest jet latitude minus that for the lowest jet latitude. Units: Sv

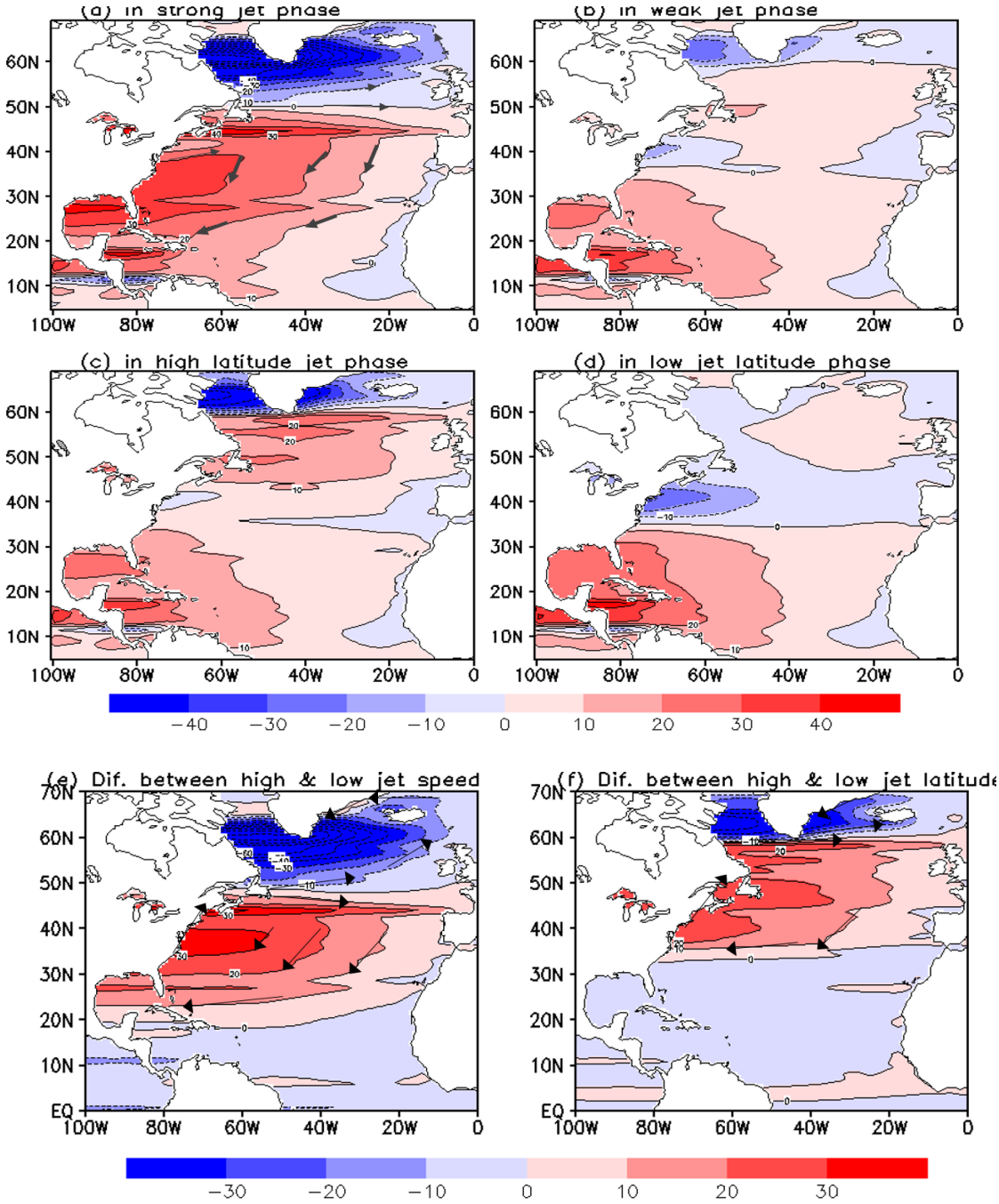

Figure 5.9: A composite mean of 50 January months across 1980 to 2014 from ensemble data of Sverdrup streamfuction Ψ, which is integrated wind stress curl westward from the eastern boundary (shaded colour, units: Sv = 10^6 m^3 s^{-1}), the positive means clockwise Sverdrup circulation, the negative means anticlockwise Sverdrup circulation) during (a) high jet speed state, (b) low jet speed state, (c) high jet latitude state, and (d) low jet latitude state; difference of Ψ between a composite of 50 January months of (e) the highest jet speed minus that for the lowest jet speed and (f) the highest jet latitude minus that for the lowest jet latitude.

When Eq.(5.11) is integrated zonally from east boundary to west boundary, the relation is written as follows (referenced from Marshall and Plumb (2008)):

$$\Psi(x,y) = \int_{x_{eastern}}^{x_{western}} {}^{boundary}_{boundary} V dx \tag{5.14}$$

The interior Sverdrup transport of the gyre is balanced by return meridional flow in the boundary currents. The southward flow in the interior over the subtropical gyre driven by negative wind stress curl in Fig. 5.9 is balanced by strong northward west boundary flow (directly calculated from meridional velocity) with equal magnitudes, such as the Gulf Stream in Fig. 5.10. Besides, a strong or more north jet enhances subtropical circulation which we can see from positive $\Psi(x,y)$ anomalies from both Fig. 5.9 e and f and Fig. 5.10 e and f.

However, northward flow in the interior over the subpolar gyre driven by positive wind stress curl is not balanced by southward boundary flow. Over the subpolar gyre, the wind stress curl induced anticlockwise circulation in the interior is associated with a strong jet showing much stronger north transport of about -80 Sv in Fig. 5.9 a compared to depth-integrated meridional return flow of about -40 Sv in Fig. 5.10. Meanwhile, from depth-integrated meridional flow anomalies in Fig. 5.9 e and f, the subpolar gyre circulation does not respond to changes in the jet speed and latitude (see Fig. 5.10 e and f).

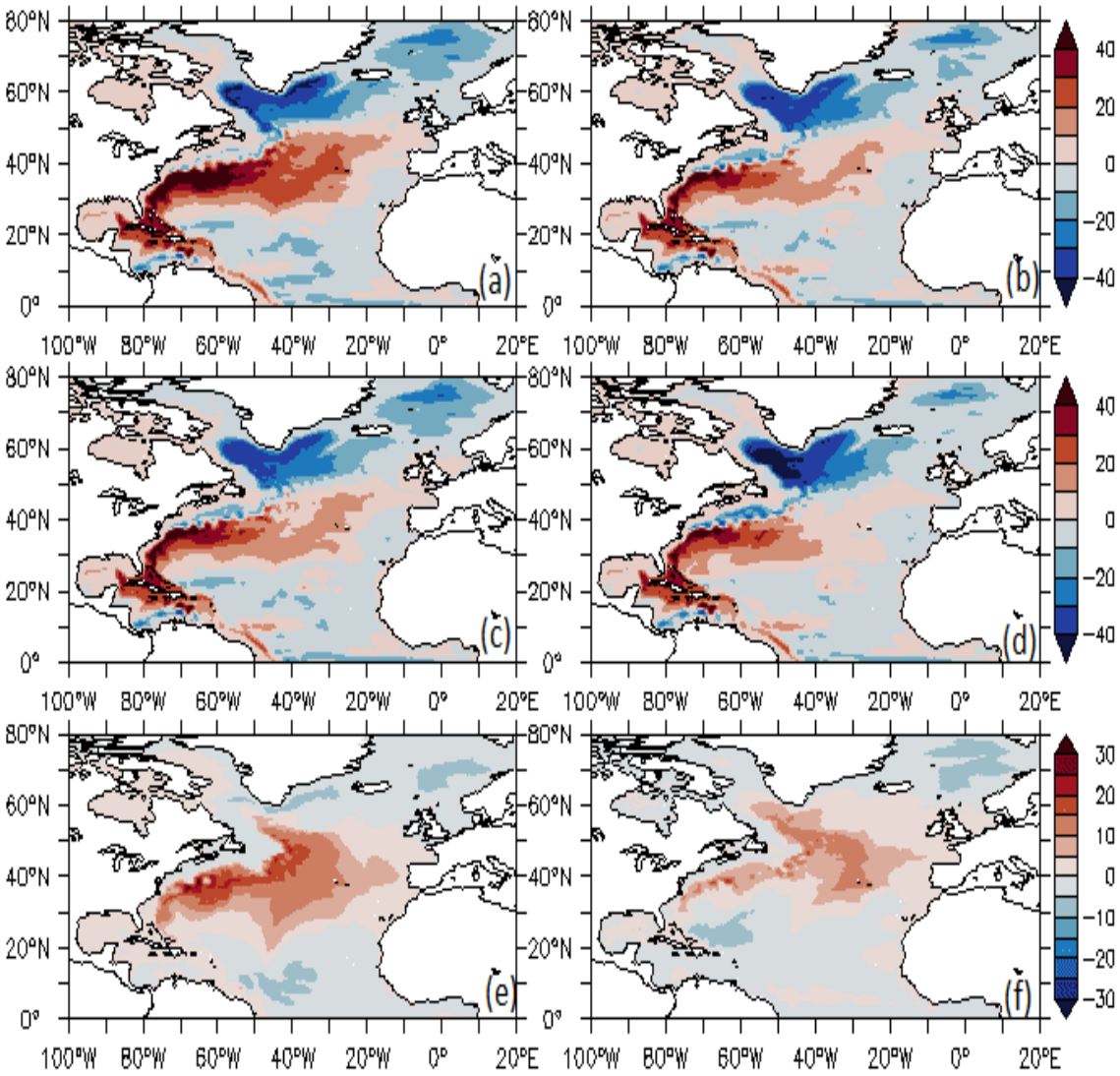

Figure 5.10: A composite mean of 50 January months across 1980 to 2014 from ocean ensemble data of Sverdrup transport obtained by vertically integrated meridional velocity and zonally integrated from east boundary to west boundary based on Eq.(5.14) during (a) high jet speed state, (b) low jet speed state, (c) high jet latitude state, and (d) low jet latitude state; Barotropic streamfunction difference between a composite of 50 January months of (e) the highest jet speed minus that for the lowest jet speed and (f) the highest jet latitude minus that for the lowest jet latitude (units: Sv = 10^6 m^3 s^{-1}).

In summary, Fig. 5.9 and Fig. 5.10 together can explain in the subtropical ocean interior that equatorward Sverdrup transport is balanced by return flow which is a strong boundary northward meridional transport. Over the subtropical gyre,

the western boundary current and interior respond to the wind stress induced Sverdrup transport. Sverdrup balance holds over the subtropical, but does not hold over the subpolar gyre. A strong jet enhances Sverdrup transport over the subtropical gyre due to enhanced wind stress curl. A more north jet enhances subtropical gyre circulation and shifting it further north at the same time.

What different possible mechanisms are there to explain the subpolar gyre circulation and transport? The next section explores this.

5.6.2 Response of barotropic flow to topographic Sverdrup and flat bottom Sverdrup

In this section, vertically depth-integrated horizontal velocity from bottom to surface is viewed as a barotropic flow (Welander, 1959) which is shown in Fig. 5.10.

The barotropic flow in the ocean over smoothly varying topography is controlled by contours of potential vorticity $\frac{f}{H}$ (Pedlosky, 1979; Koblinsky, 1990), where f is the Coriolis parameter and H is the ocean depth. Compared to barotropic flows in Fig. 5.10 and ocean bathymetry and $\frac{f}{H}$ maps (Fig. 5.11), it can be seen that the barotropic flow patterns follow $\frac{f}{H}$ contours over the subpolar gyre and along the western boundary where the flow is strongly shaped by the ocean bottom topography, whether under a strong or weak, a more north or south jet stream circumstance, in particular, the barotropic difference anomalies patterns corresponding to high and low jet indices.

The potential vorticity gradient $\Delta\frac{f}{H}$ is a key basis to measure how the barotropic flow responds to external forcing. The topographic Sverdrup gain function G' is the ratio of β/H to planetary vorticity gradient $\Delta\frac{f}{H}$ (see details in the study by Koblinsky (1990)). For β/H, where H = 5000 m, therefore, G' describes flat bottom Sverdrup response versus topographic Sverdrup response.

G'^{-1} is the "effective β " (named β') of the fluid. In Fig. 5.12, red shaded colour represents the weak β' regime $G' > 1.5$ which implies flat bottom Sverdrup response is dominant. The flat bottom regime $0.5 < G' < 1.5$ showing yellow shaded colour. The strong β' regime $G' < 0.5$ indicates where $\Delta\frac{f}{H}$ is dominant showing navy blue shaded colour.

Over the North Atlantic domain, weak β' is confined to smaller isolated regions mainly at mid-latitudes (10°N to 40°N), where the local Sverdrup response will be stronger. The local Sverdrup response refers to vorticity due to wind stress curl - relative vorticity spinning fast or slow, or moving to another latitude related to planetary vorticity. In this study case, the positive barotropic streamfunction anomalies mean a strong anticyclonic wind stress curl is located mid-latitude under a strong jet compared to a weak jet, which indicates the local response is a negative relative vorticity or an equatorward Sverdrup flow (Fig. 5.9 e). Outside of the tropics, in middle latitudes, along west and east boundaries, most of the subpolar, the Labrador Sea and along Atlantic ridge regions there are strong β' effects, which enhance the planetary vorticity gradient $\Delta\frac{f}{H}$, where the topographic

Sverdrup response dominant which shows the flow follows isolines of $\frac{f}{H}$ (see in Fig. 5.10). We can see that most of the barotropic flow follows $\frac{f}{H}$ contours at the middle latitude and subpolar regions. The barotropic flow robust anomalies signals responding to wind forcing due to jet stream strength variation and latitude shifts mainly occur in flat bottom Sverdrup response regions (Fig. 5.10 e and f).

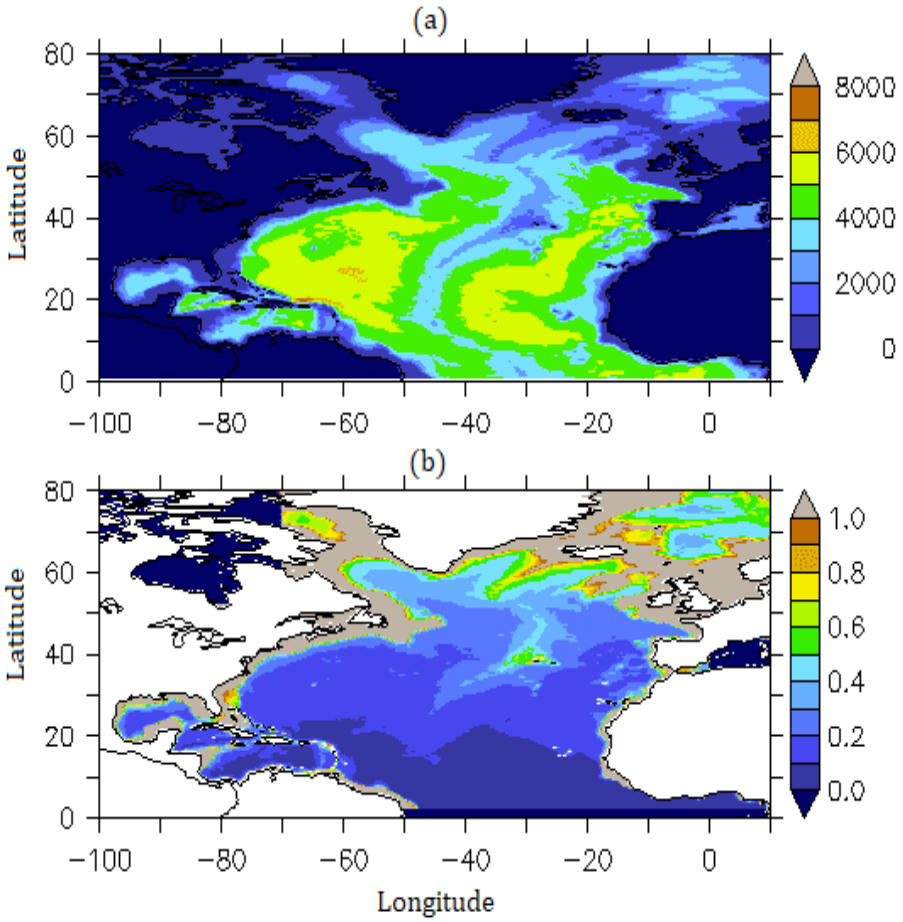

Figure 5.11: (a) Ocean bathymetry map (units: m) and (b) planetary vorticity $\frac{f}{H}$ distribution. f is Coriolis parameter and H is ocean depth. $\frac{f}{H}$ units:10^{-6} m^{-1} s^{-1}.

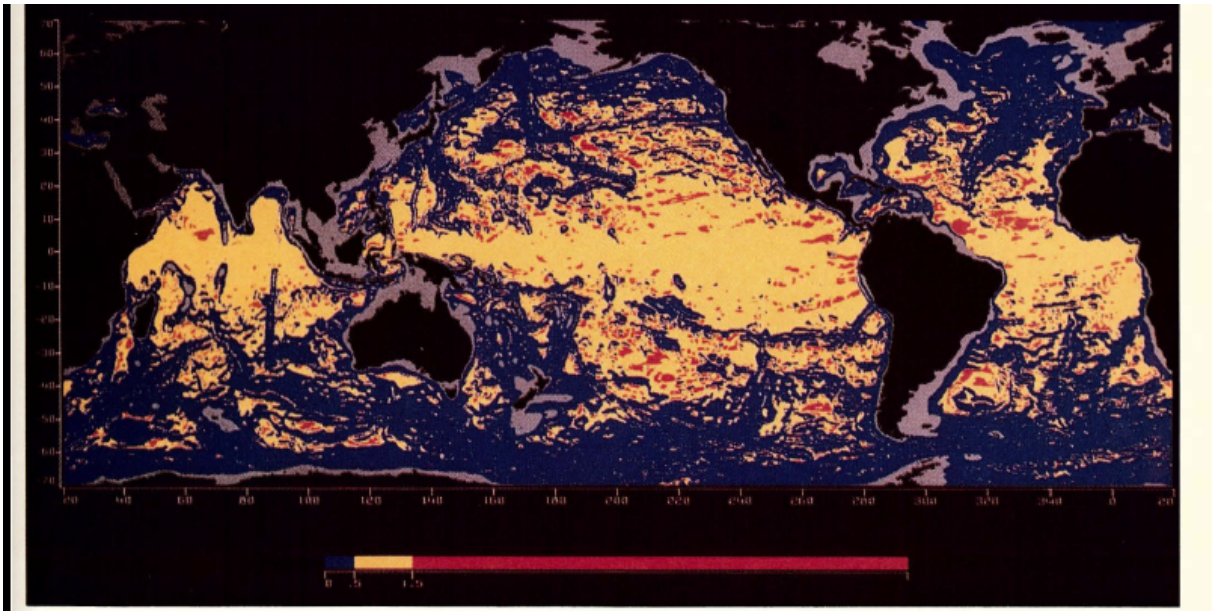

Plate 2 [*Koblinsky*]. An estimate of G' in the world ocean derived from the DBDB5 topographic data base. For this estimate the topography has been smoothed over 200 km.

Figure 5.12: Global ocean Topographic Sverdrup Gain Function from Koblinsky (1990).

In summary, the barotropic flow follows $\frac{f}{H}$ over the subpolar and western boundary regions and does not respond to the wind forcing local Sverdrup response associated with changes in jet speed and latitude. The barotropic flow over the interior of the subtropical gyre does respond to wind forcing local Sverdup response which is the flat bottom Sverdrup response regime.

5.7 Conclusion and discussion

In this study, it is found that jet stream strength and latitude location affect AMOC in different ways in the subtropical and subpolar gyres. On monthly to seasonal-time scales, with a strong jet, an AMOC cell is strengthened by about

9 Sv over the subtropical gyre, whereas, the AMOC is weakened by about -9 Sv over the subpolar gyre. AMOC anomalies associated with jet latitude are similar in pattern to the jet speed impact but shifted further north and with a weaker magnitude and narrow latitude ranges. The AMOC strengthens by about 7 Sv over the subtropical gyre and weakens by about -6 Sv over the subpolar gyre associated with a more northerly jet.

The possible mechanism is explored from wind stress induced Ekman horizontal and geostrophic transport due to the density contrast between western and eastern boundaries, as well as bottom velocity contribution. The AMOC is dynamically decomposed into Ekman MOC, geostrophic MOC and external mode MOC to investigate what is the dominant contribution for AMOC anomalies when jet stream strength and latitude shifts strike on the ocean surface.

The evidence supports my hypothesis that the AMOC strengthening or weakening signals are strongly caused by the surface wind stress induced Ekman flow plus its barotropic compensation, which is Ekman MOC, on monthly to seasonal timescales. A strong jet enhances Ekman MOC southward transport over the subpolar gyre which accounts for about 100% of the changes in total AMOC. Over the subtropical gyre, an enhanced northward Ekman transport over the subtropical gyre takes up to 80% of the changes in total AMOC. Geostrophic transport which is the thermal wind vertical shear contribution mainly over the subtropical regions at the upper ocean is about 20% of the total AMOC vari-

ability on monthly to seasonal timescales. The external mode impacts on the meridional overturning circulation in terms of of zonally nonuniform topography and frictional effects at the ocean boundaries as well as bottom velocity have very little effect at about 4% on this seasonal timescale (Fig. 5.6). Very similar AMOC balance is held for AMOC components responding to the jet latitude (Fig. 5.7) but all signals shifts further north and with weaker magnitudes.

The Sverdrup balance, or Sverdrup relation to the curl of wind stress reveals that over the subtropics, a strong or a more northward jet stream enhances negative wind stress curl of about up to -0.2 $\times 10^{-6}$ N m^{-3}, where the negative curl is consistent with southward flow in the interior, that is positive values of Sverdrup streamfunction Ψ, transporting about 40 Sv. The anomalies are about 30 Sv when the transport corresponds to that for a strong jet minus that for a weak jet. The southward Sverdrup transport is balanced by a same quantity strong northward west boundary current, such as the Gulf Stream.

Similarly, a more north jet stream offers a similar contribution for Sverdrup transport but whole signals shift further north and with weaker magnitudes over the subtropical gyre.

However, over the subpolar, where the positive curl is 0.5 $\times 10^{-6}$ N m^{-3} consistent with northward flow in the interior, northward flow in the interior of about -80 Sv is not balanced by southward boundary flow of about -30 Sv during a strong jet. Similarly with other jet states, the northward Sverdrup in the interior can not

be balanced by a southward boundary current from depth-integrated meridional flow. The Svedrup balance does not hold over the subpolar gyre. Additionaly, depth-integrated meridional flow anomalies show the subpolar gyre circulation does not respond to changes in the jet speed and latitude (see Fig. 5.10 e and f).

Horizontal circulation is measured by the barotropic streamfunction. Most of the barotropic flows respond to topographic Sverdrup with the flows following $\frac{f}{H}$ contours at the middle latitudes and subpolar regions. In these regions, enhanced the planetary vorticity gradient $\Delta\frac{f}{H}$ leads to a barotropic wind-forced response is weaker. Meanwhile, the barotropic flow robust anomalies signals responding to wind forcing due to jet stream strength variations and latitude shifts are mainly located in flat bottom Sverdrup response regions, where the wind stress curl induced Sverdrup balance holds.

On the monthly to seasonal-time scales, the effect of jet speed is more pronounced than that of jet latitude on the AMOC anomalies, Sverdrup transport and barotropic flow although the effect of jet latitude is important in shifting of the AMOC, Sverdrup transport and barotropic flow further north.

The limitations for my study about changes in the AMOC associated with the atmospheric jet stream are due to focusing on short-time scales of months to a season. Another limitation, when the AMOC is decomposed into three dynamical components, the Ekman component, geostrophic component and bottom velocity component, these are based on an assumption of no flow interaction with topo-

graphy which may show these three components mainly have an affect at the upper ocean.

The AMOC is part of a decadal to century-long time scale global ocean circulation. How much the short-time scale effect contributes to the longer-term AMOC and MOC changes will be the future scientific question. This study is based on DePreSys3 hindcast ensemble model data, there are no observational records long enough to provide a comparison to compare the results.

Chapter 6

Conclusion and Discussion

6.1 Conclusion and Discussion

The aim of the thesis is to investigate the interaction between the atmosphere and ocean in winter time since the ocean interacts with the atmosphere most actively in winter. To set up the context for this, in chapter 2, I re-investigate (i) the weather regimes' definition and frequency over the North Atlantic based on NCEP daily reanalysis sea level pressure and 500 hPa geopotential height fields from 1948 to 2016 in winter; (ii) the connection between the weather regimes and changes in ocean variables; (iii) can the eddy-driven jet stream speed strength and latitude shift reflect different weather regimes at the 850 hPa level?

My analysis reveals that there are five weather regimes which show different percentages in winter time over the North Atlantic: NAO+ (21%), NAO- (24.8%), Central Atlantic Ridge (18%), Central Atlantic Trough (19%) and Scandinavian

Blocking (20%) (see details in section 2.3 and table 1). My study shows that the weather regimes strongly affect ocean variables in different ways depending on whether they are dominated by a cyclonic or anticyclonic circulation (see section 2.4, Fig. 2.7, Fig. 2.8, Fig. 2.9, Fig. 2.10, Fig. 2.11).

The eddy-jet stream crosses the North Atlantic at different speeds and latitude locations which can well reflect multi-weather regimes over the Atlantic (see section 2.5.1 in Fig. 2.12). The link between eddy-driven jet stream variability and weather regimes in the North Atlantic sector was consistent with the previous studies.

The new aspects in the context analysis are using my own definition for weather regimes and obtaining five weather regimes based on reanalysis data as in other studies and weather maps instead of using the clustering method. Compared to how previous studies defined weather regimes based on the k-mean clustering method, there are some advantages in using my definitions: (i) these definitions are independent of the data set; (ii) it allows some days to be in more than one regime or in none.

The jet stream speed and latitude location can reflect multi-weather regimes. Therefore, the jet indices are chosen to investigate interaction between the atmosphere and the ocean which is a key new approach in the thesis. This chapter sets the scene by linking this to weather regimes. The advantages of choosing the speed and latitude of the jet: (i) two indices can reflect at least these five weather

regimes; (ii) the jet speed and latitude are simple and more direct indices to use.

The speed and latitude of the atmospheric jet stream is defined by the maximum value of the monthly-mean zonal wind at 850hPa averaged longitudinally over the North Atlantic sector (60°W to 0°).

In chapter 3, the role of the atmosphere in driving the North Atlantic ocean surface variables is explored on monthly and seasonal timescales. For each season, the evolution of forty individual ensemble members provides the ocean and atmospheric initial conditions which are perturbed, each initialised with identical ocean states and small perturbations in the atmosphere.

The atmospheric jet strongly affects the wintertime pattern of air-sea latent and sensible heat flux anomalies. 40% to 50% of the total variance in heat flux over parts of the subpolar region and up to 35% of the variance over the rest of the ocean is explained by the variance in jet speed. As a result, that changes in sea surface temperature account for up to 35% of the variance in February is explained by the January jet speed. Changes in the winter sea-ice are about up to 20% to 35% of the variance in the Labrador Sea and the east Greenland Sea. Variability in the atmospheric eddy-driven jet strongly affects seasonal variability in the surface ocean over the North Atlantic, controlling nearly half of the variance in air-sea heat fluxes and over a third of the subsequent surface temperature variance. There is also a strong imprint on sea-ice fraction, a stronger jet acting to enhance the sea-ice fraction in relatively ice-depleted regions, but to reduce the sea-ice fraction

in relatively ice-extensive regions, which is about a quarter of the variance. There are subtle differences in how indices of jet speed and location affect the surface ocean with the effect of jet speed being generally more pronounced than that of jet latitude, although the effect of jet latitude is important in defining the location of the regional response.

My study assesses the effect of the atmospheric jet on the surface ocean using monthly ensemble data, which may omit the effect of sub-monthly synoptic weather variability. To test this simplification, I compare how the jet indices connect to surface heat flux using daily reanalysis data versus monthly ensemble and reanalysis data and find that their relationships are broadly similar. Hence, monthly timescale variability in the eddy-driven jet alone can account for a significant fraction of the North Atlantic sea surface temperature changes that develop during the winter.

Ocean dynamics is important in generating ocean internal variability, which may possibly also modify atmospheric variability. However, my sensitivity analysis of the spread in ensembles for each year reveals that ocean surface temperature is not correlated to subsequent monthly estimates of the jet speed strength and latitude shifts, so I have not found any statistically-significant signals of the ocean variability driving subsequent changes in the atmospheric jet stream when averaged over the 35 years of model data.

In chapter 4, how the ocean subsurface temperature responds to the jet stream

strength and latitude location is explored. Surface ocean temperature anomalies associated with jet indices can penetrate into the subsurface revealing a tripole pattern for a depth ranging from the surface to 147 to 300m associated with jet speed and latitude, respectively. The vertical extent of subsurface temperature signals extends down to 300 metres in the subpolar gyre where the deep climatological mixed layer is located. The mixed layer depth is deepest in winter over the subpolar region based on ensemble model data and previous studies, such as (Kara et al., 2003; De Boyer Montégut et al., 2004).

The mixed layer depth is sensitive to the surface heat flux, with enhanced heat loss deepening the mixed layer. A strong or more north jet acts to enhance surface heat loss over the subpolar gyre so that the mixed layer is sensitive to the jet speed and latitude here due to enhanced heat loss. A deepening mixed layer over the subpolar gyre associated with a strong or more north jet is favourable for surface and interior communication due to the vertical convection being active and deep in winter.

The mixed layer depth is not sensitive to the jet speed and latitude over the subtropical gyre due to less heat loss here associated with a strong or more northward jet. However, the depth range over which the surface temperature anomalies over the west subtropical gyre associated with jet speed penetrate down to 200m are due to the climatological mixed layer being about 200m in this region. The surface temperature anomalies over the east region between subtropical and subpolar

gyre (intergyre region), associated with jet latitude penetrating down to 300m, are due to the climatological mixed layer being about 300m here.

In comparison, the signal of temperature anomalies associated with jet speed is more robust than that of jet latitude (Fig. 4.7). However, the temperature anomalies penetrate more deeply between a subtropical and subpolar gyre associated with jet latitude because the subtropical temperature anomalies shift further north and east associated with a more northward jet (Fig. 4.8), where the mixed layer is deeper than the west subtropical gyre (see Fig. 4.2, Fig. 4.9, Fig. 4.10).

The vertical temperature budget balance case study reveals that the surface temperature anomalies penetrate into depth via two main processes: (1) surface heat loss in winter and colder and denser water sinking by convection. (2) cold water from the thermocline entrained into the mixed layer depth by an entrainment process due to the mixed layer deepening in autumn and winter.

The three main scientific questions revealed in chapter 4 are new work: (i) subsurface temperature variation strongly responding to the surface temperature anomalies associated with jet stream speed and latitude; (ii) the surface temperature anomalies vertically penetrate into depth via the mixed layer depth; (iii) the mixed layer depth strongly responds to the jet stream speed and latitude over the subpolar gyre.

In chapter 3 and 4, my study revealed that the jet stream wind strength and

latitude location impacts on the North Atlantic ocean surface to upper ocean heat anomalies. Temperature anomalies from surface to upper ocean associated with jet strength and latitude location lead to changes in ocean buoyancy anomalies on the ocean boundaries. Consequently, changes occur in meridional geostrophic transport. Jet stream strength and latitude shifts also affect surface wind stress patterns and strength which lead to Ekman meridional transport anomalies. Hence, the final scientific question is explored in chapter 5 as to how the basin-scale AMOC cells respond to atmospheric jet stream strength and latitude variation from monthly to seasonal time scales using DePreSys3 ensemble model data in winter months from 1980 to 2014.

My study shows that the jet stream strength and latitude location affect AMOC in different ways in the subtropical and subpolar gyres. On monthly to seasonal-time scales, with a strong jet, an AMOC cell is strengthened by about 9 Sv over the subtropical gyre, whereas, the AMOC is weakened by about -9 Sv over the subpolar gyre. AMOC anomalies associated with jet latitude are similar in pattern to the jet speed impact but shifted further north and with a weaker magnitude and narrow latitude ranges. The AMOC strengthens by about 7 Sv over the subtropical gyre and weakens by about -6 Sv over the subpolar gyre associated with a more northerly jet.

The possible mechanism is explored from (i) wind stress induced Ekman horizontal transport, (ii) geostrophic transport due to the density contrast between

western and eastern boundaries, and (iii) bottom velocity contribution. The AMOC is dynamically decomposed into Ekman MOC, geostrophic MOC and external mode MOC to investigate what is the dominant contribution for AMOC anomalies when jet stream strength and latitude shifts strike on the ocean surface.

The evidence supports my hypothesis that on monthly to seasonal timescales, the AMOC strengthening or weakening signals are strongly caused by the surface wind stress induced Ekman flow plus its barotropic compensation, which is Ekman MOC. A strong jet enhances Ekman MOC southward transport over the subpolar gyre which accounts for nearly 100% of the changes in total AMOC. Over the subtropical gyre, an enhanced northward Ekman transport over the subtropical gyre takes up to 80% of the changes in total AMOC. Geostrophic transport which is the thermal wind vertical shear contribution mainly over the subtropical regions at the upper ocean is about 20% of the total AMOC variability on monthly to seasonal timescales. The external mode impacts on the meridional overturning circulation in terms of bottom velocity have very little effect, about 4% on the seasonal timescale (Fig. 5.6). Very similar AMOC components hold for the the changes in total AMOC responding to the jet latitude (Fig. 5.7) but all signals shift further north and with weaker magnitudes.

The Sverdrup balance, or Sverdrup relation to the curl of wind stress reveals that over the subtropics, during strong or more northward jet states, negative wind stress curl anomalies about up to -0.2 $\times 10^{-6}$ N m^{-3}, where the negative

curl is consistent with southward flow in the interior, that is positive values of Sverdrup streamfunction Ψ. The anomalies are about 30 Sv when the transport corresponds to that for a strong jet minus that for a weak jet. The southward Sverdrup transport is balanced by a strong northward current, such as the Gulf Stream.

However, over the subpolar region where the positive curl is 0.5 $\times 10^{-6}$ N m^{-3} consistent with northward flow in the interior, that is negative values of Ψ about -80 Sv during a strong jet and anomalies are about -30 Sv. Over the subpolar gyre, the northward Sverdrup transport based on wind stress curl in the interior is not balanced by a southward boundary current based on depth-integrated meridional flow.

Over the subtropical, the southward Sverdrup transport is balanced by a same quality strong northward west boundary current, such as the Gulf Stream. The northward Sverdrup in the interior can not be balanced by a southward boundary current. The Svedrup balance mode does not hold over the subpolar gyre.

Horizontal circulation is measured by the barotropic streamfunction. Most of the barotropic flow follows $\frac{f}{H}$ contours at some of the middle latitudes, subpolar regions, and along the west boundary, where β effects are strong, so enhancing the planetary vorticity gradient $\Delta\frac{f}{H}$, meaning a non-local response. Also, wind stress curl (relative vorticity) drives flow across $\frac{f}{H}$ contours, such as the Gulf Stream, leading to a wind-forced response. Meanwhile, the robust barotropic

positive anomalies (clockwise circulation) responding to wind forcing due to jet stream strength and latitude variation are mainly located interior of subtropical gyre where it is influenced by negative wind stress curl so that the flow may respond to both relative vorticity due to wind forcing and planetary vorticity $\frac{f}{H}$ due to potential vorticity gradient $\Delta\frac{f}{H}$ increasing (see Fig. 5.10 e and Fig. 5.11 and Fig. 5.9 e).

6.2 Future Work Discussion

Overall, throughout the whole thesis, we can see that atmospheric eddy-driven jet stream strength and latitude location strongly impact the underlying ocean from surface to interior on a seasonal timescale. This thesis has important new aspects for future study for atmosphere and ocean interaction which may be taken into account:

(i) Exploration of atmospheric influence on ocean from surface to interior in middle latitudes is viewed from the atmospheric jet stream perspective in this thesis. The atmospheric influence on the North Atlantic ocean has often been viewed in terms of the North Atlantic Oscillation (NAO) for nearly half a century even though multi-weather regimes are involved in recent studies. The main advantages for using an eddy-driven jet stream to measure middle latitude atmospheric variability are:

(a) the atmospheric jet stream in terms of jet speed strength and latitude loca-

tion can reflect multi-weather regimes which are defined in this study and other studies; (b) using atmospheric jet stream to measure atmosphere variability only has two indices which is simple and more physically direct.

(ii) In this study, the primary assumption is that the spread in different realisations of the chaotic atmospheric variability between ensemble members can drive the following SST. Another assumption is that the spread in different realisations of the perturbed ocean variability can drive atmospheric variability (jet stream) over the following few months. The sensitivity analysis of the spread in ensembles for each year, then averaged over 35 years, reveals that the spread in atmospheric variability (jet stream) can influence ocean surface temperature persisting for up to 4 months. Whereas, subsequent monthly estimates of the jet speed strength and latitude shifts variability are not sensitive to in SST variability on monthly to seasonal timescales.

However, there are studies arguing that the jet stream is influenced by ocean surface temperature on longer, interannual timescales, where the NAO is found to be sensitive to imposed surface temperature in an atmosphere-only model and where there may be a positive feedback between the atmospheric circulation and surface temperature. The study by (Dunstone et al., 2016) show the preceding SST predicted following winter NAO based on DePreSys3 hindcast ensemble model data by simply use ensemble mean data across 35 years correlation. Recent study (Baker et al., 2019) used an atmosphere-only linear statistical-dynamical

model to identify that indices of jet latitude and jet speed are sensitive to surface temperature.

Hence, in the future, more work needs to be done to identify if the SST variability influences the following atmospheric variability for different timescales, such as, seasonal, interannual and decadal timescales.

In my study the sea surface temperature variance on a seasonal time scale associated with jet takes about 35%. Here, the remaining question is 'what is the rest of the variance due to?'. It may likely be influenced by other large scale atmospheric patterns, as well as by synoptic variability and ocean internal dynamics. On the other hand, SST decadal and multi-decadal variability may have an influence on seasonal SST variability.

The remaining question is about the vertical heat balance only being about 50% balanced in later summer and autumn at 60°N,30°W and 36°N,60°W locations when summing up the components. The heat is balanced well at location 50°N,20°W. Hence, for vertical heat balance, there may be other mechanisms for later summer and autumn at different locations either different advection contribution or extra mixing due to the previous seasons' influence which needs further investigation in the future.

Meantime, SST variability on decadal or multi-decadal timescales shall be considered for the surface temperature anomalies and balance because SST variability itself has an important role instead of being influenced by local surface heat

flux. Atlantic multi-decadal variability has a significant regional climate impact. The ocean plays an important role in this long time-scale in which a warmer SST releases more heat and a colder SST releases less heat. How much do SST interannual and decadal variabilities have an effect on the surface heat flux, consequently affecting budget, instead of seasonal surface heat flux and other local processes? These will be the future scientific questions to address.

The limitations for my study about changes in the AMOC associated with the atmospheric jet stream are due to focusing on short-time scales of months to a season. Another limitation, when the AMOC is decomposed into three dynamical components, the Ekman component, geostrophic component and bottom velocity component are based on an assumption of no flow interaction with topography which may show these three components mainly have an affect at the upper ocean. Future work needs to be focused on real topography influence.

How well are the conclusions based on the DePreSys3 ensemble model data likely to translate to the real ocean? The conclusions follow general ocean dynamical and thermodynamical principles well. For example, surface strong wind causes more heat loss, cooling the surface, deepening the mixed layer depth. For another example, surface and subsurface heat anomalies generate a density difference leading to colder surface water sinking by a convection process via a deep mixed layer depth in winter. The AMOC variability is dominated by wind stress induced Ekman transport variability on seasonal timescales which is well supported by the

previous studies.

However, what level of accuracy the model data achieves is still a challenging question to answer. More observations, data and analysis are needed to compare to the model results in the future.

In summary, in the future, (i) atmosphere and ocean interaction in perspective on jet stream speed and latitude variation shall be implemented on longer timescales, such as interannual, decadal or even multi-decadal timescales; (ii) AMOC decomposed into three dynamical components needs to consider ocean topography in detail, also consider longer timescales; (iii) More observational data is needed and more observational analysis is needed to compare to the model results.

Appendix **A**

Ocean Ensemble Data Description

(A)

The Met Office Hadley DePreSys3 hindcast ocean NEMO model resolution is: the spatial coverage grids of longitude and latitude with 1442 × 1021 points. 40 ensembles monthly data is from from 1980 -2014. The ocean data is 2-D 1442 × 1021 curvilinear at latitude and longitude coordinate.

In ocean T files, the latitude and longitude ranges are -77.01048°N - 89.94787°N, -180°E to 180°E. The following variables are extracted from T files for this study:

votemper (1442 × 1201 × 40 × 75): the ocean sea water potential temperature at 75 depths. Units: °C;

rhop (1442 × 1201 × 40 × 75): Sea water sigma theta (σ_θ) at 75 depths, which is potential density minus 1000 kg m^{-3}. For example, where potential density ρ = 1024.32 kg m^{-3}, then σ_θ = 24.32 kg m^{-3}. It is the difference between the actual density and a reference value ρ_{ref} = 1000 kg m^{-3}. Units: kg m^{-3}.

somxl010 (1442 × 1021 × 40): Ocean mixed layer thickness is defined by sigma theta (σ_θ) 0.01 kg m^{-3}. The mixed layer depth is defined as the ocean depth at which σ_θ has increased by 0.01 kg m^{-3} relative to the near-surface value at 10 m depth. Units: m;

sossheig (1442 × 1021 × 40): Sea surface height. Unit: m.

sohefldo (1442 × 1021 × 40): Ocean surface net download heat flux in sea water. Units: W m^2.

nav_lat(x,y): x=1:1442; y=1:1021;

nav_lon(x,y): x=1:1442; y=1:1021;

e1t,e2t and e3t: scale factor 1, scale factor 2 and scale factor 3;

75 depths: from 1 to 75 levels, which is from surface to 5902 metres.

(B)

(i) In the U and V files, latitude and longitude ranges are -77.01048°N - 89.9976°N, -179.9991°E - 179.9996°E. The following variables are extracted from U and V files for this study:

vozocrtx (1442 × 1021 × 40 × 75): Ocean zonal current velocity at 75 depths. Units: m s^{-1};

vomecrty (1442 × 1021 × 40 × 75): Ocean meridional current velocity at 75 depths. Units: m s^{-1};

sozotaux (1442 × 1021 × 40): Ocean surface wind stress along i-axis. Units: N m^{-2};

sometauy ($1442 \times 1021 \times 40$): Ocean surface wind stress along j-axis. Units: N m^{-2};

nav_lat(x,y): x=1:1442; y=1:1021;

nav_lon(x,y): x=1:1442; y=1:1021;

e1u,e2u and e3u: scale factor 1, scale factor 2 and scale factor 3 for U;

e1v,e2v and e3v: scale factor 1, scale factor 2 and scale factor 3 for V;

75 depths: from 1 to 75 levels, which is from surface to 5902 metres.

Bibliography

M. A. Alexander, J. D. Scott, and C. Deser. Processes that influence sea surface temperature and ocean mixed layer depth variability in a coupled model. *Journal of Geophysical Research: Oceans*, 105(C7):16823–16842, 2000.

M. A. Alexander, U. S. Bhatt, J. E. Walsh, M. S. Timlin, J. S. Miller, and J. D. Scott. The atmospheric response to realistic Arctic sea ice anomalies in an AGCM during winter. *Journal of climate*, 17(5):890–905, 2004.

AMS. *Glossary of Meteorology*, accessed 2020a. URL `https://glossary.ametsoc.org/wiki/Geopotential_height`.

AMS. *Glossary of Meteorology*, accessed 2020b. URL `https://glossary.ametsoc.org/wiki/Sea_level_pressure`.

H. S. Baker, T. Woollings, and C. Mbengue. Eddy-driven jet sensitivity to dia-

batic heating in an idealized GCM. *Journal of Climate*, 30(16):6413–6431, 2017.

H. S. Baker, T. Woollings, C. E. Forest, and M. R. Allen. The linear sensitivity of the North Atlantic Oscillation and eddy-driven jet to SSTs. *Journal of Climate*, 32(19):6491–6511, 2019.

N. Barrier, C. Cassou, J. Deshayes, and A.-M. Treguier. Response of North Atlantic Ocean circulation to atmospheric weather regimes. *Journal of Physical Oceanography*, 44(1):179–201, 2014.

H. Binder, M. Boettcher, C. M. Grams, H. Joos, S. Pfahl, and H. Wernli. Exceptional air mass transport and dynamical drivers of an extreme wintertime Arctic warm event. *Geophysical Research Letters*, 44(23):12–028, 2017.

J. Bjerknes. Atlantic air-sea interaction. In *Advances in Geophysics*, volume 10, pages 1–82. Elsevier, 1964.

M. L. Blackmon. A climatological spectral study of the 500 mb geopotential height of the Northern Hemisphere. *Journal of the Atmospheric Sciences*, 33 (8):1607–1623, 1976.

M. L. Blackmon, J. M. Wallace, N.-C. Lau, and S. L. Mullen. An observational study of the Northern Hemisphere wintertime circulation. *Journal of the Atmospheric Sciences*, 34(7):1040–1053, 1977.

N. E. Bowler, A. Arribas, S. E. Beare, K. R. Mylne, and G. J. Shutts. The local ETKF and SKEB: Upgrades to the MOGREPS short-range ensemble prediction system. *Quarterly Journal of the Royal Meteorological Society*, 135 (640):767–776, 2009.

T. J. Bracegirdle, H. Lu, R. Eade, and T. Woollings. Do CMIP5 models reproduce observed low-frequency North Atlantic jet variability? *Geophysical Research Letters*, 45(14):7204–7212, 2018.

K. E. Brainerd and M. C. Gregg. Surface mixed and mixing layer depths. *Deep Sea Research-Part I-Oceanographic Research Papers*, 42(9):1521–1544, 1995.

H. L. Bryden, H. R. Longworth, and S. A. Cunningham. Slowing of the atlantic meridional overturning circulation at 25 n. *Nature*, 438(7068):655–657, 2005.

M. W. Buckley and J. Marshall. Observations, inferences, and mechanisms of the atlantic meridional overturning circulation: A review. *Reviews of Geophysics*, 54(1):5–63, 2016.

L. Caesar, S. Rahmstorf, A. Robinson, G. Feulner, and V. Saba. Observed fingerprint of a weakening Atlantic ocean overturning circulation. *Nature*, 556 (7700):191–196, 2018.

L. Caesar, S. Rahmstorf, and G. Feulner. On the relationship between Atlantic meridional overturning circulation slowdown and global surface warming. *Environmental Research Letters*, 15(2):024003, 2020.

C. Cassou, L. Terray, J. W. Hurrell, and C. Deser. North Atlantic winter climate regimes: Spatial asymmetry, stationarity with time, and oceanic forcing. *Journal of Climate*, 17(5):1055–1068, 2004.

C. Cassou, M. Minvielle, L. Terray, and C. Périgaud. A statistical–dynamical scheme for reconstructing ocean forcing in the Atlantic. Part I: weather regimes as predictors for ocean surface variables. *Climate Dynamics*, 36(1-2):19–39, 2011.

D. R. Cayan. Latent and sensible heat flux anomalies over the Northern Oceans: Driving the sea surface temperature. *Journal of Physical Oceanography*, 22: 859–881, 1992.

X. Cheng and J. M. Wallace. Cluster analysis of the northern hemisphere wintertime 500-hpa height field: Spatial patterns. *Journal of the Atmospheric Sciences*, 50(16):2674–2696, 1993.

M. F. Cronin, N. A. Pelland, S. R. Emerson, and W. R. Crawford. Estimating diffusivity from the mixed layer heat and salt balances in the North Pacific. *Journal of Geophysical Research: Oceans*, 120(11):7346–7362, 2015.

A. Czaja. Atmospheric control on the thermohaline circulation. *Journal of Physical Oceanography*, 39(1):234–247, 2009.

A. Czaja and C. Frankignoul. Observed impact of Atlantic SST anomalies on the North Atlantic Oscillation. *Journal of Climate*, 15(6):606–623, 2002.

H. F. Dacre and S. L. Gray. Quantifying the climatological relationship between extratropical cyclone intensity and atmospheric precursors. *Geophysical Research Letters*, 40:2322–2327, 2013.

C. De Boyer Montégut, G. Madec, A. S. Fischer, A. Lazar, and D. Iudicone. Mixed layer depth over the global ocean: An examination of profile data and a profile-based climatology. *Journal of Geophysical Research: Oceans*, 109(C12), 2004.

T. Delworth, S. Manabe, and R. J. Stouffer. Interdecadal variations of the thermohaline circulation in a coupled ocean-atmosphere model. *Journal of Climate*, 6(11):1993–2011, 1993.

T. L. Delworth and F. Zeng. The impact of the North Atlantic Oscillation on climate through its influence on the Atlantic meridional overturning circulation. *Journal of Climate*, 29(3):941–962, 2016.

S. Drijfhout and W. Hazeleger. Detecting Atlantic MOC changes in an ensemble of climate change simulations. *Journal of Climate*, 20(8):1571–1582, 2007.

N. Dunstone, D. Smith, A. Scaife, L. Hermanson, R. Eade, N. Robinson, M. Andrews, and J. Knight. Skilful predictions of the winter north atlantic oscillation one year ahead. *Nature Geoscience*, 9(11):809–814, 2016.

ECMWF. Geopotential 500 hPa and temperature at 850 hPa, accessed 2020a. URL `https://www.ecmwf.int/en/forecasts/charts/catalogue/`

medium-z500-t850-public?facets=undefined&time=2020092300,0,2020092300&projection=classical_europe.

ECMWF. Mean sea level pressure and wind speed at 850 hpa, accessed 2020b. URL https://www.ecmwf.int/en/forecasts/charts/catalogue/medium-mslp-wind850?facets=undefined&time=2020100300,0,2020100300&projection=classical_europe.

C. Eden and J. Willebrand. Mechanism of interannual to decadal variability of the North Atlantic circulation. *Journal of Climate*, 14(10):2266–2280, 2001.

G. Gastineau and C. Frankignoul. Influence of the North Atlantic SST variability on the atmospheric circulation during the twentieth century. *Journal of Climate*, 28(4):1396–1416, 2015.

A. Gill and P. Niller. The theory of the seasonal variability in the ocean. In *Deep Sea Research and Oceanographic Abstracts*, volume 20, pages 141–177. Elsevier, 1973.

J. P. Grist, S. A. Josey, R. Marsh, S. A. Good, A. C. Coward, B. A. de Cuevas, S. G. Alderson, A. L. New, and G. Madec. The roles of surface heat flux and ocean heat transport convergence in determining Atlantic Ocean temperature variability. *Ocean Dynamics*, 60:771–790, 2010.

S. K. Gulev, M. Latif, N. Keenlyside, W. Park, and K. P. Koltermann. North

Atlantic Ocean control on surface heat flux on multidecadal timescales. *Nature*, 499(7459):464, 2013.

T. Haine, C. Böning, P. Brandt, J. Fischer, A. Funk, D. Kieke, E. Kvaleberg, M. Rhein, and M. Visbeck. North Atlantic deep water formation in the Labrador Sea, recirculation through the subpolar gyre, and discharge to the subtropics. In *Arctic–Subarctic Ocean Fluxes*, pages 653–701. Springer, 2008.

S. Häkkinen, P. B. Rhines, and D. L. Worthen. Atmospheric blocking and Atlantic multidecadal ocean variability. *Science*, 334(6056):655–659, 2011.

R. Hall, R. Erdélyi, E. Hanna, J. M. Jones, and A. A. Scaife. Drivers of north atlantic polar front jet stream variability. *International Journal of Climatology*, 35(8):1697–1720, 2015.

A. Hannachi. On the origin of planetary-scale extratropical winter circulation regimes. *Journal of the Atmospheric Sciences*, 67(5):1382–1401, 2010.

A. Hannachi, D. M. Straus, C. L. Franzke, S. Corti, and T. Woollings. Low-frequency nonlinearity and regime behavior in the Northern Hemisphere extratropical atmosphere. *Reviews of Geophysics*, 55(1):199–234, 2017.

M. Hilmer and T. Jung. Evidence for a recent change in the link between the North Atlantic Oscillation and Arctic sea ice export. *Geophysical Research Letters*, 27(7):989–992, 2000.

J. Hirschi and J. Marotzke. Reconstructing the meridional overturning circulation from boundary densities and the zonal wind stress. *Journal of Physical Oceanography*, 37(3):743–763, 2007.

J. Hirschi, J. Baehr, J. Marotzke, J. Stark, S. Cunningham, and J.-O. Beismann. A monitoring design for the Atlantic meridional overturning circulation. *Geophysical Research Letters*, 30(7), 2003.

D. L. Hodson and R. T. Sutton. The impact of resolution on the adjustment and decadal variability of the Atlantic meridional overturning circulation in a coupled climate model. *Climate dynamics*, 39(12):3057–3073, 2012.

B. J. Hoskins and K. I. Hodges. New perspectives on the Northern Hemisphere winter storm tracks. *Journal of the Atmospheric Sciences*, 59(6):1041–1061, 2002.

B. J. Hoskins, I. N. James, and G. H. White. The shape, propagation and mean-flow interaction of large-scale weather systems. *Journal of the Atmospheric Sciences*, 40(7):1595–1612, 1983.

J. W. Hurrell. Decadal trends in the North Atlantic Oscillation: regional temperatures and precipitation. *Science*, 269:676–679, 1995.

J. W. Hurrell and C. Deser. North atlantic climate variability: the role of the North Atlantic Oscillation. *Journal of Marine Systems*, 79(3-4):231–244, 2010.

H.-J. Isemer and L. Hasse. Air-sea interactions. In *The Bunker Climate Atlas of the North Atlantic Ocean*, volume 2, page 252. Spring-Verlag, Berlin, 1987.

L. Jackson, R. Kahana, T. Graham, M. Ringer, T. Woollings, J. Mecking, and R. Wood. Global and european climate impacts of a slowdown of the AMOC in a high resolution GCM. *Climate Dynamics*, 45(11-12):3299–3316, 2015.

H. L. Johnson, P. Cessi, D. P. Marshall, F. Schloesser, and M. A. Spall. Recent contributions of theory to our understanding of the Atlantic Meridional Overturning Circulation. *Journal of Geophysical Research: Oceans*, 124(8): 5376–5399, 2019.

N. C. Johnson, S. B. Feldstein, and B. Tremblay. The continuum of Northern Hemisphere teleconnection patterns and a description of the NAO shift with the use of self-organizing maps. *Journal of Climate*, 21(23):6354–6371, 2008.

A. B. Kara, P. A. Rochford, and H. E. Hurlburt. An optimal definition for ocean mixed layer depth. *Journal of Geophysical Research: Oceans*, 105(C7): 16803–16821, 2000.

A. B. Kara, P. A. Rochford, and H. E. Hurlburt. Mixed layer depth variability over the global ocean. *Journal of Geophysical Research: Oceans*, 108(C3), 2003.

W. M. Kim, S. Yeager, P. Chang, and G. Danabasoglu. Low-frequency North Atlantic climate variability in the community earth system model large ensemble. *Journal of Climate*, 31(2):787–813, 2018.

J. R. Knight, C. K. Folland, and A. A. Scaife. Climate impacts of the Atlantic Multidecadal Oscillation. *Geophysical Research Letters*, 33(17), 2006.

C. Koblinsky. The global distribution of f/H and the barotropic response of the ocean. *Journal of Geophysical Research: Oceans*, 95(C3):3213–3218, 1990.

E. W. Kolstad, T. J. Bracegirdle, and I. A. Seierstad. Marine cold-air outbreaks in the North Atlantic: temporal distribution and associations with large-scale atmospheric circulation. *Climate Dynamics*, 33(2-3):187–197, 2009.

E. Kraus and J. Turner. A one-dimensional model of the seasonal thermocline ii. the general theory and its consequences. *Tellus*, 19(1):98–106, 1967.

E. B. Kraus and C. Rooth. Temperature and steady state vertical heat flux in the ocean surface layers. *Tellus*, 13(2):231–238, 1961.

S. Kravtsov. Pronounced differences between observed and CMIP5-simulated multidecadal climate variability in the twentieth century. *Geophysical Research Letters*, 44(11):5749–5757, 2017.

T. Lee and J. Marotzke. Seasonal cycles of meridional overturning and heat transport of the Indian Ocean. *Journal of Physical Oceanography*, 28(5):923–943, 1998.

T. Lee, W. Johns, R. Zantopp, and E. Fillenbaum. Moored observations of western boundary current variability and thermohaline circulation at 26.5N

in the subtropical North Atlantic. *Oceanographic Literature Review*, 1(44):6, 1997.

H. Lejenäs and H. Økland. Characteristics of northern hemisphere blocking as determined from a long time series of observational data. *Tellus A*, 35(5): 350–362, 1983.

S. Levitus and T. Boyer. World Ocean Atlas 1994, Vol. 4: Temperature, NOAA Atlas NESDIS 4, US Gov. *Printing Office, Wash., DC*, 117, 1994.

S. Levitus, R. Burgett, and T. Boyer. World Ocean Atlas 1994, vol. 3, Salinity, NOAA Atlas NESDIS 3. *US Department of Commerce, Washington, DC*, 1994.

M. R. Lewis, M.-E. Carr, G. C. Feldman, W. Esaias, and C. McClain. Influence of penetrating solar radiation on the heat budget of the equatorial Pacific Ocean. *Nature*, 347(6293):543–545, 1990.

Y. Liu, J. Attema, and W. Hazeleger. Atmosphere–Ocean Interactions and Their Footprint on Heat Transport Variability in the Northern Hemisphere. *Journal of Climate*, 33(9):3691–3710, 2020.

R. Lohmann, E. Jurado, H. A. Dijkstra, and J. Dachs. Vertical eddy diffusion as a key mechanism for removing perfluorooctanoic acid (PFOA) from the global surface oceans. *Environmental Pollution*, 179:88–94, 2013.

D. J. Lorenz and D. L. Hartmann. Eddy–zonal flow feedback in the Northern Hemisphere winter. *Journal of Climate*, 16(8):1212–1227, 2003.

M. Lozier, F. Li, S. Bacon, F. Bahr, A. Bower, S. Cunningham, M. De Jong, L. De Steur, B. Deyoung, J. Fischer, et al. A sea change in our view of overturning in the subpolar North Atlantic. *Science*, 363(6426):516–521, 2019.

M. S. Lozier, S. Leadbetter, R. G. Williams, V. Roussenov, M. S. C. Reed, and N. J. Moore. The spatial pattern and mechanisms of heat content change in the North Atlantic. *Science*, 319:5864, 800–803, 2008.

M. S. Lozier, V. Roussenov, M. S. C. Reed, and R. G. Williams. Opposing decadal changes for the North Atlantic meridional overturning circulation. *Nature Geoscience*, 3:728–734, 2010.

E. Madonna, C. Li, C. M. Grams, and T. Woollings. The link between eddy-driven jet variability and weather regimes in the North Atlantic-European sector. *Quarterly Journal of the Royal Meteorological Society*, 143(708):2960–2972, 2017.

J. Marotzke, R. Giering, K. Q. Zhang, D. Stammer, C. Hill, and T. Lee. Construction of the adjoint MIT ocean general circulation model and application to Atlantic heat transport sensitivity. *Journal of Geophysical Research: Oceans*, 104(C12):29529 – 29547, 1999.

J. Marshall and Coauthors. North Atlantic climate variability: phenomena, impacts and mechanisms. *Int. J. Climatol.*, 21(15):1863–1898, 2001.

J. Marshall and R. A. Plumb. *Atmosphere, Ocean and Climate Dynamics: An Introductory Text*. Academic Press, 2008.

J. Marshall, H. Johnson, and J. Goodman. A study of the interaction of the North Atlantic Oscillation with ocean circulation. *Journal of Climate*, 14(7): 1399–1421, 2001.

M. Mayer and L. Haimberger. Poleward atmospheric energy transports and their variability as evaluated from ECMWF reanalysis data. *Journal of Climate*, 25 (2):734–752, 2012.

C. Menkes, J. Vialard, S. Kennan, J. Boulanger, G. Madec, and K. Rodgers. A modelling study of the three-dimensional heat budget of tropical instability waves in the equatorial pacific. *J. Phys. Oceanogr*, 36(5):847–865, 2006.

C. Michel and G. Rivière. The link between Rossby wave breakings and weather regime transitions. *Journal of the Atmospheric Sciences*, 68(8):1730–1748, 2011.

P.-A. Michelangeli, R. Vautard, and B. Legras. Weather regimes: Recurrence and quasi stationarity. *Journal of the Atmospheric Sciences*, 52(8):1237–1256, 1995.

E. Moreno-Chamarro, P. Ortega, F. Gonzalez-Rouco, and M. Montoya. Assessing reconstruction techniques of the Atlantic Ocean circulation variability during the last millennium. *Climate Dynamics*, 48(3-4):799–819, 2017.

J. Moum and W. Smyth. Upper ocean mixing processes. *Encyclopedia of Ocean Sciences*, 6:3093–3100, 2001.

NCEP/NCAR. *NCEP/NCAR Reanalysis 1: Pressure*, accessed 2017. URL `https://psl.noaa.gov/data/gridded/data.ncep.reanalysis.pressure.html`.

NOAA. Blocking index, accessed 2017. URL `https://www.cpc.ncep.noaa.gov/products/precip/CWlink/blocking/index/index.nh.shtml`.

NOAA. *East Atlantic*, accessed 2020. URL `https://www.cpc.ncep.noaa.gov/data/teledoc/ea.shtml`.

A. Obata, J. Ishizaka, and M. Endoh. Global verification of critical depth theory for phytoplankton bloom with climatological in situ temperature and satellite ocean color data. *Journal of Geophysical Research: Oceans*, 101(C9):20657–20667, 1996.

F. Ogawa and T. Spengler. Prevailing surface wind direction during air–sea heat exchange. *Journal of Climate*, 32(17):5601–5617, 2019.

C. H. O'Reilly, S. Minobe, and A. Kuwano-Yoshida. The influence of the Gulf Stream on wintertime European blocking. *Climate Dynamics*, 47(5-6):1545–1567, 2016.

P. Ortega, J. Robson, R. T. Sutton, and M. B. Andrews. Mechanisms of

decadal variability in the Labrador Sea and the wider North Atlantic in a high-resolution climate model. *Climate Dynamics*, 49(7-8):2625–2647, 2017.

L. Papritz and T. Spengler. A Lagrangian climatology of wintertime cold air outbreaks in the Irminger and Nordic Seas and their role in shaping air–sea heat fluxes. *Journal of Climate*, 30(8):2717–2737, 2017.

R. Parfitt and H. Seo. A new framework for near-surface wind convergence over the Kuroshio extension and Gulf Stream in wintertime: The role of atmospheric fronts. *Geophysical Research Letters*, 45(18):9909–9918, 2018.

J. Pedlosky. *Geophysical Fluid Dynamics*. Springer, 1979.

B. Peña-Molino, S. Rintoul, and M. Mazloff. Barotropic and baroclinic contributions to along-stream and across-stream transport in the Antarctic Circumpolar Current. *Journal of Geophysical Research: Oceans*, 119(11):8011–8028, 2014.

A.-C. Peter, M. Le Hénaff, Y. Du Penhoat, C. E. Menkès, F. Marin, J. Vialard, G. Caniaux, and A. Lazar. A model study of the seasonal mixed layer heat budget in the equatorial Atlantic. *Journal of Geophysical Research: Oceans*, 111(C6), 2006.

J. G. Pinto and C. C. Raible. Past and recent changes in the North Atlantic oscillation. *Wiley Interdisciplinary Reviews: Climate Change*, 3(1):79–90, 2012.

D. Quadfasel. The atlantic heat conveyor slows. *Nature*, 438(7068):565–566, 2005.

I. G. Rigor, J. M. Wallace, and R. L. Colony. Response of sea ice to the Arctic Oscillation. *Journal of Climate*, 15(18):2648–2663, 2002.

C. D. Roberts, M. D. Palmer, R. P. Allan, D. G. Desbruyeres, P. Hyder, C. Liu, and D. Smith. Surface flux and ocean heat transport convergence contributions to seasonal and interannual variations of ocean heat content. *Journal of Geophysical Research: Oceans*, 122(1):726–744, 2017.

J. Robson, R. Sutton, K. Lohmann, D. Smith, and M. D. Palmer. Causes of the rapid warming of the North Atlantic Ocean in the mid 1990s. *J. Climate*, 25: 4116–4134, 2012.

M. J. Rodwell, D. P. Rowell, and C. K. Folland. Oceanic forcing of the wintertime North Atlantic Oscillation and European climate. *Nature*, 398(6725):320, 1999.

S. C. Scherrer, M. Croci-Maspoli, C. Schwierz, and C. Appenzeller. Two-dimensional indices of atmospheric blocking and their statistical relationship with winter climate patterns in the Euro-Atlantic region. *International Journal of Climatology: A Journal of the Royal Meteorological Society*, 26(2):233–249, 2006.

N. Schneider and P. Müller. The meridional and seasonal structures of the mixed-layer depth and its diurnal amplitude observed during the Hawaii-to-Tahiti Shuttle experiment. *Journal of Physical Oceanography*, 20(9):1395–1404, 1990.

I. R. Simpson, C. Deser, K. A. McKinnon, and E. A. Barnes. Modeled and observed multidecadal variability in the North Atlantic jet stream and its connection to sea surface temperatures. *Journal of Climate*, 31(20):8313–8338, 2018.

D. M. Smith and J. M. Murphy. An objective ocean temperature and salinity analysis using covariances from a global climate model. *Journal of Geophysical Research: Oceans*, 112(C2), 2007.

D. M. Smith, S. Cusack, A. W. Colman, C. K. Folland, G. R. Harris, and J. M. Murphy. Improved surface temperature prediction for the coming decade from a global climate model. *Science*, 317(5839):796–799, 2007.

M. A. Spall, R. A. Weller, and P. W. Furey. Modeling the three-dimensional upper ocean heat budget and subduction rate during the Subduction Experiment. *Journal of Geophysical Research: Oceans*, 105(C11):26151–26166, 2000.

M. Srokosz and H. Bryden. Observing the Atlantic Meridional Overturning Circulation yields a decade of inevitable surprises. *Science*, 348(6241):1255575, 2015.

V. N. Stepanov, D. Iovino, S. Masina, A. Storto, and A. Cipollone. Methods of calculation of the Atlantic meridional heat and volume transports from ocean models at 26.5N. *Journal of Geophysical Research: Oceans*, 121(2):1459–1475, 2016.

R. T. Sutton and B. Dong. Atlantic Ocean influence on a shift in European climate in the 1990s. *Nature Geoscience*, 5(11):788, 2012.

D. W. Thompson, S. Lee, and M. P. Baldwin. Atmospheric processes governing the northern hemisphere annular mode/North Atlantic Oscillation. *Geophysical Monograph-American Geophysical Union*, 134:81–112, 2003.

S. Tibaldi and F. Molteni. On the operational predictability of blocking. *Tellus A*, 42(3):343–365, 1990.

R. D. Torn, J. S. Whitaker, P. Pegion, T. M. Hamill, and G. J. Hakim. Diagnosis of the source of GFS medium-range track errors in Hurricane Sandy (2012). *Monthly Weather Review*, 143(1):132–152, 2015.

K. E. Trenberth and J. M. Caron. Estimates of meridional atmosphere and ocean heat transports. *Journal of Climate*, 14(16):3433–3443, 2001.

K. E. Trenberth and D. P. Stepaniak. Covariability of components of poleward atmospheric energy transports on seasonal and interannual timescales. *Journal of Climate*, 16(22):3691–3705, 2003.

J. Turner and E. Kraus. A one-dimensional model of the seasonal thermocline I. A laboratory experiment and its interpretation. *Tellus*, 19(1):88–97, 1967.

G. K. Vallis. *Essentials of Atmospheric and Oceanic Dynamics*. Cambridge University Press, 2019.

E. Van der Swaluw, S. Drijfhout, and W. Hazeleger. Bjerknes compensation at high northern latitudes: The ocean forcing the atmosphere. *Journal of Climate*, 20(24):6023–6032, 2007.

B. Vannière, A. Czaja, H. Dacre, and T. Woollings. A "cold path" for the Gulf Stream–troposphere connection. *Journal of Climate*, 30(4):1363–1379, 2017.

V. Vijith, P. Vinayachandran, B. G. Webber, A. J. Matthews, J. V. George, V. K. Kannaujia, A. A. Lotliker, and P. Amol. Closing the sea surface mixed layer temperature budget from in situ observations alone: operation advection during BoBBLe. *Scientific Reports*, 10(1):1–12, 2020.

M. Visbeck, E. P. Chassignet, R. G. Curry, T. L. Delworth, R. R. Dickson, and G. Krahmann. The ocean's response to North Atlantic Oscillation variability. *The North Atlantic Oscillation: climatic significance and environmental impact*, 134:113–145, 2003.

J. Wallace and D. Gutzler. Teleconnections in the geopotential height field during the northern hemisphere winter. *Monthly Weather Review*, 109:784–812, 1981.

D. Webb and N. Suginohara. Vertical mixing in the ocean. *Nature*, 409(6816): 37–37, 2001.

P. Welander. *On the vertically integrated mass transport in the oceans*. Rockefeller Institute Press, 1959.

K. Williams, C. Harris, A. Bodas-Salcedo, J. Camp, R. Comer, D. Copsey, D. Fereday, T. Graham, R. Hill, T. Hinton, et al. The Met Office global coupled model 2.0 (GC2) configuration. *Geoscientific Model Development*, 8 (5):1509–1524, 2015a.

R. G. Williams and M. J. Follows. *Ocean Dynamics and the Carbon Cycle: Principles and Mechanisms*. Cambridge University Press, 2011.

R. G. Williams, V. Roussenov, D. Smith, and M. S. Lozier. Decadal evolution of ocean thermal anomalies in the North Atlantic: the effects of Ekman, overturning, and horizontal transport. *J. Climate*, 27(2):698–719, 2014.

R. G. Williams, V. Roussenov, M. S. Lozier, and D. Smith. Mechanisms of heat content and thermocline change in the subtropical and subpolar North Atlantic. *Journal of Climate*, 28(24):9803–9815, 2015b.

T. Woollings. *Jet Stream: A Journey Through Our Changing Climate*. OUP Oxford, 2019.

T. Woollings, A. Hannachi, and B. Hoskins. Variability of the North Atlantic eddy-driven jet stream. *Q. J. R. Meteor. Soc.*, 136:856–868, 2010.

T. Woollings, C. Czuchnicki, and C. Franzke. Twentieth century North Atlantic jet variability. *Quarterly Journal of the Royal Meteorological Society*, 140(680): 783–791, 2014.

T. Woollings, C. Franzke, D. Hodson, B. Dong, E. A. Barnes, C. Raible, and J. Pinto. Contrasting interannual and multidecadal NAO variability. *Climate Dynamics*, 45(1-2):539–556, 2015.

T. Woollings, L. Papritz, C. Mbengue, and T. Spengler. Diabatic heating and jet stream shifts: A case study of the 2010 negative North Atlantic Oscillation winter. *Geophysical Research Letters*, 43(18):9994–10, 2016.

T. Woollings, E. Barnes, B. Hoskins, Y.-O. Kwon, R. W. Lee, C. Li, E. Madonna, M. McGraw, T. Parker, R. Rodrigues, et al. Daily to decadal modulation of jet variability. *Journal of Climate*, 31(4):1297–1314, 2018.

X. Zhai, R. J. Greatbatch, and J. Sheng. Diagnosing the role of eddies in driving the circulation of the northwest Atlantic Ocean. *Geophysical Research Letters*, 31(23), 2004.